

Copyright Undertaking

This thesis is protected by copyright, with all rights reserved.

By reading and using the thesis, the reader understands and agrees to the following terms:

- 1. The reader will abide by the rules and legal ordinances governing copyright regarding the use of the thesis.
- 2. The reader will use the thesis for the purpose of research or private study only and not for distribution or further reproduction or any other purpose.
- 3. The reader agrees to indemnify and hold the University harmless from and against any loss, damage, cost, liability or expenses arising from copyright infringement or unauthorized usage.

IMPORTANT

If you have reasons to believe that any materials in this thesis are deemed not suitable to be distributed in this form, or a copyright owner having difficulty with the material being included in our database, please contact lbsys@polyu.edu.hk providing details. The Library will look into your claim and consider taking remedial action upon receipt of the written requests.

INTERFACE ENGINEERING TOWARDS HIGHLY EFFICIENT INVERTED PEROVSKITE SOLAR CELLS

DONGYANG LI

PhD

The Hong Kong Polytechnic University

2025

The Hong Kong Polytechnic University

Department of Electrical and Electronic Engineering

Interface Engineering Towards Highly Efficient Inverted Perovskite Solar Cells

Dongyang Li

A thesis submitted in partial fulfillment of the requirements for the degree of Doctor of Philosophy

January 2025

CERTIFICATE OF ORIGINALITY

I hereby declare that this thesis is my own work and that, to the best of my knowledge and belief, it reproduces no material previously published or written, nor material that has been accepted for the award of any other degree or diploma, except where due acknowledgement has been made in the text.

	_(Signed)
DONGYANG LI	(Name of Student)

Abstract

The rapid advancements in perovskite solar cells (PSCs) technology have brought efficiencies comparable to silicon-based solar cells within a relatively short period. Despite these achievements, challenges such as stability, processibility and manufacturability issues hinder the developments of high efficiency PSCs. In addition, non-radiative recombination loss persists due to imperfect semiconducting properties and interfaces such as various defects.

This PhD research focus on interfacial engineering in PSCs, and three major strategies are investigated: surface passivation at the top perovskite surface, buried interface optimization, and molecular design and synthesis of self-assembled monolayers (SAMs).

Chapter 4 presents a strategy focused on enhancing the surface properties of inverted p-i-n PSCs (IPSCs) by incorporating an organic semiconductor - polymerized small molecular acceptor (PSMA) at the top surface of perovskite. This surface regulation approach led to improved grain orientation and reduced defect density, significantly boosting electron transport and overall device performance. The results demonstrated a marked power conversion efficiency (PCE) of 23.57%, with a fill factor (FF) of 84%. Stability tests showed promising results, with PSMA-treated devices retaining approximately 80% of their initial PCE after 1000 hours of continuous illumination under maximum power point (MPP) tracking. This chapter underscores the role of targeted surface passivation in achieving high efficiency and stability in IPSCs.

Chapter 5 explores a co-adsorbed (CA) approach for buried interface engineering in IPSCs. By employing 2-chloro-5-(trifluoromethyl)isonicotinic acid (PyCA-3F) between the 2PACz SAM and perovskite/organic layers, interfacial energy losses were minimized. This strategy reduced aggregation, enhanced surface smoothness, and improved the work function (W_F) of the SAM, creating a well-aligned heterointerface. The resulting devices exhibited enhanced crystallinity, minimized trap states, and

efficient charge transfer, achieving a certified PCE of 24.68%. Furthermore, the CA strategy was also effective in organic solar cells (OSCs), resulting in a PCE of 19.51%. Both device types maintained over 80% of their initial efficiency after prolonged operation, highlighting the effectiveness of this method in enhancing both performance and longevity.

Chapter 6 investigates the design and synthesis of novel self-assembled SAM in IPSCs. Two SAMs, PABDCB and MeO-PABDCB, featuring rigid phenylene linkers, were developed to construct densely packed, organized hole transport layers (HTLs). By replacing flexible carbon chains with rigid phenylene linkers, we achieve highly dense and ordered SAM coverage and preferable tridentate binding on ITO substrates. The methoxy-terminated SAM MeO-PABDCB further enhances interfacial dipole moments and passivates perovskite defects via Lewis basicity, thereby reducing trapassisted recombination. Our combined experimental and theoretical analyses reveal that rigid phenylene linkers minimize structural disorganization and improve π - π stacking, while methoxy termini align energy levels and stabilize interfaces. This SAM design yields enhancement in IPSCs with a power conversion efficiency of 26.25% and a fill factor of 86.4%, alongside exceptional operational and robust thermal cycle stability. Our work establishes a molecular engineering strategy that leverages rigidity through rigid linkers and tailored termini to advance SAM-based photovoltaics toward commercial viability.

These findings collectively underscore the importance of targeted interface engineering in enhancing the efficiency and durability of IPSCs, moving them closer to commercial applications in the near future.

Publications

- 1. **Dongyang Li**, Yulan Huang, Zhiwei Ren, Abbas Amini, Aleksandra B Djurišić, Chun Cheng* and Gang Li*. Recent Progress of Inverted Organic-inorganic Halide Perovskite Solar Cells[J]. *Journal of Energy Chemistry*, 2023, 79: 168-191. (*Chapter* 2)
- 2. **Dongyang Li**, Yulan Huang, Ruijie Ma*, Heng Liu, Qiong Liang, Yu Han, Zhiwei Ren, Kuan Liu, Patrick Wai-Keung Fong, Zhuoqiong Zhang, Qing Lian, Xinhui Lu, Chun Cheng* and Gang Li*. Surface Regulation with Polymerized Small Molecular Acceptor towards Efficient Inverted Perovskite Solar Cells [J]. *Advanced Energy Materials*, 2023, 13(18): 2204247. (*Chapter 4*)
- 3. **Dongyang Li**, Qing Lian, Tao Du, Ruijie Ma*, Heng Liu, Qiong Liang, Yu Han, Guojun Mi, Ouwen Peng, Guihua Zhang, Wenbo Peng, Baomin Xu, Xinhui Lu, Kuan Liu, Jun Yin, Zhiwei Ren*, Gang Li*, Chun Cheng*. Co-adsorbed Self-Assembled Monolayer Enables High-performance Perovskite and Organic Solar Cells[J]. *Nature Communications*, 2024. 15, 7605. (*Chapter 5*)
- 4. **Dongyang Li**, Qiming Yin, Zhiwei Ren*, Guihua Zhang, Jie Li, Qianyi Li, Yu Han, Sibo Li, Hao Xia, Guang Yang, Longbin Qiu, Ruijie Ma, Baomin Xu, Gang Li* and Chun Cheng*. Methoxy-Terminated Self-Assembled Monolayers Enable Highly Efficient Inverted Perovskite Solar Cells with Preferable Tridentate Bonding[J]. (*Under Review, Chapter 6*)
- 5. Qianyi Li, **Dongyang Li**, Zhiqi Li, Zhiwei Ren*, Yu Han, Qiong Liang, Guang Yang, Jiangsheng Yu, Peng Bai, Tao Zhu, Patrick W. K. Fong and Gang Li*, Tailoring Crystal Growth Regulation and Dual Passivation for Air Processed Efficient Perovskite Solar Cells[J]. *Advanced Science*. 2025: 2407401 (*Co-first Author*)
- 6. **Dongyang Li**, Xinyu Jiang, Peter Müller-Buschbaum, Ruijie Ma* and Gang Li, Research Comment: Enhancing Perovskite/Silicon Tandem Solar Cells through Nuclei Engineering. *Green Carbon*. 2025, 3(1): 48-49.

Acknowledgements

Time has flown by so quickly—it feels like just yesterday that I received the exciting news of starting my Ph.D. journey, and now, as it draws to a close, I am filled with gratitude. Over these past four years, I have been surrounded by the warmth, care, and generous support of my supervisors, colleagues, friends, and family. I want to extend my deepest and most heartfelt thanks to each of them for making this journey possible and so meaningful.

First and foremost, I am profoundly grateful to my supervisors, Prof. Gang Li and Prof. Chun Cheng, whose unwavering mentorship and patience guided me through every stage of this journey. Their insightful perspectives, rigorous approach to research, and deep understanding of the field have consistently pushed me to think more critically and deeply. Their expertise and enthusiasm have shaped this research and my own growth as a researcher in ways. I am especially thankful for the countless hours they devoted to reviewing drafts, providing constructive feedback, and inspiring me to keep moving forward.

I would also like to thank colleagues and friends in PolyU, including Dr. Patrick Fong, Dr. Zhiwei Ren, Dr. Ruijie Ma, Dr. Kuan Liu, Dr. Luyao Wang, Dr. Qiong Liang, Dr. Jiaming Huang, Dr. Jiehao Fu, Dr. Jiaqi He, Dr. Hao Xia, Dr. Tao Zhu, Dr. Zhiqi Li, Dr. Jiangsheng Yu, Yu Han, Zhen Lu, Zhengrong Wang, Yongwen Lang, Xiyun Xie, Lei Cheng, Yu Zheng, Jiyao Zhang and Qianyi Li. Their valuable insights, constructive criticism, and support have helped me refine my research and expand my understanding of the subject.

I would also express my special thanks to my colleagues and friends in SUSTech who made the journey more enjoyable and rewarding. Dr. Qing Lian, Dr. Yulan Huang, Dr. Zhuoqiong Zhang, Guojun Mi, Guihua Zhang, Qiming Yin, Jie Li, Hourui Ya and Chen Cheng provided constant support, encouragement, and camaraderie, and I am grateful for the collaborative and stimulating environment they helped create.

I am also deeply appreciative of the support and expertise Dr. Heng Liu and Prof.

Xinhui Lu in CUHK for their contributions to my Ph.D. study.

I am also grateful to Hongjia Huang and Yingying Huang for their continuous support, which enabled me to dedicate myself fully to this project. Their encouragement kept me grounded and motivated even in the toughest moments.

Above all, I owe my deepest gratitude to my parents. Their unconditional love, support, and belief in me have been my foundation and inspiration throughout this journey. This accomplishment is as much theirs as it is mine

To all who have been part of this journey, thank you for making this achievement possible and for enriching my life along the way.

Table of Contents

Abstract	I
Publications	III
Acknowledgements	IV
Table of Contents	VI
List of Figures	X
List of Tables	XX
List of Abbreviations	.XXI
Chapter 1 Introduction	1
1.1 Background	1
1.1.1 The Rise and Staus of Solar Cells	1
1.2 The Physics in Solar Cells	4
1.2.1 Photoelectric Effect and Carriers	4
1.2.2 Schottky-Queisser Limit	6
1.3 Fundamental Knowledge of Perovskite	8
1.3.1 Crystal Structure and Phase Transition	8
1.3.2 Optical Properties	14
1.3.3 Electronical and Mechanical Properties	14
1.4 Characterization of Solar Cells	15
1.4.1 Basic Solar Cell Photovoltaic Parameters	15
1.4.2 Real-Space Characterization Tools in Perovskite Solar	Cell
Research	18
1.4.3 Reciprocal-Space Characterization Tools in Perovskite Solar	Cell
Research	21
1.4.4 Optical Characterization Tools in Perovskite Solar Cell Rese	earch
	22
1.4.5 Photoelectron Spectroscopy Tools in Perovskite Solar	Cell
Research	24

1.5 Motivation	:6
1.6 Objectives2	27
Chapter 2 Fundamentals of Interfaces in Semiconductors and Their Role in Perovskit	te
Solar Cells	29
2.1 Introduction of Interfaces	29
2.2 Types of Interfaces in Semiconductors	9
2.2.1 Metal-Semiconductor Interfaces	29
2.2.2 Semiconductor-Semiconductor Interfaces	1
2.2.3 Interfaces within Semiconductors	2
2.3 Interface in Perovskite solar cells	4
2.3.1 Device Structure	4
2.3.2 Energy level and Working Mechanism	6
2.3.3 Defects	7
Chapter 3 Literature Review	9
3.2 Hole Transport Layers in Inverted Perovskite Solar Cells3	9
3.2.1 PTAA-based Inverted Perovskite Solar Cells	9
3.2.2 NiO _x -based Inverted Perovskite Solar Cells4	1
3.2.3 Self-assemble Monolayers based Inverted Perovskite Solar Cel	ls
4	5
3.2 Electron Transport Layer in Inverted Perovskite Solar Cells4	7
3.2.1 Fullerene-Based Inverted Perovskite Solar Cells4	7
3.2.2 Non-fullerene Acceptor-Based Inverted Perovskite Solar Cells.4	9
3.2.2 Inorganic Semiconductor-Based Inverted Perovskite Solar Cel	ls
5	51
3.3 Interface Engineering in Inverted Perovskite Solar Cells5	;4
3.3.1 Top Surface	;4
3.3.2 Buried Interface6	52
3.4 Issues and Opportunities of Inverted Perovskite Solar Cells6	55

Chapter 4 Surface Regulation with Polymerized Small Molec	ular Acceptor towards
Efficient Inverted Perovskite Solar Cells	67
4.1 Introduction	67
4.2 Experimental Section	69
4.2.1 Materials	69
4.2.2 Device Fabrication	69
4.2.3 Device Characterization	70
4.3 Results and Discussion	71
4.4 Summary	84
Chapter 5 Co-adsorbed Self-Assembled Monolayer Enabl	es High-performance
Perovskite and Organic Solar Cells	86
5.1 Introduction	86
5.2 Experimental Section	88
5.2.1 Materials	88
5.2.2 Device Fabrication	89
5.2.3 Device Characterization	90
5.3 Results and Discussion	93
5.4 Summary	120
Chapter 6 Methoxy-Terminated Self-Assembled Monolayers E	nable Highly Efficient
Inverted Perovskite Solar Cells with Preferable Tridentate Bond	ing121
6.1 Introduction	121
6.2 Experimental Section	123
6.2.1 Materials	123
6.2.2 Device Fabrication	123
6.2.3 Device Characterization	124
6.3 Results and Discussion	132
6.4 Summary	148
Chapter 7 Conclusion and Outlook	150

7.1 Conclusion	
7.2 Outlook	151

List of Figures

Figure 1.1 Development of solar cell materials and device structures. ¹ 2
Figure 1.2 The mechanism of photoelectric effect - a simple diagram of direct bandgap
semiconductor. ⁷
Figure 1.3 The intrinsic loss mechanism and the S-Q limit in solar cells. ⁷
Figure 1.4 Goldschmidt tolerance factor and the phase structures of perovskite. 10 10
Figure 1.5 Phase transition of FAPbI ₃ . 14
Figure 1.6 Typical J-V curves of solar cells
Figure 1.7 A detailed explanation of V_{OC} loss in solar cells. ²²
Figure 1.8 A typical transient PL spectrum based on MAPbI ₃ . ²⁷ 24
Figure 2.1 (a) Metal-semiconductor interface prior to thermodynamic equilibrium, both
metal and semiconductor show flat bands. (b) Metal-semiconductor interface at
thermodynamic equilibrium, showing band bending at the metal/semiconductor
interface. ²⁸ 30
Figure 2.2 (a) Schematic diagrams of energy band structures of homojunction PSCs in
non-ion migration status and (b) Schematic diagrams of energy band structures of
homojunction PSCs in ion migration status. ²⁹ 31
Figure 2.3 Schematic of energy level of planar heterojunction (PHJ) perovskite solar
cells. ³⁰
Figure 2.4 Schematic representation of band bending caused by interface states
sandwiched between two n-type semiconductor layers. ³¹
Figure 2.5 Device structures of perovskite solar cells
Figure 2.6 Typical interfaces in perovskite solar cells. ⁴⁴
Figure 2.7 (a) Scheme of the energy levels of each layer in IPSCs. (b) Working principle
of perovskite solar cells: 1) charge dissociation, 2) charge diffusion, 3) charge transport,
4) charge extraction, and 5) charge recombination. ⁴⁸
Figure 2.8 Imperfections in OIHP film and their passivation strategies. ⁵¹ 38
Figure 3.1 Schematic illustrations of charge transport between PTAA and perovskite

with/without PPS. ⁷² 41
Figure 3.2 (a) Scheme of synthesis of NiO _x and NiO _x -IL nanoparticles. ⁸⁰ (b) Mechanism
of GUA ₂ PbI ₄ interaction with NiO _x and PTAA substrate. ⁸⁶ 44
Figure 3.3 (a) Schematic demonstration and energy level alignment of SAM HTL and
perovskite in the SAM-based IPSCs. 96 (b) Molecular structures and UV-vis absorption
spectra of the Br-2EPO, Br-2EPT and Br-2EPSe. 100,101
Figure 3.4 The application of PCBM in IPSCs with grain boundary passivation. 107 48
Figure 3.5 (a) The energy level of ICBA in IPSCs. (b) The application of ICBA in Sn-
based IPSCs
Figure 3.6 (a) The synthesis route of BCM. (b) The cross-linking scheme from BCM to
CBCM. ¹¹⁰ 49
Figure 3.7 (a) The energy level of N2200 in IPSCs. 111 (b) The application of PDTzTI
in IPSCs. 114 (c) The synthesis route of PY-DFT. 113
Figure 3.8 The application of TiO ₂ ink in IPSCs. 116
Figure 3.9 The application of all-metal oxide charge transport layer IPSCs with ZnO as
ETL. ¹¹⁸ 53
Figure 3.10 The scheme of EDA bridged passivation with perovskite and SnO ₂ QDs. 120
53
Figure 3.11 (a) XRD patterns and structural images of LD perovskite single crystals. 121
(b) Scheme of 2D passivation with varied n layers under annealing and room
temperature. (c) Integrated GIWAXS maps and cross-sectional HR-STEM image. (d)
Energy level scheme. ⁹⁷
Figure 3.12 (a) The interaction between PPP polymer and perovskite and device
structure of IPSCs. (b) The calculated FF loss. 137
Figure 3.13 (a) SEM images of different perovskite thin film with various concentration
of MABr. (b) TA spectra of perovskite films. 136
Figure 3.14 (a) Cross-sectional HR-TEM image of perovskite interface and enhanced
water resistance and suppressed ion migration by the lead sulfate surface. 141 (b)

Schematic diagram of surface sulfidation treatment (SST). 133
Figure 3.15 (a) Peak force infrared mapping of MA in the control and FcTc ₂ -treated
perovskite films after aging. ⁶² 61
Figure 3.16 (a) GIWAXS patterns of control film and perovskite film with BDAI. 14663
Figure 3.17 (a) Schematic illustration of the lift-off process. 147 (b) Schematic
illustration of mechanical peel-off process. 148
Figure 3.18 (a) The energy level of IPSCs with ZIF-67. 145 (b) Bending stability of IPSCs
based on ZIF-67. ¹⁴⁸ 65
Figure 4.1 (a) Chemical structure of PY-IT and schematic illustration of film deposition
procedure. Top-view SEM images of the (b) control and (c) PSMA-perovskite films.
AFM height images of the (d) control and (e) PSMA-perovskite films72
Figure 4.2 ToF-SIMS profiles of (a) control and (b) PSMA perovskite films. (c) The 3D
signals distributions of segments73
Figure 4.3 XPS spectra of (a) S 2p and (b) Pb 4f of control and PSMA perovskite films.
(c) The FTIR spectra of PY-IT, perovskite and PSMA. (d) FTIR spectra of PSMA and
PSMA-PbI ₂ 74
Figure 4.4 (a) UV-Vis of control and PSMA perovskite films. The insert is the derived
Tauc-Plots. (b) XRD images for control and PSMA perovskite films. Contact angles of
(c) control and (d) PSMA-based films76
Figure 4.5 2D GIWAXS patterns of (a) control and (b) PSMA perovskite films, (c)
corresponding in-plane and out-of-plane line-cuts. (d) Out-of-plane GIWAXS line-cuts
of the control and PSMA perovskite films76
Figure 4.6 (a) PL spectra of control and PSMA perovskite films. (b) TRPL of (a) control
and PSMA perovskite films and (b) Perovskite/PCBM and Perovskite-PSMA/PCBM.
77
Figure 4.7 (a) Energy level of control and PSMA perovskite films. KPFM images of (b)
control and (c) PSMA perovskite films. The bottom curves represent the surface
potentials. (d) SCLC curves of control and PSMA perovskite with electron-only

structure of ITO/SnO ₂ /Perovskite/PCBM/BCP/Ag. (e) Light-dependent V _{OC} of the
control and PSMA perovskite devices. (f) Nyquist plots of the control and PSMA
perovskite devices
Figure 4.8 Mechanism of the defect passivation and improved electron transport
properties with PSMA80
Figure 4.9 (a) Device structure of the IPSCs (b) J-V curves of the best performance
devices. Parameters distribution of IPSCs fabricated by control and PSMA, (a) V_{OC} , (b)
J _{SC} , (c) FF and (d) PCE81
Figure 4.10 (a) Summary of recent reported PCEs for NFA-treated IPSCs. ²¹⁴⁻²²² (b)
EQE curves, and (d) stabilized output curves of control and PSMA devices82
Figure 4.11 J-V curves IPSCs for (a) control and (b) PSMA devices with different scan
rates. (c) J-V curves of narrow bandgap Pb-Sn IPSCs with/without PSMA. (d) J-V
curves IPSCs for PSMA as single ETL
Figure 4.12 (a) long-term storage stability in N ₂ atmosphere, and (b) operational
stability under MPP tracking of control and PSMA perovskite devices84
Figure 5.1 (a) Chemical structures of 2PACz and PyCA-3F, and schematic diagram of
HTL/SAM fabrication. The AFM height images and KPFM images of (b) ITO (c)
2PACz and (d) CA substrates94
Figure 5.2 (a) Potential distribution plots of ITO, 2PACz and CA films, the full width
at half maximum (FWHM) values of ITO, 2PACz and CA are 25 mV, 29 mV and 20
mV. (b) The transmittance spectra of ITO and 2PACz and CA substrates. (c) UPS
spectra of ITO and 2PACz and CA substrates. (d) General XPS spectra for ITO, 2PACz
and CA95
Figure 5.3 SEM-EDX mapping images of ITO, 2PACz and CA substrates96
Figure 5.4 (a) DLS micellar size distributions of 2PACz, CA, and PyCA-3F in EtOH
with concentration of 1 mg/ml. The hydrodynamic diameters are around 70 nm, 40 nm
and 9 nm for 2PACz, CA and PyCA-3F solutions. (b) Contact angles of 2PACz and CA
substrates

Figure 5.5 AFM-IR topographic and corresponding IR images of 2PACz, CA and mixed
on ITO substrates
Figure 5.6 (a) Electrostatic potential distribution of 2PACz and PyCA-3F calculated by
DFT, the colors represent electron-rich area (blue) and electron-poor area (red). (b)
Calculated Work Function of ITO. (c) Calculated Work Function of 2PACz. (d)
Calculated Work Function of CA
Figure 5.7 (a) Top view of equilibrated molecular representations on the ITO surface.
(b) Fractional coverage of ITO surface by the 2PACz and 2PACz with PyCA-3F
molecules. Note that the projected area of the simulated substrate is around $10,000~\text{Å}^2$.
(c) The adsorption process of 2PACz and PyCA-3F molecules on the ITO substrate.
The interfacial structures within small circles are magnified in larger circle areas100
Figure 5.8 Coverage surfaces of the 2PACz and 2PACz with PyCA-3F molecules on
the ITO substrate at different simulated times from classical molecular dynamics
simulations. 100
Figure 5.9 The lift off scheme of perovskite film with/without PyCA-3F101
Figure 5.10 Top-view SEM images of perovskite film growth on (a) 2PACz and (b) CA.
Top-view SEM images of the buried interface on (c) 2PACz and (d) CA101
Figure 5.11 XRD images of perovskite film growth on 2PACz and CA102
Figure 5.12 AFM height images of perovskite film growth on (a) 2PACz top surface,
(b) CA top surface, (c) 2PACz buried interface (d) and CA buried interface102
Figure 5.13 (a) The illustration of grain groove angles at the buried interface. (b) The
illustration of the flattened grain groove angles with PyCA-3F. (c) high-resolution AFM
images of the buried interface of 2PACz-based perovskite film, the grain boundary
groove angles are estimated to be 51°. (d) high-resolution AFM images of the buried
interface of CA-based perovskite film, the grain boundary groove angles are estimated
to be 118°
Figure 5.14 (a) TOF-SIMS images of the buried interface of 2PACz-based perovskite
film. (b) TOF-SIMS images of the top surface of CA-based perovskite film. (c) 3D

signals images of TOF-SIMS for perovskite film growth on 2PACz and CA104
Figure 5.15 (a) XPS spectra of Pb_{4f} and I_{3d} at the top surface of $2PACz$ and CA
perovskite films. (b) XPS spectra of Pb_{4f} and I_{3d} the buried interface of $2PACz$ and CA
perovskite films
Figure 5.16 (a) ATR-FTIR spectrum of the surface of 2PACz and CA. (b) ATR-FTIR
spectrum of $2PACz-PbI_2$ and $CA-2PACz-PbI_2$. (c) The feature peak of $1460\ cm^{-1}$ used
for AFM-IR test, corresponding to -CH ₂ - vibration
Figure 5.17 GIWAXS of perovskite top surface and buried interface 2PACz107
Figure 5.18 GIWAXS of perovskite top surface and buried interface CA107
Figure 5.19 Two-dimensional patterns and integral GIWAXS profiles at Qz and Qr.
Figure 5.20 (a) UPS data of top surface and buried interface for both 2PACz and CA
based perovskite films. (b) KPFM images of top surface for both 2PACz and CA
perovskite films. (c) KPFM images of buried interface for both 2PACz and CA
perovskite films
perovskite films
Figure 5.21 Steady-state PL and TRPL spectra for 2PACz and CA perovskite films.
Figure 5.21 Steady-state PL and TRPL spectra for 2PACz and CA perovskite films.
Figure 5.21 Steady-state PL and TRPL spectra for 2PACz and CA perovskite films. 110 Figure 5.22 SCLC results for 2PACz and CA devices with hole-only devices structure
Figure 5.21 Steady-state PL and TRPL spectra for 2PACz and CA perovskite films.
Figure 5.21 Steady-state PL and TRPL spectra for 2PACz and CA perovskite films.
Figure 5.21 Steady-state PL and TRPL spectra for 2PACz and CA perovskite films
Figure 5.21 Steady-state PL and TRPL spectra for 2PACz and CA perovskite films.
Figure 5.21 Steady-state PL and TRPL spectra for 2PACz and CA perovskite films. 110 Figure 5.22 SCLC results for 2PACz and CA devices with hole-only devices structure of ITO/2PACz/Perovskite/PTAA/Cu. The calculated N _t s are 3.09 × 10 ¹⁵ cm ⁻³ and of 2.08 × 10 ¹⁵ cm ⁻³ . 111 Figure 5.23 (a) J–V curves of 2PACz- and CA-based devices. (b) EQE curves of both 2PACz- and CA-based devices. (c) Bandgap of CA-based IPSCs calculated from the EQE plots. (d) Steady-state output of 2PACz- and CA-based devices. (e) Thermal
Figure 5.21 Steady-state PL and TRPL spectra for 2PACz and CA perovskite films. 110 Figure 5.22 SCLC results for 2PACz and CA devices with hole-only devices structure of ITO/2PACz/Perovskite/PTAA/Cu. The calculated N _t s are 3.09 × 10 ¹⁵ cm ⁻³ and of 2.08 × 10 ¹⁵ cm ⁻³
Figure 5.21 Steady-state PL and TRPL spectra for 2PACz and CA perovskite films. 110 Figure 5.22 SCLC results for 2PACz and CA devices with hole-only devices structure of ITO/2PACz/Perovskite/PTAA/Cu. The calculated N _t s are 3.09 × 10 ¹⁵ cm ⁻³ and of 2.08 × 10 ¹⁵ cm ⁻³ . 111 Figure 5.23 (a) J–V curves of 2PACz- and CA-based devices. (b) EQE curves of both 2PACz- and CA-based devices. (c) Bandgap of CA-based IPSCs calculated from the EQE plots. (d) Steady-state output of 2PACz- and CA-based devices. (e) Thermal stability of 2PACz- and CA-based devices. (f) Operational stability of 2PACz- and CA-based devices. 112

Center, CAS
Figure 5.26 The SEM images of the perovskite buried interface before and after the
aging test
Figure 5.27 (a) Chemical structures of PM1, PTQ10, m-BTP-phC6, PBQx-Cl and PY-
IT, which are materials used in spin-coating devices. (b) J-V characteristics and (c) EQE
spectra of PM1:PTQ10:m-BTP-phC6 (weight ratio = 0.8:0.2:1.2) ternary blend devices
based on bare ITO, PEDOT:PSS, 2PACz and CA. (d) Normal distribution of PCEs and
(e) dark current curves of above systems
Figure 5.28 Transmittance spectra versus EQE spectra based on (a) ITO, (B)
PEDOT:PSS, (c) 2PACz and, (d) CA
Figure 5.29 The normal distributional plot of (a) V_{OC} , (b) J_{SC} , and (c) FF for different
anode-based PM1:PTQ10:m-BTP-phC6 devices. (d) dark current data derived
photocurrent (J _{ph}) vs effective voltage (V _{eff}) relationships based on ITO, PEDOT:PSS,
2PACz and CA. Semi-log (e) and full-log (f) of the light intensity dependent V_{OC} and
J _{SC} values relationships based on ITO, PEDOT:PSS, 2PACz and CA117
Figure 5.30 (a) Open-circuit type MPP tracking curves of the devices based on
PEDOT:PSS, 2PACz and CA. (b) J-V characteristics and (c) EQE spectra all-polymer
blend PBQx-Cl:PY-IT based devices of PEDOT:PSS, 2PACz and CA. (d) Schematic
diagram of open-air blade coating device fabrication by using PM6:eC11 blend solution
dissolved in ortho-xylene on PEDOT:PSS, 2PACz and CA surface. Relative (e) J-V
characteristics and (f) EQE spectra. 119
Figure 6.1 The synthetic route of PABDCB
Figure 6.2 ¹ H NMR results of BrBDCB (7-(4-bromophenyl)-7H-
dibenzo[c,g]carbazole)127
Figure 6.3 ¹ H NMR results of BDCB-PO(OEt) ₂ (diethyl (4-(7H-dibenzo[c,g]carbazol-
7-yl)phenyl)phosphonate)
Figure 6.4 ¹ H NMR results of PABDCB (4-(7H-dibenzo[c,g]carbazol-7-
yl)phenyl)phosphonic acid)129

Figure 6.5 The synthetic route of MeO-PABDCB
Figure 6.6 ¹ H NMR results of MeO-BrBDCB (7-(4-bromophenyl)-3,11-dimethoxy-7H-
dibenzo[c,g]carbazole)
Figure 6.7 ¹ H NMR results of MeO-BDCB-PO(OEt) ₂ (diethyl (4-(3,11-dimethoxy-7H-
dibenzo[c,g]carbazol-7-yl)phenyl)phosphonate))
Figure 6.8 ¹ H NMR results of MeO-PABDCB (4-(3,11-dimethoxy-7H-
dibenzo[c,g]carbazol-7-yl)phenyl)phosphonic acid)
Figure 6.9 (a) chemical structures of 4PADCB, PABDCB and MeO-PABDCB. (b)
electrostatic surface potential (ESP) of 4PADCB, PABDCB and MeO-PABDCB. (c)
contact angles on 4PADCB, PABDCB and MeO-PABDCB substrates of perovskite
precursor
Figure 6.10 The calculated HOMO and LUMO of 4PADCB, PABDCB and MeO-
PABDCB. 134
Figure 6.11. Thermogravimetric analysis results of 4PADCB, PABDCB and MeO-
PABDCB. 135
Figure 6.12 Water contact angle of 4PADCB, PABDCB and MeO-PABDCB135
Figure 6.13 XPS spectra of In 3d, P 2p and N 1s of 4PADCB, PABDCB and MeO-
PABDCB
Figure 6.14 Adsorbing conditions of 4PADCB, PABDCB and MeO-PABDCB on ITO.
Figure 6.15 (a) C 1s XPS spectra of 4PADCB, PABDCB and MeO-PABDCB covered
ITO . (b) O 1s XPS spectra of 4PADCB, PABDCB and MeO-PABDCB covered ITO.
(c) I-V curves of hole-only device based on ITO/SAMs/Au on 4PADCB, PABDCB and
MeO-PABDCB. (d) Schematic binding diagram of alkyl-chain based SAMs and phenyl
based SAMs. (e) Energy diagram of ITO/4PADCB/perovskite. (f) Energy diagram of
ITO/PABDCB/perovskite. (g) Energy diagram of ITO/MeO-PABDCB/perovskite. 139
ITO/PABDCB/perovskite. (g) Energy diagram of ITO/MeO-PABDCB/perovskite. 139 Figure 6.16 KPFM images of 4PADCB, PABDCB and MeO-PABDCB140

Figure 6.18 UPS spectra of 4PADCB, PABDCB and MeO-PABDCB
Figure 6.19 Single-carrier devices with device structure of ITO/SAM/Au based on
4PADCB, PABDCB and MeO-PABDCB
Figure 6.20 (a) Scheme of 4PADCB on perovskite. (b) Scheme of PABDCB on
perovskite. (c) Scheme of MeO-PABDCB on perovskite. (d) Steady-state PL spectra of
perovskite films on 4PADCB, PABDCB and MeO-PABDCB substrates. (e) Transient
PL spectra of perovskite films on 4PADCB, PABDCB and MeO-PABDCB substrates.
(f) Surface potential distribution of perovskite films on 4PADCB, PABDCB and MeO-
PABDCB substrates. (g) GIXRD spectra and corresponding linear fit plots for
perovskite films on 4PADCB. (h) GIXRD spectra and corresponding linear fit plots for
perovskite films on PABDCB. (i) GIXRD spectra and corresponding linear fit plots for
perovskite films on MeO-PADCB. 142
Figure 6.21 SEM top images of perovskite surface deposited on 4PADCB, PABDCB
and MeO-PABDCB143
Figure 6.22 AFM and KPFM images of the perovskite surface deposited on 4PADCB,
PABDCB and MeO-PABDCB. 144
Figure 6.23 XRD images of perovskite surface deposited on 4PADCB, PABDCB and
MeO-PABDCB. 144
Figure 6.24 (a) Device structure of IPSCs based on 4PADCB, PABDCB and MeO-
PABDCB. (b) J-V curves of 4PADCB, PABDCB and MeO-PABDCB based IPSCs. (c)
Steady-output of the champion devices based on MeO-PABDCB. (d) Light intensity-
dependent V_{OC} of IPSCs based on 4PADCB, PABDCB and MeO-PABDCB. (e) tDOS
distribution defect energy level $E\omega$ of 4PADCB-PABDCB and MeO-PABDCB. (f)
Operational stability of IPSCs based on 4PADCB, PABDCB and MeO-PABDCB. (g)
Cycle stability of IPSCs based on 4PADCB, PABDCB and MeO-PABDCB 145
Figure 6.25 Devices performance on 4PADCB, PABDCB and MeO-PABDCB 146
Figure 6.26 Reverse and forward scans based on 4PADCB, PABDCB and MeO-
PABDCB

Figure 6.27 EQE spectra and its 1 st derived plot of the best performance	ce IPSCs based
on MeO-PABDCB.	146
Figure 6.28 SCLC results with device structure of ITO/SAM/Perove	skite/PTAA/Au
based on 4PADCB, PABDCB and MeO-PABDCB	146

List of Tables

Table 4.1 Summary of TRPL lifetimes of CsFAMA-based perovskite films with
different treatments
Table 5.1 The values of Fermi Level, Potential, and W _F for the structures98
Table 5.2 Calculated lifetime of TRPL results
Table 5.3 Calculated Trap density from SCLC results
Table 5.4 Optimization of PM1:PTQ10:m-BTP-phC6 ternary blend ratio
Table 5.5 Dark current parameters of ITO, PEDOT:PSS. 2PACz and CA118
Table 5.6 Photovoltaic parameters for OSCs based on different photo-active systems
and anodes
Table 6.1 The fitted XPS area of P 2p and In 3d
Table 6.2 The fitted carrier lifetime of perovskite films obtained from the TRPL
measurements
Table 6.3 Summarized trap density and hole mobility from SCLC results148

List of Abbreviations

Si Silicon

Cd Cadmium

Sm Samarium

Cs Cesium

Rb Rubidium

K Potassium

Pb Lead

Sn Tin

Cl Chlorine

Br Bromine

I Iodine

CIGS Copper Indium Gallium Selenide

CdTe Cadmium Telluride

GaAs Gallium Arsenide

PCE Power Conversion Efficiency

DSSCs Dye-sensitized Solar Cells

QDSCs Quantum Dot Solar Cells

CZTS Cooper Zin Tin Sulfide

OSCs Organic Solar Cells

OPVs Organic Photovoltaics

PSCs Perovskite Solar Cells

IPSCs Inverted Perovskite Solar Cells

LED Light-emitting Diodes

2T Two-terminal

4T Four-terminal

S-Q limit Schottky-Queisser Limit

Effective Tolerance Factor teffective

SRH Recombination Shockley-Read-Hall Recombination

V_{OC} Open-circuit Voltage

J_{SC} Short-circuit Current Density

FF Fill Factor

P_{max} Maximum Power Output

MPP Maximum Power Point

MPPT Maximum Power Point Tracking

R_s Series Resistance

R_{sh} Shunt Resistance

P_{out} Electrical Power Output

P_{in} Incident Light Power

HTL Hole Transport Layer

ETL Electron Transport Layer

TCO Transparent Conductive Oxides

HOMO Highest Occupied Molecular Orbital

LOMO Lowest Unoccupied Molecular Orbital

VBM Valence Band Maximum

CBM Conduction Band Minimum

W_F Work Function

EQE External Quantum Efficiency

SEM Scanning Electron Microscopy

AFM Atomic Force Microscopy

KPFM Kelvin Probe Force Microscopy

CPD Contact Potential Difference

XRD X-ray Diffraction

PL Photoluminescence

TRPL Time-resolved Photoluminescence

XPS X-ray Photoelectron Spectroscopy

UPS Ultraviolet Photoelectron Spectroscopy

EIS Electrochemical Impedance Spectroscopy

GIWAXS Grazing-incidence Wide-angle X-ray Scattering

TAS Transient Absorption Spectra

FTIR Fourier Transform Infrared Spectroscopy

ToF-SIMS Time-of-flight Secondary-ion Mass Spectroscopy

UV-Vis Ultraviolet Visible Absorption

SCLC Space Charge Limited Current

V_{TFL} Trap-filling Limit Voltage

AFM-IR Atomic Force Microscopy-infrared Spectroscopy

DLS Dynamic light scattering

DFT Density Functional Theory

MD Molecular Dynamic

FWHM Full Width at Half Maximum

ESP Electrostatic Potential

GIXRD Grazing Incidence X-ray Diffraction

PFIR Peak Force Infrared Microscopy

0D 0-dimension

1D 1-dimension

2D 2-dimension

3D 3-dimension

t_{effective} Goldschmidt tolerance factor

SAM Self-assembled Monolayer

MA Methylammonium

FA Formamidinium

CsI Cesium Iodide

MABr Methylamine Hydrobromide

MACl Methylamine Hydrochloride

FAI Formamidinium Iodide

PbBr₂ Lead Bromide

PbI₂ Lead Iodide

PbCl₂ Lead Chloride

BCP Bathocuproine

MAPbBr₃ Methylammonium Lead Bromide

MAPbI₃ Methylammonium Lead Iodide

FAPbI₃ Formamidinium Lead Iodide

PPS 3-(1-pyridinio)-1-propane sulfonate

MoO₃ Molybdenum Oxide

VO_x Vanadium Oxide

 NiO_x Nickel Oxide

BA N-butylammonium

EA Ethylammonium

DMA Dimethylammonium

GUA Guanidinium

PI Piperazinium Iodide

PDI Piperazinium Diiodide

CB Chlorobenzene

DE Diethyl Ether

EA Ethyl Acetate

IPA Isopropyl Alcohol

EtOH Ethanol

[BMIm]BF₄ 1-butyl-3-methylimidazolium Tetrafluoroborate

2PACz [2-(9H-Carbazol-9-yl)ethyl]phosphonic Acid

PbS Lead-sulfur

InBr₃ Indium Bromide

FcTc₂ Ferrocenyl-bis-thiophene-2-carboxylate

PEAI Phenylethylammonium Iodide

BDAI 1,4-butanediammonium Iodide

GAI Guanidinium Iodide

AEPI Aminoethylpyridine Iodide

PDMAI₂ Phenyldimethylammonium Iodide

MPA Methyl Phosphonic Acid

3-MPA 3-mercaptopropionic Acid

PSMA Polymerized Small Molecular Acceptor

PyCA-3F 2-chloro-5-(trifluoromethyl)isonicotinic acid

GBP Grain Boundary Passivation

SP Surface Passivation

Chapter 1 Introduction

1.1 Background

1.1.1 The Rise and Staus of Solar Cells

In the 21st century, the global economic landscape is significantly influenced by economic challenges and rising energy demands, both of which warrant attention. The intersection of economic growth and energy consumption plays a pivotal role in influencing global climate change, particularly in rapidly industrializing nations such as China, southeast Asia and India. As such, the advancement of clean energy technologies has become imperative to enhance the sustainability and security of energy resources. China, however, faces considerable challenges in achieving this transition due to its geographical and resource constraints. Despite being the country with the third-largest landmass in the world, China possesses relatively limited reserves of noncoal fossil fuels. This scarcity of domestic fossil fuel resources, especially those like oil and natural gas, compels China to rely heavily on large-scale imports to meet its energy needs. Consequently, these factors underscore the urgency of diversifying and expanding the development of renewable energy sources within the country to ensure long-term energy security and mitigate environmental impacts.

Moreover, the combustion of fossil fuels inevitably results in the emission of pollutants such as nitrogen oxides, sulfur oxides, and airborne particles, which contribute significantly to environmental issues like acid rain, ozone layer depletion, and PM 2.5 pollution. These environmental consequences underscore the critical need to develop and utilize clean energy alternatives to replace fossil fuels. This transition is not only essential for sustainable development but also for achieving carbon neutrality goals.

Among the various renewable energy sources, solar energy emerges as particularly advantageous due to its widespread availability and straightforward application. The development of solar cells has progressed over the past seven decades since the first silicon solar cell invented by Bell Lab, and more recently, leading to the

innovation of various types of solar cell technologies categorized based on their materials and structural designs. These developments have resulted in three main generations of solar cells: the 1st generation, the 2nd generation, and the 3rd generation as shown in **Figure 1.1**. Each generation represents significant advancements in either efficiency, cost-effectiveness, and/or application potential, making solar energy a cornerstone of today's and future sustainable energy strategies.

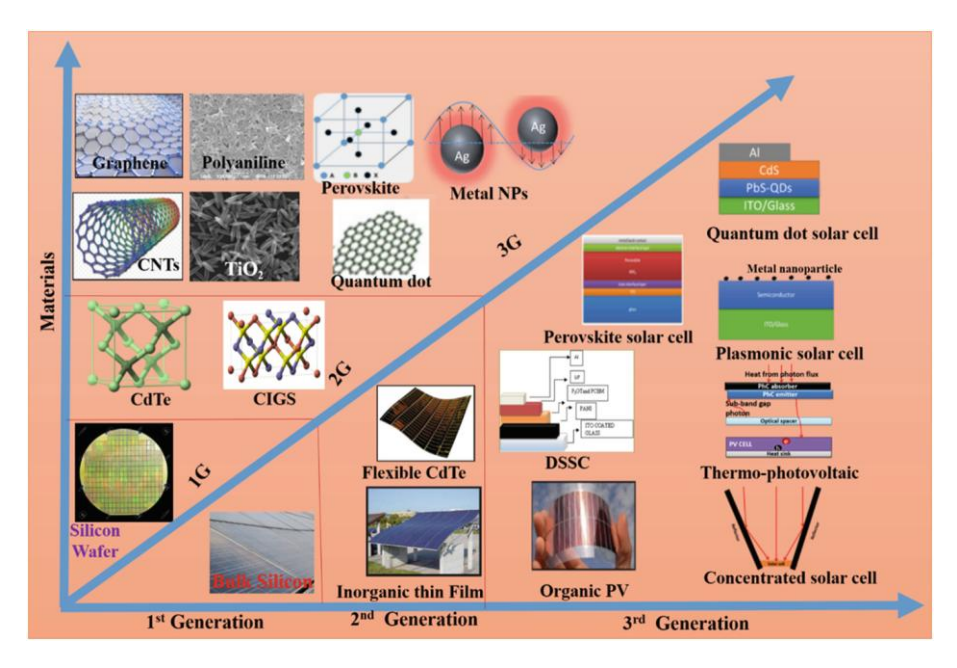


Figure 1.1 Development of solar cell materials and device structures.¹

1st generation solar cells predominantly consist of silicon-based solar cells, including single crystal, heterojunctions silicon solar cells, with monocrystalline silicon solar cells being the major commercial type to date. Due to their earliest development, their manufacturing processes are relatively mature. Currently, silicon solar cells dominate the photovoltaic market, and monocrystalline silicon has achieved the highest certified efficiency of 27.6% (with concentrator), and 26.1% (non-concentrator) up to date. However, despite the high efficiency of monocrystalline silicon solar cells, the indirect bandgap nature of silicon and the relatively high production costs due to high purity requirements (>99.999%) of the source materials and high temperature process, which limit future up-scaling commercialization.

2nd generation solar cells, also known as thin-film solar cells, use absorber layers

such as copper indium gallium selenide (CIGS), cadmium telluride (CdTe), gallium arsenide (GaAs), and amorphous silicon. These materials have lower absorber layer thickness compared to monocrystalline silicon, and their purity requirements are less stringent. In recent years, these solar cells have met rapidly development with both efficiency and cost-effective. The certified efficiency of CIGS solar cells has reached 23.6%, 22.3% efficiency for CdTe solar cell, and an efficiency of 29.1% for GaAs thin-film solar cells. Though overcoming the drawback of indirect bandgap of monocrystal silicon semiconductors, the manufacturing processes of these thin-film solar cells are also complex and often require stringent manufacturing conditions including high vacuum and high temperature. Additionally, the use of certain elements (such as Cd) can cause severe environmental pollution, limiting their application to specific areas such as space, and making industrial-scale application future challenging.

3rd generation solar cells include dye-sensitized solar cells (DSSCs), quantum dot solar cells (QDSCs), cooper zin tin sulfide (CZTS) organic solar cells (OSCs) and perovskite solar cells (PSCs) which also regarded as emerging photovoltaics. The third-generation solar cells present higher light-absorption properties with reduced manufacturing costs and simplified processes. Solution processable properties can be one of the most attractive merits of 3rd generation solar cells. The efficiency of dye-sensitized solar cells has reached 13%, organic solar cells have exceeded 20%, quantum dot solar cells have achieved an efficiency of 18.1%, and PSCs have rapidly improved to certified 26.7% within a short span of 14 years. The rise of third-generation solar cells has further advanced the field of photovoltaics.

The above three generations of solar cells are classified based on single-junction (single absorber layer) solar cells, in which the efficiency limitation exists considering the trade-off between photocurrent (prefer low bandgap absorbing wider solar spectrum) and photovoltage (prefer wider bandgap) with thermodynamic efficiency limited at ~33% called S-Q limit. Multi-junction solar cells are proposed to overcome S-Q limit. They consist of two or more light absorbers with different bandgaps, each with

complementary absorption capabilities to capture a broader spectrum of sunlight while at the same time achieve high photovoltage. After sunlight passes through the top cell, the remaining photon energy is absorbed by the bottom cell, allowing multi-junction solar cells to surpass the efficiency limit of single-junction solar cells.² Common types of multi-junction solar cells include two-terminal tandem solar cells (2T) and four-terminal tandem solar cells (4T).³

1.2 The Physics in Solar Cells

1.2.1 Photoelectric Effect and Carriers

Solar cells convert solar energy into electricity through the photoelectric effect. The discovery of semiconductors generating a weak electric current when exposed to light was made by Edmund Becquerel in 1839.⁴ Subsequently, German physicist Heinrich Hertz made further advancements in understanding this phenomenon, known as the photoelectric effect in 1887 under classical physics framework.⁵ The classical picture, however, cannot explain the inner physical mechanism. In 1905, Albert Einstein proposed that the energy of light is not distributed uniformity but capped with discrete photons with distinct light frequency.⁶ This breakthrough theory not only explained the photoelectric effect but also propelled the development of quantum mechanism, which later won him Nobel prize in 1921. With continuous scientific research, this theory has been refined, and solar cells and devices have emerged as a significant focus of scientific inquiry and research.

The photoelectric effect process consists of charge generation, separation, transport, and collection. Charge generation begins with the absorption of photons, where photons with energy equal to or greater than the absorber's bandgap excite electrons from the valence band to the conduction band, creating electron-hole pairs. After generation, these electron-hole pairs will be separated and diffused to opposite directions. In conventional solar cells, this separation is facilitated by the built-in electric field at the p-n junction. Electrons and holes will transfer to the n-type region

p-type region by the built-in electric field. In heterojunction and other advanced solar cells, charge separation is further differing from the bandgap and the electron affinity. In the transport process, charge carriers will transfer to the electrodes. This process is influenced by the mobility of the carriers and the quality of the transport layers. High mobility reduces the likelihood of recombination, while well-designed transport layers ensure that carriers reach the electrodes with minimal resistance. However, not all carriers contribute to the current; recombination, where electrons and holes recombine before reaching the electrodes, remains a significant loss mechanism. Recombination processes in solar cells include radiative recombination, where energy is lost as emitted photons, and non-radiative recombination, where energy is dissipated as heat. Non-radiative recombination, including Shockley-Read-Hall (SRH) recombination and Auger recombination, reduces the efficiency of solar cells through generating heat. The charges eventually are collected in electrons and generating current. The scheme is shown in Figure 1.2.7 The efficiency of this process depends on the interfaces such as the alignment of energy levels between the transport layers and electrode.

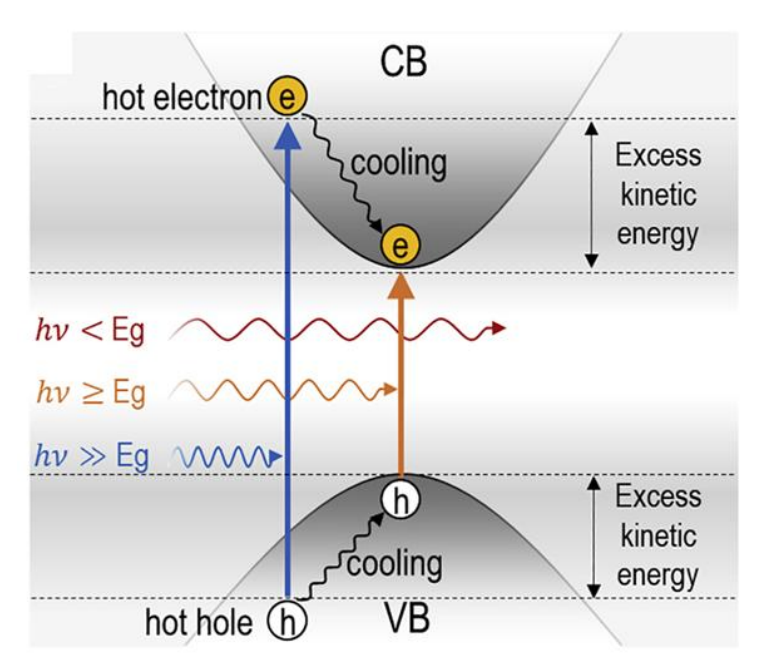


Figure 1.2 The mechanism of photoelectric effect - a simple diagram of direct bandgap semiconductor.

The key factors influencing carrier dynamics in solar cells include carrier mobility, lifetime, and diffusion length. High mobility and long carrier lifetimes allow carriers to

reach the electrodes before recombining, while a longer diffusion length than the absorber layer thickness ensures efficient charge collection.

1.2.2 Schottky-Queisser Limit

The Schottky-Queisser limit (S-Q limit) is a theoretical maximum efficiency that a single junction solar cell can achieve under illumination. This limit was first proposed by William Shockley and Hans Queisser in 1961, and it has since become a fundamental benchmark in the field of photovoltaic. There are four assumptions based on detailed balance model: (1) Assuming the solar spectrum is approximated by the emission of a black body with a surface temperature of $T_s = 6000$ K. (2) Assuming that in an ideal solar cell, the only recombination pathway that cannot drop to zero is radiative recombination, defining an upper limit on the minority carrier lifetime. (3) Assuming that the photons with energy below E_g do not interact with the solar cell, while photos with energy above Eg are converted into electron-hole pairs with quantum efficiency of 100%. (4) Assuming the temperature of solar cells is $T_c = 300K$. 8 At the core of the S-Q limit is the interaction between the absorption of photons and the loss mechanisms, such as thermalization and radiative recombination. Photons with energy greater than the absorber's bandgap generate electron-hole pairs, but excess energy beyond the bandgap is lost as heat through thermalization. Similarly, radiative recombination, where excited electrons fall back into the valence band and emit photons, also contributes to energy loss. The balance between these factors leads to the derivation of the efficiency limit. As shown in Figure 1.3, the energy loss within the S-Q limit can be categorized into five distinct types: (1) Coherent absorption-emission losses, which are governed by Kirchhoff's law of thermal radiation, describing the relationship between absorption and emission processes in solar cells. (2) Carnot losses, which arise from the thermodynamic inefficiencies inherent in the operation of a solar cell as a heat engine, specifically the temperature difference between the heat source (the sun) and the heat sink (the environment). (3) Boltzmann losses, which occur due to the angular

mismatch between the absorption and emission spectra, leading to entropy generation. (4) Thermalization losses, which are associated with the dissipation of energy by hot carriers as they lose excess energy to the lattice, thus reaching the bandgap energy. (5) In-band losses, which arise from the inherent transparency of the absorber material to photons with energy below the bandgap, causing them to pass through without being absorbed..⁷

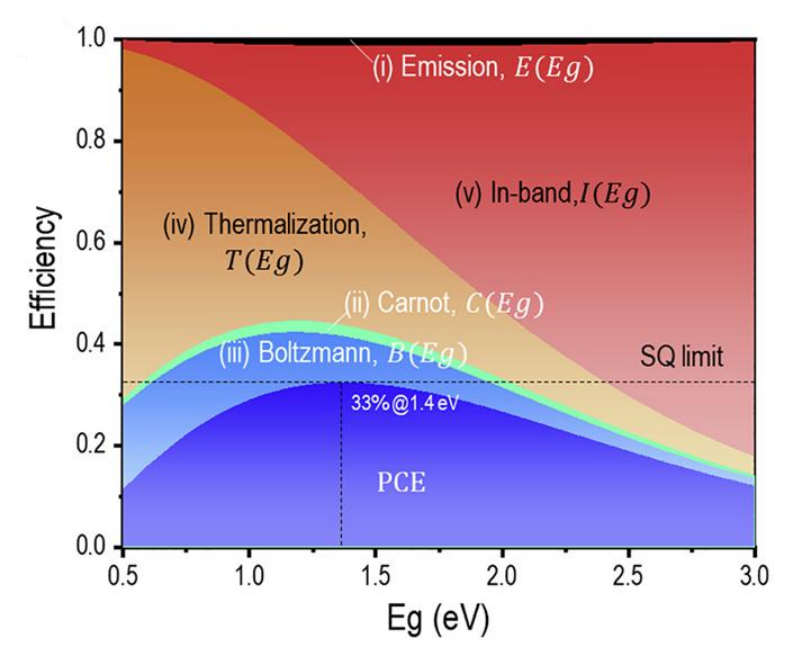


Figure 1.3 The intrinsic loss mechanism and the S-Q limit in solar cells.⁷

The S-Q Limit is calculated by optimizing the bandgap energy to maximize efficiency while minimizing losses. For a solar cell under the 1-sun AM 1.5G solar spectrum, the bandgap within 1.0 eV and 1.6 eV can reach the potential efficiency over 30%, for example, the maximum efficiency is around 33.7% for a single-junction cell with a bandgap of approximately 1.34 eV.9 This efficiency represents the highest theoretical Power Conversion Efficiency (PCE) for a single-junction device under ideal conditions. Several intrinsic factors contribute to the limitations defined by the S-Q Limit. Photons with energy lower than the bandgap pass through the solar cell without generating carriers, while higher-energy photons lose excess energy as heat. Non-radiative recombination mechanisms, though not accounted for in the ideal case, further reduce the practical efficiency of solar cells.

Despite its theoretical nature, the S-Q Limit serves as a critical benchmark for single junction solar cell design. Researchers have sought ways to surpass this limit by developing multi-junction solar cells, which stack layers with different bandgaps to capture a broader range of the solar spectrum while significantly enhances photon utilization efficiency – remove the tradeoff between open-circuit voltage (V_{OC}) and short-circuit current density (J_{SC}) in single junction solar cells. Other strategies, such as intermediate band and hot carrier solar cells, aim to reduce losses associated with the traditional single-junction approach, but not as effective as tandem/multijunction strategy. The ongoing pursuit of technologies that exceed the S-Q Limit highlights the importance of this concept in advancing photovoltaic research.

1.3 Fundamental Knowledge of Perovskite

1.3.1 Crystal Structure and Phase Transition

Perovskite-related minerals were reported as early as the last century. The term "perovskite" originally referred to a specific mineral structure, with the chemical formula CaTiO₃, this mineral was firstly discovered by Gustav Rose and is named in honor of the contribution of the Russian mineralogist Lev Perosvki. Later on, it was broadly extended to the general crystal structure of ABX₃. In this structure, the A ions occupy the eight corners of the unit cell, the B ions reside at the body center, and the X ions occupy the six face centers.

The Goldschmidt tolerance factor (t) has historically served as a foundational metric for assessing the geometric compatibility of ionic constituents within the perovskite lattice framework. It is mathematically expressed as:

$$t = \frac{R_A + R_X}{\sqrt{2}(R_B + R_X)} \tag{1.1}$$

where R_A , R_B and R_X correspond to the ionic radii of the A-site cation, B-site cation, and X-site anion, respectively. A value of t close to unity typically denotes a favorable configuration for the formation of a stable, cubic perovskite structure. Deviations from this idealized value are often indicative of lattice strain and predispose the material to symmetry-lowering distortions, resulting in non-cubic phases such as tetragonal,

orthorhombic, or hexagonal variants.

In the case of simple oxide perovskites (e.g., ABO₃ systems), empirical observations consistently validate the predictive utility of the Goldschmidt factor. Stable perovskite phases are frequently observed when t falls within the range of 0.8 to 1.0. Perovskite structures used in PSCs typically consist of hybrid organic-inorganic metal halide perovskites, and also all inorganic perovskites. The A-site ions are usually organic cations such as methylammonium (CH₃NH₃⁺, MA⁺), formamidinium (NH=CHNH₃⁺, FA⁺), or inorganic cations like Cs⁺, Rb⁺, K⁺, etc., or their combinations. The B-site ions are typically divalent metal cations such as Pb²⁺ and Sn²⁺ or their combinations. X represents halide ions such as Cl⁻, Br⁻, l⁻, etc. or their combinations. Take a simple CsSnI₃ perovskite structure as an example, as shown in **Figure 1.4**, adjusting the Cs content leads to different t values, resulting in the following conclusions: When t < 0.9, it corresponds to the orthorhombic δ -phase perovskite structure. When 0.9 < t < 1, it corresponds to the cubic perovskite structure. When t > 1, it corresponds to the hexagonal non-perovskite structure.

Having an effective tolerance factor in the range of 0.94-0.98 can provide high structural stability for perovskite materials. Conversely, PSCs based on a tolerance factor below 0.85 exhibit inferior performance and are more prone to form non-perovskite structures. However, the underlying assumptions of this traditional model, namely, the spherical symmetry of ions and static consideration of ionic sizes derived from Shannon radii, limit its applicability to systems where electronic polarizability, covalent bonding, or molecular asymmetry play significant roles. Consequently, the Goldschmidt approach often fails to provide accurate structural predictions for halide perovskites or hybrid organic-inorganic variants, where such factors are non-negligible.¹¹

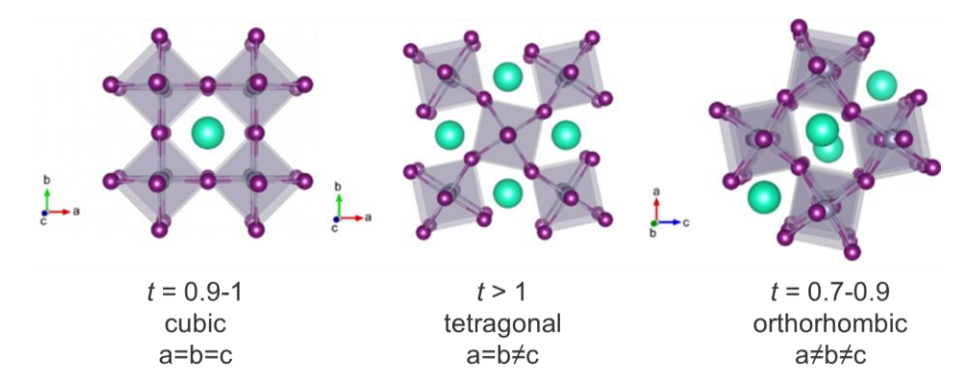


Figure 1.4 Goldschmidt tolerance factor and the phase structures of perovskite. 10

To address these limitations, the effective tolerance factor (t_{eff}) has emerged as a modified metric that accounts for compositional diversity and ionic heterogeneity inherent in complex perovskite systems. This parameter is particularly relevant for materials incorporating mixed A-site and X-site components. The effective ionic radii for these sites are calculated using mole-fraction weighted averages:

$$r_{A,eff} = \sum_{i} x_i R_{A,i} \tag{1.2}$$

$$r_{X,eff} = \sum_{j} y_j R_{X,j} \tag{1.3}$$

where x_i and y_j represent the molar proportions of the respective A-site and X-site species. The resulting effective tolerance factor is given by:

$$t_{eff} = \frac{r_{A,eff} + r_{X,eff}}{\sqrt{2}(R_B + r_{X,eff})}$$
(1.4)

This refined descriptor facilitates a more accurate estimation of structural compatibility in multi-component perovskites such as $Cs_xMA_yFA_{1-x-y}Pb(I_zBr_{1-z})_3$, where each constituent ion contributes to the overall lattice dynamics. For example, the inherent instability of α -FAPbI₃, characterized by a high t value, can be mitigated by partial substitution with Cs^+ , thereby adjusting t_{eff} toward unity and promoting the formation of a more stable cubic phase . Similarly, the orthorhombic distortion observed in $CsPbI_3$ due to a low t can be suppressed through analogous compositional engineering. Empirical studies have consistently demonstrated that effective tolerance factors within the interval of 0.9 to 1.0 are conducive to achieving the thermodynamically favorable perovskite black phase with improved optoelectronic

characteristics.

Nevertheless, *t_{eff}* is not devoid of limitations. Although it incorporates compositional averaging, it continues to rely on spherical ionic approximations and lacks sensitivity to local structural phenomena such as hydrogen bonding, dipole interactions, and dynamic disorder effects that are particularly pronounced in hybrid perovskites. Moreover, the assumption of linearity in radius-weighted contributions may oversimplify the nuanced, often non-additive interactions among mixed ionic constituents.¹²

The following section will introduce several structural phases of perovskite, taking the classical methylammonium lead iodide (MAPbI₃) as an example:

(1) Orthorhombic Phase (T < 165 K):

Below 165 K, the MAPbI₃ perovskite maintains a stable orthorhombic δ-phase, belonging to the Pnma space group. The orthorhombic phase exhibits a superlattice expansion compared to the simple cubic perovskite structure. In this low-temperature phase, the CH₃NH₃⁺ sub-lattice is completely ordered (low entropy). However, this ordered state can easily change during material preparation, such as under quasi-thermodynamic equilibrium conditions. Additionally, under stress and electric field forces, the orthorhombic phase may simultaneously exhibit several different ordered structures.

(2) Tetragonal phase (165 K < T < 327 K): At 165 K, MAPbI₃ undergoes the first phase transition from the orthorhombic phase to the tetragonal β -phase (I4/mcm). As the temperature continues to rise to 327 K, a second phase transition occurs to the cubic perovskite phase. Similar to the cubic perovskite unit cell, the tetragonal phase also exhibits a superlattice expansion, consistent with the orthorhombic phase.

However, in the tetragonal phase, the ions in the orthorhombic phase no longer occupy specific positions. The CH₃NH₃⁺ cations exist between the PbI₆ octahedra. The tetragonal phase exhibits a distortion factor greater than 1, which is consistent with the elongation of the PbI₆ octahedra along the c-axis.

(3) Cubic Phase (T > 327 K): As the temperature increases, the tetragonal phase lattice gradually becomes more isotropic. The degree of molecular disorder also approaches the transition to the cubic phase. The cubic α -phase belongs to the Pm3m space group, but the structure typically has lower symmetry. This phenomenon becomes more pronounced when Cl and Br substitute I in MAPbI₃.

In pursuing high efficiency solar cells, guided by S-Q theory, lower bandgap perovskites in particular FAPbI₃ become the research focus. Compared with MAPbI₃, FAPbI₃ perovskite structure catches much attention recently due to its better thermal stability and narrower bandgap with promising efficiency beyond 30%. FAPbI₃ can exist in several crystal phases, primarily including α -FAPbI₃ (cubic), β -FAPbI₃ (orthorhombic), γ -FAPbI₃ (tetragonal) and non-photoactive yellow γ -FAPbI₃ phase (hexagonal), each of which exhibits distinct crystallographic structures and optoelectronic properties. The stability and phase transitions of these polymorphs are critical factors influencing the performance and longevity of PSCs. The phase transitions between α , β , γ , and δ phases of FAPbI₃ are influenced by temperature and humidity. α - FAPbI₃ is the most desirable phase due to its optimal bandgap (\sim 1.48 eV) and excellent charge transport properties. However, maintaining the α -phase under operational conditions remains challenging, as it tends to transition to undesirable β , γ and δ phases. 13,14

The α -phase of FAPbI₃ adopts a cubic perovskite structure, characterized by a three-dimensional framework of corner-sharing PbI₆ octahedra, with formamidinium (FA⁺) cations occupying the interstitial sites. α -FAPbI₃ shows superior optoelectronic properties, including a direct bandgap (1.48 eV), which is ideal for efficient absorption of visible light. The α -phase also exhibits high charge carrier mobility and long carrier diffusion lengths, making it particularly suitable for high-efficiency PSCs. However, this phase is thermodynamically unstable at room temperature because of its relatively low tolerance factor (<0.8). The instability of the α -phase poses a significant challenge for the long-term performance of FAPbI₃ devices, necessitating strategies to stabilize

this phase in operational environments.

The β -FAPbI₃ is structurally similar to the α -phase but exhibits slight distortions that lead to an orthorhombic or hexagonal symmetry. This phase is an intermediate structure that can form as the α -phase begins to degrade under less favorable conditions. The β -phase has a wider bandgap compared to the α -phase, resulting in reduced optical absorption and less favorable charge transport properties. In PSCs, the presence of the β -phase is generally undesirable as it leads to reduced device efficiency.

The γ - FAPbI₃, often referred to as the yellow phase, is another orthorhombic or hexagonal polymorph that is thermodynamically more stable than the α -phase at room temperature. This phase is characterized by further lattice distortions compared to the β -phase and is typically formed under conditions of increased humidity or lower temperatures. The γ -phase has a significantly larger bandgap of around 2.43 eV, which renders it non-photoactive in the visible spectrum. The transition from the α -phase to the γ -phase is marked by a noticeable change in color from black to yellow, signaling a loss of photovoltaic activity. The stability of the γ -phase, while advantageous from a thermodynamic perspective, is detrimental to the performance of PSCs, because of poor light absorption.

The δ -FAPbI $_3$ is a hexagonal non-perovskite structure that is considered the most thermodynamically stable phase at ambient conditions, especially in the presence of moisture. However, unlike the α -phase, the δ -phase does not have the three-dimensional network of corner-sharing octahedra typical of perovskite structures. Instead, it forms a two-dimensional layered structure, which is highly stable but non-photoactive. The δ -phase shows a large bandgap, typically exceeding 2.5 eV, which precludes efficient absorption of visible light. The formation of the δ -phase is a major concern in the stability of FAPbI $_3$ -based solar cells, as its presence indicates non-photoactive properties. Strategies to inhibit the transition to the δ -phase are critical for maintaining the long-term performance of PSCs.

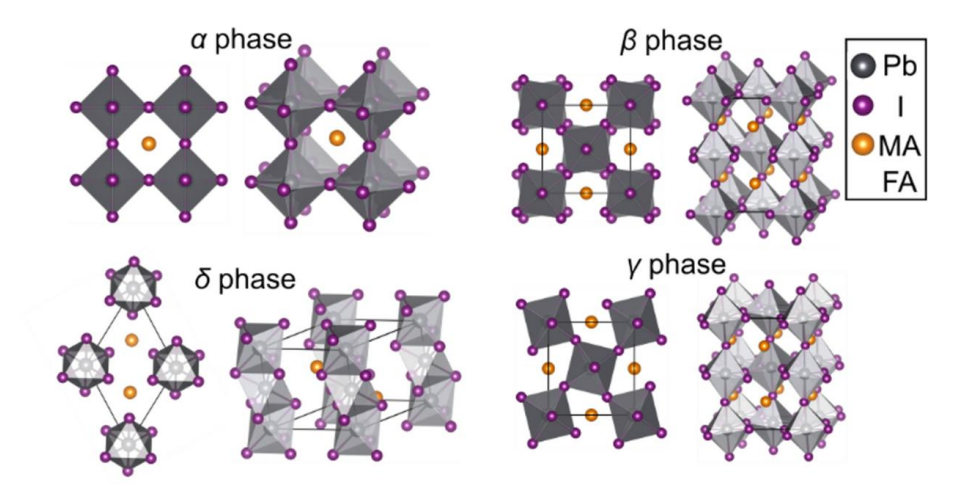


Figure 1.5 Phase transition of FAPbI₃.¹⁴

1.3.2 Optical Properties

Perovskite materials are particularly valued for their optical properties, which are highly tunable and crucial for their applications in various optoelectronic devices. The bandgap of perovskites can be tuned via composition engineering, allowing for bandgaps ranging from approximately 1.1 eV to 3 eV. This tunability also contributes to the material's impressive absorption properties, which are critical for enhancing the efficiency of solar cells. Moreover, perovskite absorbers merits from high absorption coefficients, surpassing 10⁴ cm⁻¹, enabling efficient capture of various wavelengths of sunlight and improving solar energy conversion efficiency. ¹⁵ In addition to the strong absorption, many perovskites exhibit significant photoluminescence, making them attractive for applications beyond photovoltaics, such as in LEDs and lasers. The high photoluminescence quantum yield observed in some lead halide perovskites underscores their potential in various optoelectronic devices. ¹⁶

1.3.3 Electronical and Mechanical Properties

The electronic properties of perovskites are critical to their function in optoelectronic devices, influencing the efficiency of energy conversion. For example, perovskites are characterized by high charge carrier mobility which is essential for the efficient transport of electrons and holes.¹⁷ Charge carrier mobility in perovskites typically ranges from 10 to 100 cm²/Vs, resulting from the composition and fabrication

methods. In addition, perovskites show high diffusion length up to several micrometers, allowing carriers diffuse across the perovskite film and effectively collect charges. Moreover, perovskites generally exhibit relatively low recombination rates, enabling higher open-circuit voltages and enhance power conversion efficiency.¹⁸

Perovskites also possess distinctive mechanical properties, notably their softness and flexibility, which offer potential advantages for applications in flexible electronics. Perovskites to traditional inorganic semiconductors, perovskites exhibit a softer and more flexible nature, making them ideal candidates for integration into wearable electronics and other flexible devices. However, the mechanical flexibility of perovskites comes with certain challenges. Perovskites can be susceptible to fracture or degradation under mechanical stress, particularly in thin-film applications. This susceptibility to mechanical damage necessitates careful material selection and device design to ensure the long-term durability and stability of perovskite-based devices.

Ensuring mechanical stability through proper material selection and device design is critical for the durability of perovskite-based devices.

1.4 Characterization of Solar Cells

1.4.1 Basic Solar Cell Photovoltaic Parameters

In photovoltaic devices, when light illuminates the absorber layer, electron-hole pairs are generated through the absorption of photons. The photogenerated electrons and holes are then separated and transported towards opposite terminals of the solar cell, leading to the formation of photovoltage and photocurrent. The performance of a solar cell is evaluated through several key parameters that reflect its efficiency in converting sunlight into electrical energy. These parameters provide critical insights into the solar cell's power generation capabilities and its overall effectiveness under operational conditions.

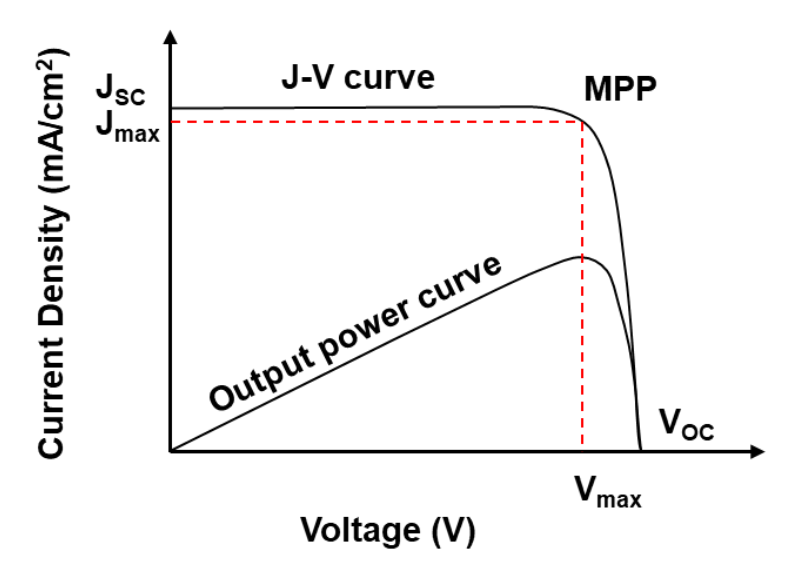


Figure 1.6 Typical J-V curves of solar cells.

One of the fundamental parameters is the V_{OC} , which represents the maximum voltage a solar cell can produce when no external load is connected (i.e., under open-circuit conditions). V_{OC} is determined by the energy difference between the quasi-Fermi levels of electrons and holes within the solar cell. This parameter is intrinsically related to the bandgap energy of the absorber material and is influenced by the quality of the interfaces and the extent of nonradiative recombination losses within the devices. The V_{OC} loss can be attributed to the following three factors:

$$q\Delta V = E_{g} - qV_{OC}$$

$$= (E_{g} - qV_{OC}^{SC}) + (qV_{OC}^{SC} - qV_{OC}^{rad}) + (qV_{OC}^{rad} - qV_{OC})$$

$$= (E_{g} - qV_{OC}^{SC} + q\Delta V_{OC}^{SC}) + q\Delta V_{OC}^{rad} + q\Delta V_{OC}^{non-rad}$$

$$= q(\Delta V_{1} + \Delta V_{2} + \Delta V_{3})$$
(1.5)

Where q refers to the elementary charge, ΔV is the total voltage loss, Eg is the bandgap of perovskite. $V_{\rm OC}^{\rm SC}$ is the S-Q limit, $V_{\rm OC}^{\rm rad}$ is the V_{OC} when only radiative recombination occurred, $\Delta V_{\rm OC}^{\rm SC}$ is the V_{OC} loss due to the non-ideal EQE above bandgap, $\Delta V_{\rm OC}^{\rm rad}$ is the V_{OC} loss of the sub-bandgap radiative recombination and $\Delta V_{\rm OC}^{\rm non-rad}$ is the V_{OC} loss of non-radiative recombination.²¹ The detailed V_{OC} loss analysis can be found in **Figure 1.7**.²²

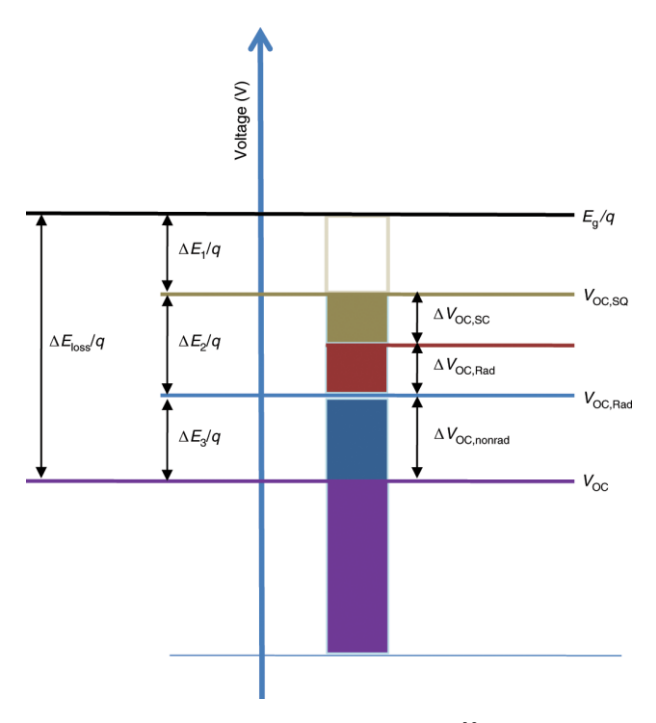


Figure 1.7 A detailed explanation of V_{OC} loss in solar cells.²²

Another crucial parameter is the J_{SC} , which denotes the current generated per unit area of the solar cell when its terminals are short-circuited (i.e., when the external load is zero). J_{SC} is a key indicator of the solar cell's ability to absorb photons and convert them into charge carriers. The value of J_{SC} is influenced by several factors, including the absorption characteristics of the material, the efficiency of charge carrier collection, and the spectral response of the device.

The fill factor (FF) is a dimensionless parameter that quantifies the degree to which the current-voltage curve of a solar cell approaches an ideal rectangular shape. It is defined as the ratio of the maximum power output (P_{max}) to the product of V_{OC} and J_{SC} :

$$FF = \frac{P_{max}}{V_{OC} \times I_{SC}} \times 100\% \tag{1.6}$$

A higher fill factor indicates that the solar cell operates closer to its theoretical maximum power point (MPP), thus reflecting a more efficient device. FF is influenced by factors such as series resistance (R_s) and shunt resistance (R_{sh}). Specifically, a lower series resistance and higher shunt resistance generally lead to an improved fill factor, which is critical for optimizing the overall performance of the solar cell.

PCE is the most critical parameter for assessing the performance of a solar cell. It

represents the ratio of the electrical power output (P_{out}) to the incident light power (P_{in}) and is expressed as a percentage. The PCE is calculated using the following equation:

$$PCE = \frac{P_{out}}{P_{in}} \times 100\% = V_{OC} \times J_{SC} \times 100\%$$
 (1.7)

A higher PCE indicates a more efficient solar cell, as it signifies that a greater proportion of the incident solar energy is being converted into electrical power. The PCE is intrinsically linked to the values of V_{OC} , J_{SC} and FF, making the optimization of these parameters essential for enhancing the efficiency and performance of photovoltaic devices.

The MPP is the point on the I-V curve where the solar cell produces its maximum power output. The voltage and current at this point are denoted as respectively. The MPP is critical for optimizing the operational performance of the solar cell, and tracking this point is essential for maximizing energy generation in real-time applications.

Series resistance (R_s) refers to the resistance encountered by charge carriers as they move through the solar cell. High Rs values can lead to significant power losses, reducing the FF and PCE. Shunt resistance (R_{sh}) is the resistance associated with leakage currents within the solar cell. A low R_{sh} can result in significant energy losses by allowing current to bypass the external load, thus reducing the V_{OC} and FF.

The external quantum efficiency (EQE) denotes to the ratio of the conversion of incident photons into charge carriers (holes and electrons) which contribute to the current density. It is expressed as a percentage and represents the fraction of incident photons at a given wavelength that are successfully converted into electric current and can be calculated by following equation:

$$EQE(\lambda) = \frac{N_{carrier}}{N_{Photons}} \times 100\%$$
 (1.8)

A higher EQE at a particular wavelength indicates that the solar cell can effectively convert photons into electrical current.

1.4.2 Real-Space Characterization Tools in Perovskite Solar Cell Research Scanning Electron Microscopy (SEM) is an advanced imaging technique that utilizes a focused beam of high-energy electrons to generate detailed images of a sample's surface. SEM is widely employed in fields such as materials science, biology, and nanotechnology, owing to its exceptional resolution and depth of field.

The operational mechanism of SEM can be divided into several key stages. Initially, a beam of electrons is produced by an electron gun. These electrons are then accelerated through an electric field to energies typically ranging from 1 to 10 keV. The accelerated electron beam is focused into a fine spot and raster-scanned across the surface of the sample. Upon striking the sample, the high-energy electrons interact with the atoms in the material, leading to the emission of secondary electrons and backscattered electrons.

Secondary electrons are primarily responsible for generating high-resolution images of the sample's surface, while backscattered electrons provide compositional contrast, as their intensity is dependent on the atomic number of the elements present. The signals generated by these interactions are detected and processed, translating into pixel intensity values that correspond to specific coordinates on the sample surface. This process culminates in the formation of an image that reveals the surface morphology, texture, and composition of the sample.

Transmission Electron Microscopy (TEM) is a powerful analytical tool that uses a focused beam of high-energy electrons to investigate materials at the atomic level.²³ Unlike visible light, which has limited resolution due to its wavelength, the much shorter wavelength of accelerated electrons allows TEM to achieve sub-nanometer spatial resolution. As the electron beam passes through an ultrathin sample, interactions with the material's atoms provide critical information about its structural and chemical properties. Elastic scattering contributes to imaging and diffraction, while inelastic scattering underpins analytical techniques such as electron energy loss spectroscopy (EELS).

A TEM operates through the integration of several core components that manage the electron beam and capture its interactions. An electron gun, typically thermionic or field emission-based, generates a coherent electron beam, which is shaped and focused by electromagnetic lenses. The electron beam interacts with the thin specimen, producing transmitted and scattered electrons, which are further magnified and projected onto a detector to form an image. Imaging modes, such as bright-field and dark-field, provide contrast based on differences in material thickness or electron scattering. Additionally, high-resolution TEM (HRTEM) employs interference effects to visualize atomic structures, while diffraction techniques extract crystallographic information.

Atomic Force Microscopy (AFM) is a high-resolution scanning probe technique that enables the visualization of surface topography at the atomic scale.²⁴ AFM operates by measuring the interaction forces between a sharp tip and the sample surface as the tip is raster-scanned across the surface. Depending on the nature of the interaction between the tip and the sample, AFM can be operated in several modes, with the two primary modes being contact mode and tapping mode.

In contact mode, the AFM tip remains in constant contact with the sample surface. The deflection of the cantilever holding the tip is directly related to the topography of the sample, as variations in surface height cause changes in the cantilever's position. This mode is particularly useful for imaging hard surfaces but may exert significant lateral forces on softer materials, potentially causing damage. In tapping mode, the cantilever oscillates near its resonance frequency, and the tip intermittently contacts the surface. As the tip interacts with the surface, changes in the amplitude of oscillation provide topographical information. Tapping mode reduces the lateral forces applied to the sample, making it suitable for imaging delicate or soft materials. During scanning, the cantilever deflection is influenced by various forces, including van der Waals forces, electrostatic forces, and mechanical contact forces, which are then converted into a topographical image of the sample.

Kelvin Probe Force Microscopy (KPFM) is an advanced technique based on AFM that measures the surface potential and work function of a sample's surface. KPFM is

particularly valuable for studying the electronic properties of materials and interfaces, making it an essential tool in semiconductor research and other fields involving electronic materials.²⁵

KPFM operates by detecting the contact potential difference (CPD) between the AFM tip and the sample surface. The CPD is directly related to the difference in work function between the tip and the sample, which provides information about the surface potential. By mapping the CPD across the sample surface, KPFM enables high-resolution mapping of variations in surface potential and work function. This technique is widely used in the characterization of semiconductors, conductive polymers, and nanomaterials, providing insights into charge distribution, local electronic properties, and the behavior of materials in various electronic devices. The work function of sample can be determined by following equation:

$$V_{CPD} = -\frac{\Phi_{tip} - \Phi_{sample}}{e} \tag{1.9}$$

Where Φ_{tip} and Φ_{sample} are the work functions of conductive tip and samples, respectively.²⁵

1.4.3 Reciprocal-Space Characterization Tools in Perovskite Solar Cell Research

X-ray Diffraction (XRD) is a fundamental characterization of crystal structure. XRD provides valuable information about the atomic arrangement, phase composition, and structural properties of a wide range of materials and is widely used in materials to characterize crystalline materials.

The basic principle of XRD is based on Bragg's Law, which relates the angles at which X-rays are diffracted by the planes of atoms in a crystal. When a monochromatic X-ray beam is directed at a crystalline material, the X-rays are scattered by the electrons surrounding the atoms in the crystal. Constructive interference occurs when the path difference between X-rays scattered by successive planes of atoms is an integer multiple of the wavelength. This condition is described by Bragg's Law:

$$n\lambda = 2d\sin\theta \tag{1.10}$$

Where n is the order of the diffraction, λ is the wavelength of the X-ray, d is the interplanar spacing between the crystal planes, θ is the angle of incidence. By measuring the angles and intensities of these diffraction peaks, the crystallographic structure of the material can be determined.

Grazing Incidence Wide-Angle X-ray Scattering (GIWAXS) is a specialized technique designed to study the structural properties of thin films, surfaces, and nanostructures with high sensitivity to surface and near-surface regions. ²⁶ By utilizing X-rays at grazing incidence angles, GIWAXS minimizes bulk contributions while probing molecular and crystalline arrangements within the sample. This method is particularly suited for materials where surface properties, such as molecular orientation and lattice organization, play critical roles, including organic semiconductors, block copolymers, and self-assembled monolayers.

The core principle of GIWAXS involves directing a collimated X-ray beam at the sample at an incidence angle below the critical angle for total reflection. This setup ensures that the X-rays interact primarily with the surface and subsurface layers. Scattered X-rays are captured by a two-dimensional detector, allowing the simultaneous collection of both in-plane and out-of-plane scattering data. The resulting patterns are analyzed in terms of reciprocal space coordinates, such as q_{xy} (in-plane) and q_z (out-of-plane), to extract detailed information of crystalline, orientation, and molecular packing.

1.4.4 Optical Characterization Tools in Perovskite Solar Cell Research

Photoluminescence (PL) is a process in which a material absorbs photons from light and subsequently re-emits photons. This process involves the excitation of electrons from the valence band to the conduction band when the material absorbs photons with energy equal to or greater than its bandgap. The excited electrons then relax back to lower energy states, emitting photons in the process. The emitted light, known as photoluminescence, provides valuable information about the electronic and optical properties of the material.

When a semiconductor is illuminated by a light source, such as a laser or LED, photons with sufficient energy are absorbed, promoting electrons from the valence band to the conduction band. This creates electron-hole pairs, also known as excitons, within the material. Following excitation, the electron-hole pairs undergo relaxation through various mechanisms. Some of the excited carriers may relax non-radiatively, releasing energy to defects or phonons within the material. Ultimately, radiative recombination occurs, where electrons and holes recombine, resulting in the emission of photons. The energy of these emitted photons corresponds to the energy difference between the recombining states, which can be detected and analyzed through PL spectroscopy. The resulting PL spectrum provides insights into the material's band structure, defect states, and excitonic properties.

Time-Resolved Photoluminescence (TRPL) spectroscopy extends the capabilities of traditional PL spectroscopy by measuring the time dynamics of photoluminescence. TRPL provides critical information on the lifetimes of excited states, carrier recombination rates, and energy transfer mechanisms within materials. In TRPL, after excitation, the photoluminescence intensity decays as the excited states relax to lower energy levels through radiative and non-radiative processes. The decay of the PL signal is measured using a time-correlated single-photon counting system, allowing for precise measurement of the photoluminescence intensity as a function of time. This temporal information is crucial for understanding the dynamics of excited states and optimizing materials for optoelectronic applications.

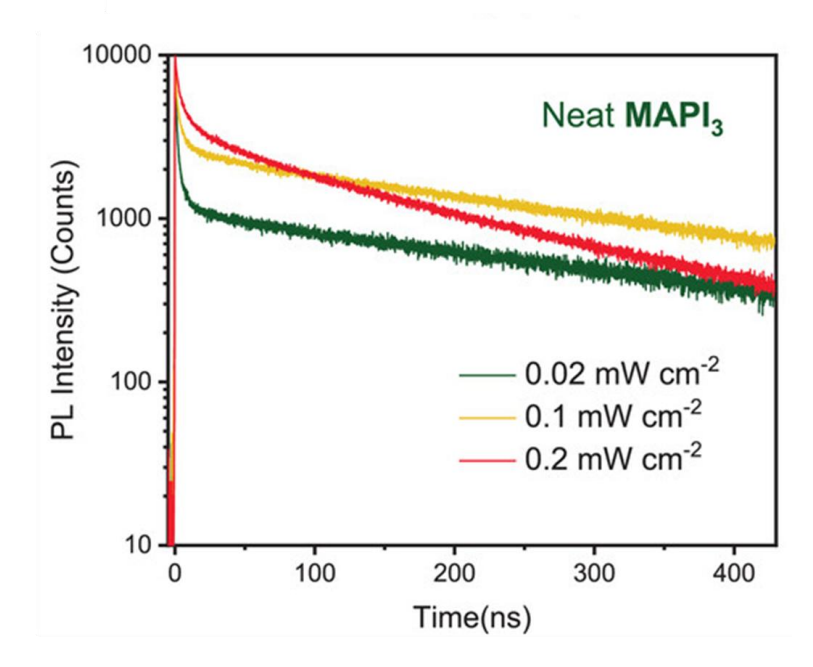


Figure 1.8 A typical transient PL spectrum based on MAPbI₃.²⁷

As illustrated a typical transient PL spectrum in **Figure 1.7**, there are two typical decays of PL lifetime, and the PL decay can be analyzed using a biexponential fitting function:

$$I(t) = A_1 \exp\left(-\frac{t}{\tau_1}\right) + A_2 \exp\left(-\frac{t}{\tau_2}\right)$$
 (1.11)

Where I(t), A_1 , A_2 , τ_1 and τ_2 represent to PL intensity, amplitudes of the fast decay, amplitudes of the slow decay, fast decay lifetime and slow decay, respectively. A high-quality perovskite films exhibit long τ_2 lifetimes (up to μ s), indicating suppressed non-radiative recombination, whereas low-quality perovskite films suffer from shorter τ_2 and dominant τ_1 , reflecting significantly nonradiative loss.

1.4.5 Photoelectron Spectroscopy Tools in Perovskite Solar Cell Research

Ultraviolet photoelectron spectroscopy (UPS) are surface-sensitive analytical techniques used to investigate the chemical composition and electronic structure of materials. UPS measurement utilizes ultraviolet photons excite electrons. UPS is primarily used to study the valence band structure and the electronic states near the Fermi level of materials. In UPS, ultraviolet photons, typically from a helium lamp, are

used to excite electrons from the valence band or shallow core levels. The kinetic energy of the emitted photoelectrons is measured to determine the binding energy of these electrons. Due to the lower energy of UV photons compared to X-rays, UPS is more sensitive to valence band states and the work function of the material, making it an essential tool for analyzing electronic properties and surface chemistry, particularly in semiconductors and organic materials.

The UPS and KPFM tool are widely used to determine the work function of samples surface, unlikely KPFM directly contact with samples, UPS use UV photos to eject electrons to get the sample surface under ultra-high vacuum. In UPS, the work function of the materials can be calculated by following equation:

$$\phi = hv - E_{kin} - E_{B} \tag{1.12}$$

Whereas ϕ represents to the work function of samples, hv is the energy of incident UV photon (21.22 eV for He-I), $E_{\rm kin}$ is the kinetic energy of emitted photoelectron and $E_{\rm B}$ represent to the binding energy of the electron in the materials.

In X-ray photoelectron spectroscopy (XPS) measurement, when an X-ray photon with sufficient energy interacts with an atom, it can eject a core-level electron, resulting in the emission of a photoelectron. The kinetic energy of this emitted photoelectron is measured and used to calculate the binding energy of the electron within the atom. The binding energy (E_b) of the electron is given by the equation:

$$E_b = h\nu - E_k - \phi \tag{1.13}$$

Where hv is the energy of the incident X-ray photon, E_k is the kinetic energy of the emitted photoelectron and ϕ is the work function of the spectrometer. The binding energy is characteristic of the specific element from which the electron was emitted and provides information about the atom's chemical environment. This makes XPS a powerful tool for elemental identification and chemical state analysis, particularly for the surface layers of materials.

Time-of-Flight Secondary Ion Mass Spectrometry (TOF-SIMS) is a highly sensitive surface characterization technique that enables detailed analysis of the chemical composition and molecular structure of materials. It operates by bombarding a sample with a focused primary ion beam, which induces the emission of secondary ions from the surface. These secondary ions are then analyzed based on their time of flight through a mass spectrometer, where lighter ions travel faster than heavier ones, allowing for precise mass-to-charge ratio determination. This technique is particularly effective in probing the outermost layers of materials, providing invaluable insights into surface chemistry at nanometer resolutions. TOF-SIMS is widely utilized in fields such as materials science, nanotechnology, and surface engineering for studying the composition of thin films, coatings, and complex surfaces.

TOF-SIMS can be operated in various modes, each tailored to specific analytical requirements. The static mode, characterized by low ion doses, is ideal for surface-sensitive analysis and prevents significant alteration of the sample, making it suitable for delicate biological samples and thin films. In contrast, the dynamic mode uses higher ion doses for depth profiling, allowing for the analysis of multilayered materials and the distribution of dopants in semiconductor devices. TOF-SIMS provides spatially resolved chemical mapping, which is crucial for understanding the distribution of different elements or molecular species across a sample surface. Additionally, TOF-SIMS offers excellent sensitivity, with detection limits reaching parts per million, and high mass resolution, which is essential for identifying complex molecular structures and trace contaminants.

1.5 Motivation

The low-cost, high absorption coefficient and exceptional charge mobility of solution-processed organic-inorganic metal halide perovskite have garnered significant attention due to their promising optoelectronic properties. The certificated PCE of inverted perovskite solar cells (IPSCs) has met an incredible increase from 3.9% in 2009 to 26.7% in 2024. It is indeed a miracle which is comparable with silicon solar cells. It is truly remarkable to witness such significant progress achieved within such a short period, especially when considering that conventional silicon solar cells required

more than forty years to reach the current level of development. However, the PCE of PSCs is remains lag far behind their theoretical limit, which is approximately 86% for a bandgap in the range of 1.5 to 1.6 eV. The energy loss in PSCs primarily arises from issues related to perovskite bulk crystallinity and the interfaces. Reducing this energy loss is essential to minimizing non-radiative recombination, particularly at defect-rich interfaces. Improving crystallinity and optimizing interfaces are therefore critical steps in enhancing the efficiency and performance of these devices. PSCs, with their combination of cost-effectiveness and high performance, has the potential to significantly impact the renewable energy field and contribute to a rapid transformation of the global energy landscape. To achieve both high efficiency and stability in IPSCs, we mainly focus on two crucial interfaces: surface passivation of the top surface and optimization of the buried interface.

1.6 Objectives

This thesis mainly focuses on three parts:

In chapter 4, we focus on the top surface of IPSCs, simply introducing a celebrity n-type polymeric semiconductor material, PY-IT, at the perovskite top surface. Encouragingly, this polymerized small molecular acceptor (PSMA) exhibits significant effectiveness in passivation of traps and enhancing electron transport on merits of strong planarity and rotatable linkers, which significantly optimized perovskite grain growth orientation and added charge transport channels. As a result, the PSMA-treated IPSCs obtain an optimal efficiency of 23.57% with a FF of 84%, representing one of the highest efficiency among PSMA-based IPSCs. Meanwhile, the PSMA PSCs exhibit impressive photo-stability, retaining approximately 80% of its initial PCE after 1000 hours of simulated 1-sun illumination under MPP tracking.

In chapter 5, we demonstrated a co-adsorbed (CA) strategy aimed at minimizing interfacial energy losses at the buried interface in IPSCs. By employing a novel small molecule, 2-chloro-5-(trifluoromethyl)isonicotinic acid (PyCA-3F), which is incorporated at the buried interface between 2PACz and the perovskite/organic layers.

The CA approach effectively reduces 2PACz aggregation, enhances surface smoothness, and increases the work function of the modified self-assembled monolayer (SAM), resulting in a flattened buried interface with a favorable heterointerface for the perovskite. The resultant improvements in crystallinity, minimized trap states, and augmented hole extraction and transfer capabilities have propelled PCEs beyond 25% in PSCs with a p-i-n structure (certified at 24.68%). OSCs employing the CA strategy achieve remarkable PCEs of 19.51% based on PM1:PTQ10:m-BTP-PhC6 photoactive system. After a 1000-hour maximal power point tracking, the encapsulated IPSCs and OSCs retain approximately 90% and 80% of their initial PCEs, respectively.

In chapter 6, we investigates the synthesis and application of novel SAMs in IPSCs. Two SAMs, PABDCB and MeO-PABDCB, featuring rigid phenylene linkers, were developed to construct densely packed, organized (hole transport layers) HTLs. Both SAMs form strong preferrable tridentate binding modes with ITO substrates, as confirmed by theoretical analysis. Moreover, through methoxy group modification in terminal group, MeO-PABDCB demonstrated significantly enhanced charge transport and passivation properties, leading to a high PCE of 26.25%. These emphasize that the molecular structure can play a pivotal role in enhancing photovoltaic performance, demonstrating the potential of SAM's design in next-generation photovoltaic applications.

This research thesis aims to develop cost-effective and high-performance IPSCs with a focus on top surfaces and buried interfaces. Through these efforts, we seek to unlock the full potential of IPSCs and contribute positively to advancements in the renewable energy field.

Chapter 2 Fundamentals of Interfaces in Semiconductors and Their Role in Perovskite Solar Cells

2.1 Introduction of Interfaces

In semiconductor-based devices, interfaces are critical regions where two distinct materials meet, and their physical properties interact. The behavior of these interfaces plays a pivotal role in determining the performance of semiconductor-based devices, including photovoltaic cells, photodetectors and transistors. The efficiency of solar cells, particularly in the case of PSCs, is influenced by the interaction between the perovskite absorber and the adjacent layers, including charge transport layers and electrodes. These interfaces impact processes such as charge generation, separation, transport, and extraction, all of which are central to the performance of solar cells.

The behavior of these interfaces is complex and can lead to challenges such as energy level misalignment, surface defects, and recombination centers, all of which can degrade the efficiency and stability of the solar cells. Understanding the fundamental physics of charge injection, transport, and recombination at these interfaces is, therefore, essential for optimizing the performance of PSCs. This chapter provides a comprehensive overview of the various types of interfaces in semiconductor materials, focusing on their influence on the development and optimization of PSCs.

2.2 Types of Interfaces in Semiconductors

Semiconductor devices generally consist of multiple layers with distinct materials, each creating unique interfaces. These interfaces directly affect the behavior of charge carriers and impact on the charge carriers and performance of the device. The primary types of interfaces encountered in semiconductor materials include metal-semiconductor interfaces (M-S contact), semiconductor-semiconductor interfaces (S-S contact), surface-related interfaces, and grain boundaries.

2.2.1 Metal-Semiconductor Interfaces

Metal-semiconductor interfaces, commonly referred to as Schottky interfaces, occur when a metal comes into direct contact with a semiconductor material. At such

interfaces, the metal and semiconductor materials form a potential barrier due to differences in their work functions and electron affinities. At these interfaces, a Schottky barrier forms due to the difference in work functions and electron affinities between the metal and the semiconductor. This potential barrier can either facilitate or hinder the injection of charge carriers, depending on its height and nature. As shown in **Figure 2.1a**, when a metal and semiconductor are brought into contact before reaching thermodynamic equilibrium, the semiconductor remains neutral charge, which results in a flat band structure. If the semiconductor is lightly doped, significant charge transfer occurs from the metal to the semiconductor to align their Fermi levels. This process continues until the Fermi energy of both materials is in equilibrium. As a result, a spacecharge region is formed at the interface, with a concentration of electrons near the metal-semiconductor boundary (**Figure 2.1b**).²⁸

In photovoltaic devices, metal-semiconductor interfaces are crucial for charge extraction. Metal contact serves as the extraction point for electrons or holes, and its effectiveness is determined by the properties of the Schottky barrier. A too high Schottky barrier that may impede charge injection, while a lower barrier allows for more efficient carrier flow. Additionally, the contact resistance between the metal and semiconductor can affect the performance of the solar cells. In the case of PSCs, metal contacts play a crucial role in charge extraction, and optimizing this interface is essential for minimizing energy losses.

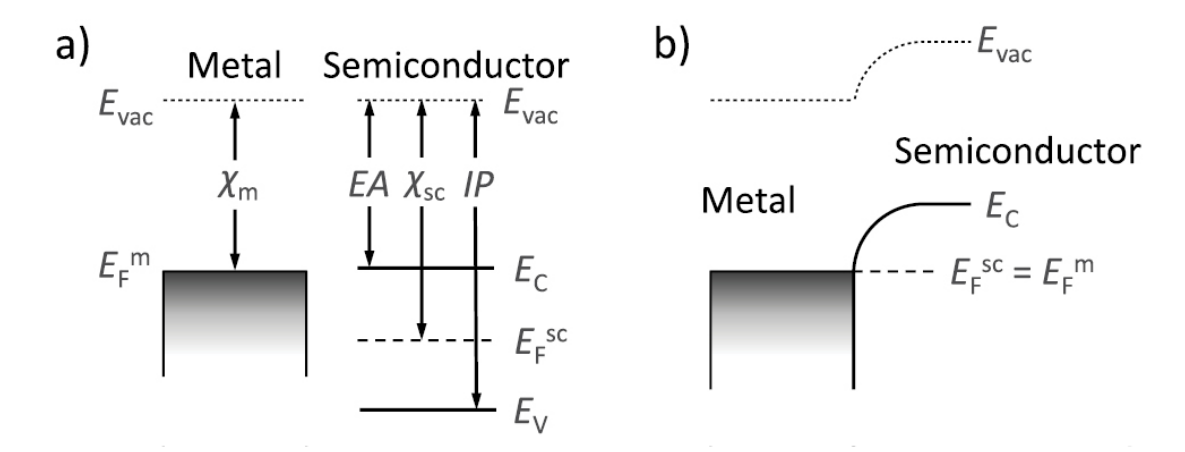


Figure 2.1 (a) Metal-semiconductor interface prior to thermodynamic equilibrium, both metal

and semiconductor show flat bands. (b) Metal-semiconductor interface at thermodynamic equilibrium, showing band bending at the metal/semiconductor interface.²⁸

2.2.2 Semiconductor-Semiconductor Interfaces

Semiconductor-semiconductor interfaces occur when two different semiconductors with distinct electronic properties come into contact. Semiconductor-semiconductor interfaces can be broadly categorized into homojunctions and heterojunctions:

Homojunctions: Shown in **Figure 2.2**, a homojunction occurs when two identical semiconductors with different doping levels are brought into contact.²⁹ This results in an internal electric field due to the difference in carrier concentration on either side of the junction. The band bending at the junction forms a built-in potential that drives charge separation when the material is exposed to light. Homojunctions are relatively simple to fabricate but are less efficient for broader bandgap solar cells, such as those needed in multi-junction or tandem solar cell designs.

While homojunctions are not typically used in PSCs, they offer insight into the basic principles of p-n junctions, which are essential for understanding charge separation in photovoltaic devices. In some PSCs, homojunction behavior can occur between layers of perovskite material with different doping concentrations, contributing to the efficiency of charge separation.

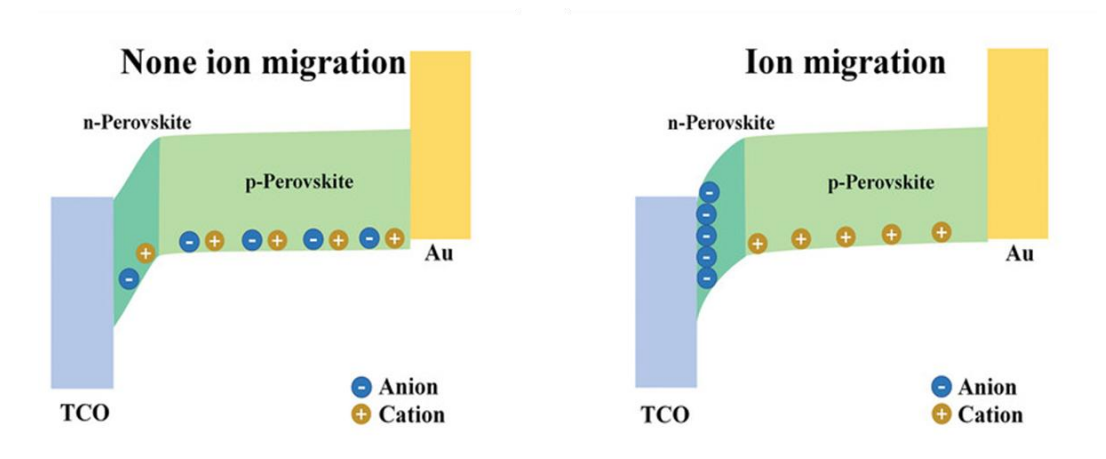


Figure 2.2 (a) Schematic diagrams of energy band structures of homojunction PSCs in nonion migration status and (b) Schematic diagrams of energy band structures of homojunction PSCs

Heterojunctions: As illustration in **Figure 2.3**, a heterojunction occurs when two different semiconductor materials with distinct electronic properties come into contact, forming an interface with unique behavior that is crucial in solar cells.³⁰ The primary advantage of heterojunctions over homojunctions is the ability to combine materials with different bandgaps, which allows for a more efficient absorption of the solar spectrum. The band alignment of the conduction and valence bands at the heterojunction interface determines the efficiency of charge transfer between the two materials. If the bands align favorably, charge carriers can move efficiently from one material to the other, contributing to better performance. On the other hand, poor alignment can result in charge accumulation at the interface, increasing recombination losses and reducing device efficiency.

Heterojunctions are central to the operation of PSCs, as the perovskite material typically forms a heterojunction with the ETL and the HTL. The interface between the perovskite and these transport layers must be carefully engineered to ensure optimal charge injection, transport, and extraction. Furthermore, heterojunctions are key to the development of tandem solar cells, where different materials with complementary bandgaps are stacked to maximize light absorption and conversion efficiency.

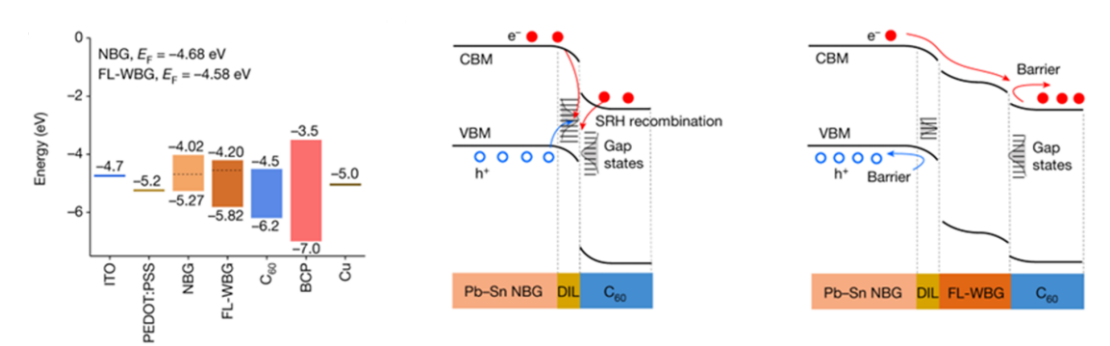


Figure 2.3 Schematic of energy level of planar heterojunction (PHJ) perovskite solar cells.³⁰

2.2.3 Interfaces within Semiconductors

The surfaces of a semiconductor often behave differently from the bulk material, exhibiting unique electronic properties due to the presence of surface states or defects.

These surface states can act as recombination centers, where photo-generated charge carriers are trapped and recombine before they can be extracted, leading to a loss in efficiency. This is particularly problematic in thin-film solar cells, such as perovskite devices, where the surface-to-volume ratio is large.

Moreover. many semiconductor materials, including perovskite, are polycrystalline, meaning they are composed of many smaller crystals, or grains, that are joined together at grain boundaries. These boundaries can introduce structural defects and create barriers to carrier transport, thereby limiting device performance. Grain boundaries can also serve as recombination centers, where charge carriers are trapped and prematurely recombine. For example, considering the case of a grain boundary in n-type material, as illustrated in Figure 2.4, the defect states within the band gap are typically distributed local neutrality level and close to the center of the bandgap. In these conditions, the defect states behave as acceptors, trapping electrons. This results in a plane of fixed negative charge at the grain boundary and a corresponding layer of positive space charge in the surrounding depleted n-type material. The resulting electrostatic field generates a potential barrier that impedes the migration of majority carriers. Conversely, minority carriers are attracted to the potential well formed at the grain boundary, which facilitates their migration towards this region. Therefore, they are more likely to recombine with trapped majority carriers and cause energy loss at the interface.³¹ The grain size and grain boundary are critical factors that influence the interface states as well as the transport properties of polycrystalline semiconductors.

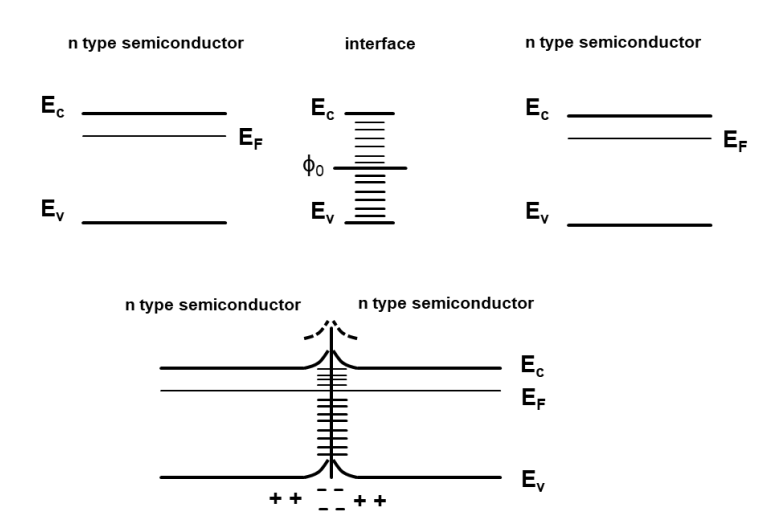


Figure 2.4 Schematic representation of band bending caused by interface states sandwiched between two n-type semiconductor layers.³¹

In PSCs, strategies to improve grain growth and reduce defects at surface and grain boundaries are critical for optimizing carrier mobility and reducing recombination losses. interface engineering within perovskite is thus a key aspect of developing high-performance perovskite devices.

2.3 Interface in Perovskite solar cells

2.3.1 Device Structure

Solution-processed organic-inorganic halide perovskites have attracted considerable attention because of their unique optoelectronic characteristics, such as high charge mobility, long carrier lifetime, and high absorption coefficient. To date, PSCs have achieved PCE of 26.7%, which is comparable to the recorded monocrystalline silicon solar cell (~26.7%) and is approaching the Schottky-Queisser limit of single-junction solar cells. In 2009, Miyasaka et al. developed organometal trihalide perovskites as sensitizers in the study of dye-sensitized solar cells (DSSCs), which pioneered the use of organometallic halide perovskites in solar cells. 32,33

The structures of PSCs are generally divided into two categories: regular (n-i-p) and inverted (p-i-n) configurations, where the regular can be subdivided into mesoporous (with a mesoporous scaffold) and planar configurations (without a mesoporous scaffold), as shown in **Figure 2.5** The high-efficiency regular PSCs

typically utilize spiro-OMeTAD as the hole transport layer, however, this organic material requires complicated doping and oxidation processes, which are less compatible with up-scaling and flexible applications. Compared to PSCs with regular structures, IPSCs are attractive and may be suitable for flexible, roll-to-roll, and tandem applications. 34,35 Based on the unique photophysical and electrical properties of perovskites, extensive research has been conducted to develop IPSCs. IPSCs emerged in 2014 using NiO_x or PEDOT:PSS as the HTL and PCBM or n-type metal oxides like ZnO as the ETL. 36-38 The concept mimics earlier organic solar cells (OSCs) with versatile device architectures, where "inverted" OPVs were introduced in 2006 and assisted with the application of p-type metal oxides in OPVs. ^{39,40} This p-i-n structure has been applied as another type compared to the regular (n-i-p) structure. 41-43 A general structure of IPSCs consists of transparent conductive oxides (TCO)/ HTL/perovskite active layers (perovskite)/ ETL/buffer layers/metal contacts. IPSCs typically operate as follows: when illuminated by solar irradiation, the active perovskite layer absorbs the photons and generated excitons. These excitons are dissociated into hole-electron pairs, which are further separated and diffused into the transport layer by the built-in electric field. The holes are transferred to the ITO side through the HTL, while the electrons propagate into the metal contacts through the ETL and buffer layer.

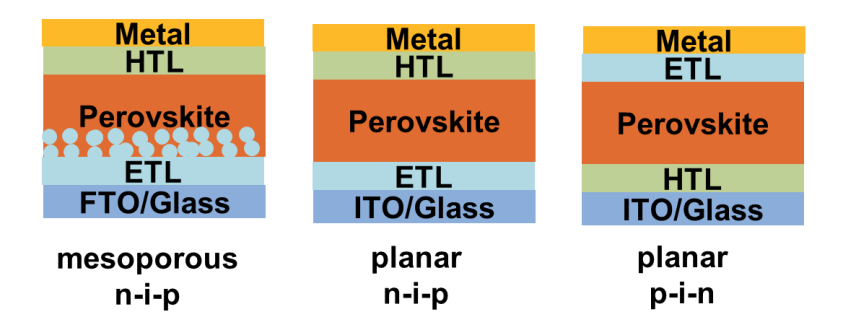


Figure 2.5 Device structures of perovskite solar cells.

The multiple functional layers in PSCs are integral to the overall device performance, with each layer contributing to the optical, electrical, and mechanical properties that enable efficient energy conversion. These layers include the perovskite light absorber, HTLs, ETLs, and electrodes, each of which introduces distinct interfaces that significantly influence the functionality of the device.

As illustrated in **Figure 2.6**, the interfaces between these layers, particularly the perovskite/HTL (ETL) interface, are crucial for optimizing charge extraction and minimizing losses, thus directly affecting the performance metrics of PSCs.

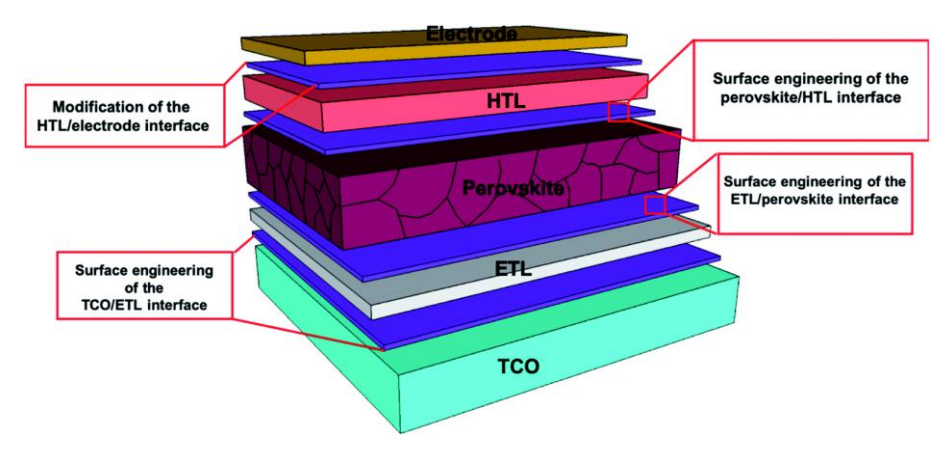


Figure 2.6 Typical interfaces in perovskite solar cells.⁴⁴

2.3.2 Energy level and Working Mechanism

Compared to inorganic photovoltaics with large dielectric constants, such as silicon, perovskite photovoltaics are well suited to the free-carrier model, where charges can be easily separated and transported.²⁷ The typical energy level diagram of IPSCs is shown in **Figure 2.7a.**⁴⁵ The interfacial energy level affects the dynamics of charge injection and transport. A well-balanced energy level will facilitate charge transfer and extraction, resulting in improved device performance. The charge transport dynamics is related to the highest occupied molecular orbital (HOMO) (or the valence band maximum, VBM) in classical semiconductors and the lowest unoccupied molecular orbital (LUMO) (or the conduction band minimum, CBM) of the device's layers, including ITO, ETL, active perovskite, HTL, and metal contact. According to Murata, the mismatch between the band levels should be within 0.2 eV to reduce interfacial loss and obtain high performance. If the energy band is not properly aligned, the energy barrier will increase, resulting in significant energy loss.^{46,47}

The working principle of IPSCs is illustrated in Figure 2.7b. When the IPSCs are

not photoactivated, Fermi-level equilibration/alignment happens in all layers of the device, resulting in an electric field at the interface. When the devices are activated by solar energy entering nonequilibrium conditions, the electrons are excited from the valence band to the conduction band. Then the photogenerated electron-hole pairs are separated into electrons and holes by a built-in electric field. The anode and cathode are responsible for collecting electrons and holes following the diffusion, transport, and extraction processes.⁴⁸ Nevertheless, the charges undergo non-radiative recombination due to the bulk or interfacial traps.

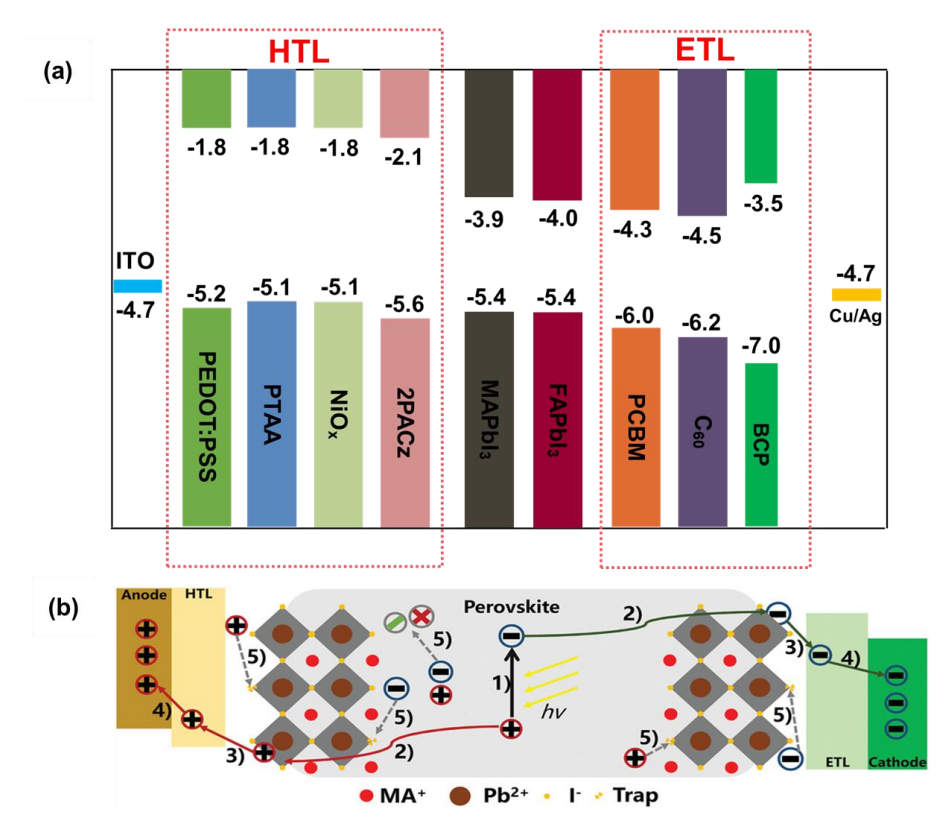


Figure 2.7 (a) Scheme of the energy levels of each layer in IPSCs. (b) Working principle of perovskite solar cells: 1) charge dissociation, 2) charge diffusion, 3) charge transport, 4) charge extraction, and 5) charge recombination.⁴⁸

2.3.3 Defects

The inherent defects in hybrid perovskites induce a significant amount of traps states, which result in nonradiative charge recombination and damage device performance in terms of PCE and stability.⁴⁹⁻⁵¹ The trap-assisted recombination in IPSCs can be described by Shockley-Read-Hall (SRH) theory. When defects create

deep-level traps, they only trap electrons or holes that cannot escape by thermal activation and then annihilate with oppositely charge carriers. Figure 2.8 shows two types of traps in IPSCs, including shallow-level and deep-level traps. Shallow-level traps are originated from point defects such as cation vacancies and halide vacancies. Both vacancies are not harmful to the performance of perovskite devices and can be remitted as charges into CBM or VBM via phonon absorption. However, carrier migration at such point defects can result in unintentional shallow gaps, hysteresis, phase separation, and degradation of IPSCs. Another type of trap, deep-level traps, such as uncoordinated Pb²⁺, metallic lead clusters, and Pb-I anti-site defects, are deteriorating the performance of photovoltaic devices. The SRH recombination induced by deep-level traps in perovskites is the primary source of charge carrier loss. This phenomenon can be caused by a variety of factors, including the non-stoichiometric ratio of lead iodide and organic cations and the prolonged thermal annealing process. Signature of the prolonged thermal annealing process.

Defects can be located on the surface, at the grain boundaries, or within the grain interiors of IPSCs. Charge extraction and transport are affected by interfacial defects, increasing series resistance and reducing J_{SC} and FF. Defect passivation is considered an effective strategy to reduce non-radiative recombination and suppress ion migration in IPSCs.

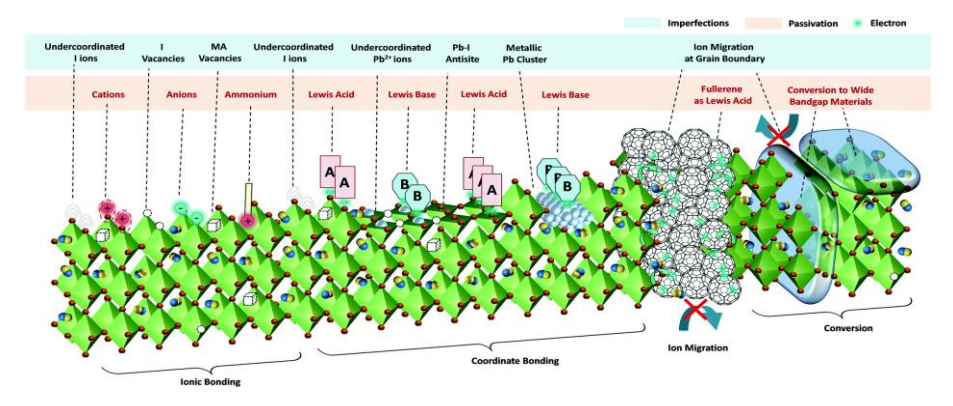


Figure 2.8 Imperfections in OIHP film and their passivation strategies.⁵¹

Chapter 3 Literature Review

3.2 Hole Transport Layers in Inverted Perovskite Solar Cells

The inferior performance of IPSCs is primarily due to the sluggish charge extraction and severe non-radiative recombination at the interfaces, which limit the $V_{\rm OC}$ and FF. The growth of perovskite crystals is highly dependent on the HTLs. It is found that perovskites form larger grains on hydrophobic substrates rather than hydrophilic substrates.⁵⁴ Furthermore, trap states at the bottom interface of perovskite can result in severe charge accumulation and recombination in IPSCs. Both the crystallization and growth of perovskite grains the extraction and transport of holes are also related to the HTLs.⁵⁵ A prerequisite for obtaining high-quality perovskite films is to reduce defect density, which significantly depends on the beneath substrate on which the perovskite crystallizes and grows into films. IPSCs cannot be fully optimized without considering the effect of the HTLs. Perovskite films are affected by the wettability of the substrates used during grain crystallization and growth. Compared to the larger quantity of droplets on hydrophilic substrates, perovskite precursors form relatively few nucleation sites on hydrophobic substrates, such as PTAA, poly-TPD, and some metal oxides. 54,56 Typically, fewer nucleation sites favor the development of larger and high-quality grains. However, non-wetting hydrophobic substrates with poor affinity to the precursor may result in poor continuity and o incomplete coverage of perovskite film with pinholes.⁵⁷ Therefore, the quality of perovskite films and device performance can be effectively controlled by manipulating the HTLs. To date, several materials are regarded as the most efficient HTLs in IPSCs, including PTAA, NiOx and Selfassemble monolayers (SAMs).

3.2.1 PTAA-based Inverted Perovskite Solar Cells

PEDOT:PSS was initially used in IPSCs, but the acidity and hydroscopic group were detrimental to the device stability, which resulted in serious degradation of IPSCs.

Other p-type organic semiconductor materials are required to be developed as new

HTLs. PTAA is currently one of the most promising candidates for IPSCs because it is efficient and stable. Most recent PCEs of PTAA-based IPSCs showed an efficiency over 25%. S8-62 Although PTAA has the potential to have high efficiency and stability, there is an excessive amount of small-sized crystals that resulted in high trap density at the interface between PTAA and perovskites. A slight mismatch in energy levels between the HOMO of PTAA and the VBM of perovskite also brings unfavorable energy losses at the interface.

The modification of PTAA by surface treatment is considered an effective method to improve the performance of devices. It is worthwhile investigating the PTAA/perovskite interface to improve the quality of perovskite films in IPSCs 65,66. Recently, Neher and Zhang adopted a conjugated polyelectrolyte (PFN-Br) as an interfacial layer for both PTAA and poly-TPD. ^{67,68} The PFN-Br plays several functions. First, the incorporation of PFN-Br is suggested to improve the wettability and surface energy of PTAA substrate by the polar quaternary ammonium group. Second, the quaternary group tends to interact with $[PbX_6]^{4-}$ octahedral via electrostatic interaction. Finally, the Br groups in PFN-Br can passivate the halide vacancy, resulting in highquality perovskite film with reduced defects.⁶⁹⁻⁷¹ Combined with a LiF treatment at the perovskite/ETL interface, the non-radiative recombination loss was suppressed at both interfaces, resulting in higher V_{OC} and FF. Similarly, Zhang and co-workers proposed the use of 3-(1-pyridinio)-1-propane sulfonate (PPS) as a chemical bridge at the PTAA/perovskite interface. 72 The PPS molecule with the functional pyridine group is expected to passivate the interfacial defects and suppress non-radiative recombination. Meanwhile, the S=O bond in PPS exhibits strong coordination with the empty orbital of Pb²⁺ in the perovskite. As a further illustration of the passivation properties of PPS molecules, Figure 3.1 shows the charge collection and recombination scheme at the two interfaces. The molecular can be used to reduce the density of traps in perovskites by passivating halide and cation vacancies. Also, PPS can adapt PTAA to achieve a more favorable energy alignment within IPSCs, facilitating hole extraction and carrier transfer at the interface.

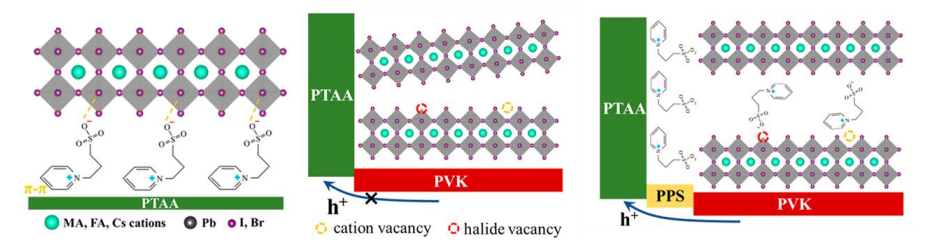


Figure 3.1 Schematic illustrations of charge transport between PTAA and perovskite with/without PPS.⁷²

In addition to the interface engineering of PTAA, the target design of new PTAA molecules with functional groups has been reported to enhance wettability, build deeper energy levels, and passivate interfacial traps. Gao et al. introduced polar methoxy groups into the para and ortho positions of the dangling benzene in the PTAA molecular structure and produced 2MeO-PTAA. Asymmetric methoxy groups with electron-donating properties increase the surface energy, facilitating tight interfacial contacts and hole extraction at the PTAA/perovskite interface. The PCE and FF of the 2MeO-PTAA-based device increased to 20.23% and 0.84 with negligible hysteresis, which is possibly due to decreased surface defects and reduced shunt resistance losses. Similarly, Wu et al. substituted the alkyl groups in PTAA with multifunctional pyridine groups to change the ortho- (o-PY), meta- (m-PY) linking site of the pyridine unit to para-location (p-PY); this modification improved the performance of IPSCs. In addition to the hydrophilicity, the passivation efficacy was enhanced using the pyridine functionalized PTAA. It showed 22% efficiency for a small-size device (0.09 cm²) and 20% for an upscaled device (1 cm²).

3.2.2 NiO_x-based Inverted Perovskite Solar Cells

Organic HTMs suffer from the high cost of their raw materials, the drawback of upscaling fabrication, and undesirable thermal stability; these restrict the application and commercialization of IPSCs. Alternatively, inorganic p-type metal compounds with high transparency, such as cooper families (Cu_2O , CuSCN, CuI, $CuGaO_3$), molybdenum oxide (MoO_3), vanadium oxide (VO_x), and nickel oxides (VO_x) have

attracted much attention. Along them, NiO_x has attracted extensive attention because of its suitable work function, high transmittance, and high thermal/light stability. However, NiO_x HTLs have unsatisfactory conductivity and a large number of surface defects, which would cause severe interfacial charge recombination, resulting in poor V_{OC} and FF.

Various strategies, such as metal doping and surface treatment, have been employed to optimize the performance and reduce the energy loss of NiO_x-based IPSCs. Intrinsic NiO with stoichiometric Ni²⁺ and O²⁻ is insulation; it always requires selfdoping of Ni³⁺ to construct p-type NiO_x. However, the considerable ionization of Ni³⁺ hinders the conductivity, thus limiting the application of NiO_x. In this regard, universal doping strategies have been proposed to optimize the energy structure and conductivity. 76-78 Liu et al. synthesized Samarium-doped nickel oxide (Sm:NiO_x) using a facile chemical precipitation method. 79 It is suggested that the Sm³⁺ doping can reduce the formation energy of Ni vacancy and increase the density of Ni vacancies, therefore increasing the hole density. Consequently, IPSCs based on Sm:NiOx HTL delivers a champion efficiency of 20.71%, which is ascribed to enhanced conductivity and work function. More importantly, Sm:NiO_x is also compatible with larger-area applications, which delivers PCE of 18.51% (area 1 cm²) and 15.27% (16 cm²). Another ionic liquidassisted synthesis strategy (NiO_x-IL) was recently proposed by Li et al. by adding 1butyl-3-methylimidazolium tetrafluoroborate ([BMIm]BF₄) into Ni(NO₃)₂ precursor; the synthesis scheme is illustrated in **Figure 3.2a**. 80 It is illustrated that [BMIm]⁺ cation had lower adsorption energy than NO₃⁻ to be adsorbed with Ni(OH)₂ via hydrogen bonding in the precursor solution. This setup effectively increased the conductivity of as-prepared NiO_x-IL films and suppressed the redox reaction in the buried NiO_x-IL/perovskite interface. The energy band diagram of NiO_x-IL-based devices has been alleviated by downshifting closer to the valance band of perovskite, where the hole transfer and injection are improved at the NiO_x-IL/perovskite interface. As a result, the NiO_x-IL-based IPSCs delivered an efficiency as high as 22.62% with superior stability,

which maintained 92% of its initial value under maximum power point tracking and 1000-hour sun illumination.

Surface treatment by inorganic and organic materials is denoted as another effective strategy to improve the conductivity and optimize interfacial defects of NiO_x. 81-83 Recently, Chang et al. recently adopted CsBr as an interfacial buffer layer between NiO_x and perovskite layer. 84 Confirming by the XRD results, it is demonstrated that the smaller Young's modulus of CsBr (16.2 GPa) is expected to reduce the lattice strain of initial perovskite (17.8 GPa) under the thermal annealing process. Consequently, IPSCs with the relieved perovskite lattice strain and reduced interface traps delivered an efficiency of up to 19.7%. In addition, Chen and colleagues developed a series of molecules, including TCNQ, F2TCNQ, F4TCNQ, and F2HCNQ on the NiO_x/perovskite interface to control the electron affinity. 85 It was found that the conductivity of NiO_x is improved more than tenfold after the introduction of F2HCNQ, which could be resulted from the deeper LUMO and increased hole concentration in the VB. Moreover, the energy gap between E_F and VB is decreased from 0.5 eV (control) to 0.24 eV (F2HCNQ), resulting in fast hole extraction with lower interfacial energy loss. This method drastically enhanced the V_{OC} and FF of IPSCs, which obtained the PCEs of 22.13% for small rigid (0.09 cm²) and 12.85% for the flexible mini module (36.1 cm²). Sargent et al. recently modified the surface of NiO_x using organic spacer cations with -NH₂-rich groups such as n-butylammonium (BA), ethylammonium (EA), dimethylammonium (DMA), guanidinium (GUA).86 It is proved that the highly symmetric structure of GUA and -NH₂ functional groups have a large binding affinity to O atoms on the NiO_x surface via hydrogen bonding (**Figure 3.2b**); this induces the formation of 2D perovskite at the buried interface. The 2D perovskite can act as both seeds for perovskite crystallization and passivation layer for reducing defect density. As a result, the wide-bandgap (1.7 eV) device based on GUAI seeds showed a champion PCE of 20.1%. Meanwhile, the method could be compatible with 1.55-eV bandgap perovskite system, which yielded an efficiency of up to 22.9%, a milestone

among the highest efficiency of NiO_x-based IPSCs.

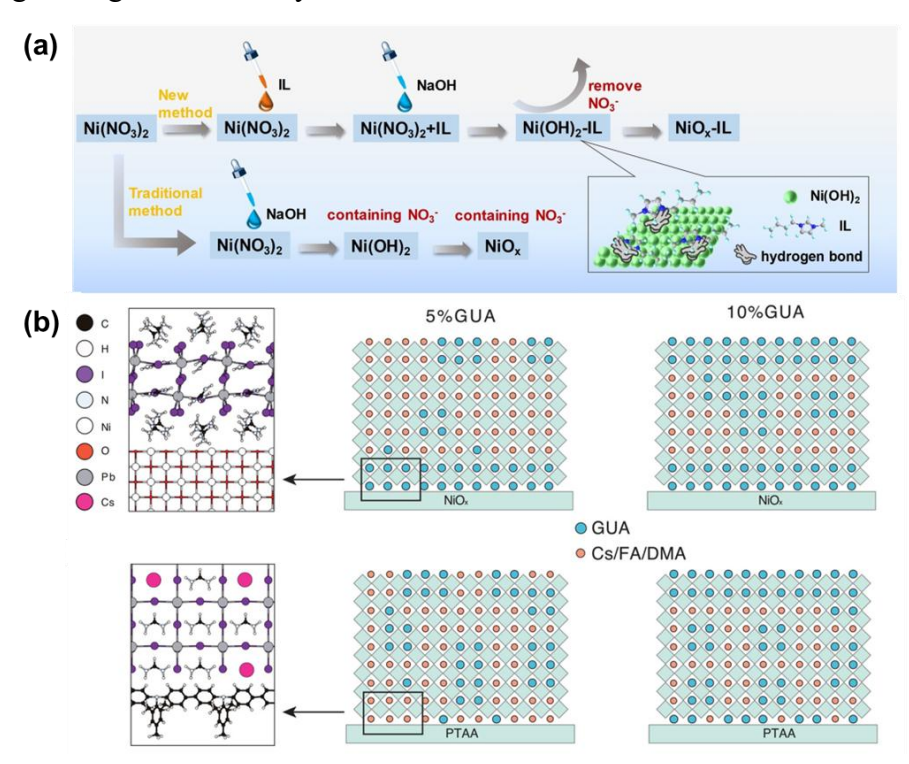


Figure 3.2 (a) Scheme of synthesis of NiO_x and NiO_x -IL nanoparticles.⁸⁰ (b) Mechanism of GUA_2PbI_4 interaction with NiO_x and PTAA substrate.⁸⁶

Inspired by regular mesoporous structure, NiO_x with mesoporous scaffold has also attracted the attention of researchers. The mesoporous structure can provide light management and increase the contact area of HTM/perovskite for efficient hole extraction and transport. There are desirable candidates of mesoporous scaffold for IPSCs such as NiO_x, Al₂O₃ and CuGaO₂. Zhang et al. proposed a mesoporous CuGaO₂ as mesoporous layer for IPSCs. ⁸⁷⁻⁸⁹ The mesoporous CuGaO₂ severs as a perovskite scaffold, enabling increased light absorption due to light scattering and reduced reflection in the device. In addition, the graded energy alignment shows superior charge transfer and collection at the NiO_x/perovskite interface. Furthermore, they later reported that the performance of mesoporous CuGaO₂ could be further increased by doping Zn²⁺. ⁹⁰ These advantages of mesoporous CuGaO₂ enabled high efficiency and superior stability compared to planar NiO_x IPSCs. Similarly, the utilization of mesoporous NiO_x (mp-NiO_x) was employed via triblock copolymer template-assisted strategy by Tress et al. ⁸⁸ The mp-NiO_x-based IPSCs delivered a higher J_{SC} of 23.8 mA/cm² compared to

22.9 mA/cm² for planar NiO_x devices, which could be ascribed to the enhanced light trapping and absorption in the adjacent perovskite film in the mp-NiO_x structure.

Most recently, the PCE of NiOx-based IPSCs exceeded 25% via precursor engineering and interface engineering. For example, by treating NiOx to forming H₂O₂-NiOx, certificated PCE of 25.2% is achieved.⁹¹ Up to date, an extraordinary PCE up to 26.4% (certificated 25.9%) is obtained with NiOx as HTL for IPSCs.⁹²

3.2.3 Self-assemble Monolayers based Inverted Perovskite Solar Cells

Self-assemble monolayers (SAMs) contain organic molecules that are anchored as a monolayer to substrates (typically metals and metal oxides) via chemical bonds. SAMs can be tailored to fulfil the intermolecular interaction with high affinity to the substrates. SAMs can be attached to the surface by simple spin-coating or dip-coating methods to form extremely thin and stable layers. Moreover, the optoelectrical properties of SAMs, such as conductivity and work function, can be tuned by functionalization of different groups. These SAMs are currently regarded as novel HTL candidates for IPSCs with high efficiency and high stability. In IPSCs, SAMs of organic molecules on the ITO surface are usually denoted as conventional single-atom HTL to facilitate hole injection at the ITO side. 93-95 The use of carbazole bodies with phosphonic acid groups (2PACz, MeO-2PACz and V1036) was firstly reported as SAMs for IPSCs by Albrecht and co-workers. 96 As shown in Figure 3.3a, the 2PACz and MeO-2PACz are expected to form strong bonds with ITO to provide deeper work function SAMs. From the band edge positions shown in Figure 3.3a, it is demonstrated that the HOMO of 2PACz is closest to the VBM of perovskite, which is beneficial to hole extraction and transport. Moreover, they conducted ultraviolet photoelectron spectroscopy (UPS) and photoluminescence (PL) measurements to further verify the minimized interfacial recombination and extended carrier lifetime of perovskite on 2PACz. As a result, the 2PACz-based IPSCs delivered a PCE of 20.9% with a high V_{OC} of 1.19 V. The most important reason for the improved performance can be derived from the surface dipole and shifted vacuum level of ITO coated with SAMs such as

2PACz and MeO-2PACz. 95 To date, 2PACz and MeO-2PACz-based IPSCs have been reported to be among the most efficient IPSCs, with the efficiency exceeding 24% and 25%. 97,98 Hereafter, they designed a novel SAM with methyl group ([4-(3,6-dimethyl-9H-carbazol-9-yl)butyl]phosphonic acid, Me-4PACz). 99 The Me-4PACz enabled fast hole extraction with reduced phase segregation for wide bandgap (1.68 eV) IPSCs. The ultra-thin SAM (<1 nm) with high conductivity was also found to reduce the transport loss, resulting in a PCE of >20% and an ultra-high FF of 0.84 for wide-bandgap IPSCs. The fast hole extraction property of Me-4PACz could be transferred to monolithic tandem solar cells, which enabled the perovskite/Si tandem to obtain a high efficiency of >29% and superior operational stability. Most recently, Hong's group reported a series of halogenated phenothiazine-based SAMs. 100,101 As shown in Figure 3.3b, the SAMs containing O, S, or Se heteroatoms can interact with perovskite absorber with increasing order of Se > S > O. In fact, the increased interaction energy reduces the interfacial trap density and increases in the lifetime of charge carrier at the SAM/perovskite interface. These resulted in maximum PCEs of 22.73% (Br-2EPSe), 21.63% (Br-2EPT), and 21.02% (Br-2EPO) for SAM-based PSCs, respectively.

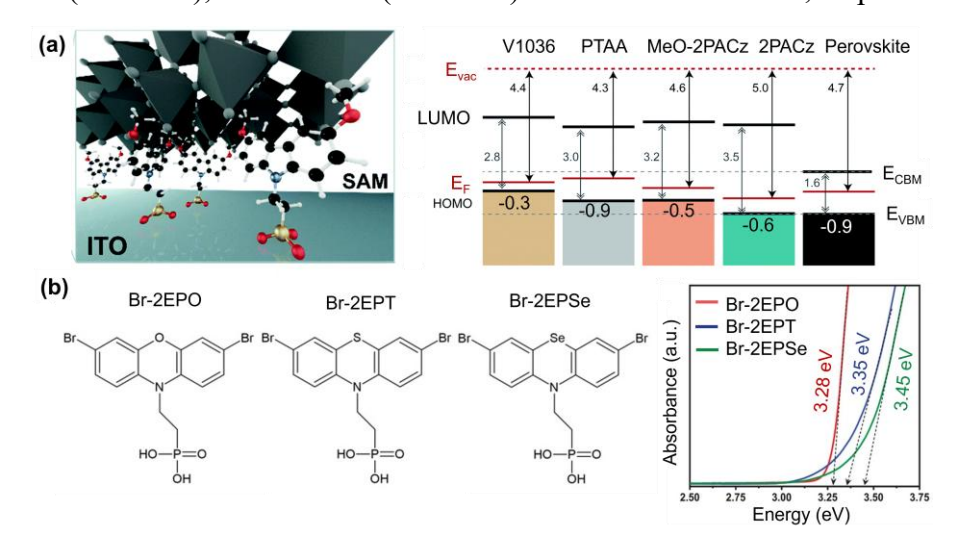


Figure 3.3 (a) Schematic demonstration and energy level alignment of SAM HTL and perovskite in the SAM-based IPSCs.⁹⁶ (b) Molecular structures and UV-vis absorption spectra of the Br-2EPO, Br-2EPT and Br-2EPSe.^{100,101}

Considerable breakthroughs have been achieved most recently. For example, recent innovations in new SAMs design, such as the synthesis of 4PADCB, Ph-2PACz

and CbzNaphPPA, have enabled devices to achieve PCE exceeding 26%. ¹⁰²⁻¹⁰⁴ Moreover, NiOx/SAM bilayer structures are developed with both high efficiency and stability, NiOx/MeO-4PADBC bilayer structure achieved a PCE of 25.6% results from a robust and stable HTL. ¹⁰⁵ In addition to these developments, a novel SAM based on a trimethoxysilane group, known as DC-TMPS, has been synthesized. Devices incorporating DC-TMPS have shown remarkable durability, retaining nearly 99% of their initial efficiency after damp-heat testing at 85°C and 85% RH for 1000 hours. ¹⁰⁶ These advances in new HTLs and engineering approaches highlight the ongoing efforts to improve both the efficiency and longevity of PSCs, bringing them closer to commercial viability.

3.2 Electron Transport Layer in Inverted Perovskite Solar Cells

The development of ETLs in IPSCs plays a pivotal role in enhancing device performance by facilitating efficient electron extraction and minimizing recombination at the interfaces. In IPSCs, the perovskite/ETL interface directly influences the electron mobility and overall efficiency of the device. The performance of IPSCs is often hindered by sluggish electron extraction and significant non-radiative recombination at the perovskite/ETL interface, which limits the $V_{\rm OC}$ and FF. A key factor in optimizing the ETL is ensuring a seamless electron transfer from the perovskite layer to the electrode, which requires excellent energy level alignment and interface engineering.

3.2.1 Fullerene-Based Inverted Perovskite Solar Cells

Fullerene-based materials and their derivatives, including C_{60} , PCBM, and ICBA, have been widely explored as efficient ETLs in IPSCs, following the initial application of C_{60} in these devices. C_{60} is particularly valued for its excellent electron mobility, high conductivity, and favorable energy level alignment with perovskite, making it one of the most effective ETLs in IPSCs to date. Additionally, its highly symmetrical structure, coupled with delocalized π -electrons, facilitates efficient electron transport. Despite

these advantages, C_{60} suffers from limitations such as poor solubility, a weak passivation effect, and the requirement for complex deposition techniques, which hinder its broader application.

In contrast, PCBM, a derivative of C_{60} , has emerged as a promising alternative due to its superior solution processability and enhanced passivation properties. PCBM was first introduced in IPSCs by Huang and colleagues, who demonstrated its ability to mitigate hysteresis and significantly enhance the PCE of IPSCs (**Figure 3.4**). The improvement was attributed to the Lewis acidic nature of PCBM, which allows it to infiltrate the perovskite layer through pinholes or grain boundaries during device fabrication. This infiltration leads to the formation of a PCBM/perovskite radical, which interacts with mobile ions and reduces anion migration induced by the electric field, thereby mitigating hysteresis.

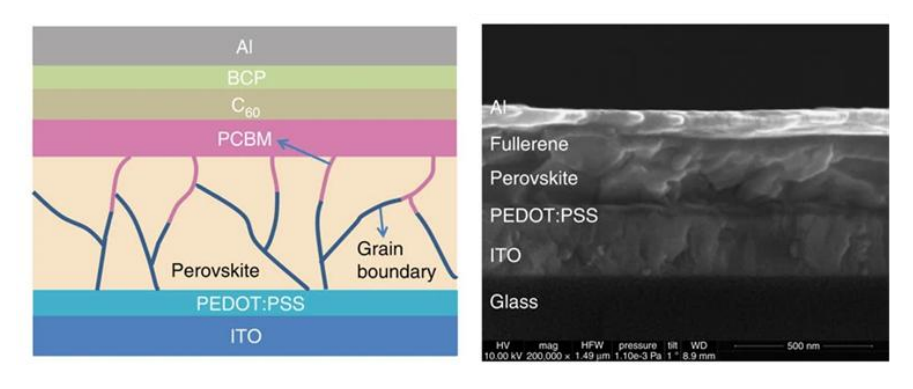


Figure 3.4 The application of PCBM in IPSCs with grain boundary passivation. 107

ICBA, another fullerene derivative, has also gained attention as promising ETL material in recent years. Chang et al. deposited ICBA on the surface of MAPbBr₃ perovskite and observed that its lower viscosity compared to PCBM enables better diffusion into the perovskite film's voids (**Figure 3.5a**). This enhanced diffusion contributed to a record V_{OC} of 1.60 V in single-junction solar cells. More recently, Ning and co-workers achieved an ultra-high V_{OC} of 0.94 V in tin-based IPSCs, demonstrating the potential of ICBA in these systems. The favorable LUMO energy level of ICBA helps to suppress interface recombination, resulting in a certified PCE of 12.4% for tin-based IPSCs, marking a significant advancement in the field (**Figure 3.5b**). 109

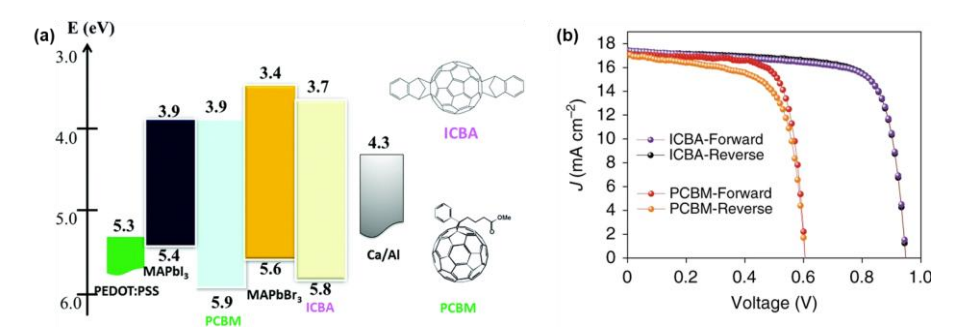


Figure 3.5 (a) The energy level of ICBA in IPSCs. (b) The application of ICBA in Sn-based IPSCs.

Recent developments have also led to the creation of novel fullerene derivatives, such as BCM, synthesized by Wei and co-workers (**Figure 3.6a**). BCM exhibits a cross-linkable nature, which allows for in situ cross-linking to form cross-linked BCM (CBCM) upon annealing at 100°C (**Figure 3.6b**). CBCM demonstrates improved passivation properties, achieving a PCE of 25.89%, along with excellent stability and density. Furthermore, the robust nature of the CBCM film provides internal encapsulation, preventing the diffusion of external moisture and oxygen, as well as the migration of internal perovskite components. This advancement highlights the potential of fullerene-based ETLs in enhancing both the efficiency and stability of IPSCs. 110

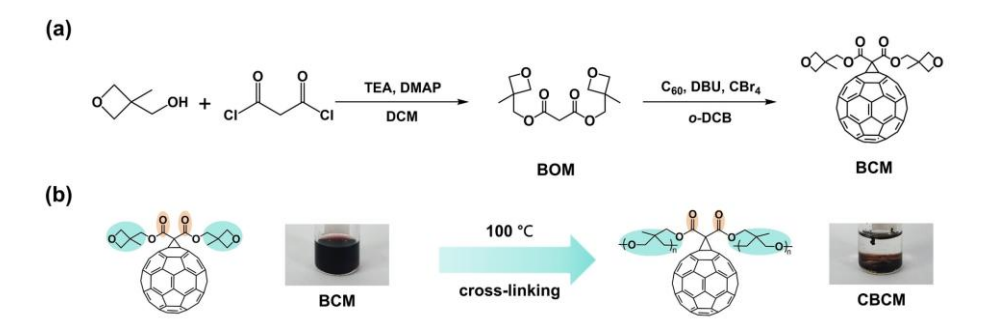


Figure 3.6 (a) The synthesis route of BCM. (b) The cross-linking scheme from BCM to CBCM. 110

3.2.2 Non-fullerene Acceptor-Based Inverted Perovskite Solar Cells

Although the application of fullerene and its derivatives in ETLs have significantly improved the performance of IPSCs, it is important to recognize that fullerenes and their derivatives are costly, contributing to the overall expense of IPSCs. This cost factor presents a major obstacle to the large-scale commercialization of IPSCs. Therefore, there is a strong drive to identify alternative materials that can replace

fullerenes, reducing production costs while maintaining or enhancing performance.

Non-fullerene acceptors promising solutions of ETLs to low cost and efficient IPSCs. By effectively passivating defects in the perovskite layer, improving hydrophobicity, and offering greater chemical stability, non-fullerene acceptors processes both efficient PCE and stability. These properties contribute to more durable and efficient devices, addressing key issues such as moisture and ion migration that can degrade IPSCs. While many of the non-fullerene acceptors currently used in IPSCs are adapted from OPVs, there is considerable opportunity to modify their molecular structures specifically for IPSCs. This could involve reducing synthetic complexity and material costs, resulting in simpler, more cost-effective ETLs that still deliver high performance.

The first use of the n-type polymer N2200 in IPSCs was pioneered by Ma and colleagues.¹¹¹ Shown in **Figure 3.7a**, The polymer's favorable energy level alignment and high electron mobility enabled a PCE exceeding 8%, approaching that of PCBM while offering a more cost-effective alternative. Later, He et al. introduced PDTzTI, a thienylthiazole imide-based polymer, as an electron transport layer (ETL) in IPSCs (**Figure 3.7b**). Due to its hydrophobic nature and ability to block mobile ions, PDTzTI-based ETLs demonstrated superior long-term stability and operational performance compared to devices with PCBM-based ETLs.¹¹² In more recent work, Peng and collaborators developed a polymerized non-fullerene small acceptor, PY-DFT, for use in IPSCs. The design of PY-DFT enhanced electron transport through the polymer backbone and effectively passivated defects in the perovskite layer. Moreover, its absorption in the near-infrared (NIR) region increased the current density by 0.25 mA/cm², resulting in a remarkable PCE of 24.5% (**Figure 3.7c**).¹¹³

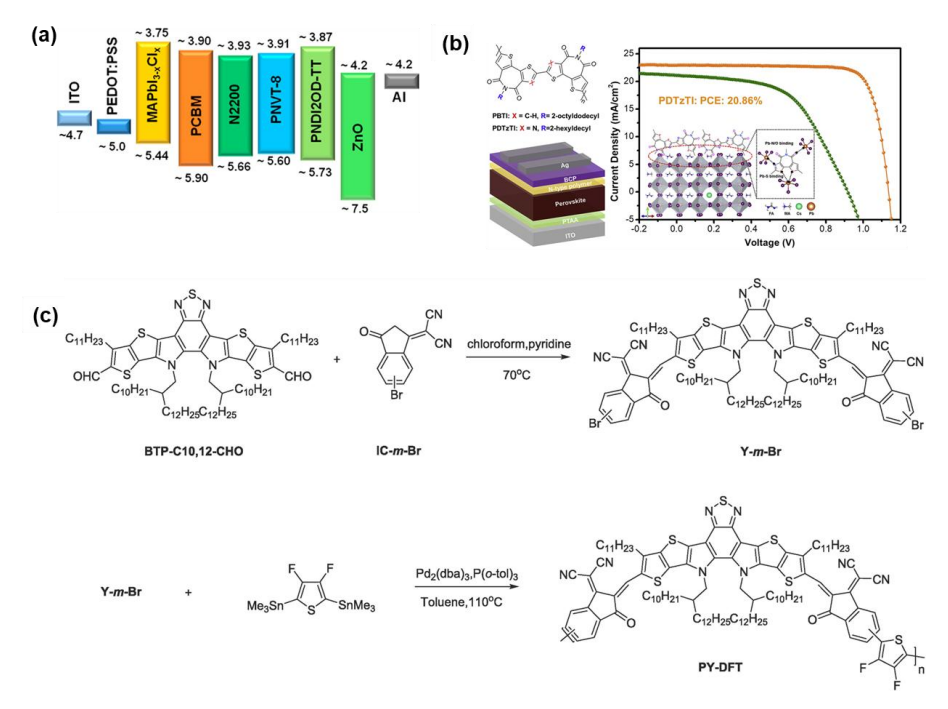


Figure 3.7 (a) The energy level of N2200 in IPSCs.¹¹¹ (b) The application of PDTzTI in IPSCs.¹¹⁴ (c) The synthesis route of PY-DFT.¹¹³

3.2.2 Inorganic Semiconductor-Based Inverted Perovskite Solar Cells

Over the past decade, inorganic semiconductors such as titanium dioxide (TiO_x), zinc oxide (ZnO), and tin oxide (SnO_2) have been investigated as potential ETLs for IPSCs due to their high electron mobility, environmental stability, and ability to form uniform, defect-free films.

Among these, TiO_x , initially developed for DSSCs, typically requires high-temperature annealing, which can degrade the perovskite layer. Therefore, achieving low-temperature processing of TiO_x films with high crystallinity and compactness is crucial for their application in IPSCs. Snaith and colleagues successfully demonstrated a low-temperature TiO_x film, resulting in a PCE of 9.8% and 6.4% for rigid and flexible IPSCs, respectively. Subsequently, Choy et al. developed a thick TiO_2 ETL for IPSCs, incorporating a TiO_2 /fullerene composite that formed a void-free and compact ETL structure, leading to a champion PCE exceeding 20% (**Figure 3.8**). The enhanced performance and stability can be resulted from suppressed interfacial recombination and conductivity.

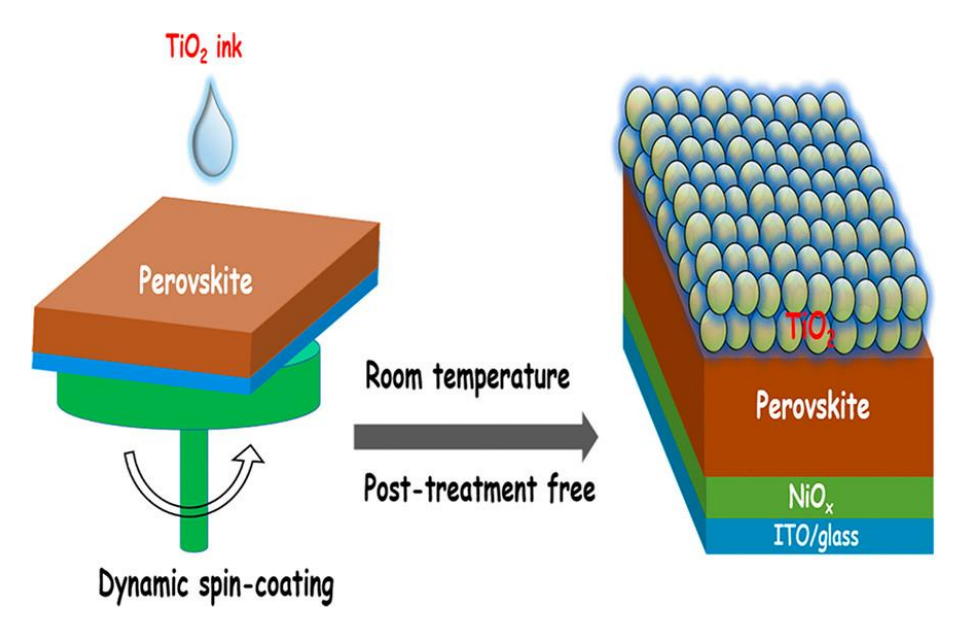


Figure 3.8 The application of TiO₂ ink in IPSCs. 116

ZnO, renowned for its excellent performance in OPVs, has also been explored as an inorganic ETL for IPSCs. However, ZnO faces several challenges that impact its long-term stability and performance, particularly its sensitivity to moisture. This sensitivity can lead to degradation of the ZnO layer and its interaction with the perovskite material. Ma et al. were the first to transfer a ZnO:PFN composite from OPVs to IPSCs, using a solvent system of methanol and n-butanol. This approach minimized the damage typically caused by conventional polar solvents, thereby enhancing the performance of the IPSCs. Similarly, as shown in **Figure 3.9**, Yang and colleagues demonstrated a solution-processed all-inorganic metal oxide charge transport layer for IPSCs, combining NiOx as HTL and ZnO as the ETL. This configuration effectively prevented undesirable interactions between PCBM and the electrode, and the all-solution-processed metal oxide layers showed significantly improved stability under ambient conditions. 118

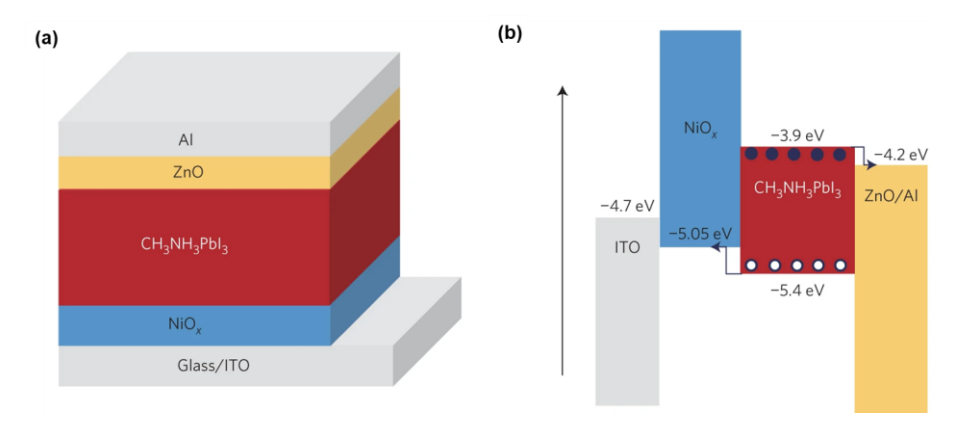


Figure 3.9 The application of all-metal oxide charge transport layer IPSCs with ZnO as ETL. 118

SnO₂ has emerged as a promising inorganic ETL for IPSCs. In 2016, Jen and colleagues pioneered the use of solution-processed SnO₂ nanocrystals as ETL for IPSCs. Due to their high crystallinity, excellent electron mobility, and low trap density, the compact SnO₂ films enabled efficient charge transport while providing robust protection against oxygen and moisture. This resulted in IPSCs with enhanced performance and exceptional ambient stability.¹¹⁹ More recently, Noh and collaborators introduced a novel approach by directly depositing SnO₂ quantum dots onto the perovskite layer using ethylenediamine (EDA) as a ligand. The EDA ligand acted as a molecular bridge between the perovskite and SnO₂, improving charge extraction, as illustrated in **Figure 3.10**. This strategy demonstrated significant potential for fullerene-free IPSCs, achieving an impressive PCE of 18.9% with a bandgap of 1.77 eV. Furthermore, by combining this SnO₂-based ETL with a 1.25 eV Pb-Sn perovskite absorber in a 4-terminal (4T) all-perovskite tandem architecture, a remarkable PCE of 27% was achieved.¹²⁰

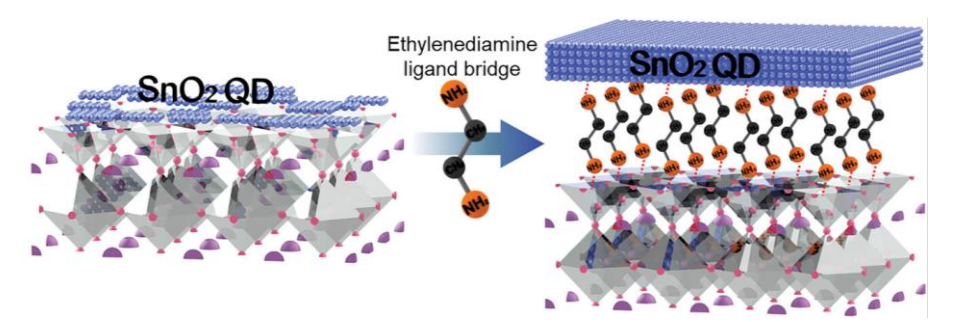


Figure 3.10 The scheme of EDA bridged passivation with perovskite and SnO₂ QDs. 120

3.3 Interface Engineering in Inverted Perovskite Solar Cells 3.3.1 Top Surface

The top surface of IPSCs is responsible for electron extraction and hole blocking in IPSCs. Similar to traditional solar cells, e.g., silicon and GaAs, surface passivation is an effective way to migrate perovskite's surface defects. This strategy is more efficient for organic-inorganic halide perovskites, as the trap types and distributions are complex. Surface charge trap sites, such as undercoordinated Pb or halide vacancies, are detrimental to the performance and stability of perovskite devices. Numerous approaches, such as surface passivation using organic and inorganic materials, are applied to reduce surface recombination and match surface energy level and passivate the surface defects. Several steps can be applied to improve the device performance of IPSCs including construction of LD/3D perovskite heterojunction, organic bonding and inorganic bonding at the top surface.

Organic salts are regarded as efficient passivation agents for IPSCs. Organic spacers tend to form low-dimension (LD) perovskite and construct LD/3D heterojunction at the top surface of perovskite. Suppressing the non-radiative recombination loss by surface passivation with organic materials, such as organic salts and polymers, has been devoted to improving the performance of IPSCs. $^{58,97,112,121-130}$ Bifunctional molecules like Piperazinium iodide (PI) and Piperazinium diiodide (PDI) are also introduced to the top surface of perovskite. 121 As shown in **Figure 3.11a**, compared with two $R_2NH_2^+$ groups in the PDI molecule, the PI molecule contains one R_2NH group and one $R_2NH_2^+$ group in the same six-membered ring, which can act as both an electron donor to passivate undercoordinated Pb^{2+} and an electron acceptor to react with the FA^+/MA^+ vacancies. Meanwhile, the residual strains of control, PDI-perovskite and PD-perovskite are systematically investigated through the grazing incidence X-ray diffraction (GIXRD) measurement. It is demonstrated that the scattering peaks gradually shift to the left by varying φ from 10° to 60° at different levels; this indicates the existence of tensile stress at the perovskite film. The residual

strain can be released after the surface treatment, decreasing from 61.57 ± 6.92 MPa for the control film to 27.54 ± 2.16 and 40.15 ± 3.89 MPa for PI and PDI-based perovskite films, respectively. Moreover, after coating PI on the perovskite surface, the VBM and E_F shift 180 meV and 350 meV towards the vacuum. This observation indicates better energy level alignment and improves electron transfer, thus resulting in an enhanced PCE (23.37%). Recently, it was reported that growing 2D perovskite layers on the top surface of 3D perovskite to form 2D/3D junctions could effectively passivate surface trap states and inhibit ion migration among the devices.¹³¹ However, this strategy was more suitable for regular structured PSCs where the 2D perovskite layer is inserted between the 3D perovskite layer and HTL; the try failed for the ETL side of IPSCs. Wolf's group reported an ultra-high efficiency of IPSCs using oleylammoniumiodide (OLAI) molecules. 97 They found that the passivation of the 2D perovskite could compensate the weak passivation property of fullerene through tuning the dimension (n value) of the 2D perovskite in the IPSC. Indeed, the post treatment of 2D perovskite tends to form low-dimensionality (n=1) after thermal annealing (2D-TA). However, higher dimensionality ($n \ge 2$) could become more pronounced when the post treatment with OLAI molecule was performed at room temperature (2D-RT) (Figure 3.11b). As expected, the 2D-TA films were dominated by low dimension (n=1) layers in GIWAXS results. In contrast, the 2D-RT films exhibited diffraction peaks at n=1 and 2, with the n=2 peak being more prominent. Cross-sectional HR-TEM images also showed the existence of n=1 and 2 layers in 2D-RT samples Figure 3.11c. Meanwhile, compared to higher CBM of 2D-TA perovskite, the 2D-RT perovskite film showed closer CBM to the C₆₀, resulting in more efficient charge transfer between the 2D/3D perovskite and C₆₀ interface (**Figure 3.11d**). The 2D-RT-based IPSCs showed a substantially improved PCE of 24.3% with an ultra-low Voc deficit of 0.34 eV. Besides, the 2D-RT-based IPSCs exhibited high stability, passing the industry-relevant damp test after 1000 h. Furthermore, quasi-2D surface treatment was also conducted by Sargent and colleagues, who verified that a capping layer with $n \ge 3$ 2D ligands could reduce resistance and

carrier transport, which was also beneficial for an inverted structure. But for 2D layer with n=1, the unfavorable energy level alignment would lead to inferior device performance. 132,133

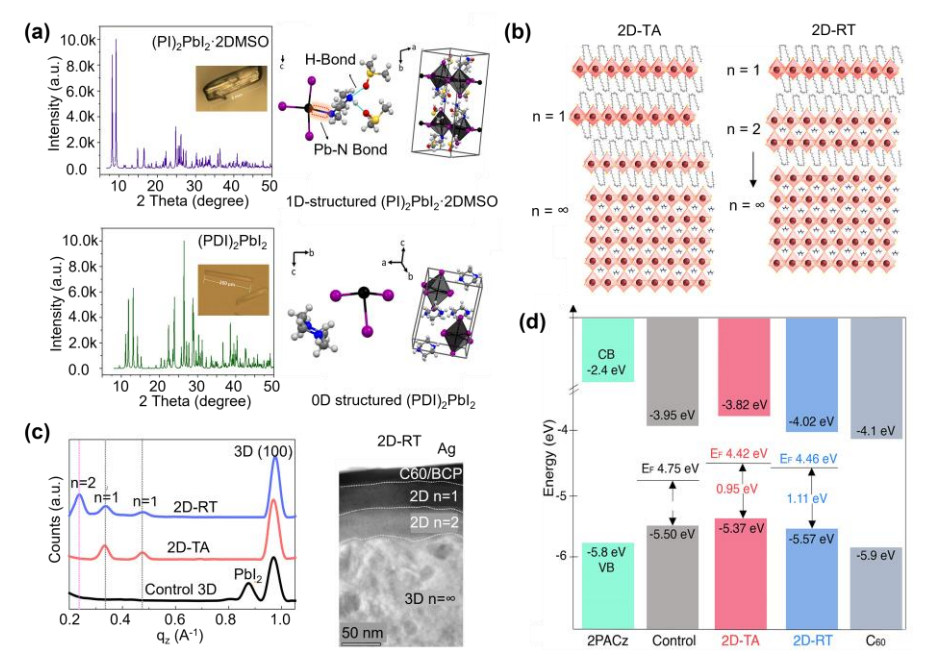


Figure 3.11 (a) XRD patterns and structural images of LD perovskite single crystals. ¹²¹ (b) Scheme of 2D passivation with varied n layers under annealing and room temperature. (c) Integrated GIWAXS maps and cross-sectional HR-STEM image. (d) Energy level scheme. ⁹⁷

Among the various strategies that have been applied to reduce nonradiative recombination losses in IPSCs, dual passivation of additives, especially double-side treatment using long-chain alkylammonium salts, are suggested to be one of the most effective passivation methods for efficient IPSCs. ¹³⁴ Paetzold et al. used a long-chain alkylammonium salt phenethylammonium chloride (PEACl), as addictive (grain boundary passivation, GBP), surface passivation (surface passivation, SP) and simultaneous GBP&SP treatment. ¹³⁵ After the latter treatment, the PEACl could simultaneously passivate the grain boundaries and perovskite/C₆₀ interfaces. The energy band diagrams of SP, GBP and GBP&SP-treated perovskites showed a more n-type property, specifically GBP&SP treatment. The GSP-treated device showed an enhancement of 26 mV in V_{OC}, whereas the SP-treated device exhibited a significant improvement in both V_{OC} (1.09 V to 1.13 V) and FF (0.79 to 0.82), resulting effective defect passivation. Upon the dual passivation via GBP&SP treatment, the device

performance increased to 22.7%. Owing to the improved electron mobility, reduced trap density, and optimized energy level structure by PEACl treatment, the GBP&SP device obtained the highest efficiency of MA-free IPSC to date. In another study, double-side treatment of the perovskite layer with PEAI was proved to be an efficient method for improving the HTL/perovskite and ETL/perovskite interfaces. First, modifying the buried interface could form a uniform film without nanovoids. In addition, top surface modification effectively passivates the defects and alleviates the energy alignment in the perovskite/ETL; this setup improves electron extraction and reduces interfacial recombination. As a result, J_{SC}, FF and V_{OC} are improved, reaching a prominent PCE as high as 23.7%.

Another efficient strategy is to introduce organic materials, including polymers and organic salts, into antisolvents in the one-step spin-coating process. This facile method without additional post treatment has attracted much attention in PSC fields. 122,129,136-139 An ultra-high FF of 0.86 can be obtained by incorporating a novel polymer (PPP) with a 3D star-shape into CB antisolvent. 137 The 3D PPP molecule has multiple chemical anchor joints with perovskite, including the interaction of C=O with PbI₂ and hydrogen bonding between -CF₃ and FA⁺/MA⁺ of the perovskite (Figure 3.12a). In addition, the PPP molecular existing in the grain boundaries of perovskite can also regulate the crystallization of perovskite films, contributing to the regular vertical and dense arrangement of larger grains. The PPP-based PSCs deliver an improved PCE (22.1%) with an ultra-high FF (0.86). The increased FF value, approaching the S-Q limit (0.904) of single-junction solar cells, originates from the increased carrier mobility (Figure 3.12b). Star-shaped polyhedral oligomeric silsesquioxane-poly(methyl methacrylate) polymer (POSP) was also developed as an interfacial modification for IPSCs. 122 POSP is suggested to induce a POSP-CsFAMA intermediate phase with perovskite, mainly due to the strong bonding of C=O in the POSP polymer with the Pb²⁺ in perovskite. The intermediate phase causes the crystal growth rate to slow down. This phenomenon randomly forms the nuclei to regulate the growth orientation and minimize the Gibbs free energy in the thermal annealing process, thereby enlarging the grain sizes and reducing trap states. Moreover, the operational stability of PSOP-modified perovskite is impressively improved, with T80 (time to retain 80% of the initial efficiency) over 3982 h. Introducing organic salts, e.g., MA⁺/FA⁺, into the antisolvent is another effective strategy to re-regulate the perovskite grain growth and crystallization.

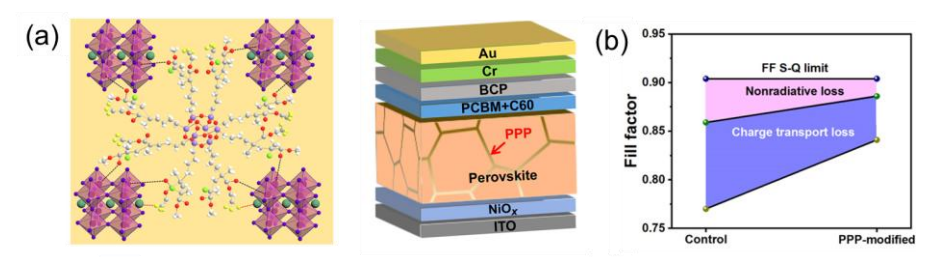


Figure 3.12 (a) The interaction between PPP polymer and perovskite and device structure of IPSCs. (b) The calculated FF loss. ¹³⁷

However, the poor solubility of these organic salts in common non-polar antisolvent, such as chlorobenzene (CB), diethyl ether (DE) and ethyl acetate (EA), obstructs the development of PSCs. Fortunately, polar solvents, such as isopropyl alcohol (IPA) and ethanol (EtOH), were found to be efficient as antisolvents for PSCs as well. 140 There are some challenges that still need to be addressed, for example, the use of ethanol as an antisolvent can partially decompose the perovskite surface and lead to ununiform and low-quality perovskite film. Besides, high polarity and low boiling point of ethanol contribute to unfavorable trap-rich perovskite surfaces. More recently, Wei and co-workers adopted methylamine bromide (MABr) into ethanol antisolvent as an additive to solve these hurdles. 136 On the one hand, MABr is suggested to compensate the vacancy of organic salts (FAI) during the reaction and decomposition processes. As shown in Figure 3.13a, ethanol-perovskite thin films exhibited a network of layered crystals with sizes ranging from 100 to 400 nm and many surface pinholes. Upon the addition of 1 mg/mL MABr into ethanol, the crystal size is increased and the pinholes are significantly reduced. Once the MABr concentration is increased to 2 mg/mL, the perovskite film shows high quality without defects and larger crystal sizes of up to 500 nm; this facilitates the charge carrier transport by suppressing carrier

recombination. However, needle-like crystals are seen with an increased density of up to 5 mg/mL; the insulating properties tend to impede carrier transport. **Figure 3.13b** shows the transient absorption spectra (TAS), which verify the lower density of surface defects after passivation by MABr. The TAS result is direct evidence for the inhibition of nonradiative recombination by incorporating MABr into ethanol as an antisolvent to fabricate perovskite films. As a result, the incorporation of MABr can improve the device performance through improved high-quality perovskite films and reduced nonradiative recombination loss.

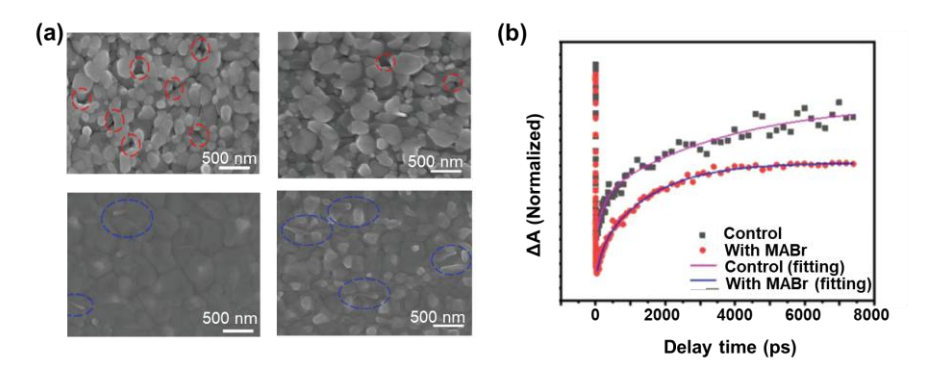


Figure 3.13 (a) SEM images of different perovskite thin film with various concentration of MABr. (b) TA spectra of perovskite films.¹³⁶

The weak bonding nature of organic materials with perovskite is undesirable and may lead to stability issues in some cases. Beyond organic materials, using inorganic materials has been considered an efficient passivation strategy for IPSCs. The sulfur-containing compounds are developed as novel passivators because of the strong coordination nature of Pb–S bond. Water-insoluble lead oxysalt was introduced as a capping layer by Huang and co-workers. He oxyacid ions are expected to react with perovskite to form wide-bandgap PbSO4. The sulfate anions play a dominant role in ion compensation and surface passivation effect, which ultimately improve device performance and stability. As shown in **Figure 3.14a**, the compact and uniform lead sulfate layer is formed between perovskite and C₆₀ films. Moreover, the ion migration is effectively suppressed, which may be originated from the immobilization of surface defects by the lead sulfate layer. The water resistance property of lead sulfate on perovskite single crystal is also presented. After coating with a lead sulfate layer, the

device can remain black for 3 min, whereas the control film is quickly decomposed into PbI₂. Similarly, lead-sulfur (PbS) is deposited on the top surface of perovskite to construct heterojunctions for IPSCs via surface sulfidation treatment (SST) (Figure 3.14b). 133 A shallow Fermi level with more n-type properties can be obtained by SST, implying that an extra back-surface field shows the same direction with the built-in potential. The strong coordinative nature of Pb-S bonds can suppress interfacial recombination and inhibit degradation reactions in the device. Moreover, the lattice matching of PbS and perovskite can stabilize the FA-based perovskite structure. Consequently, the SST-IPSCs achieve an ultra-high efficiency of 24.3% and respectively retain 91.8% and 90% of their initial efficiencies after aging at 85 °C for 2200 h and MPP tracking for 1000 h. Metal halide materials are also reported as efficient post-treatment candidates for PSCs. A trace of indium bromide (InBr₃) is adopted as a beneficial surface n-doping of perovskite, which is able to construct n/n⁺ homojunction at the top of perovskite's surface. 142 It is demonstrated that the work function of the doped perovskite film is downshifted by 0.49 eV compared to control film. This leads to the band bending at the interface of perovskite/ETL and regulates the interfacial charge dynamics with minimized electron injection barrier. As a result, the IPSCs with InBr₃ surface treatment attain a high PCE of 22.2% and V_{OC} of 1.18 V, respectively.

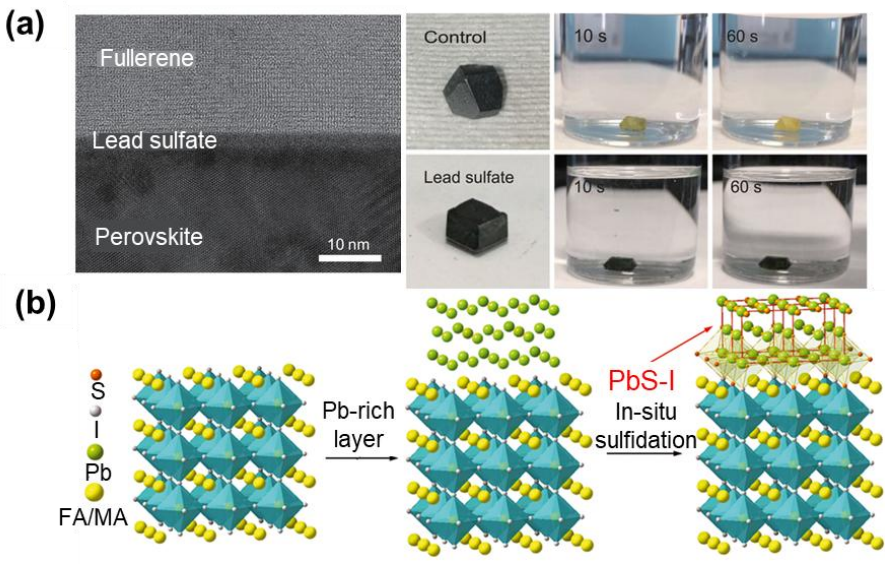


Figure 3.14 (a) Cross-sectional HR-TEM image of perovskite interface and enhanced water resistance and suppressed ion migration by the lead sulfate surface. ¹⁴¹ (b) Schematic diagram of surface sulfidation treatment (SST). ¹³³

Most recently, an organometallic compound, ferrocenyl-bis-thiophene-2carboxylate (FcTc₂), was developed as an efficient interface functionalization agent for IPCs by Zhu and co-workers.⁶² It was demonstrated that FcTc₂ could provide strong chemical Pb-O bonding with perovskite and enhance electron extraction and transfer through electron-rich and electron-delocalizable ferrocene units. In this study, peak force infrared (PFIR) spectroscopy was conducted to confirm the signal of MA ions in perovskite; this signal variation of MA can represent the stability of perovskite films. As shown by PFIR mapping in Figure 3.15, the intensity and distribution of MA⁺ cations were well maintained in the FcTc₂-treated sample after 1000 h of aging, where the MA signal in the control sample was significantly reduced in intensity and distribution was broadened. This result indicated that FcTc2 was able to block the movement of surface ions, leading to a more uniform and stable distribution of surface components along with highly thermal-stable and water-resistant perovskite film. The device delivered an efficiency up to 25% (certificated 24.3%) with ultra-high stability. Also, the devices showed excellent long-term stability (at room temperature with AM 1.5 G simulated solar illumination, T₉₈ > 1500 h), damp-heat stability with IEC61215:2016 qualification (85 °C and 85% RH, T₉₅ > 1000 h) and cycle stability (cycle shocks of -40 °C and 85 °C, $T_{85} >$ cycles).

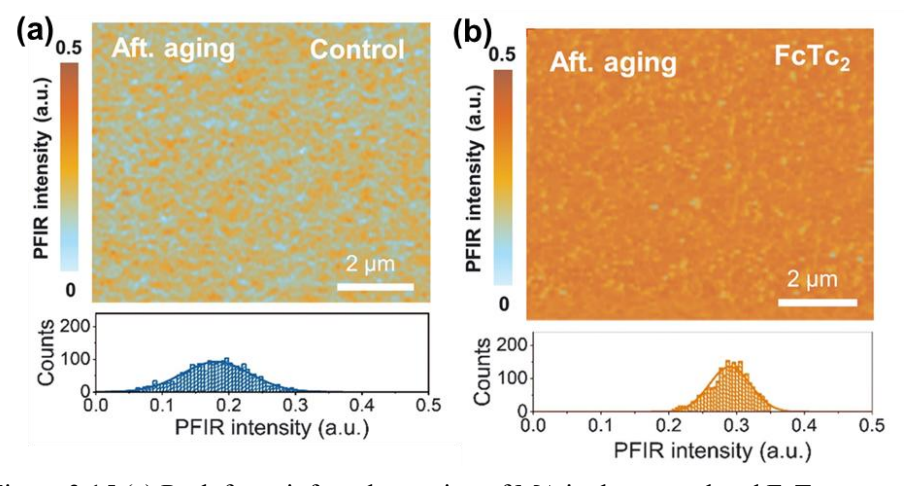


Figure 3.15 (a) Peak force infrared mapping of MA in the control and FcTc2-treated perovskite

films after aging.62

3.3.2 Buried Interface

The buried interface is the interface that is in direct contact with the bottom of the perovskite film. This property of the buried interface in IPSCs makes it difficult to characterize and thus has been a challenging research topic. In addition, the sequential spin-coating deposition of perovskite films involves perovskite formation, ink formulation, crystal nucleation and growth, morphology, and defects formation, posing more challenges to the way of studying the buried interfaces. 127,143-145 Due to its non-exposed nature, the fundamental properties of buried interfaces are very difficult to investigate directly. Researchers have largely ignored the direct characterization of charge accumulation at the deep-level traps on the buried interface, which causes non-radiative recombination and limits the device performance.

Recently, several attempts are aimed to minimizing the energy loss at the buried interface. Jen et al. used large alkylammonium interlayers to modify the buried interface, such as phenylethylammonium iodide (PEAI), 1,4-butanediammonium iodide (BDAI), and guanidinium iodide (GAI), which suppress interface recombination and reduce trap states at the PTAA/perovskite interface. As illustrated in **Figure 3.16**, the GIWAXS images show that the diffraction rings of LAIs-based perovskite films are sharper and brighter than those of control films, indicating that LAIs modified PTAA can enhance the crystallinity of perovskite films. As a result, high efficiency of 22.3%, with BDAI as the bottom interlayer between PTAA and perovskite, has been achieved. Due to the limitations of characterization technologies, however, a comprehensive analysis of the buried interface has not been conducted.

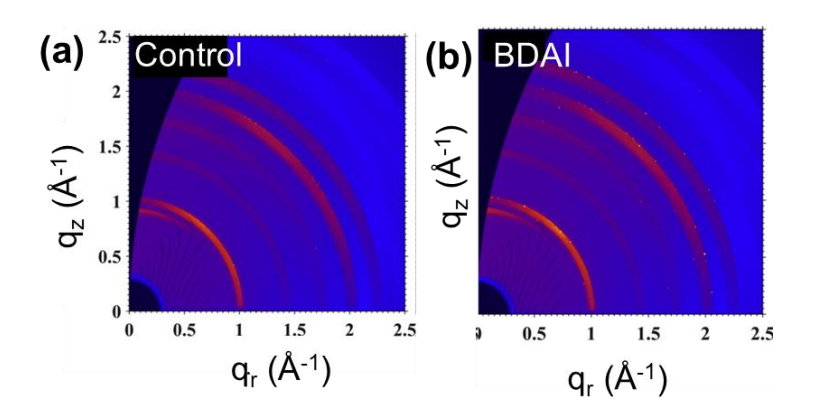


Figure 3.16 (a) GIWAXS patterns of control film and perovskite film with BDAI. 146

Impressively, several methods have been applied to solve this dilemma. For instance, Zhu and colleagues reported a lift-off method that uses orthogonal solvents for the PTAA (CB) and perovskite precursor (DMF/DMSO) where the as-prepared perovskite films cannot be dissolved in CB. Upon immersing the quasi-PSC device into CB solution, the as-formed PTAA layer can be re-dissolved, and the perovskite films can be lifted-off without any change in the structure, morphology and polycrystalline features. The lift-off stage is illustrated in Figure 3.17a. 147 In this study, they observed that the recombination loss is originated from sub-microscale imperfections and inhomogeneities at the buried interfaces. Besides, the bright grains composed of PbI₂ and PbBr₂ are distributed throughout the perovskite film, with smaller grains near the top surface and larger grains near the buried interface. Moreover, the buried interface displays lower PL intensity with the presence of lead halides, which is due to the annihilation of the photo-generated charge carriers. Similar to dissolution of PTAA in CB, Huang and co-workers developed another approach by using epoxy and cover glass taped with perovskite to mechanically peel off the PTAA/ITO substrate; this method is illustrated in Figure 3.17b. 148 They revealed that the polycrystalline perovskite films fabricated by one-step spin-coating and blade-coating possessed a downward grain growth direction. This phenomenon is less sensitive to the wettability of substrates or the compositions of perovskites due to the escape of residual solvent.

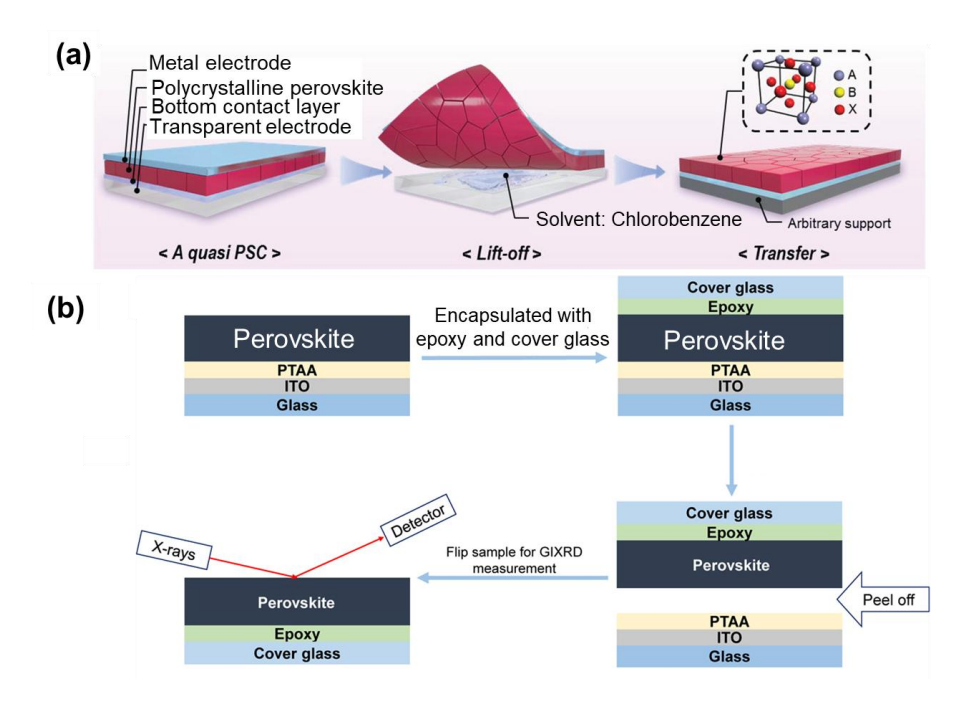


Figure 3.17 (a) Schematic illustration of the lift-off process. ¹⁴⁷ (b) Schematic illustration of mechanical peel-off process. ¹⁴⁸

Removing detrimental lead halides is vital to the efficient operation of devices. phenylethylammonium Chen al. further developed iodide (PEAI), aminoethylpyridine iodide (AEPI), and phenyldimethylammonium iodide (PDMAI₂) as 2D spacers in the buried interface. 149 Combining the lift-off method with 2D spacers, they found that the 2D spacers at the bottom tended to form 2D perovskite structures, indicating that a major amount of 2D spacers would remain and form 2D/3D perovskite heterojunction. With the APEI modification, the VBM of the bottom of the perovskite shifts upward from -5.58 eV (control) to -5.51 eV (AEPI modification). The 2D/3D heterojunctions were induced due to the distribution of the 2D perovskite upon formation, which facilitated hole transfer and suppressed interfacial charge recombination. Most recently, Zhang et al reported ion compensation of pre-buried interfaces for mesoporous IPSCs. 150 FAI solution treatment effectively compensated I ion vacancy and regulated the interfacial band energy. This ion compensation strategy could not only repair the ion loss in-situ and improve the built-in electric field, but it also lowered the charge injection barrier and suppressed the interfacial recombination. Owing to these merits, the resultant Cs/FA-based IPSCs demonstrated a PCE of 22.42%

and excellent thermal and light stability, and a high PCE (23.11%) was obtained for the CsFAMA triple-cation IPSCs. Except for 2D spacers, most recently, a zeolitic imidazolate framework (ZIF-6) containing metal and organic functional groups was applied to the buried interface between perovskite and PTAA. The N atoms of ZIF-67 serve as an anchor point for the uncoordinated Pb²⁺ in perovskite, in which the Co element in ZIF-67 is simultaneously coordinated with the N atoms of PTAA. The flexible IPSCs with ZIF-67 were able to offer high efficiency of up to 20.2% due to the reduced energy level (**Figure 3.18a**). Notably, the flexible device exhibited a long lifespan and remained 78% of its initial PCE after 10000 cycles (**Figure 3.18b**).

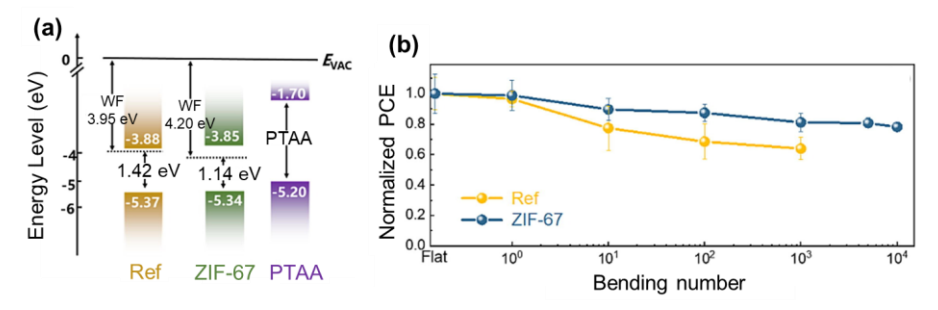


Figure 3.18 (a) The energy level of IPSCs with ZIF-67. 145 (b) Bending stability of IPSCs based on ZIF-67. 148

3.4 Issues and Opportunities of Inverted Perovskite Solar Cells

The past decade has witnessed rapid development of PSCs, with the certificated power conversion efficiency reaching 26.7%. The low-temperature and solution processable nature of perovskite enables the efficiency competitive with commercial silicon, CdTe and CIGS solar cells. Additionally, perovskites offer the unique capability of being integrated with commercial photovoltaic technologies to form multi-junction solar cells, expanding their potential for high efficiency applications. However, despite the significant progress, several challenges persist, particularly in the development of inverted PSCs. A critical issue lies at the interfaces within these devices, where defect-rich regions lead to severe non-radiative recombination losses, significantly hindering overall device performance. The presence of defects at these interfaces compromises both the efficiency and long-term stability of the cells, posing a major obstacle to their

broader application and commercialization. Addressing these interfacial challenges is the pursuit in my Ph.D. research. Overcoming the issues of non-radiative recombination and poor interfacial quality is essential for realizing the full potential of inverted PSCs. To achieve highly efficient and stable inverted PSCs, the major approaches are adopted and introduced for this dissertation:

- 1. Reducing the trap states and alleviating the energy at the top surface through polymerized small molecular acceptor.
- 2. Inhibiting the self-aggregation self-assemble monolayer and minimizing the energy loss at the buried interface with co-adsorbed strategy.
- 3. Constructing new structures of SAM at the hole-selective side with enhanced efficiency and stability.

Chapter 4 Surface Regulation with Polymerized Small Molecular Acceptor towards Efficient Inverted Perovskite Solar Cells

4.1 Introduction

Over the last decade, organic-inorganic metal halide PSCs have been extensively researched and demonstrated an unprecedented improvement in PCE. 151-154 Though regular devices (n-i-p) have kept the record PCE values for single-junction PSCs these years, it is widely acknowledged that inverted PSCs (p-i-n) are more promising in the future, due to their negligible hysteresis, and easily large-scale fabrication, and compatibility with flexible substrates and tandem configurations. 41,43 Therefore, pushing the PCE and stability of IPSCs to a higher level is still the priority in this research field. 62,121,155,156

The reasons for limited PCE in IPSCs are mainly recognized to be: (i) serious non-radiative recombination caused by defects on film surfaces and grain boundaries; (ii) poor energy level alignment between ETL, such as PCBM—and C₆₀, and perovskite active layers. ^{51,157-161} To simultaneously address these issues, materials that can passivate the defects and adjust the energy level distribution are highly desired. ^{162,163} Compared with traditional passivators that cannot passivate two kinds of defects at the same time, conjugated organic semiconducting small molecules have gradually taken the dominant position as effective passivators. ^{48,155,164,165} Specifically, small molecular acceptors with ring fusion developed from the field of organic photovoltaics (OPVs), including ITIC, IT-M, IT4F, Y6, etc., ^{162,166-172} have been proven to be good candidates. However, these small molecules are found to be intrinsically fragile in film and unstable under continuous operation, which would restrict the further development of IPSCs: from rigid to flexible, from unstable to stable. ¹⁷³

Drawing on the development of OSCs material design and synthesis, a novel concept of polymeric small molecule acceptor (PSMA) has been proposed in recent years. These kinds of materials can be efficient in charge transport as small molecules are, and stable as polymers. Therefore, PSMAs are not only efficient in

constructing all-polymer OSCs, but also promising in regulating the perovskite/ETL interface properties as a multi-functional passivators, thereby enhancing the PCE and stability of IPSCs. Besides, the use of PSMA as a passivator has not been reported in the field, which may open up a new direction of perovskite passivation engineering. 178,179

In this work, we reported a surface reconstruction strategy by the incorporation of a PSMA named PY-IT, which created record efficiency in all-polymer OSCs. 41,155,180,181 The PY-IT acts as the perovskite/ETL interface modulator to reduce defect states and enhance electron extraction/transfer for highly efficient IPSCs. It is found that PY-IT is mainly distributed at the top surface of perovskite, where it functions in three ways. First, its functional groups can interact with undercoordinated Pb²⁺, providing strong passivation effect of the defects of the perovskite film and effectively suppressing the non-radiative recombination. ¹⁸² In addition, the n-type property of PSMA promotes electron transport between perovskite and ETL. 157,183 Furthermore, due to the molecular interaction with perovskite, the localization of PY-IT on the surface is long-range ordered and intrinsically face-on oriented, which is also beneficial for electron transport between the perovskite and ETL. 41,184 Upon the powerful regulation, the PSMA-treated IPSCs yielded a champion PCE of 23.57% with an outstanding fill factor (FF) of 84% compared to the control (21.96%) for 1.53 eV perovskite system. In addition, the PSMA-incorporated IPSCs retained 86% and 80% of their initial PCE storing in N₂ atmosphere (unencapsulated) and light soaking in air (encapsulated and under maximal power point tracking) for 1000 h, respectively. These are also far more excellent than those of counterparts. Furthermore, this strategy is potentially generally applicable, of **PCE** of supported by the increase narrow bandgap system $(Cs_{0.1}FA_{0.6}MA_{0.3}Pb_{0.5}Sn_{0.5}I_3, 1.25 \text{ eV})$, from 17.38% to19.62% after PSMA treatment. All in all, the performance of IPSCs was significantly improved by rationally selecting passivation materials, regardless of the composition of perovskites. This provides a new direction for perovskite/ETL interface manipulation and demonstrates an encouraging

case of successfully combining results from two fields: OPV material science and PSC devices engineering.

4.2 Experimental Section

4.2.1 Materials

Cesium iodide (CsI), Methylamine hydrochloride (MACl), Formamidinium iodide (FAI) and Lead bromide (PbBr₂) were purchased from Xi'an Polymer Light Co., Ltd. Methylamine hydrobromide (MABr) and Lead iodide (PbI₂) were received from Advanced Election Technology. 2PACz was purchased from TCI Co., Ltd. PCBM was obtained from Nano-C Co., Ltd. PY-IT was purchased from Solarmer Inc. Other chemicals and solvents were purchased from Sigma-Aldrich Co., Ltd. and used without further purification.

4.2.2 Device Fabrication

15*15 mm ITO glass (Advanced Election Technology) was sequentially ultrasonicate cleaned by detergent, acetone and isopropanol. The cleaned substrates were dried with a N₂ flow and treated with UV light for 20 min. Afterward, SAM (2PACz, 0.3 mg/ml in EtOH) was spin-coated to the substrates at 4000 rpm for 30 s, followed by annealing at 100°C for 10 min. After cooling down to room temperature, SAM/ITO was washed by EtOH dripping (50 μL) at 5000 rpm for 30s and annealed at 100°C for 5 min to improve its wettability.

Perovskite precursor solution with a molar concentration of 1.73 M was prepared elsewhere with a stoichiometric composition of Cs_{0.05}(FA_{0.98}MA_{0.02})_{0.95}Pb(I_{0.98}Br_{0.02})₃ by adding corresponding CsI, MACl, FAI, PbI₂ and MAPbBr₃ in to mixed DMF/DMSO solution (8:1). After stirring for 2 h at room temperature, 50 μL precursor is dripped onto substrates and spin-coating at 5000 rpm for 30 s (2000 ramp), while antisolvent (CB) is dripped after 17 s. Then the perovskite films are immediately annealed at 120°C for 20 min.

Then desirable concentration PY-IT (dissolved in CB, diluted from 10 mg/ml) is dripped onto perovskite and stand for 30 s before coating at 5000 rpm for 30 s, it is noted that the standing process is critical to enable effective passivation, then the films are further annealed at 100°C for 1 min.

For deposition ETL, PCBM (20 mg/ml in CB) and BCP (1 mg/ml in EtOH) are further coated successively at 1000 rpm and 4000 rpm and annealed at 65°C for 5 min. The devices are transferred to thermal evaporator for deposition 100 nm silver to finish the device.

For narrow bandgap Pb-Sn IPSCs, PEDOT:PSS is spin coated on the substrate at 4000 rpm 30s and annealed for 150°C for 20 min. Then the ITO/PEDOT:PSS is transferred into N₂ glovebox. The mixture of 46.8 mg CsI, 185.7 mg FAI, 85.8 mg MAI, 335.3 mg SnI₂, 414.9 mg PbI₂, 14.1 mg SnF₂, and 2.7 mg NH₄SCN in mixed solvents (DMF:DMSO = 3:1) is used to form the Cs_{0.1}FA_{0.6}MA_{0.3}Sn_{0.5}Pb_{0.5}I₃ perovskite precursor solution. After stirring overnight, the precursor is filtered through 0.45 PTFE filter before use. 50 μL precursor is dripped onto substrates and spin-coating at 1000 rpm for 10 s (500 ramp) and 4000 rpm for 40 s (2000 ramp), antisolvent (CB) is dripped at 20 s before the end of the program. The as-prepared perovskite film is immediately annealed at 65°C for 5 min and 100°C for 10 min.

4.2.3 Device Characterization

The X-ray diffraction information was collected on a Rigaku SmartLab X-ray diffractometer with Cu Kα radiation in a step of 0.01° and θ-2θ scan mode from 5° to 50°. The surface roughness and potential were tested using a MultiMode 8-HR Atomic Force Microscope (AFM, Bruker) with a tapping amplitude modulation mode. Film morphology of the perovskite was measured using a high-resolution field emission SEM (TESCAN VEGA3). GIWAXS was investigated using a Xeuss 2.0 SAXS/WAXS laboratory beamline with a Cu X-ray source (8.05 keV, 1.54 Å) and a Pilatus3R 300K detector. UV–vis absorption spectra were measured by using a UV–vis

spectrophotometer (CARY5000, Varian). Steady-state PL and TRPL transient decay spectra were measured using a PL spectrometer (Edinburgh Instruments, FLS920) with the excitation source of 636.2 nm picosecond pulsed diode laser (EPL-635, \approx 5 nJ cm⁻²) and detected at 780 nm. Photoelectron spectroscopy measurements were conducted by an electron analyzer (ESCALAB XI, Thermo Fisher Scientific) with a UV source (He $I\alpha$, $h\nu = 21.22 \text{ eV}$) for UPS and a monochromatic X-ray source (Al $K\alpha$, $h\nu = 1486.7 \text{ eV}$) for XPS in an ultrahigh vacuum chamber. In a UPS test, a bias voltage of 5 V was used to avoid the influence of the work function of the instrument, so that the electrons reaching the surface of the sample could be collectively captured by the detector. For the completed devices, J-V curves were obtained using a Keithley 2400 Source Meter under standard AM 1.5 G illumination (Enli Technology Co. Ltd., Taiwan), and the light intensity was calibrated by a standard KG-5 Si diode. Both forward (from -0.02 to 1.20 V) and reverse scanning (from 1.20 to -0.02 V) was performed with a delay time of 1 ms. The test areas (0.04 cm²) were typically defined by a metal mask (0.0324 cm²) with an aperture aligned with the active area. EQE spectra were measured with a QE-R 3011 EQE system (Enli Technology Co. Ltd., Taiwan) using 210 Hz chopped monochromatic light ranging from 300 to 850 nm. The ToF-SIMS was conducted to evaluate the depth distributions of PbI-, PO2- and S- ions in the perovskite and PSMA-perovskite. The films were tested using a ToF-SIMS instrument (ION-ToF GmbH, Germany) with a Bi⁺ primary beam (30 keV and 1 pA) and a Cs⁺ sputter beam (0.5 keV and 40 nA). The sputter size was $350 \mu m \times 350 \mu m$, and the analysis was $100 \mu m \times 100 \mu m$.

4.3 Results and Discussion

The chemical structure of PY-IT is shown in **Figure 4.1a**, in which the S, N and O contained functional groups with high electron density are supposed to play as Lewis base to passivate undercoordinated Pb²⁺ in perovskite films. ^{51,185} To prepare the IPSCs with PSMA, the Cs_{0.05}(FA_{0.98}MA_{0.02})_{0.95}Pb(I_{0.98}Br_{0.02})₃ perovskite layer was first fabricated via one-step antisolvent method. Then, PY-IT was dropped on the perovskite

surface by spin coating, combined with thermal annealing to enable effective interaction. Hereafter, the perovskite films with PY-IT are denoted as PSMA for simplicity.

The morphology is first performed using scanning electron microscopy (SEM) to explore the effect of PSMA surface treatment. As shown in Figures 4.1b and 4.1c, both samples displayed clear perovskite grains with obvious grain boundaries and white Pbrich phase, indicating well-prepared perovskites with high crystallinity. 186-188 However, the perovskite film tended to be blurred and to have strips on the surface after PSMA treatment, which suggests that PY-IT has been successfully coated and attached on the surface of perovskite film.¹⁶⁸ The atomic force microscopy (AFM) images of the two perovskite films displayed grain sizes ~600 nm (Figures 4.1d and 4.1e), consistent with the SEM results. In addition, the root-mean-square roughness of the control film (33.0 nm) was much higher than that of the PSMA-modified counterpart (22.5 nm), indicating that the film became more uniform after the incorporation of PSMA. 189,190 These results imply that the PSMA modification has negligible effect on the perovskite grain size but significantly reduces the surface roughness. Therefore, PY-IT is supposed to be located at the grain boundaries and possibly enriched on the top of perovskite film. To verify this hypothesis, the time-of-flight secondary-ion mass spectroscopy (ToF-SIMS) of both samples were conducted with the structure of ITO/SAM/perovskite (with or without PY-IT).

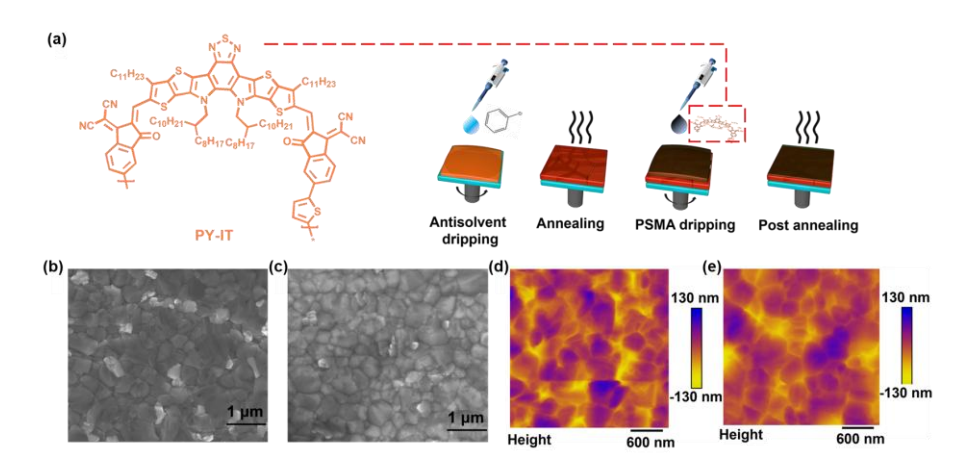


Figure 4.1 (a) Chemical structure of PY-IT and schematic illustration of film deposition

procedure. Top-view SEM images of the (b) control and (c) PSMA-perovskite films. AFM height images of the (d) control and (e) PSMA-perovskite films.

As shown in **Figures 4.2a** and **4.2b**, the intensity traces of S⁻, PbI⁻, PO₃⁻, and InO are performed on both control and PSMA modified films, which refer to the component of PY-IT, perovskite, 2PACz (self-assemble monolayer: SAM), and ITO electrode, respectively. The 3D signal distribution of segments was also presented in **Figure 4.2c**. Based on the signal intensity along with sputtering time, we could have a well understanding of the vertical distribution of PY-IT and perovskite. The signal of S⁻ in the PSMA-modified film appeared in the first 60s of sputtering, proving the enrichment of PY-IT on the top part of perovskite film. Specifically, after a rapid drop in the S⁻ signal at the beginning, the reduction rate became slower from 10 s to 60 s sputtering time, which implies that this PSMA penetrated into the bulk (probably located at grain boundaries). ¹⁶⁶

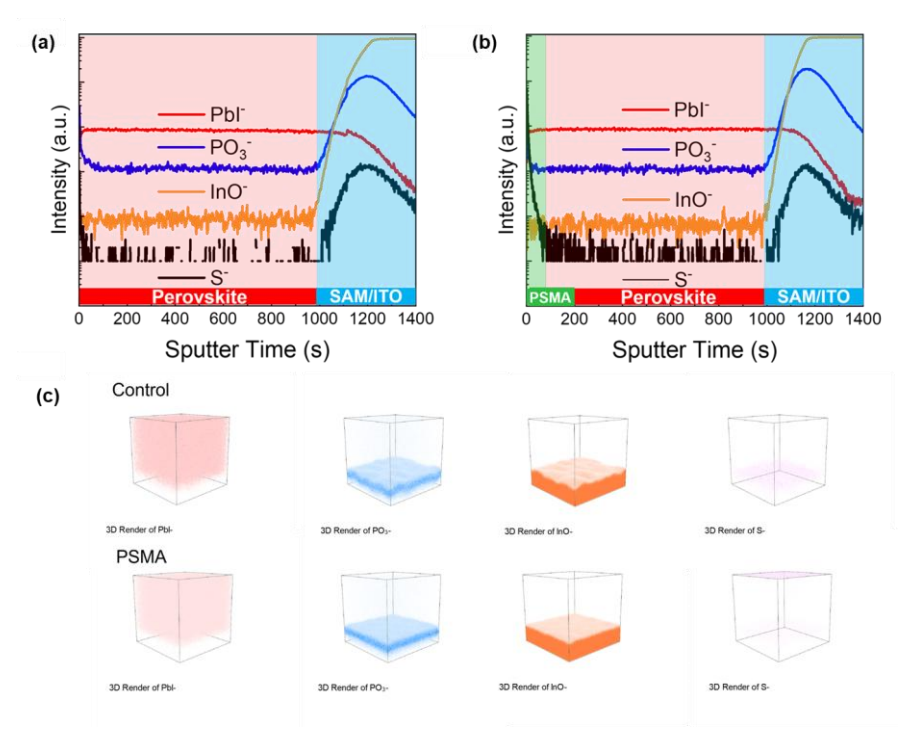


Figure 4.2 ToF-SIMS profiles of (a) control and (b) PSMA perovskite films. (c) The 3D signals distributions of segments.

One step further, X-ray photoelectron spectroscopy (XPS) was employed to investigate the interaction between perovskite and PY-IT. XPS spectra showed that the S 2p peak can be observed ~ 165 eV for PSMA-treated film, further confirming the

presence of PSMA (**Figure 4.3a**). ¹⁹¹ Interestingly, compared to the control, the slightly downshifted binding energy of Pb 4f at 143 eV and 138 eV could be attributed to the interaction between undercoordinated Pb²⁺ and electron-rich groups (C-N, C=O and thiophene) (**Figure 4.3b**). ⁷⁸ Moreover, Fourier transform infrared spectroscopy (FTIR) was conducted to confirm the interaction between the PSMA and perovskite (**Figure 4.3c**). As shown in **Figure 4.3d**, the stretching vibration peak of C=O shifted from 1690 cm⁻¹ for PSMA to 1694 cm⁻¹ for PSMA-PbI₂ and the stretching vibration peak of C≡N shifted from 2214 cm⁻¹ for PSMA to 2218 cm⁻¹ for PSMA-PbI₂, representing a significant interaction between perovskite and the PSMA. ^{183,192-194} These characterizations well elucidate the distribution of the PSMA and its interaction with perovskite.

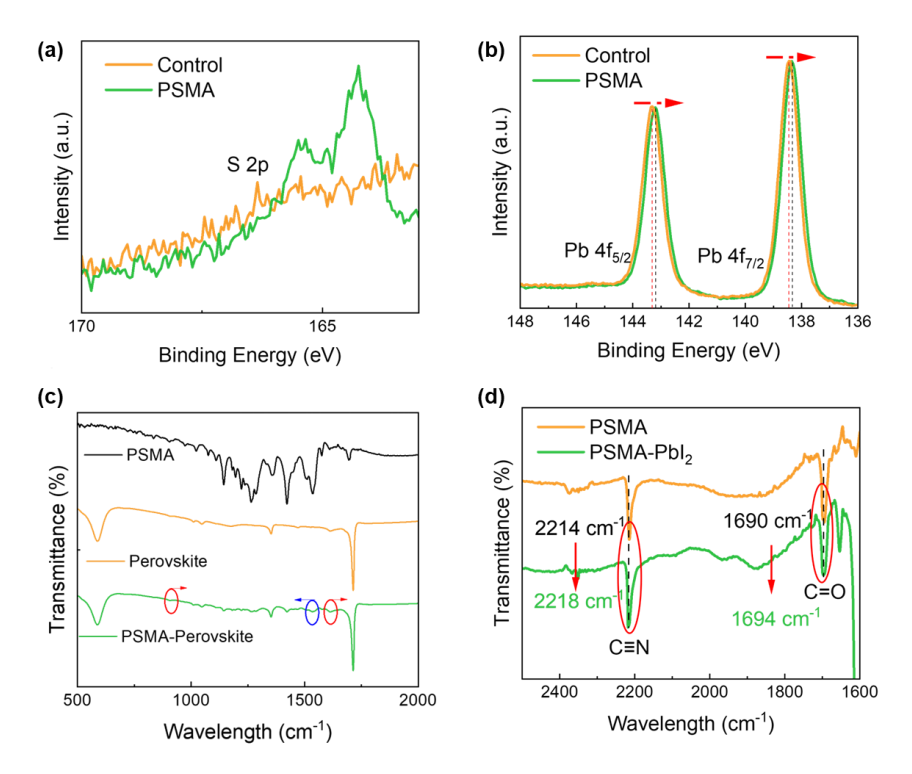


Figure 4.3 XPS spectra of (a) S 2p and (b) Pb 4f of control and PSMA perovskite films. (c) The FTIR spectra of PY-IT, perovskite and PSMA. (d) FTIR spectra of PSMA and PSMA-PbI₂.

To figure out the opto-electronic property and morphology tuning effect of PSMA passivation strategy, ultraviolet visible absorption (UV-Vis) and X-ray diffraction (XRD) measurements were performed. As shown in **Figure 4.4a** and **4.4b**, the UV-Vis absorption spectra and XRD patterns showed similar characteristics of the control and

PSMA perovskite films. The optical bandgap of both perovskite films was 1.53 eV. Besides, the characteristic XRD peaks of both perovskite films remained unchanged, which is consistent with the fact from SEM and AFM results. 183,195 However, the grazing-incidence wide-angle X-ray scattering (GIWAXS) results showed that the notable diffraction peak at 0.85 Å⁻¹ (Figures 4.5a and 4.5b), corresponding to the hexagonal non-perovskite δ phase of FAPbI₃ in the control film, could be fully eliminated by PSMA treatment. 85,196,197 Besides, the intensity of (100) peak of PSMAtreated film at 1.02 Å⁻¹ is significantly improved, demonstrating that the upper part of perovskite film has more face-on orientation (Figure 4.5c). 41,191 A slightly decreased peak of PbI₂ could also be observed at 0.94 Å⁻¹ after PSMA treatment(Figure 4.5d), which might be related to the formation of amorphous PSMA-PbI₂ compounds, further supporting the interaction between perovskite and PSMA. 198,199 The more face-on orientated upper active layer is suggested to provide more electron transport channels, enhancing the charge transport and extraction.²⁶ Moreover, the contact angle is shown in Figure 4.4c and 4.4d, the results show that more hydrophobic surface of PSMA treatment (27° for control and 70° for PSMA), confirming the presence and improved moisture resistance. 183,200

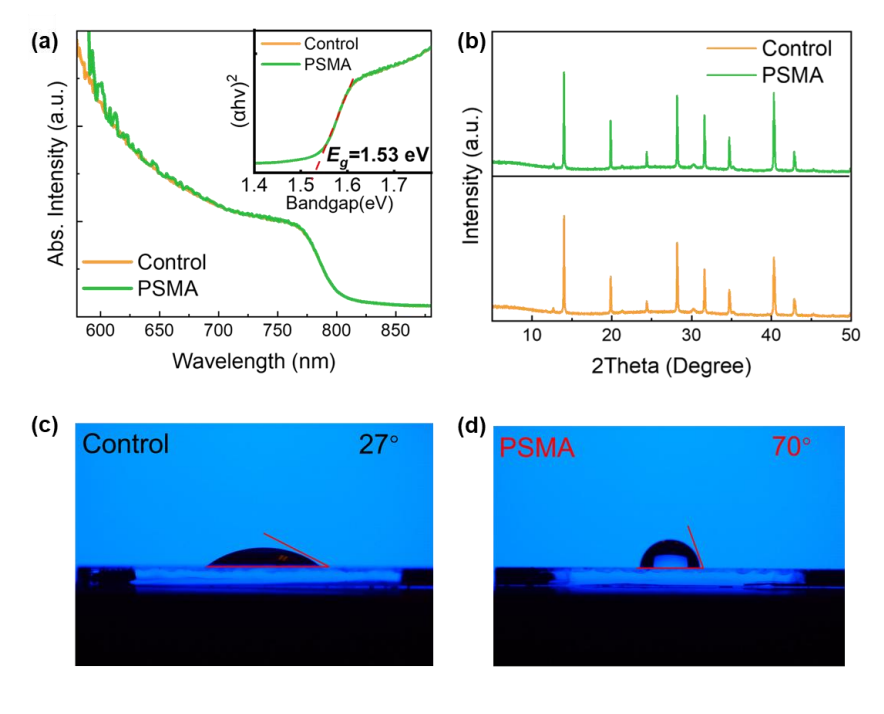


Figure 4.4 (a) UV-Vis of control and PSMA perovskite films. The insert is the derived Tauc-Plots. (b) XRD images for control and PSMA perovskite films. Contact angles of (c) control and (d) PSMA-based films.

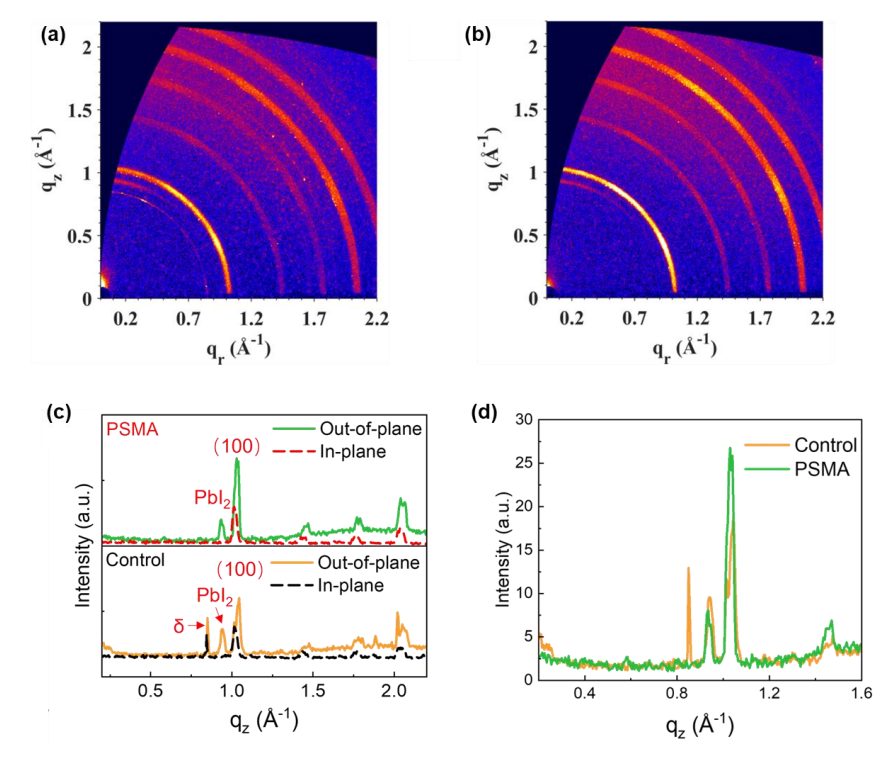


Figure 4.5 2D GIWAXS patterns of (a) control and (b) PSMA perovskite films, (c) corresponding in-plane and out-of-plane line-cuts. (d) Out-of-plane GIWAXS line-cuts of the control and PSMA perovskite films.

Steady-state photoluminescence (PL) and time-resolved photoluminescence (TRPL) spectroscopy were performed to investigate the defect passivation and electron transport. In the steady-state PL spectra (Figure 4.6a), the PL quenching of PSMA-treated perovskite film was observed compared to the initial control film, demonstrating efficient charge transfer at the perovskite/PSMA interface. In addition, the initial perovskite film produced a PL emission peak ~802 nm, which was shifted to 799 nm after PSMA modification, indicating reduced defects by effective passivation. According to the TRPL spectra (Figure 4.6b and 4.6c) for control and PSMA; perovskite/PCBM and perovskite-PSMA/PCBM, the nonradiative recombination caused by the interface (τ_1 , fast decay lifetime) and the radiative recombination in the bulk perovskite (τ_2 , slow decay lifetime) could be evaluated. The fitted parameters were listed in Table 4.1. The fast decay lifetime dominated in both control and PSMA-treated perovskite films, suggesting that nonradiative recombination is the main factor of

performance loss. The carrier lifetime reduced from 323 ns for control to 89 ns for PSMA-coated perovskite film, supporting the effectiveness of PY-IT passivation that enabled faster charge transfer and suppressed non-radiative recombination. 161,193,204

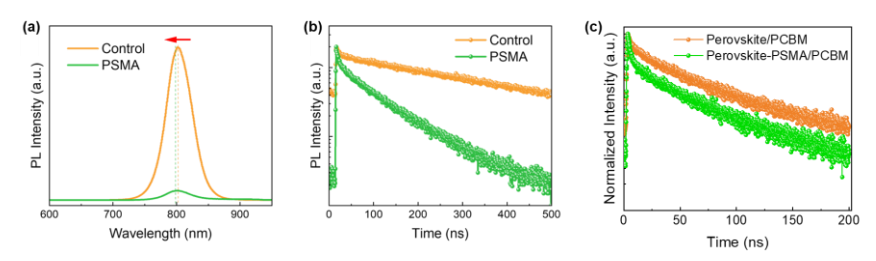


Figure 4.6 (a) PL spectra of control and PSMA perovskite films. (b) TRPL of (a) control and PSMA perovskite films and (b) Perovskite/PCBM and Perovskite-PSMA/PCBM.

Table 4.1 Summary of TRPL lifetimes of CsFAMA-based perovskite films with different treatments.

Sample	τ_1 (ns)	τ_2 (ns)	τ _{ave} (ns)
Control	6.96	323.27	246.63
PSMA	5.47	89.58	53.26
Perovskite/PCBM	5.73	64.90	32.29
Perovskite-PSMA/PCBM	2.69	56.39	19.59

Next, ultraviolet photoelectron spectroscopy (UPS) was measured to evaluate the energy band structure (**Figure 4.7a**). The PSMA-treated perovskite exhibited a sharp upward shift of the Fermi level (E_F) from -4.87 eV (control) to -4.53 eV, indicating more n-type perovskite surface and thus favorable for electron extraction.²⁰⁵ To confirm that a more n-type surface was obtained, Kelvin probe force microscopy (KPFM) measurements were conducted to observe the electrostatic potential distribution. The average potential of the control film was -430 mV (**Figure 4.7b**), higher than that of the PSMA-treated film (-400 mV) (**Figure 4.7c**), consistent with UPS results. The KPFM image of the control film exhibited clear edges associated with the inhomogeneous surface potential of perovskite film, where detrimental defects existed. In contrast, for the PSMA-treated perovskite film, it showed a more uniform

distribution of potential (less fluctuation), suggesting a reduction in local surface defects.²⁰⁶ In addition, combined with the above AFM results, the perovskite/ETL interface is smoother and has fewer defects, which could benefit the electrons extraction. Furthermore, the high electron affinity of PY-IT with PCBM can promote fast electron transport from perovskite with improved electron channels from GIWAXS results.^{207,208}

Based on the space charge limited current (SCLC) methods, electron-only devices were fabricated using the structure of ITO/SnO₂/active layer/PCBM/BCP/Ag with or without PSMA treatment to further investigate the effectiveness of surface passivation. The transition voltage from the ohmic region to the trap-filling limit region is referred to the trap-filling limit voltage (V_{TFL}), and it is associated to the trap density (N_t) by the equation:

$$N_t = \frac{2\varepsilon_0 \varepsilon V_{TFL}}{eL^2} \tag{4.1}$$

Where ε , ε_0 , e and L represent dielectric constant, vacuum permittivity, element charge, and thickness of perovskite films, respectively. The control device delivered a V_{TFL} of 0.237 V and N_t of 5.73 × 10¹⁵ cm⁻³, while the PSMA enabled devices to show a much smaller V_{TFL} of 0.121 V and N_t of 2.93 × 10¹⁵ cm⁻³ (**Figure 4.7d**). Lower trap density can reduce the nonradiative recombination of charge carriers. These results further verify the effectiveness of our passivation strategy.

The ideality factor (n) is usually used to describe the recombination loss in the perovskite. Typically, n = 1 denotes that radiative recombination completely dominates the recombination dynamics, and n = 2 represents nonradiative recombination through imperfections and traps dominates.²⁰⁹ As shown in **Figure 4.7e**, the light intensity-dependent V_{OC} variation was investigated. The PSMA-treated device showed an n of 1.29, which was quite smaller than that of the control device (1.50), indicating that the trap/defect-induced recombination was effectively suppressed.²¹⁰ Besides, electrochemical impedance spectroscopy (EIS) was measured, and the Nyquist plots were displayed in **Figure 4.7f**. Specifically, the semicircles contain the information on the series resistance (R_s) and the recombination resistance (R_{rec}) for devices that are

empirically associated with charge transfer and recombination, respectively. 112,211 Obviously, the PSMA-treated device showed smaller R_s and larger R_{rec} , implying that the nonradiative recombination was significantly inhibited.

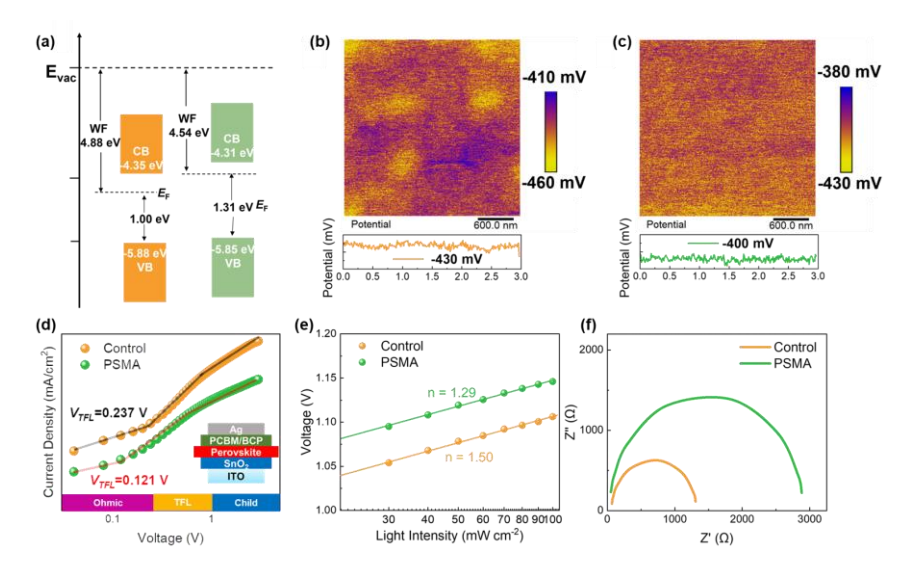


Figure 4.7 (a) Energy level of control and PSMA perovskite films. KPFM images of (b) control and (c) PSMA perovskite films. The bottom curves represent the surface potentials. (d) SCLC curves of control and PSMA perovskite with electron-only structure of ITO/SnO₂/Perovskite/PCBM/BCP/Ag. (e) Light-dependent $V_{\rm OC}$ of the control and PSMA perovskite devices. (f) Nyquist plots of the control and PSMA perovskite devices.

According to the above results, PSMA is mainly distributed on the perovskite surface and is supposed to penetrate the perovskite grain boundary near the top surface with a graded distribution. A reasonable working mechanism for the PSMA-regulated IPSCs performance improvement could be proposed and illustrated in **Figure 4.8**. It mainly contains several aspects. First, the interactions between perovskite and PSMA (especially for the interaction between -C \equiv N and -C \equiv O groups with PbI₂) are fully conducted across the surface and extended to the grain boundary near the top surface. The -C \equiv N and -C \equiv O groups firmly bond with the undercoordinated Pb²⁺ of perovskite by Lewis base sites, resulting in reduced trap states and suppressed nonradiative recombination. In addition, the increased surface potential and up-shifted E_F with PSMA contribute to a more n-type perovskite surface, which is beneficial for fast electron transport. Moreover, the smooth perovskite surface with low surface potential variations by PY-IT significantly improved electron transfer with reduced

recombination. Notably, ring fusion endowed strong planarity and polymer nature for PY-IT makes it capable of orderly self-arranging at the upper surface of perovskite; and its rotatable linker demonstrates the applicability of PSMA's inserting into grain boundaries as shown in **Figure 4.8**. Therefore, it is anticipated that electron can transport along the highway of PSMA among the boundaries and electron transport can be enhanced between PSMA and PCBM due to their strong π - π interaction. Furthermore, the reduced δ -FAPbI₃ by PSMA is suggested to increase the inherent phase stability of perovskite structure. As a result, this strategy helps to minimize the energy loss at the interface between perovskite and ETL, thus improving the performance of IPSCs.

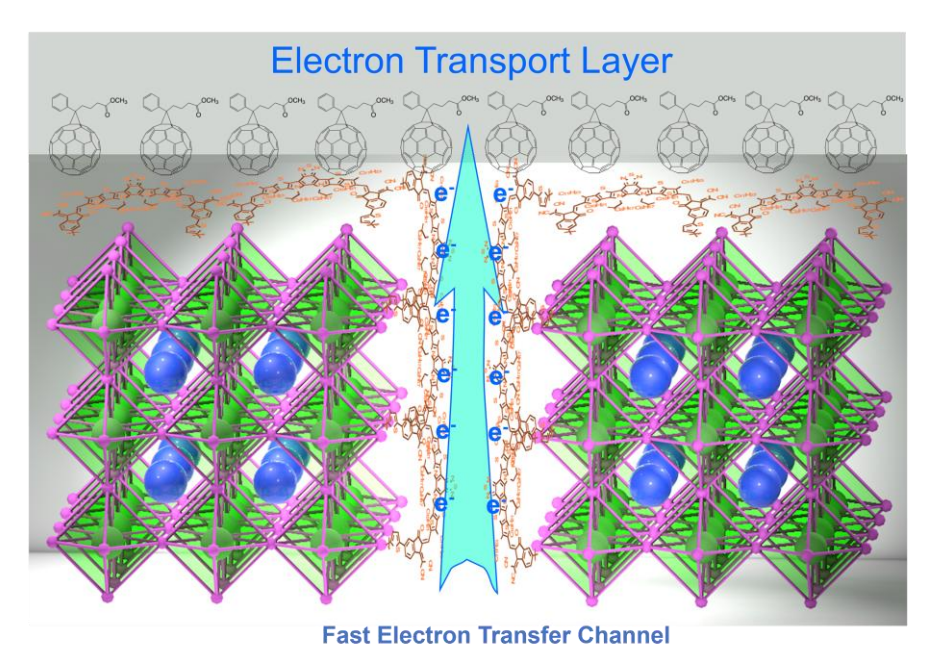


Figure 4.8 Mechanism of the defect passivation and improved electron transport properties with PSMA.

To investigate the effect of defect passivation and regulated electron transport on device performance, IPSCs with the structure of ITO/2PACz/Cs_{0.05}(FA_{0.98}MA_{0.02})_{0.95}Pb(I_{0.98}Br_{0.02})₃/PCBM/BCP/Ag were fabricated, where PSMA was coated onto the perovskite surface as an interlayer (**Figure 4.9a**). As the typical J-V curves of the devices shown in **Figure 4.9b**, the control device delivered a PCE of 21.98% with V_{OC} of 1.12 V, J_{SC} of 24.14 mA/cm² and FF of 81%, whereas the champion PSMA-based PSC achieved a high PCE of 23.57% with V_{OC} of 1.15 V, J_{SC}

of 24.37 mA/cm² and FF of 84%. The concentration of PSMA was optimized as 1 mg/ml in chlorobenzene (**Figure 4.9c to 4.9d**). In a lower concentration, the introduction of PSMA can contribute to effective passivation and interfacial charge transfer, which increased the V_{OC} and FF. And the concentration is optimized at 1 mg/ml for a high efficiency of 23.57%. However, when the concentration is going higher, the lower electron mobility of PY-IT (compared with PCBM) may cause undesirable energy loss which causes the drop of FF and J_{SC} .

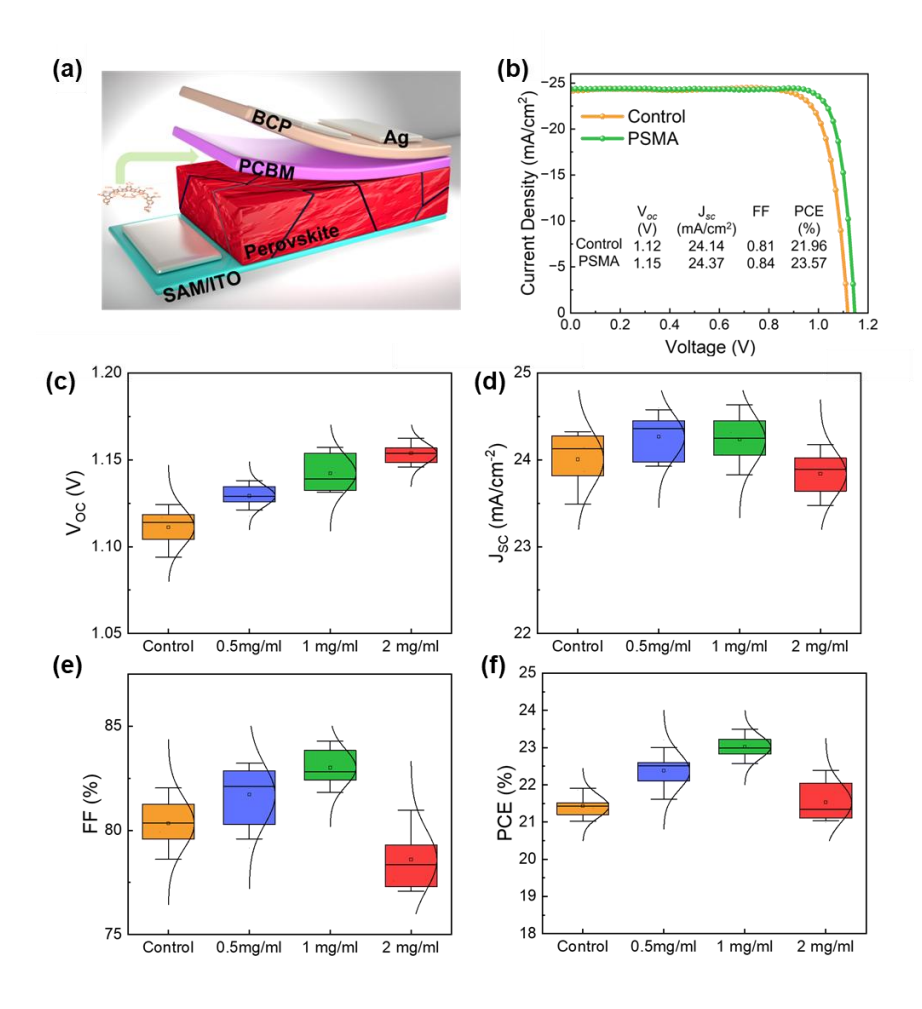


Figure 4.9 (a) Device structure of the IPSCs (b) J-V curves of the best performance devices. Parameters distribution of IPSCs fabricated by control and PSMA, (a) V_{OC} , (b) J_{SC} , (c) FF and (d) PCE.

To our best knowledge, the PCE of this PSMA-based IPSCs is competed with the highest PCEs of other non-fullerene acceptors (small molecule counterparts) incorporated IPSCs (**Figure 4.10a**). A slight improvement in J_{SC} was observed, while V_{OC} and FF were significantly enhanced with PSMA, which could be ascribed to the

reduced traps and facilitated electron transport. The external quantum efficiency (EQE) was conducted to evaluate the accuracy of J_{SC}, as shown in **Figure 4.10b**, the control IPSC exhibited an integrated J_{SC} of 23.50 mA/cm², whereas the PSMA-based IPSCs delivered a slightly higher integrated J_{SC} up to 23.72 mA/cm², in accordance with the results from J-V curves. Additionally, devices incorporating PSMA exhibited negligible hysteresis (**Figure 4.11a to 4.11b**). Under the bias voltage of 1.00 V, the stabilized output efficiency of PSMA-based device was 22.86%, which was higher than that of the control device (20.52% under a bias voltage of 0.98 V)(**Figure 4.10c**). **Figure 4.9c to 4.9d** displayed the histogram of PCE distribution, suggesting excellent reproducibility of PSMA-based IPSCs.

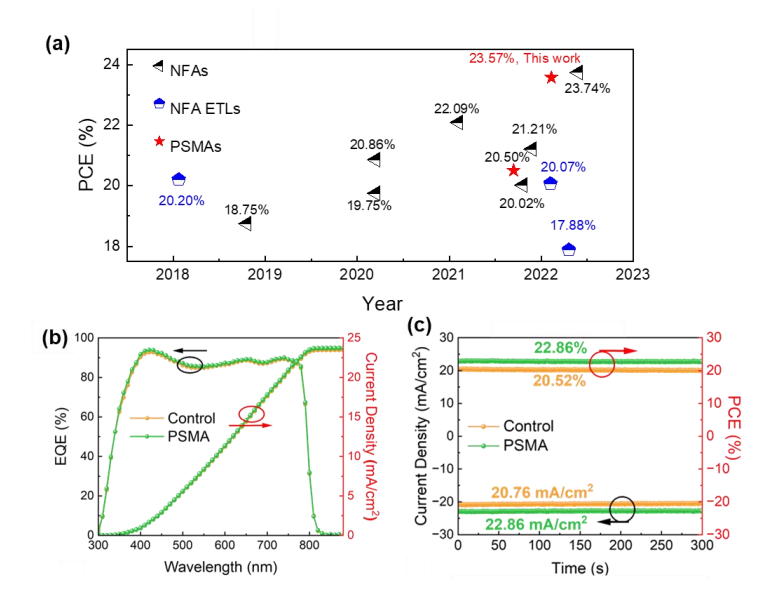


Figure 4.10 (a) Summary of recent reported PCEs for NFA-treated IPSCs.²¹⁴⁻²²² (b) EQE curves, and (d) stabilized output curves of control and PSMA devices.

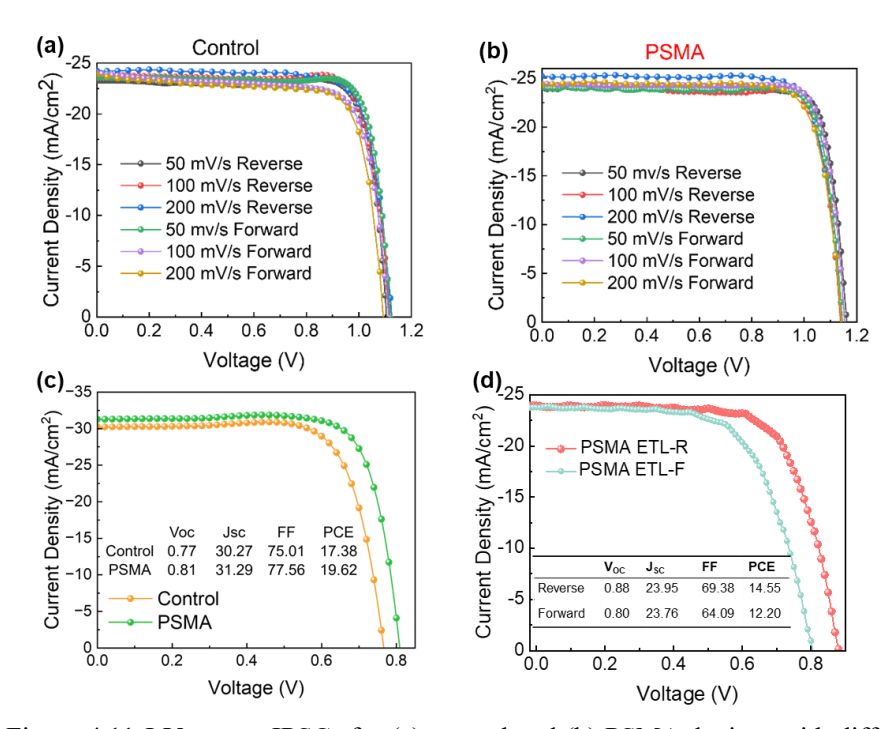


Figure 4.11 J-V curves IPSCs for (a) control and (b) PSMA devices with different scan rates. (c) J-V curves of narrow bandgap Pb-Sn IPSCs with/without PSMA. (d) J-V curves IPSCs for PSMA as single ETL.

further prove the applicability of this strategy, narrow-bandgap (Cs_{0.1}FA_{0.6}MA_{0.3}Pb_{0.5}Sn_{0.5}I₃, 1.25 eV) IPSCs were fabricated.²²³ As shown in Figure **4.11c**, the champion efficiency of Pb-Sn-based IPSC with PSMA was close to 20%, while that of the control device was 17.38%. The improved efficiency is ascribed to the enhanced V_{OC}, J_{SC}, and FF, indicating that trap states in the device are reduced, which further confirms the effective passivation by PSMA. The observed enhancement in device efficiency is attributed to synergistic improvements in Voc, Jsc, and FF. These advancements suggest a marked reduction in trap states within the perovskite active layer, a phenomenon consistent with the passivation mechanism observed in regularbandgap IPSCs when modified with PSMA. This corroborates the hypothesis that PSMA effectively passivates interfacial defects, thereby suppressing non-radiative recombination and enhancing charge carrier dynamics. Moreover, it is quite interesting that the PY-IT itself can work effectively as ETL for IPSCs. As shown in Figure 4.11d, the PY-IT (ETL) shows an efficiency of 14.55% with a Voc of 0.88 V, a J_{SC}, of 23.94 mA/cm² and FF of 0.69 at reverse scan. In contrast, PSMA-based ETL devices yielded a reduced PCE of 12.20% under forward scan conditions, highlighting pronounced hysteresis and interfacial limitations. The inferior performance of PSMA as an ETL is likely attributable to suboptimal electron extraction kinetics and an energy level misalignment at the perovskite/ETL interface, which exacerbate charge accumulation and recombination losses. Further advancements in NFAs and PSMAs, particularly through rational molecular design, are anticipated to overcome this dilemma. 113,224

In addition to improved efficiency, the stability of devices was also assessed. Upon storage in N₂, the device is stored with light illumination and open circuit. The PSMA-based device can retain 86% of its initial efficiency without encapsulation after 1000 h, while the control device dropped to 78% after only 400 h (Figure 4.12a). Furthermore, the operational stability was measured under continuous 1 sun illumination (white LED lamp) under maximum power point (MPP) tracking. In this situation, the ion migration in the device is accelerated by both light and applied bias.^{225,226} The encapsulated PSMA-based device retained 80% of its initial efficiency for 1000 h under MPP tracking in the ambient atmosphere (25°C and 65% RH). In contrast, the control device showed noticeable degradation and retained 50% of its initial value after MPP tracking for 750 h (Figure 4.12b). Accordingly, the surface reconstruction of perovskite film by PSMA successfully achieves enhanced device stability. ^{119,227,228}

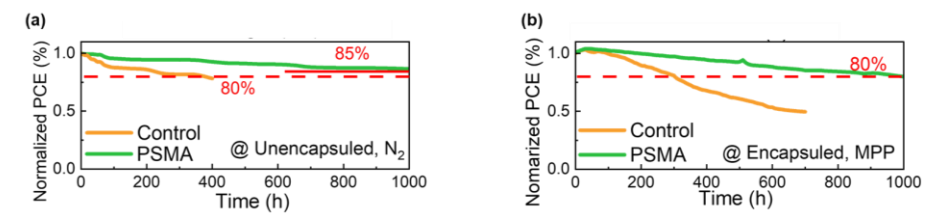


Figure 4.12 (a) long-term storage stability in N_2 atmosphere, and (b) operational stability under MPP tracking of control and PSMA perovskite devices.

4.4 Summary

In conclusion, to avoid the potential disadvantages of small molecules, a PSMA named PY-IT was incorporated into the perovskite/ETL interface as the modulator. Detailed characterizations revealed that PSMAs were located on the perovskite top

surface and grain boundaries, thus reducing trap states while constructing an n-type surface and charge-transport-friendly perovskite orientation. Due to the effective interfacial modulation of PSMA, the champion devices delivered PCEs of 23.57% and 19.62% for 1.53 eV and 1.25 eV bandgap IPSCs, respectively. Moreover, the incorporation of PSMA enhanced the storage and operational stability of IPSCs, which retained 86% and 80% of their initial PCEs. Taking together, our work provides a novel pathway to optimize the top surface of perovskites with high efficiency and operational reliability.

Chapter 5 Co-adsorbed Self-Assembled Monolayer Enables Highperformance Perovskite and Organic Solar Cells

5.1 Introduction

Interface engineering has made a great contribution to the development of solution-processable third-generation photovoltaic (PV) devices, bearing the hope of achieving carbon neutrality via sustainable energy production, like perovskite/organic solar cells (OSCs & PSCs). 213,229-237 Poly(3,4-ethylenedioxythiophene) polystyrene sulfonate (PEDOT:PSS) is a benchmark HTL, which has enabled continuous PCE breakthroughs, especially for those p-i-n structural PV devices, due to its favorable energy level and electron blocking ability. 148,233,238-240 However, its instability under external stress (light or heat) and acidity strongly restricted the device stability. 3,241,242 Therefore, constructing low-cost and green solvent-processable HTL has become a critical research topic in recent years. 155,243-245

SAMs, particularly phosphonic acid based ones, are nowadays the emerging star HTLs used in both PSCs and OSCs to boost PCE and stability. 174,246-249 Principally, SAM materials consist of (a) anchoring groups of bond with oxide substrates (e.g.: ITO) via covalent/coordinative bonds, (b) the terminal groups that determine the surface properties such as W_F, and (c) the backbones called spacer groups connect anchoring and terminal groups. The ultrathin nature of SAMs can maintain the high transmittance of substrates well, which is beneficial to J_{SC}. Meanwhile, SAM's chemical bonding with substrates and non-acidity further guarantee the device stability. 250-252 Furthermore, the low-cost and alcohol-processable features make them adaptive for photovoltaic commercialization.

Notwithstanding their potential, the attainment of high-density, closely packed SAMs remains challenging, resulting in unpredictable interfacial properties. For instance, the inherent amphiphilic characteristics of SAMs often lead to undesirable self-aggregation, particularly in alcoholic solvents, inducing the formation of micelles.²⁵³ An additional energetic barrier might be consequently formed during the

disassembly of micelles while SAM molecules bind to the substrate surface. Thereby, a tightly compacted SAM structure cannot be easily and stably obtained.²⁵³ Moreover, due to the rough substrate and solution-deposited methods, defects become inevitable in monolayer, particularly for those regions that lack of SAMs coverage. These defects are potentially inducing current leakage at the buried interface, causing the energy loss and instability of optoelectronic devices.²⁵⁴

Terminal functional groups within SAMs frequently experience significant aggregation, leading to notable losses at interfaces. To address this issue, numerous strategies have been investigated, such as optimizing SAM layer deposition techniques, implementing bilayer structures, and incorporating additives. 253,255 For example, the evaporation of Me-4PACz enhances the wettability and alters the morphology of perovskites without considerably impacting their chemical attributes. This approach effectively enhances the quality of interfaces on textured surfaces, contributing to near-lossless contacts. The employment of a bilayer structure incorporating NiOx and SAM demonstrates promise in reducing interfacial losses and increasing surface coverage, fostering enhanced device stability. Furthermore, employing small molecules such as methyl phosphonic acid (MPA) and 3-mercaptopropionic acid (3-MPA) are able to minimize the interfacial energy loss at the SAM/perovskite with reduced aggregation. 258,259 These methodologies are primarily directed toward augmenting surface coverage, adjusting energy levels, and reducing energy dissipation at the perovskite/SAM junction.

In the realm of dye-sensitized solar cells (DSSCs), researchers have employed a co-adsorbed strategy to mitigate dye aggregation and enhance device performance by a small molecule. The co-adsorbed strategy is originally utilized to combine dye absorption and reduce charge recombination on the surface of TiO₂.²⁶⁰ Leveraging the widely utilized [2-(9H-Carbazol-9-yl)ethyl]phosphonic acid (2PACz) as the HTL in both PSCs and OSCs, we incorporate a small molecule 2-chloro-5-(trifluoromethyl)isonicotinic acid (PyCA-3F) with 2PACz to form a functionalized

ultrathin layer, which is aimed to reduce SAM's self-aggregation. 258,261,262 Our characterizations reveal that the 2PACz/PyCA-3F co-adsorbed surface (denoted as CA) is more smooth in surface roughness, with fewer agglomerates, and minimized interfacial nanovoids. Furthermore, the increased W_F and narrower surface potential distribution at the SAM/perovskite interface enables a more p-type and uniform behavior, facilitating the hole extraction and transfer process at the buried interface. For PSCs, the CA surface helps enhance grain grooves and increases the interfacial energy, which contributes to a flattened perovskite buried interface and reduced photovoltaic inactive phase, resulting in a remarkable PCE exceeding 25% for p-i-n devices. These advantages can be also extended to OSCs, with PM1:PTQ10:m-BTP-PhC6 photoactive system realizing a PCE of 19.51%, among the leading values. Furthermore, PBQx-Cl:PY-IT blend achieves a PCE of 17.77%, a decent value among all-polymer binary OSCs; PM6:eC11 combination attains 17.71%, representing one of the best results for open-air blade coating devices cast by non-halogenated solvents ortho-xylene (o-XY). Notably, the operational stability, as indicated by maximal power point tracking (MPPT) results, scores the superiority of the CA approach for both PSCs and OSCs. In summary, our work presents a facile, rational, and effective co-adsorbed strategy to enhance the performance of SAM-based devices, resulting in efficiency breakthroughs for both PSCs and OSCs based on p-i-n device structure, coupled with enhanced operational stability.

5.2 Experimental Section

5.2.1 Materials

Cesium iodide (CsI), Methylamine hydrochloride (MACl), Formamidinium iodide (FAI), Lead bromide (PbBr₂) Methylamine hydrobromide (MABr) and Lead iodide (PbI₂) are purchased from Advanced Election Co., Ltd. C60, and BCP are obtained from Xian Yurisolar Co., Ltd. PyCA-3F is obtained from Bidepham. PEDOT:PSS (Al 4083) is from Hareus. 2PACz and is obtained from TCI. Co., Ltd.. PM1, PBQx-Cl, PY-IT, PM6 and eC11 are from solarmer Inc.. m-BTP-PhC6 is from eFlex PV Inc.. PTQ10 is

from 1-Materials Inc.. Other chemicals and solvents were purchased from Sigma-Aldrich Co., Ltd. and used without further purification.

5.2.2 Device Fabrication

HTLs fabrication: The ITO substrates were first washed by detergent and then sonicated with deionized water, acetone and isopropanol subsequently, and dried by N₂. The cleaned substrates were treated with UV-Ozone for 20 min. Afterward, SAM (2PACz, 0.5 mg/ml in EtOH) was spin-coated to the substrates at 4000 rpm for 30 s, followed by annealing at 100°C for 10 min. After cooling down to room temperature, the 2PACz film surface was washed by ethanol at 3000 rpm for 30 s and annealed at 100°C for 10 min subsequently. As for co-adsorption depostion, EtOH solution was replaced by PyCA-3F (1 mg/ml in EtOH) and annealed at 100°C for 10 min. For mixed HTL, 2PACz and PyCA-3F (9:1, w/w) were mixed with a total concentration of 0.5 mg/ml and were spin-coated onto the ITO substrates at 4000 rpm for 30 s, followed by annealing at 100°C for 10 min to achieve mix substrate. For PEDOT:PSS depostion, PEDOT:PSS (Al4083 from Hareus) was spin-cast onto the ITO substrates at 7500 rpm for 30 s, and then dried at 160 °C for 15 min in N₂ atmosphere.

PSCs fabrication: For perovskite precursor deposition, perovskite solution with a molar concentration of 1.6 M was prepared elsewhere with a stoichiometric composition of Cs_{0.05}(FA_{0.98}MA_{0.02})_{0.95}Pb(I_{0.98}Br_{0.02})₃ by adding corresponding CsI, MACl, FAI, PbI₂ and MAPbBr₃ in to mixed DMF/DMSO solution (4:1). After virgous stirring for 2 h at room temperature, 50 μL precursor is dripped onto different HTL substrates and spin-coating at 1000 (200 ramp) for 10 s and 5000 rpm for 30 s (2000 ramp), while antisolvent (anisole) is dripped after 27 s. Then the perovskite films are immediately annealed at 110°C for 20 min. Then the films are transferred to evaporation chamber, C₆₀ and BCP are thermal evaporated successively for 40 nm and 8 nm, respectively. The devices are completed with deposition 100 nm Cu.

Organic solar cell fabrication: As for organic photoactive layer, the

PM1:PTQ10:m-BTP-PhC6 blend (weight ratio is 0.8:0.2:1.2), is dissolved in chloroform (the concentration of donor was 7 mg mL⁻¹), with 1-chloronaphthalene (0.7% vol) as additive, and stirred at 45 °C hotplate for 1 hours. The blend solution was spin-cast at 3000 rpm for 30 s onto HTLs followed by a temperature annealing of 100°C for 1 min. A thin PFN-Br-MA layer (0.5 mg/mL in methanol and 0.25% *wt*% melamine, 3000 rpm) was coated on the active layer, followed by the deposition of Ag (evaporated under 3×10⁻⁴ Pa through a shadow mask). The optimal active layer thickness measured by a Bruker Dektak XT stylus profilometer was about 110 nm..

5.2.3 Device Characterization

UV-vis absorption spectra were measured using a Shimadzu UV-2500 recording spectrophotometer. AFM measurements were obtained by using a MultiMode 8-HR Atomic Force Microscope (AFM, Bruker) in a tapping mode, KPFM measurements were recorded using FM-KPFM mode. SEM-EDX were recorded by a Hitachi SU8230 scanning electron microscope (SEM) with an accelerating voltage of 5 kV. The samples for GIWAXS measurements were fabricated on silicon substrates using the same recipe for the devices. X-ray diffraction (XRD) analyses were conducted utilizing a Bruker ECO D8 diffractometer, equipped with Cu K α radiation ($\lambda = 1.5418$ Å). X-ray photoelectron spectroscopy (XPS) and ultraviolet photoelectron spectroscopy (UPS) measurements were performed using an ESCALAB XI electron analyzer (Thermo Fisher Scientific) with a X-ray source (Al K α , h ν = 1486.7 eV) and helium ionization source (He I α , hv = 21.22 eV). To mitigate the impact on the measured work function by the instrument, a bias voltage of -7 V was systematically applied during the (PL) experiments. Steady-state photoluminescence and time-resolved photoluminescence (TRPL) transient decay spectra were acquired using an FLS920 PL spectrometer from Edinburgh Instruments, attenuated total reflection Fourier transform infrared spectroscopy (ATR-FTIR) measurements utilized a Bruker Vertex 70v system. And atomic force microscopy-infrared spectroscopy (AFM-IR) analyses were conducted with a nano-IR3 system from Bruker. Dynamic light scattering (DLS) measurement were performed using Malven Zetasizer Nano ZS.

The J-V curves of devices were measured using a Keysight B2901A Source Meter in glove box under AM 1.5G (100 mW cm⁻²) using an Enlitech solar simulator (Enlitech SS-F7-3A). The device contact area was 0.086 cm², device illuminated area during testing was 0.084 cm², which was determined by a non-reflective metal mask. The J-V curves were measured by reverse scanning (from 1.30 V to -0.02 V) and then forward scanning (from -0.02 V to 1.30 V), the voltage step of 0.02 V and the delay time of 10 ms. The EQE spectra were measured using a Solar Cell Spectral Response Measurement System QE-R3011 (Enlitech Co., Ltd.) with AC mode. The light intensity at each wavelength was calibrated using a standard monocrystalline Si photovoltaic cell. The MPP tracking was carried out upon epoxy encapsulated devices under 1-sun white LED array in air.

The Analysis of J_{ph} vs V_{eff} relationships

The definition of J_{ph} is the current density under illumination (J_L) minus the dark current density (J_D), and V_0 refers to the voltage value when $J_{ph} = 0$. Accordingly, $V_{eff} = V_0 - V_{appl}$, where V_{appl} represents applied voltage, has a clear meaning. Importantly, when V_{eff} reaches a high value (> 2V) it is normally believed that generated excitons are fully collected, in which J_{ph} is equal to saturated current density (J_{sat}). Then, we can calculate J_{SC}/J_{sat} and J_{max}/J_{sat} to describe exciton dissociation (η_{diss}) and charge collection (η_{coll}) efficiency. J_{max} is the J_{ph} at the maximal output point.

Computational details.

DFT calculation: First-principles calculations were carried out on the basis of periodic DFT using a generalized gradient approximation within the Perdew-Burke-Ernzerh of exchange correction functional. 2PACz and PyCA-3F molecules were adsorbed on the ITO surface. The wave functions were constructed from the expansion of plane waves with an energy cutoff of 500 eV. Gamma centered k points of $3\times3\times1$ have been used for geometry optimization. The consistence tolerances for the geometry

optimization are set as 1.0×10^{-5} eV/atom for total energy and 0.05 eV/Å for force, respectively. In order to avoid the interaction between the two surfaces, a large vacuum gap of 15 Å has been selected in the periodically repeated slabs. The structural stability was checked with frequency calculation.

Classical Molecular Dynamic (MD) Simulations

Following the methodology from Park. S. M. et al ²⁵⁹, the adsorption process of 2PACz and PyCA-3F on the ITO surface was further investigated by classical MD simulations using the Large-scale Atomic/Molecular Massively Parallel Simulator (LAMMPS) package. 263 The atomic interactions within the 2PACz and PvCA-3F molecules were described using the OPLS-AA force field,²⁶⁴ where the detailed parameters were generated using the LigParGen software.²⁶⁵ To better describe the conformation of the phosphonic functional group, the interactions within this group were switched to a specially designed force field developed by Meltzer et al..²⁶⁶ Inspired by Park. S. M. et al ²⁵⁹, the ITO substrate was simplified as In₂O₃ and simulated using the Buckingham potential, which can effectively reproduce the In₂O₃ structure. The interactions between molecules and the substrates were simulated using the Lennard-Jones (LJ) and Coulombic interactions, where the parameters of the LJ terms were obtained from the Universal force field using geometric mixing rules.²⁶⁷ Initially, 2PACz molecules (controlled system) and PyCA-3F molecules (mixed system, with the experimental molar ratio 2PACz:PyCA-3F = 9:1) were randomly placed near the surface of In₂O₃ substrate with a minimum interatomic distance of 2.0 Å to avoid atomic overlap. The interfacial systems were then equilibrated in the canonical NVT ensemble at 300 K for 1.0 ns which is long enough to converge the potential energy. The In₂O₃ substrate was fixed during the equilibration to avoid unexpected structure changes. The motion of the atoms was integrated using the velocity-Verlet algorithm with a time step of 1 fs. During the simulations, the atomic trajectories were visualized using the Ovito software. 268 The aggregation of molecules was determined by the coverage surface on the substrate, which is calculated by creating a surface mesh using the method

implemented in Ovito. The interfacial adsorption energy was calculated as $E_{\rm adsorption} = E_{\rm total} - E_{\rm In_2O_3} - E_{\rm SAMs}$, where $E_{\rm total}$, $E_{\rm In_2O_3}$, and $E_{\rm SAMs}$ are the potential energy of the whole system, In₂O₃ substrate, and SAM molecules, respectively.

5.3 Results and Discussion

The chemical structures of 2PACz and PyCA-3F are presented in Figure 5.1a. Concurrently, there also shows the HTL fabrication schemes of 2PACz SAMs and CA SAMs; the latter is formed by sequentially depositing 2PACz and PyCA-3F and a coabsorbed 2PACz/PyCA-3F dual molecule surface is expectedly constructed. The surfaces of ITO and HTLs are firstly investigated by atomic force microscopy (AFM) measurements. From the height images displayed in Figure 5.1b-d, it is found that ITO has a highly rough surface, which is harmful for thin film formation, no matter perovskite (thickness around 800 nm) or organic (thickness around 100 nm) ones, leading to poor crystallite organization order and general crystallinity, thus unsatisfying photovoltaic performance. The ITO itself demonstrates surface roughness around 3.71 nm. However, 2PACz SAM on ITO can lead to a slightly higher roughness of 4.02 nm, which can be resulted from the aggregation of disordered 2PACz molecules on ITO.²⁵⁴ Since the SAM's thickness is within 5 nm, this can be taken as a trade-off of maintaining transmittance and smoothening surface. Moreover, the surface potential distribution of ITO, 2PACz and CA is also measured by Kevin Probe Force Microscopy (KPFM), as shown in right panels of Figures 5.1b-d.

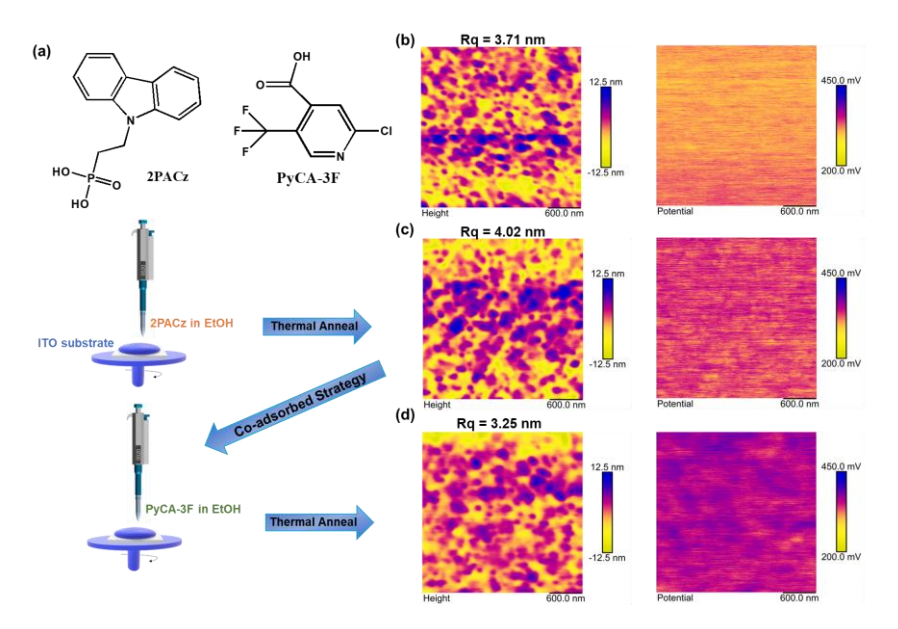


Figure 5.1 (a) Chemical structures of 2PACz and PyCA-3F, and schematic diagram of HTL/SAM fabrication. The AFM height images and KPFM images of (b) ITO (c) 2PACz and (d) CA substrates.

The contact potential difference (CPD) that can reflect the surface potential variations is extracted and shown in **Figure 5.2a**. The bare ITO demonstrates a CPD of around 310 meV. For 2PACz, the CPD increases to 380 meV, indicating a more p-type surface with SAM deposition. 106,269 For CA, the CPD of 417 meV is obtained, demonstrating that the incorporation of PyCA-3F can further increase the W_F. ^{25,270,271} Moreover, the CA surface gives a narrower full width at half maximum (FWHM) value of 20 mV than those of ITO (25 mV) and 2PACz (29 mV), demonstrating that a smooth and uniform surface is obtained. Parallelly, the general X-ray photoelectron spectroscopy (XPS) detection is carried out. As shown in **Figure 5.2b**, the results show that the incorporation of PyCA-3F brings negligible changes to the general distribution of elements on ITO surfaces of 2PACz. Next, the substrate transmittance spectra are measured as plotted in Figure 5.2c. 2PACz and CA SAMs lead to almost no change to ITO's original transmittance, so parasitic light absorption from HTLs is fundamentally eliminated and better J_{SC} values can be foreseeable. Work function (W_F) is an important factor for surface property of HTLs, which represents the electron blocking ability. Thereby, ultraviolet photoelectron spectroscopy (UPS) experiments are conducted to figure out the W_F values, through locating the secondary electron cut-offs. As a result,

the W_F of three kinds of anode surfaces are 4.30 eV (ITO), 5.10 eV (2PACz) and 5.16 eV (CA) in **Figure 5.2d**, respectively. Principally, possessing a high W_F for HTL is beneficial to boosting hole extraction and transfer at p-side, and dense coverage contributes, as well. The 2 or 3 nm thick 2PACz though with higher W_F, but less complete coverage and aggregation can risk in performance loss. However, the CA surface with further improved W_F and reduced aggregation is supposed to compensate for the energy loss at the HTL side.

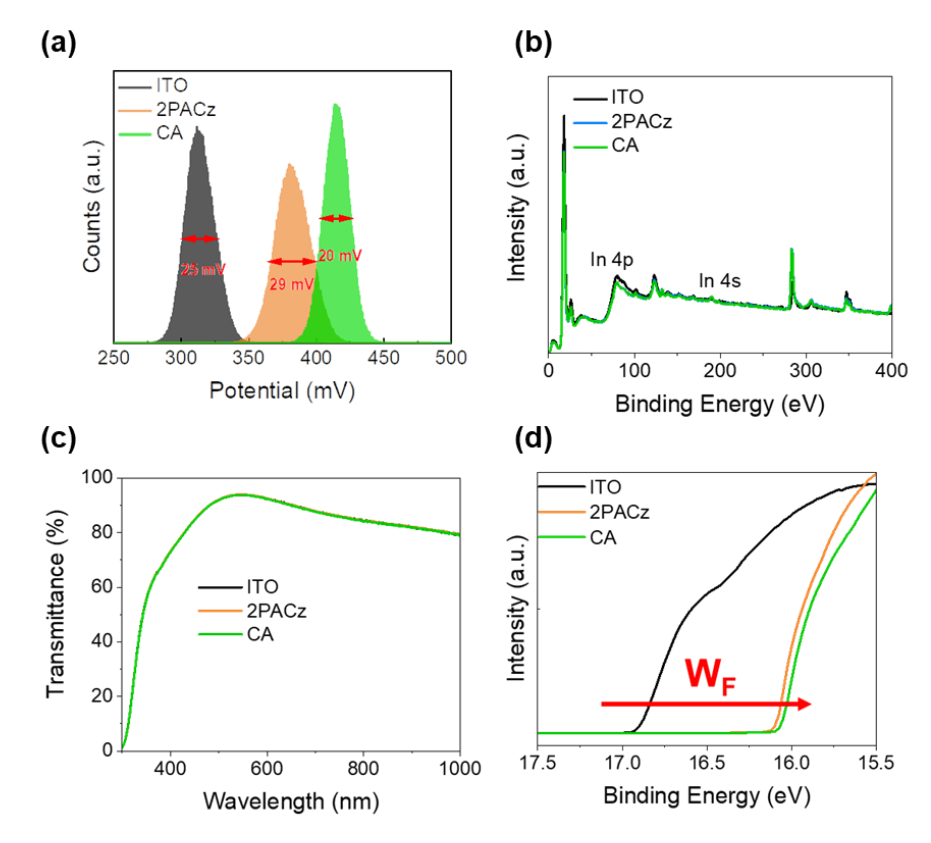


Figure 5.2 (a) Potential distribution plots of ITO, 2PACz and CA films, the full width at half maximum (FWHM) values of ITO, 2PACz and CA are 25 mV, 29 mV and 20 mV. (b) The transmittance spectra of ITO and 2PACz and CA substrates. (c) UPS spectra of ITO and 2PACz and CA substrates. (d) General XPS spectra for ITO, 2PACz and CA.

To gain more insight into SAM distribution, we perform the Scanning Electron Microscopy with Energy Dispersive X-Ray Analysis (SEM-EDX) upon ITO, 2PACz and CA, and the results are shown in **Figure 5.3**. The characteristic element Indium of ITO is easily observed in all three samples, facilitated by the ultrathin nature of SAM. For 2PACz/ITO surface, phosphorus element's signal is clearly stronger than others;

and CA surface exhibits more fluorine response from PyCA-3F. Therefore, the special co-adsorbed strategy may result in a dual-molecule structured SAM surface, which is smoother, more uniform with reduced aggregation and thus could further improve optoelectronic properties of photovoltaic devices.

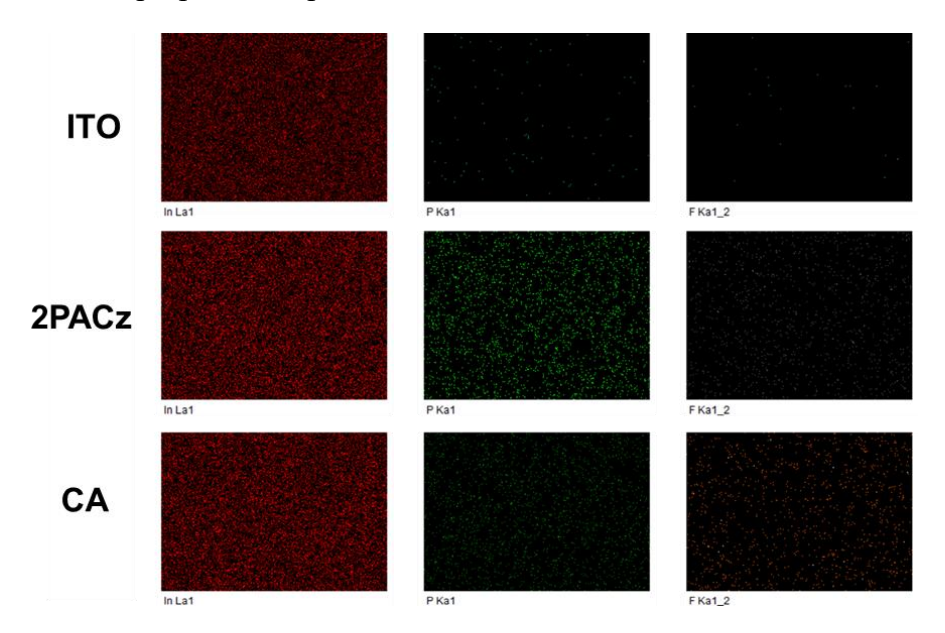


Figure 5.3 SEM-EDX mapping images of ITO, 2PACz and CA substrates.

To investigate the role of 2PACz in preventing molecular aggregation in solution, dynamic light scattering (DLS) analyses were conducted to examine the size distributions of 2PACz, CA, and PyCA-3F. The results, illustrated in **Figure 5.4a**, reveal that 2PACz exhibits a substantial hydrodynamic diameter of approximately 70 nm. In contrast, the incorporation of PyCA-3F results in a significant reduction in the hydrodynamic diameter of CA to about 40 nm. This reduction underscores the effectiveness of PyCA-3F in substantially diminishing the tendency of 2PACz molecules to aggregate in solution.²⁵⁹ As evidence for inhibited aggregation in film, Atomic Force Microscopy-Infrared spectroscopy (AFM-IR) was utilized to explore the composition heterogeneity and identify specific moiety with a feature peak of 1460 cm⁻¹ in 2PACz, as shown in **Figure 5.5**.^{256,272} Compared to 2PACz/ITO substrate, the CA sample exhibits a markedly more uniform distribution of 2PACz ITO surface. This improved homogeneity suggests that the incorporation of PyCA-3F not only promotes even dispersion but also substantially reduces the clustering of 2PACz molecules on

ITO. Additionally, in the mix sample (mixing 2PACz and PyCA-3F in EtOH) a similar impediment to the aggregation of 2PACz is evidenced, further highlighting the efficacy of PyCA-3F.²⁵⁹ Moreover, the hygroscopic nature of CA substrate with a higher contact angle shown in **Figure 5.4b** would be beneficial for enhanced crystallinity and reduced charge recombination at the HTL interfaces.^{273,274}

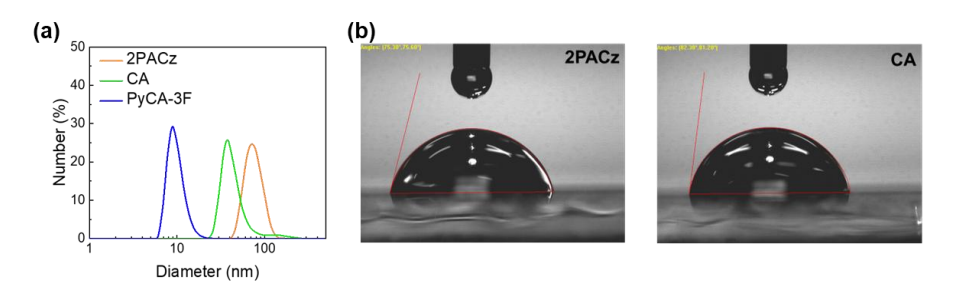


Figure 5.4 (a) DLS micellar size distributions of 2PACz, CA, and PyCA-3F in EtOH with concentration of 1 mg/ml. The hydrodynamic diameters are around 70 nm, 40 nm and 9 nm for 2PACz, CA and PyCA-3F solutions. (b) Contact angles of 2PACz and CA substrates

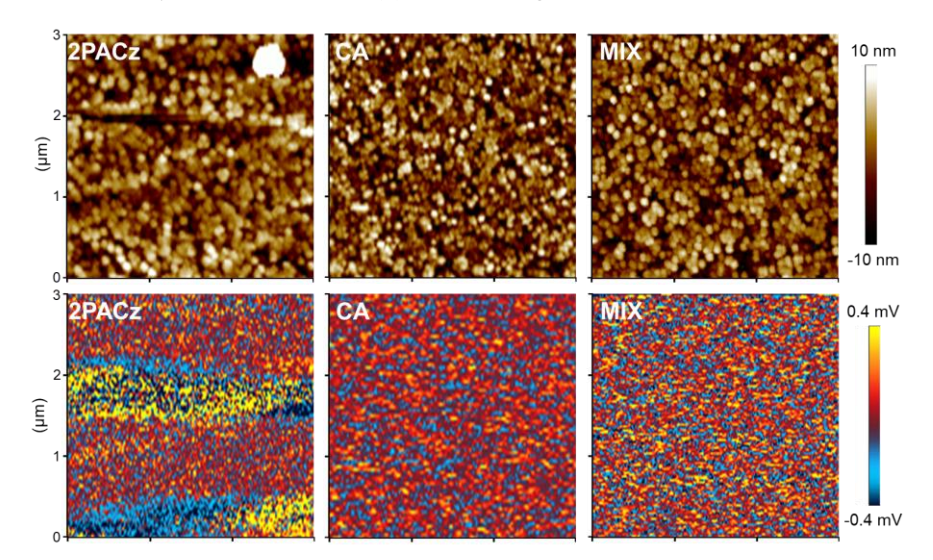


Figure 5.5 AFM-IR topographic and corresponding IR images of 2PACz, CA and mixed on ITO substrates.

Subsequently, density functional theory (DFT) calculation is utilized to obtain more understanding on the incorporation of PyCA-3F on 2PACz. The electrostatic potentials (ESP) of 2PACz and PyCA-3F are displayed in **Figure 5.6a**. For 2PACz, the electron-rich area (blue) and electron-poor area (red) are located in the carbazole group and phosphate group, giving the highest occupied molecular orbit (HOMO) and lowest unoccupied molecular orbit (LUMO) value of -4.82 eV and -1.61 eV, respectively. As

for PyCA-3F, the electron-rich area and electron-poor area are located on pyridine group and trifluoromethyl group, providing a HOMO and LOMO of -3.54 eV and -2.49 eV, respectively. Both the electron-rich group and electron-poor group are potentially beneficial for the passivation of the negative and positive defects at the perovskite interface. **Figure 5.6b to Figure 5.6d** and **Table 5.1** offer the calculated W_F from potential and E_F. The derived W_F values for 2PACz and CA SAMs are 5.09 eV and 5.18 eV, respectively.^{275,276} The incorporation of PyCA-3F leading to a more p-type surface of CA SAMs is in consistent with KPFM and UPS results above.

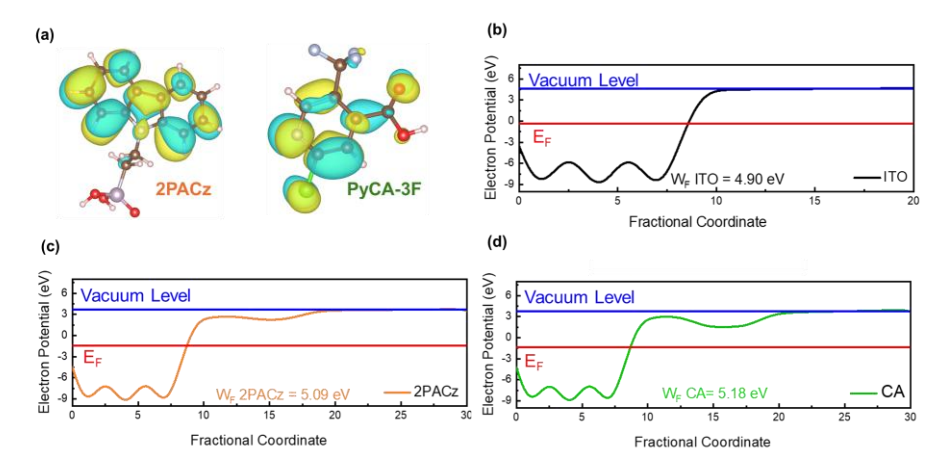


Figure 5.6 (a) Electrostatic potential distribution of 2PACz and PyCA-3F calculated by DFT, the colors represent electron-rich area (blue) and electron-poor area (red). (b) Calculated Work Function of ITO. (c) Calculated Work Function of 2PACz. (d) Calculated Work Function of CA.

Table 5.1 The values of Fermi Level, Potential, and W_F for the structures

Structure	Fermi Level (eV)	Potential (eV)	$W_{F}\left(eV\right)$
ITO	-0.3157	4.5855	4.9012
2PACz/ITO	-1.4418	3.6519	5.0937
CA/ITO	-1.3921	3.7843	5.1764

To better elucidate the interaction mechanism between 2PACz and PyCA-3F, classical molecular dynamics simulations have been performed to elucidate the interaction mechanisms between 2PACz and PyCA-3F molecules on the ITO substrate in **Figure 5.7a**. The simulation results indicate that the 2PACz/ITO surface experiences pronounced phase segregation, even though the molecules are initially uniformly

placed near the ITO surface. As shown in Figure 5.7b and Figure 5.8, the coverage surface of 2PACz with PyCA-3F is always larger than that of 2PACz on ITO, indicating that PyCA-3F can effectively reduce the aggregation of 2PACz. The coverage surfaces of both systems increase and then level off as a function of the simulation time, which confirms the SAMs reach an equilibrium state on the ITO surface. Figure 5.7c further illustrates the interfacial structure between 2PACz and PyCA-3F on the ITO surface. The molecular dynamics simulations results reveal that PyCA-3F restricts the mobility of 2PACz molecules by creating a complex structure, significantly mitigating their tendency to clump together. In particular, the trifluoromethyl groups in PyCA-3F form hydrogen bonds with the phosphonic acid groups of 2PACz. These resulting complexes play a crucial role in curbing the development of larger aggregates by constraining the interactions among adjacent 2PACz molecules. It has been observed that PyCA-3F can assume a transient surface adsorption mode, wherein the carboxylate groups are anchored to the surface while the trifluoromethyl groups extend nearby. This configuration can facilitate the attraction of other unanchored 2PACz molecules that are diffusing freely, guiding them toward the surface.

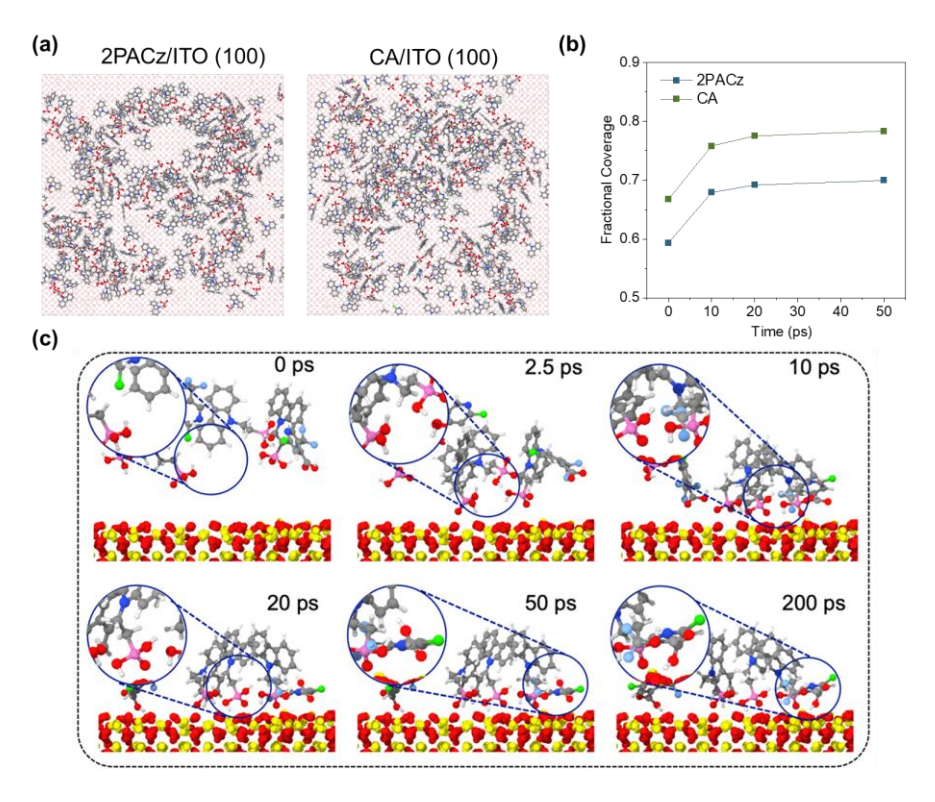


Figure 5.7 (a) Top view of equilibrated molecular representations on the ITO surface. (b) Fractional coverage of ITO surface by the 2PACz and 2PACz with PyCA-3F molecules. Note that the projected area of the simulated substrate is around 10,000 Å². (c) The adsorption process of 2PACz and PyCA-3F molecules on the ITO substrate. The interfacial structures within small circles are magnified in larger circle areas.

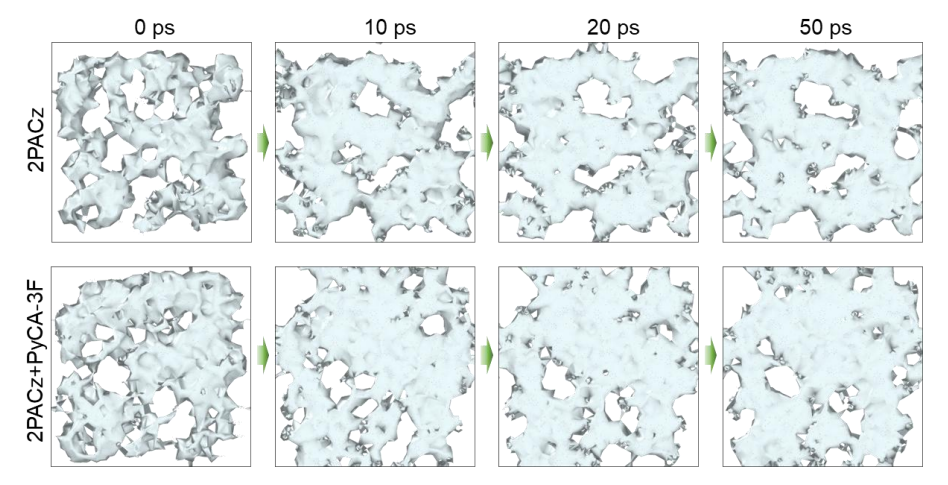


Figure 5.8 Coverage surfaces of the 2PACz and 2PACz with PyCA-3F molecules on the ITO substrate at different simulated times from classical molecular dynamics simulations.

We firstly examine the growth of perovskite films on 2PACz substrates with and without PyCA-3F. The perovskite films are carefully lifted off using UV epoxy and cover glass, enabling the examination of both the top and buried surfaces of perovskite films shown in **Figure 5.9**. ¹⁴⁸ The top-view SEM images in **Figure 5.10a** and **Figure 5.10b** reveal similar top surface morphology for the two perovskite films, regardless of the presence of PyCA-3F. In both perovskite films, discernible perovskite grains with grain sizes approaching 1 um are prominently observed, where the excess Pb-rich phase is distributed around the perovskite grain boundaries in both cases, in consistent with the excess PbI₂ that is regarded as better perovskite growth and trap passivation. The buried interface for both perovskite films show analogous morphology without excess Pb-rich phase in **Figures 5.10c** and **Figure 5.10b**, conforming to the "From top to down" perovskite growth orientation. ¹⁴⁸ However, noticeable nanovoids are observed at the buried surface when perovskite film is directly deposited on 2PACz similar to previous report. ²⁷⁷ In contrast, the buried surface of perovskite films on CA are flat and densely compacted. ^{278,279}

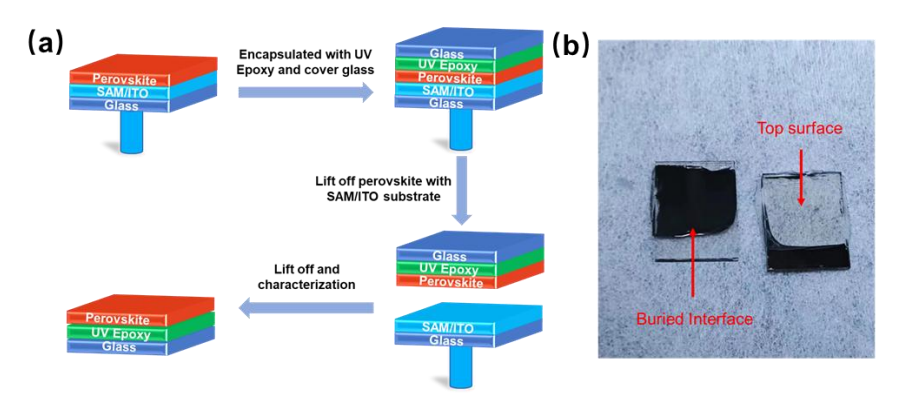


Figure 5.9 The lift off scheme of perovskite film with/without PyCA-3F.

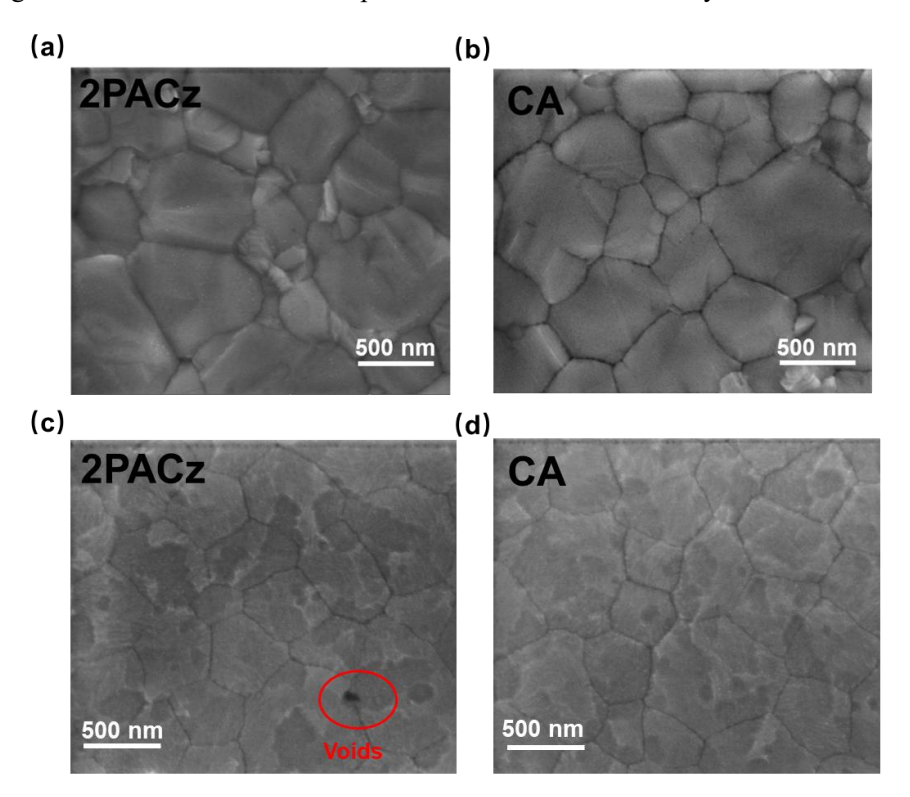


Figure 5.10 Top-view SEM images of perovskite film growth on (a) 2PACz and (b) CA. Top-view SEM images of the buried interface on (c) 2PACz and (d) CA.

These results are also supported by the XRD results in **Figure 5.11a**: the excess Pb-rich phase is absent at the buried side of perovskite films but exists on the top side for both cases. ²⁸⁰ Similarly, to visualize the roughness of both top/buried interfaces, atomic force microscopy (AFM) measurement is conducted. As shown in **Figures 5.12a to 12d**, AFM height images for the top surface and buried interfaces of both perovskite films reveal a subtle reduction in surface roughness with the incorporation of PyCA-3F. This observation suggests that the co-adsorbed strategy employed does not induce significant changes in surface morphology, but is more likely to change the properties

of buried interface.

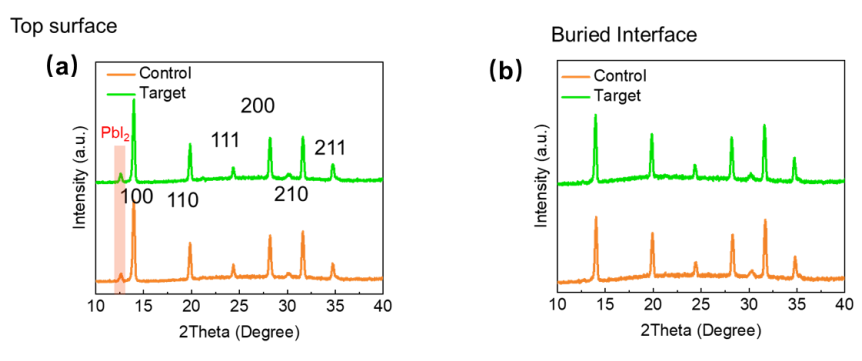


Figure 5.11 XRD images of perovskite film growth on 2PACz and CA.

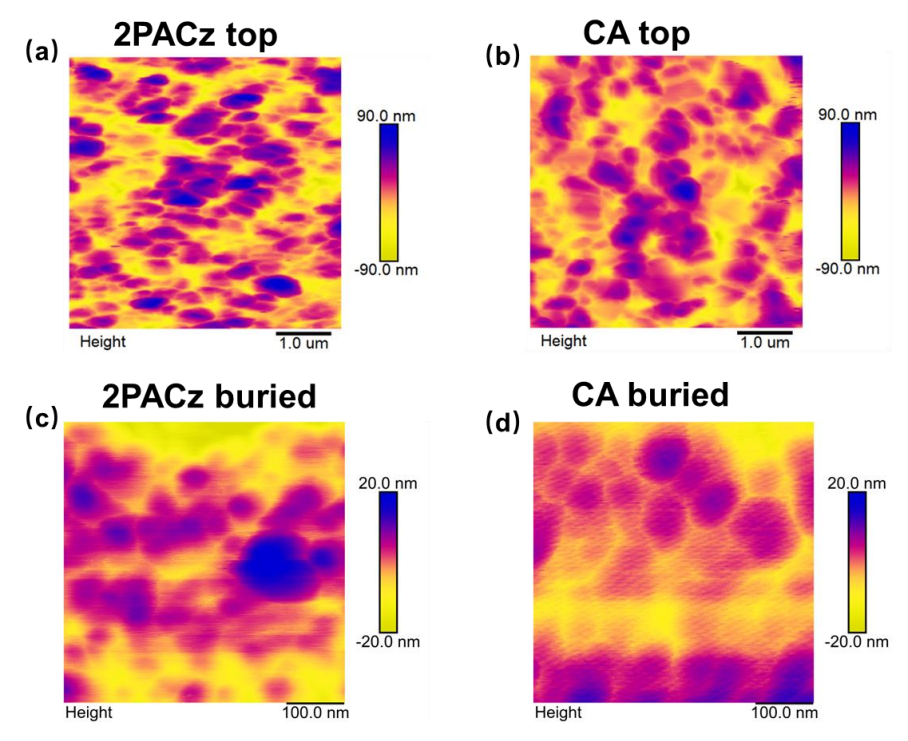


Figure 5.12 AFM height images of perovskite film growth on (a) 2PACz top surface, (b) CA top surface, (c) 2PACz buried interface (d) and CA buried interface.

To gain deeper insights into the impact of PyCA-3F incorporation at the buried interface, we introduce perovskite grain boundary groove angles, which are consistently formed through the residue solvent evaporation process, guiding the top-down grain growth direction. ^{148,278} We postulate that PyCA-3F serves as a mediating bridge, influencing the modification of heterointerface energy at the perovskite/2PACz interface. In **Figure 5.13a**, the interplay between grain boundary energy (γ_{GB}), heterointerface energy (γ_{HI}), grain boundary groove dihedral angle (φ), and the side angle (φ) between SAM/ITO and perovskite film is illustrated. The relationship between

 γ_{GB} and γ_{HI} is defined by the following equation:

$$\frac{\gamma_{GB}}{\gamma_{HI}} = 2\cos\left(\frac{\varphi}{2}\right) = 2\sin(\theta) \tag{5.1}$$

Figures 5.13c and 5.13d presents the peel-offed buried interface height profiles obtained through high-resolution AFM. The control film (peeled from 2PACz) exhibits a buried grain boundary groove angle (φ_1) of 51°. In contrast, the incorporation of PyCA-3F results in a substantially larger groove angle (φ_2) of 118°, indicative of a notably higher heterointerface energy. As the scheme of groove angles shown in **Figure 5.13b**, the significant augmentation in groove dihedral angles, evident in the presence of PyCA-3F, plays a pivotal role in mitigating the occurrence of physical nanovoids at the buried interface. This notable increase stands as a strategic advantage, contributing to the effective reduction of interfacial traps and nonradiative centers at the buried interface.

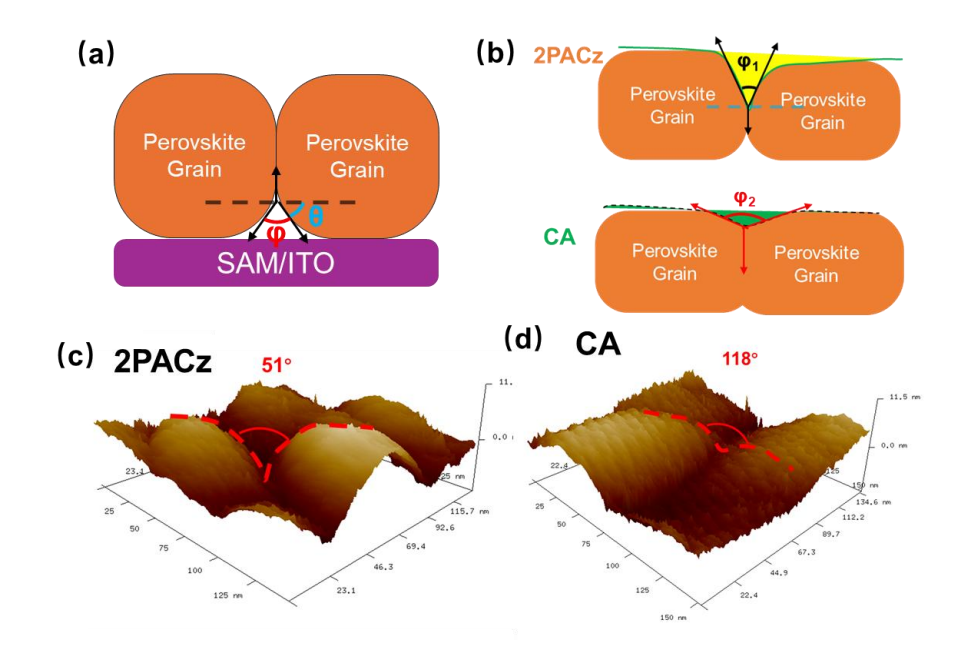


Figure 5.13 (a) The illustration of grain groove angles at the buried interface. (b) The illustration of the flattened grain groove angles with PyCA-3F. (c) high-resolution AFM images of the buried interface of 2PACz-based perovskite film, the grain boundary groove angles are estimated to be 51°. (d) high-resolution AFM images of the buried interface of CA-based perovskite film, the grain boundary groove angles are estimated to be 118°.

The distribution of PyCA-3F in perovskite films is investigated by time-of-flight secondary-ion mass spectroscopy (ToF-SIMS) for ITO/2PACz (with or without PyCA-

3F)/Perovskite. As shown in **Figures 5.14a and 5.14b**, the intensity tracing of SnO₂⁻, PO₂⁻, PbI⁻ and F⁻ are prosecuted for both perovskite films with and without PyCA-3F, which referred to the existence of ITO, 2PACz, perovskite and PyCA-3F, respectively. In the target film, a notable signal attributed to the presence of PyCA-3F becomes evident within the time range of 800 to 1000 seconds, represented by a significant F⁻ signal. Additionally, the shared positions of SnO₂⁻, PO₂⁻, and F⁻ signals indicate chemisorption interactions occurring among ITO, 2PACz, and PyCA-3F on the ITO surface, particularly in proximity to the interface between the perovskite and ITO as shown in **Figure 5.14c**. These observations collectively suggest that the inclusion of PyCA-3F may not happen in the perovskite formation process or penetrate to the perovskite grain boundary and the top surface but firmly anchoring at the perovskite/2PACz interface.

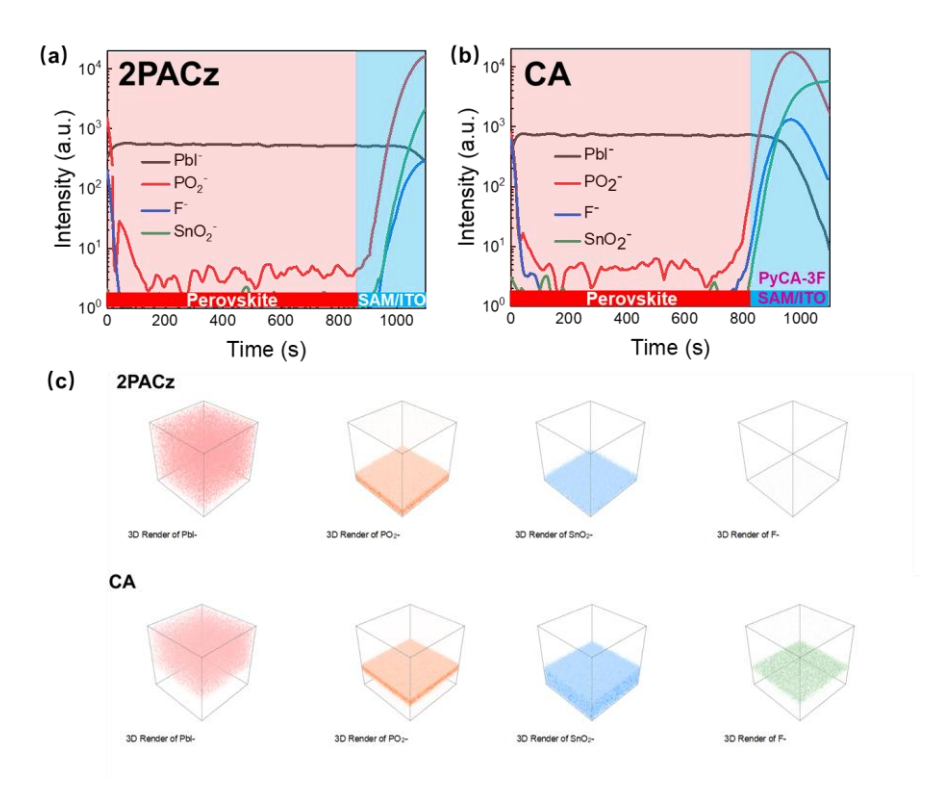


Figure 5.14 (a) TOF-SIMS images of the buried interface of 2PACz-based perovskite film. (b) TOF-SIMS images of the top surface of CA-based perovskite film. (c) 3D signals images of TOF-SIMS for perovskite film growth on 2PACz and CA.

The interaction between perovskite and PyCA-3F is carried out by X-ray photoelectron spectroscopy (XPS) and shown in **Figure 5.15a and 5.15b**. At the top

surface, no apparent shifting can be observed in either Pb_{4f} or the I_{3d} peaks, indicating that the PyCA-3F does not participate in the interaction at the top surface. In contrast, at the buried interface, the Pb_{4f} and I_{3d} peaks have shifted: from 143.0 eV and 138.2 eV to 142.8 eV and 138.0 eV for Pb_{4f}, and for I_{3d}, shifted from 630.6 eV and 619.1 eV to 630.4 eV and 618.9 eV, respectively, demonstrating the interaction between perovskite and molecule at the buried interface. The slight downward shift observed in the binding energies of Pb_{4f} and I_{3d} can be attributed to the interaction between Pb²⁺ and PyCA-3F. This suggests that PyCA-3F can passivate uncoordinated Pb²⁺ ions, consequently diminishing the propensity for metallic lead formation.²⁸¹⁻²⁸³

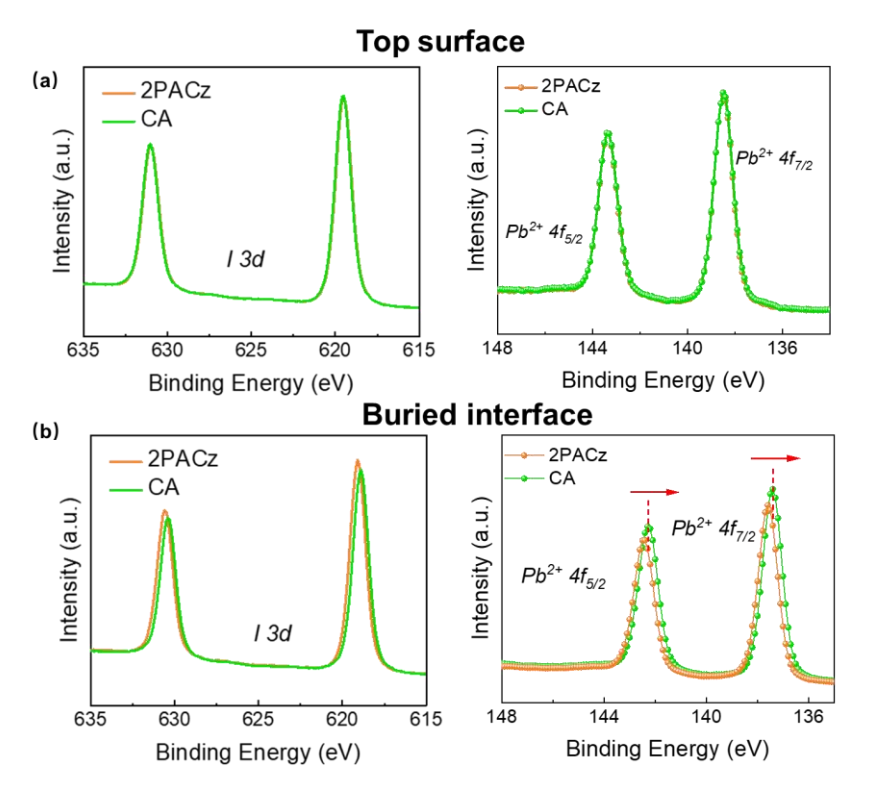


Figure 5.15 (a) XPS spectra of Pb_{4f} and I_{3d} at the top surface of 2PACz and CA perovskite films. (b) XPS spectra of Pb_{4f} and I_{3d} the buried interface of 2PACz and CA perovskite films.

Moreover, attenuated total reflectance Fourier transform infrared spectroscopy (ATR-FTIR) measurement is conducted for both 2PACz and CA films in **Figure 5.16**. The presence of 2PACz is clearly indicated by the peaks in the vicinity of 1234 cm⁻¹, corresponding to P=O vibrations, which shift to 1236 cm⁻¹ with the incorporation of PyCA-3F. ^{230,284,285} To further confirm the interaction at the buried interface, as shown in the FTIR results of 2PACz-PbI₂ and CA-PbI₂, the C-N vibrations and C-H vibrations,

initially identified around 1065 cm⁻¹ and 800 cm⁻¹, respectively, experience a shift of approximately 2 cm⁻¹ in the presence of PyCA-3F. These observed shifts signify the enhanced binding of perovskite and 2PACz following the incorporation of PyCA-3F. ^{286,287}

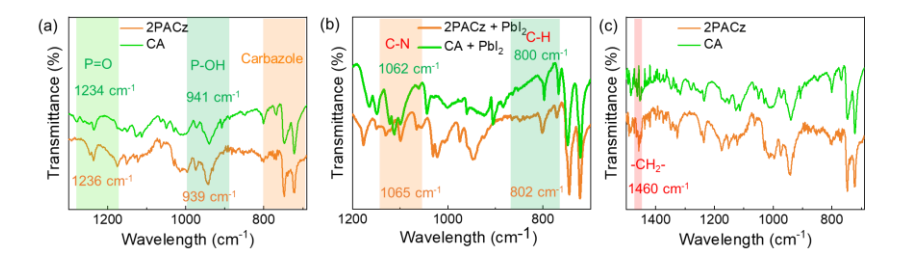


Figure 5.16 (a) ATR-FTIR spectrum of the surface of 2PACz and CA. (b) ATR-FTIR spectrum of 2PACz-PbI₂ and CA-2PACz-PbI₂. (c) The feature peak of 1460 cm⁻¹ used for AFM-IR test, corresponding to -CH₂- vibration.

The crystalline structure of perovskite films is investigated using angel-dependent grazing incidence wide-angle X-ray scattering (GIWAXS) measurements for both perovskite top surface and buried interface in Figure 5.17 and 5.18. Three different incidence angles (0.05°, 0.3°, and 0.5°) are selected to analyze the perovskite film's characteristics at the top surface, bulk, and near the buried interface, respectively. ^{26,288} Similarly, the perovskite films exhibit a predominant peak at a q ~ 1.02 Å⁻¹, corresponding to the (100) plane of FAPbI₃.²⁸⁹ Interestingly, the presence of a PbI₂ phase at $q = 0.94 \text{ Å}^{-1}$ can be observed in the 2PACz-based perovskite films (both top and buried), but this peak tends to vanish in the buried interface of the control perovskite film with an incidence angle of 0.05°, indicating that the PbI₂ is more likely to distribute at the top surface/bulk rather than the buried interface.²⁸⁰ However, this PbI₂ peak is not detected in any of the perovskite buried interfaces, which agrees with the XRD results. Furthermore, a small peak corresponding to the δ-FAPbI₃ phase at approximately 0.77 Å⁻¹ is exclusively observed in the 2PACz-based buried interface, while both the top surface and buried interface of the CA-based perovskite films are free of δ-FAPbI₃ and shown in Figure 5.19.²⁰² The presence of the photoinactive δ phase, with its low absorption coefficient and non-perovskite nature, could inherently hinder the device performance. Consequently, the utilization of PyCA-3F is found to be advantageous in reducing the photoinactive PbI₂ and δ -FAPbI₃ and enhancing perovskite crystallinity.

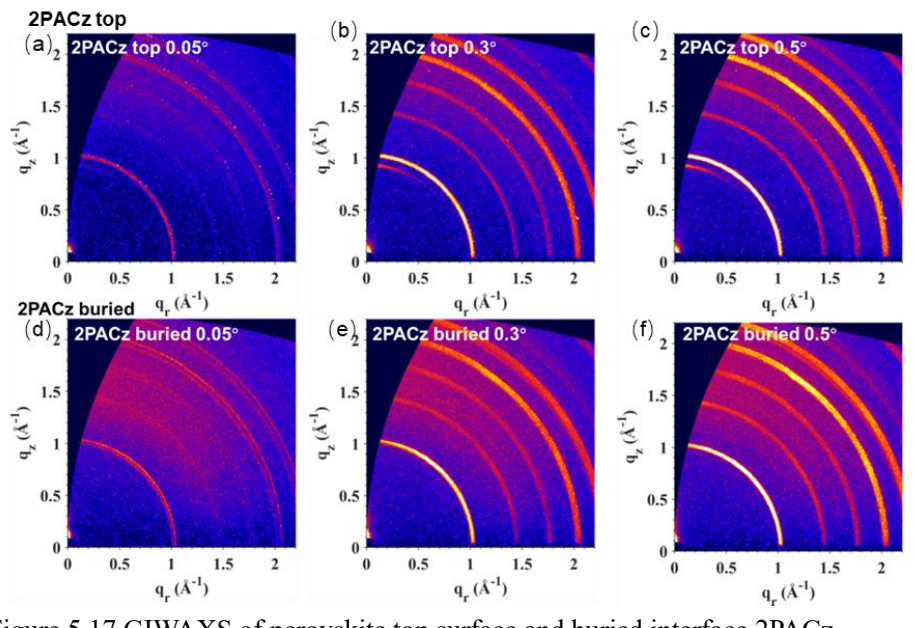


Figure 5.17 GIWAXS of perovskite top surface and buried interface 2PACz.

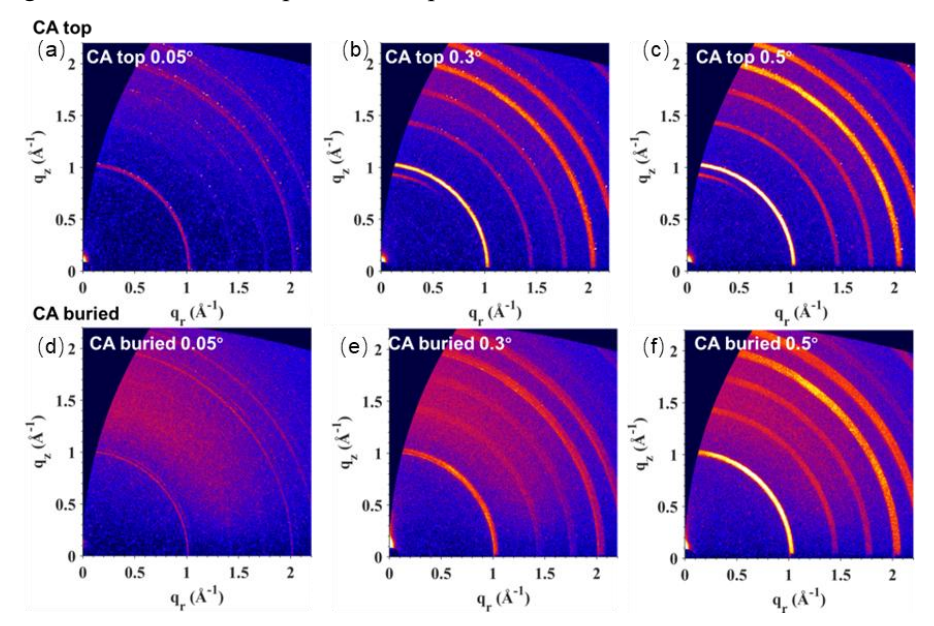


Figure 5.18 GIWAXS of perovskite top surface and buried interface CA.

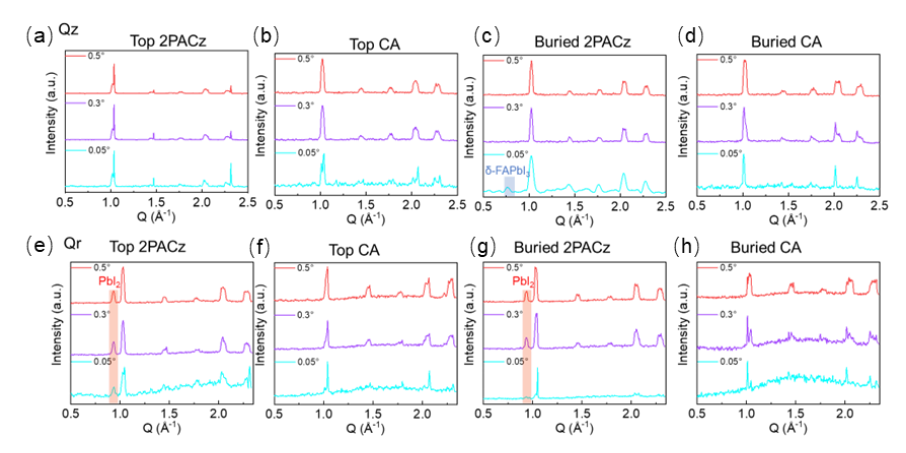


Figure 5.19 Two-dimensional patterns and integral GIWAXS profiles at Qz and Qr.

Energy level variations are characterized using ultraviolet photoelectron spectroscopy (UPS). As depicted in Figure 5.20a, no significant changes are observed for the top surface of either the control or target perovskite films. However, a substantial variation in energy levels can be detected at the buried interface of target perovskite film compared with the control. The initial valence band maximum (VBM) and work function (W_F) at the buried interface are measured to be -5.42 eV and 4.20 eV, respectively. With the presence of PyCA-3F, VBM, and E_F were found at -5.49 eV and 4.57 eV.²⁹⁰ These findings are similar to the UPS and KPFM results obtained for ITO/2PACz and ITO/CA discussed earlier. In addition, the downshifted VBM and slight p-typed shifting of the buried interface in the CA perovskite film contributes to a narrower energy gap across the top/buried interface, resulting in a reinforced built-in electric field that improves carrier extraction and transfer.²⁹¹ These analogous results can also be obtained from the KPFM images shown in Figure 5.20b and 5.20c. The top surface for both perovskite films demonstrated a close surface contact potential difference (CPD) of around -330 meV. In contrast, the buried interface growth on 2PACz delivers a CPD of around 5 meV. With PyCA-3F, the CPD increases to 25 meV for the buried interface of CA. Moreover, the buried interface of CA shows a more centralized distribution, demonstrating a flattened surface with less potential distribution difference. Furthermore, the similar results of the buried interface that the increased W_F, accompanied by a more p-type behavior in the CA-based perovskite films, is expected to facilitate hole extraction and transfer at the buried interface with a p-type contact.²⁰⁵

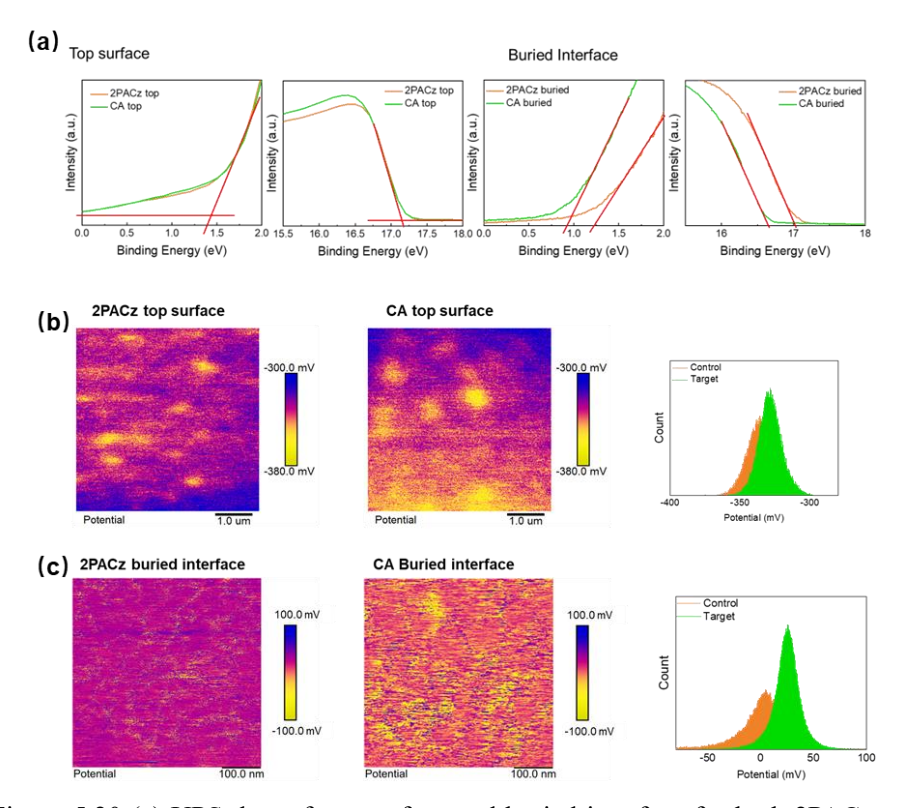


Figure 5.20 (a) UPS data of top surface and buried interface for both 2PACz and CA based perovskite films. (b) KPFM images of top surface for both 2PACz and CA perovskite films. (c) KPFM images of buried interface for both 2PACz and CA perovskite films.

To investigate the introduction of PyCA-3F on carrier dynamics, steady-state photoluminescence (PL) and time-resolved photoluminescence (TRPL) measurements are performed. As illustrated in **Figure 5.21**, both perovskite films exhibit similar PL peak positions, centered around 790 nm. Notably, the CA/perovskite film shows an enhanced PL intensity compared to the control film, suggesting a reduction in trap states and suppressed nonradiative recombination.²⁵⁹ This phenomenon of enhanced PL intensity is also observed at the buried interface. Additionally, the TRPL results (**Figure 5.21** and **Table 5.2**) demonstrate that the carrier lifetime of the perovskite film cast on CA was prolonged, indicating the suppression of trap-assisted nonradiative recombination with the incorporation of PyCA-3F at the buried interface.²⁹⁰ The suppression of nonradiative recombination and favorable carrier dynamics can

inherently contribute to the improved device performance, particularly in terms of V_{OC} and FF.

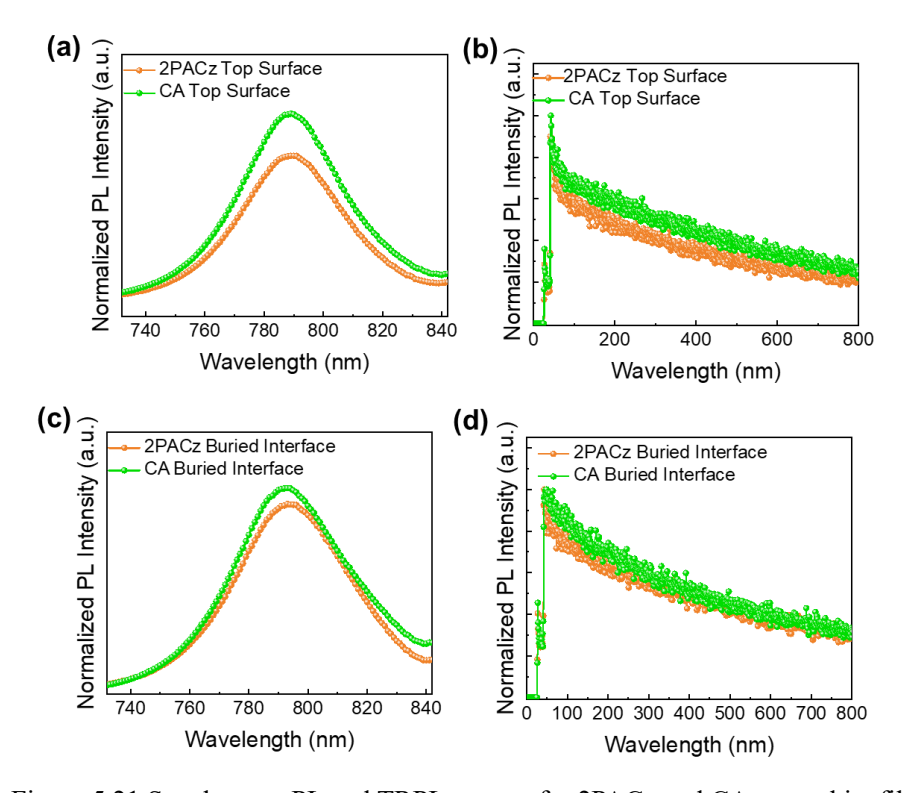


Figure 5.21 Steady-state PL and TRPL spectra for 2PACz and CA perovskite films.

Table 5.2 Calculated lifetime of TRPL results

Sample	τ_1 (ns)	τ ₂ (ns)	τ _{ave} (ns)
2PACz top surface	12.96	534.26	250.78
CA top surface	15.80	738.39	660.12
2PACz buried interface	24.96	567.27	525.04
CA buried interface	84.20	597.14	544.69

Furthermore, space-charge-limited current (SCLC) measurement is conducted with the device structure of ITO/2PACz (with or without PyCA-3F)/Perovskite/PTAA/Cu. The trap-filling limit voltage (V_{TFL}) is denoted to be the transition of the ohmic region and TFL region, where the trap density (N_t) is associated with V_{TFL} and can be calculated by the equation:

$$N_t = \frac{2\varepsilon_0 \varepsilon V_{TFL}}{eL^2} \tag{5.2}$$

 ε_0 , ε represent vacuum permittivity, dielectric constant and e, L represent element charge, perovskite film thickness, respectively. As shown in **Figure 5.22 and Table 5.3**, the control devices deliver a V_{TFL} of 1.28 V, corresponding to a N_t of 3.09 × 10¹⁵ cm⁻³, while the device with PyCA-3F performed a V_{TFL} of 0.86 V, showing a much smaller N_t of 2.08 × 10¹⁵ cm⁻³, indicating that the trap density is reduced in CA-based PSCs, which can result from the smooth and uniform buried interface.

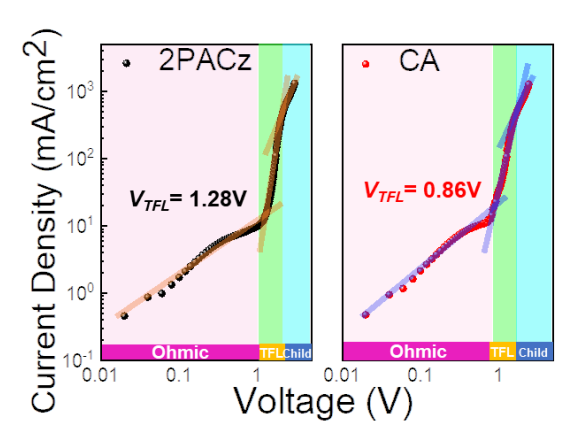


Figure 5.22 SCLC results for 2PACz and CA devices with hole-only devices structure of ITO/2PACz/Perovskite/PTAA/Cu. The calculated $N_t s$ are 3.09×10^{15} cm⁻³ and of 2.08×10^{15} cm⁻³.

Table 5.3 Calculated Trap density from SCLC results

Sample	$V_{TFL}\left(\mathbf{V}\right)$	$N_t (10^{15} \text{cm}^{-3})$
2PACz	1.28	3.09
CA	0.86	2.08

To investigate the impact of the buried interface on photovoltaic performance, inverted **PSCs** fabricated with following are the architecture: $ITO/2PACz/Cs_{0.05}(FA_{0.98}MA_{0.02})_{0.95}Pb(I_{0.98}Br_{0.02})_3/C_{60}/BCP/Cu$, where the deposition of PyCA-3F process is before the fabrication of perovskite films. Figure 5.23a showed that the control device achieved a peak PCE of 23.3%, with a V_{OC} of 1.14 V, J_{SC} of 24.85 mA/cm², and FF of 82%. In contrast, the device based on CA realizes a champion efficiency over 25%, featured by an V_{OC} of 1.17 V, a J_{SC} of 25.21 mA/cm², and an outstanding FF of 86%. Additionally, external quantum efficiency (EQE) measurements are conducted (Figure 5.23b), supporting an integrated current density

of 24.7 mA/cm² for the control and a slightly higher one of 25.0 mA/cm² for the target, which suggests the high-accuracy of J-V measurement. The CA-based device exhibits a stabilized PCE of 24.84% and a stabilized V_{OC} of 1.04 V, while the 2PACz-based device could only produce a 23.04% stabilized PCE (**Figure 5.23d**). The statistic distribution of 2PACz and CA are shown in **Figure 5.24**, where the Mixed devices (by mixing 2PACz and PyCA-3F as HTL) also show superior performance to 2PACz based devices. The enhancement in PCE can be ascribed to the rise in both V_{OC} and FF, leading to a minimized voltage loss of 0.36 eV for 1.53 eV bandgap perovskite (as determined from the EQE plots, certified 24.68%, **Figure 5.23c and 5.25**).

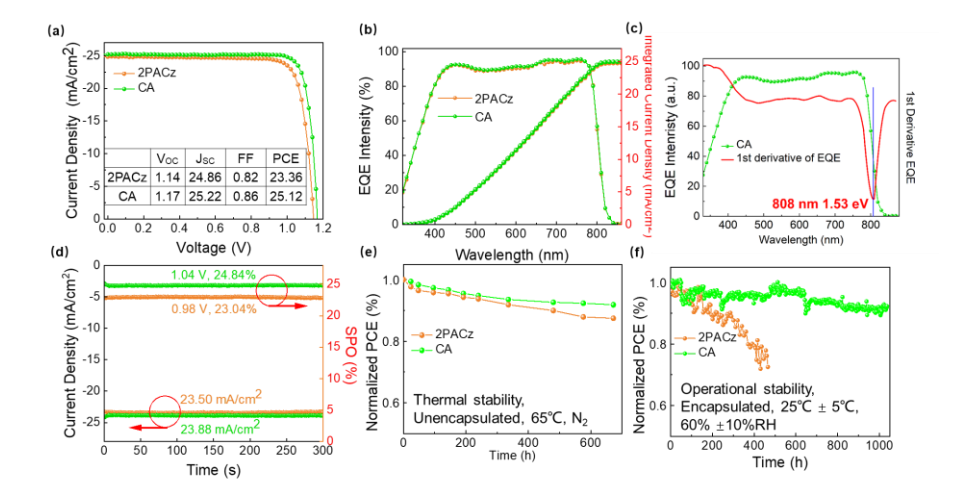


Figure 5.23 (a) J–V curves of 2PACz- and CA-based devices. (b) EQE curves of both 2PACz- and CA-based devices. (c) Bandgap of CA-based IPSCs calculated from the EQE plots. (d) Steady-state output of 2PACz- and CA-based devices. (e) Thermal stability of 2PACz- and CA-based devices. (f) Operational stability of 2PACz- and CA-based devices.

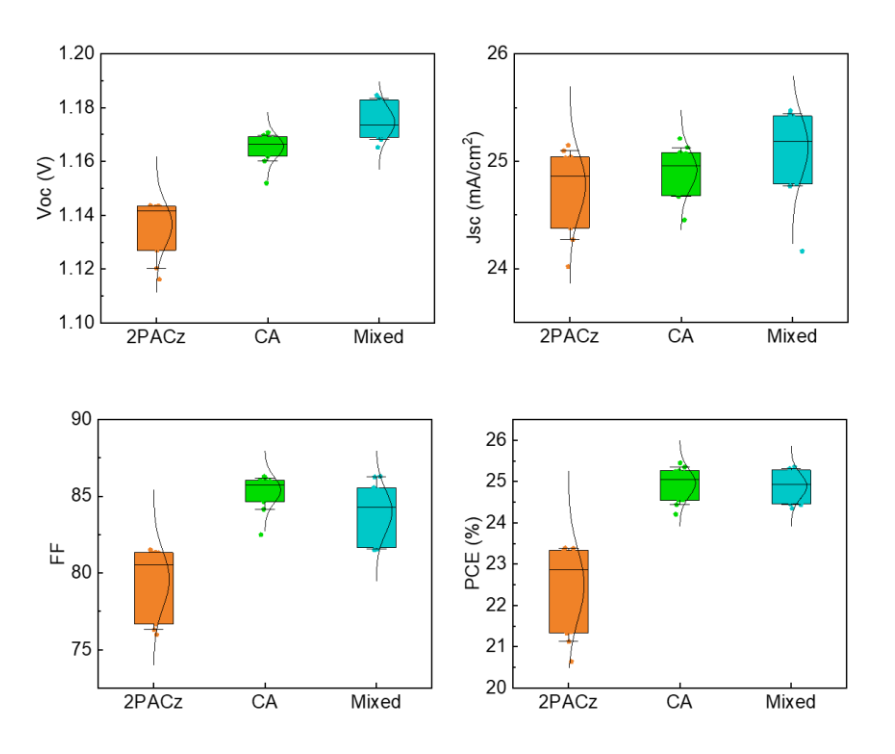


Figure 5.24 Photovoltaic parameters of perovskite devices based on 2PACz-, CA-, and Mixed substrates.

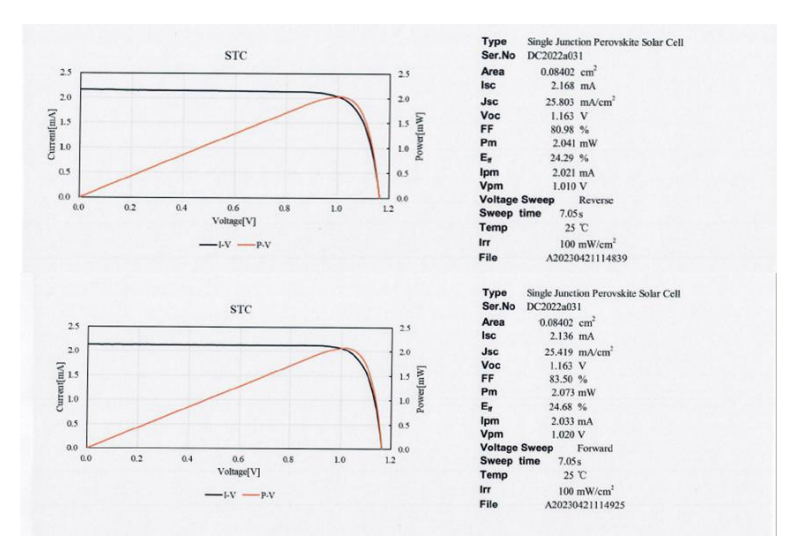


Figure 5.25 Certificated efficiency from Photovoltaic and Wind Power System Test Center, CAS.

We also evaluate the thermal stability of the devices under continuously annealing at 65°C for ~650 h. The target device maintained 92% of its initial efficiency, outperforming the control device which retained 87% (**Figure 5.23e**). More critically, the operational stability of the devices is evaluated by maximum power point tracking

(MPPT) under ambient atmosphere conditions.²⁹² As shown in the Figure 5.23f, the CA devices can retain approximately 90% of their initial efficiency after 1000 hourstracking, while the control devices suffers from a rapid fall, with efficiency dropping to 72% after approximately 450 hours. To further confirm the enhanced stability by the CA approach, we used an accelerating aging test by deliberately annealing the devices at 85°C with light soaking, as shown in Figure 5.26. After aging for ~ 200 h, the increased amount of unwanted nanovoids can be observed at the buried interface of the 2PACz-based device. Under operational conditions, these nanovoids were found to be sensitive to light irradiation and thermal disturbance and initialize the structural evolution and degradation of solar cells. One possible degradation mechanism of the buried interface is the formation and expansion of a void structure under light and thermal stimuli. The existence of nanovoids within the 2PACz device amplifies inhomogeneity, leading to an intensified current near the tip in areas abundant with defects. This intensification can generate additional Joule heating, potentially accelerating the evolution of the perovskite structure. Moreover, these voids can block the transport of charge carriers, resulting in less efficient collection in areas near the voids. Conversely, a buried interface that is free of voids and an HTL surface with reduced aggregation contribute to enhanced device stability.²⁹³ Therefore, the device performance of inverted PSCs can be comprehensively (both efficiency and stability) improved by the CA approach.

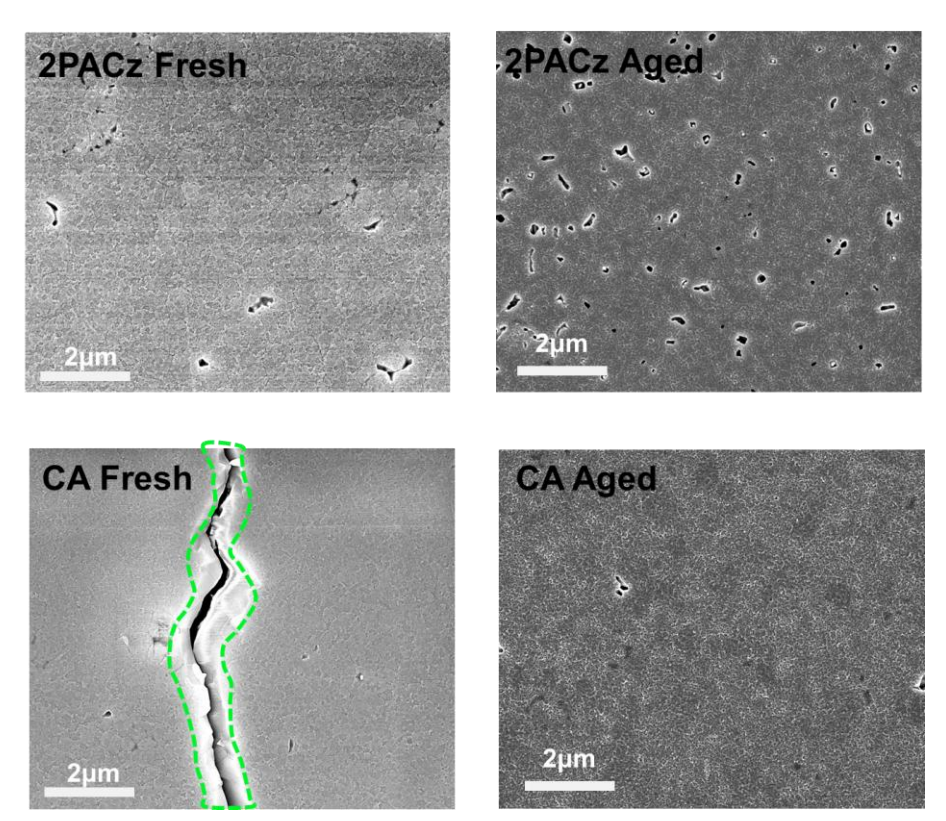


Figure 5.26 The SEM images of the perovskite buried interface before and after the aging test.

Evaluation of 2PACz/PYCA-3F based organic solar cells (OSCs)

To comprehensively assess the general applicability of our CA approach, based on ITO/HTL/PM1:PTQ10:m-BTP-phC6/PFN-Br-MA/Ag p-i-n configuration, we also fabricated a series of OSCs to compare the performance of PEDOT:PSS, 2PACz and CA.^{294,295} The optimization of PM1:PTQ10:BTP-phC6 ternary system weight ratio is presented in **Table 5.4**. Poor efficiency is observed in ITO-only devices, due to severe surface recombination. PEDOT:PSS can effectively promote the PCE to a near 19% level, contributed by decent V_{OC}, J_{SC} and FF. Alternated by 2PACz, the target device can achieve a 19.06% efficiency, generated by J_{SC} increase, but limited by the tiny reductions in V_{OC} and FF. Next, 19.51% PCE is realized by CA strategy, where SAM enabled J_{SC} promotion is kept, and V_{OC} × FF gets closer to PEDOT:PSS based devices. The mentioned materials are drawn in **Figure 5.27a**; J-V characteristics are in **Figure 5.27b**. Nevertheless, The PCE of OSCs is influenced by an amalgamation of both surface electronic and morphological properties. The elevated contact angle observed with CA substrates could lead to suboptimal surface coverage in comparison to the

hygroscopic PEDOT:PSS, thereby resulting in marginally reduced V_{OC} and FF. 296 To assure the measurement accuracy, the EQE spectra of them are also given in Figure **5.27c.** The integrated J_{SC} values guarantee that errors are within 5%. Besides, the spectra shape of PEDOT:PSS device is different from others, in consistence with its transmittance tuning effect. Furthermore, we compare the transmittance spectra and EQE spectra of devices, to assure there's not abnormally high EQE spectra in Figure **5.28**. In addition, the PCE average values are collected from at least 20 independent devices in Figure 5.27d and Figure 5.29, confirming the reliability and reproducibility and corresponding to the J-V results. Corresponding basic device physics characterizations are implemented upon all four groups of OSCs. The dark current curves of them are demonstrated in Figure 5.27e, in the form of semi-log coordination. The bare ITO based device presents a high dark current signal and a low turning point of applied voltage, indicating severe current leakage and poor diode ideality. Meanwhile, 2PACz enabled device exhibits a higher dark current than PEDOT:PSS based one, but CA modified anode can realize dark current nearly identical to that in PEDOT:PSS case. These results imply the CA-based OSCs can play similar role in realizing high FF as PEDOT:PSS does.

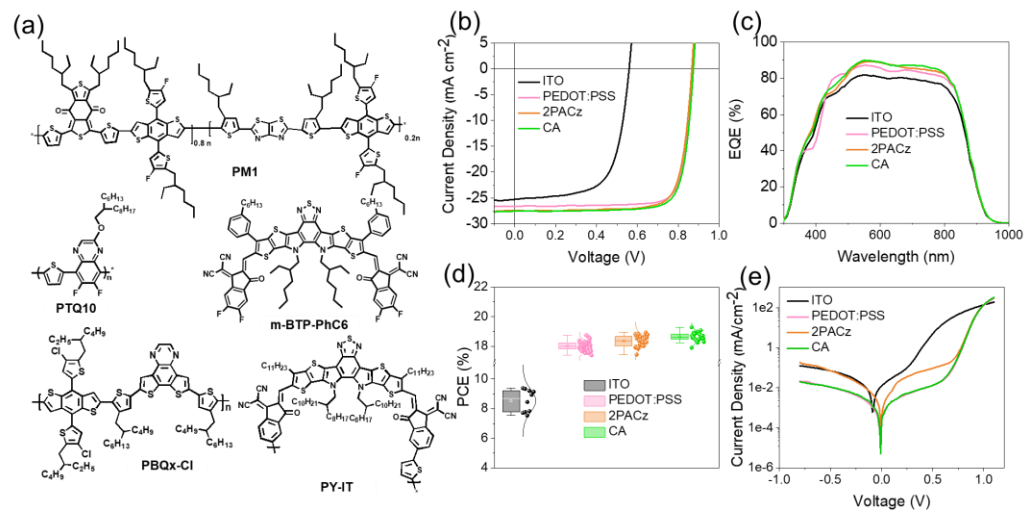


Figure 5.27 (a) Chemical structures of PM1, PTQ10, m-BTP-phC6, PBQx-Cl and PY-IT, which are materials used in spin-coating devices. (b) J-V characteristics and (c) EQE spectra of PM1:PTQ10:m-BTP-phC6 (weight ratio = 0.8:0.2:1.2) ternary blend devices based on bare ITO, PEDOT:PSS, 2PACz and CA. (d) Normal distribution of PCEs and (e) dark current curves of above

systems.

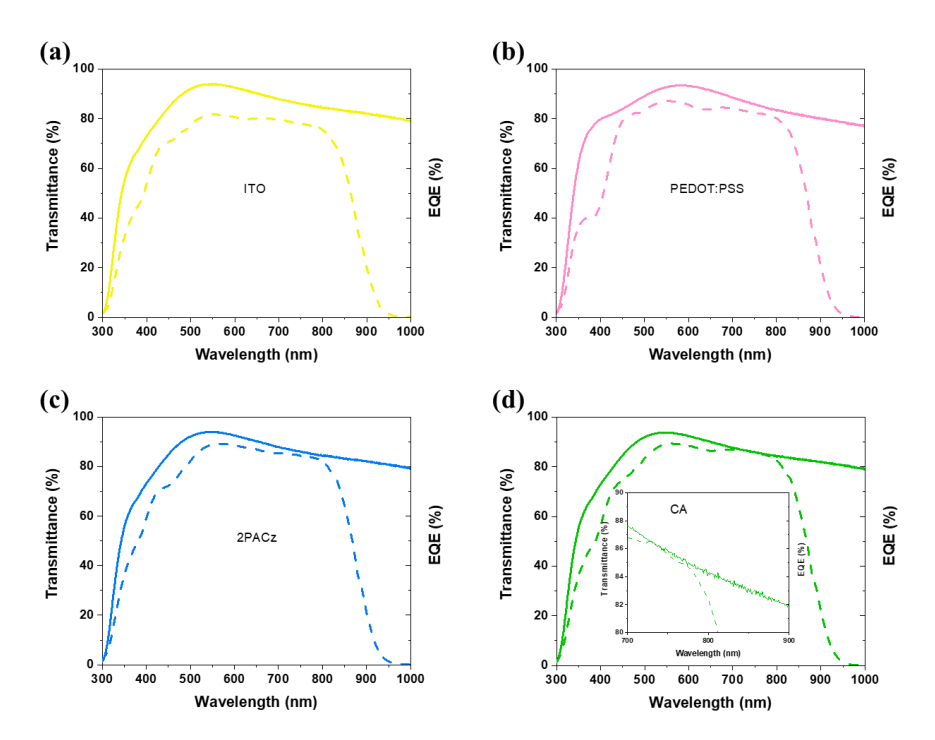


Figure 5.28 Transmittance spectra versus EQE spectra based on (a) ITO, (B) PEDOT:PSS, (c) 2PACz and, (d) CA.

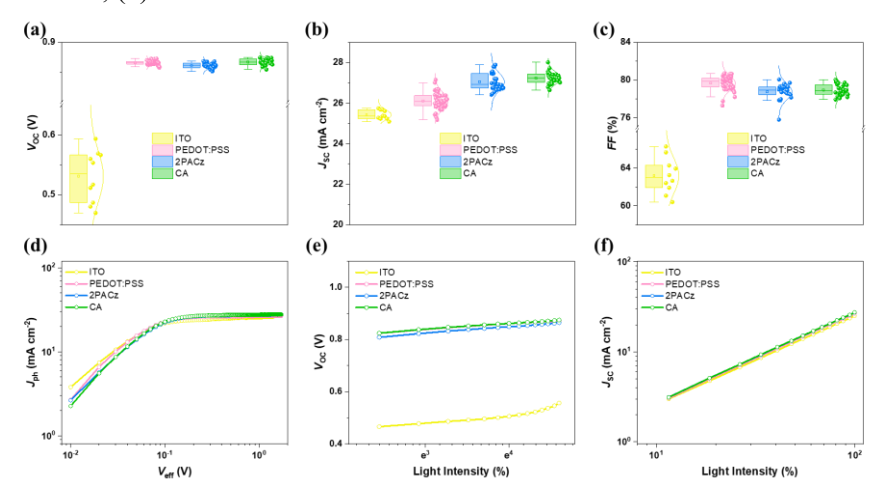


Figure 5.29 The normal distributional plot of (a) V_{OC} , (b) J_{SC} , and (c) FF for different anode-based PM1:PTQ10:m-BTP-phC6 devices. (d) dark current data derived photocurrent (J_{ph}) vs effective voltage (V_{eff}) relationships based on ITO, PEDOT:PSS, 2PACz and CA. Semi-log (e) and full-log (f) of the light intensity dependent V_{OC} and J_{SC} values relationships based on ITO, PEDOT:PSS, 2PACz and CA.

Table 5.4 Optimization of PM1:PTQ10:m-BTP-phC6 ternary blend ratio

PM1:PTQ10:m-BTP-phC6	$V_{OC}(V)$	J_{SC} (mA cm ⁻²)	FF (%)	PCE (%)
1:0:1.2	0.874	26.12	80.3	18.33
0.8:0.2:0.2	0.878	26.65	81.0	18.95
-	·	•	•	•

0.5:0.5:1.2	0.880	26.03	80.2	18.37	
0.2:0.8:0.8	0.881	25.77	80.0	18.14	
0:1.2:1.2	0.883	25.56	79.5	17.94	

Besides, dark current data derived photocurrent (J_{ph}) vs effective voltage (V_{eff}) relationships of them are illustrated in **Figure 5.28d**. The details for derived parameters and methods are elaborated in **Table 5.5**. These results support the best FF of PEDOT:PSS, and high J_{SC} of SAM. Moreover, the light intensity dependent V_{OC} and J_{SC} values are depicted in semi-log and full-log forms in **Figure 5.28e** and **Figure 5.28f**, respectively. As a result, the main difference among four groups is the competition between trap-assisted recombination and surface recombination, while the bimolecular one is found to be similar.²⁹⁷ Last, the operational stability of the devices under 1-sun illumination is tracked shown in **Figure 5.29a**. PEDOT:PSS based devices are observed a very fast degradation, within 500 hours. 2PACz is better and maintains c.a. 60% initial efficiency after nearly 1000-hour tracking. The hybrid CA based PM1:PTQ10:m-BTP-phC6 cells display two times longer lifetime compared with 2PACz, where 80% initial PCE is kept at >1000-hour point and 60% maintaining rate at c.a. 2000-hour tracking time in total.

Table 5.5 Dark current parameters of ITO, PEDOT:PSS. 2PACz and CA.

PM1:PTQ10:m-BTP-phC6	$J_{\rm sat}$ (mA cm ⁻²)	$J_{ m max}$ (mA cm ⁻²)	$\eta_{ m diss}$	$\eta_{ m coll}$
bare ITO	26.08	21.33	96.9%	81.8%
PEDOT:PSS	26.92	24.69	99.0%	91.7%
2PACz	27.88	25.48	98.5%	91.4%
CA	27.95	25.39	98.6%	90.8%

After the success in high-efficiency polymer donor vs small molecular acceptor type OSCs, CA strategy is also extended to some other organic systems: 1) non-halogenated solvent processed binary all-polymer solar cells (PBQx-Cl:PY-IT);^{27,298} 2) non-halogenated solvent-based room temperature open-air blade coating binary OSCs

(PM6:eC11).²⁹⁹ As given in **Figure 5.30b**, **5.30c** and **Table 5.6**, SAM (2PACz or CA) type modifications can promote the PCE in a similar way, and results in one of the highest efficiencies of hydrocarbon solvent processed binary all-polymer solar cells. In **Figure 5.30d** we provide a schematic diagram for open-air blade coating photoactive layer fabrication. Both PEDOT: PSS and SAM are air-stable, supporting the feasibility of this experiment. Similarly, the results in **Figures 5.30e**, **5.30f** and **Table 5.6** substantiate the general applicability of CA's efficiency enhancement effect. Meanwhile, 17.71% is one of the greatest PCEs for high-boiling point green solvent enabled blade coating OSCs.

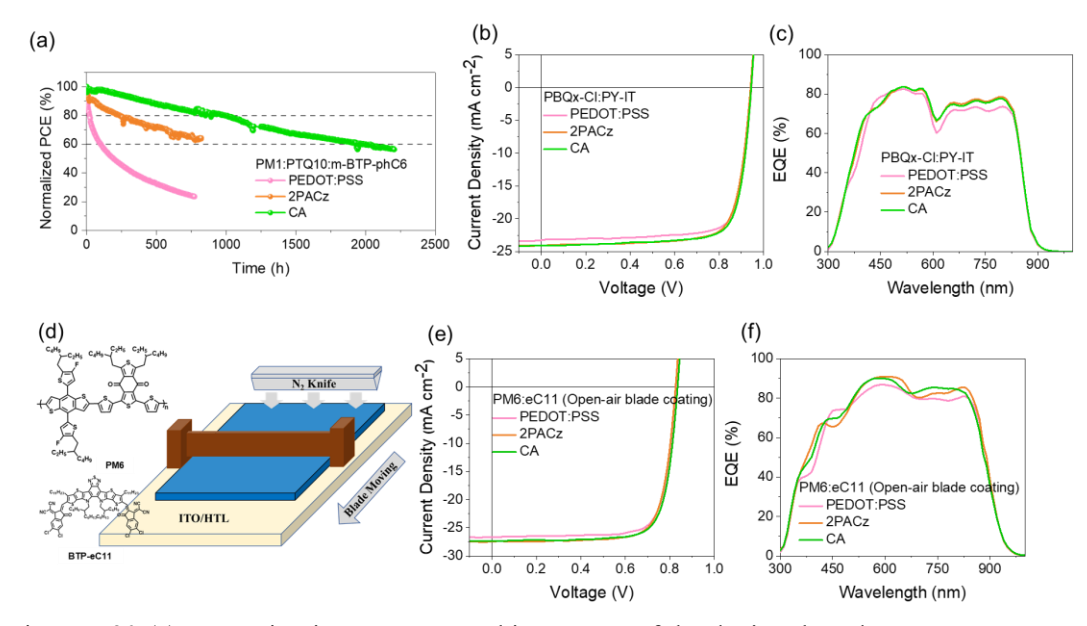


Figure 5.30 (a) Open-circuit type MPP tracking curves of the devices based on PEDOT:PSS, 2PACz and CA. (b) J-V characteristics and (c) EQE spectra all-polymer blend PBQx-Cl:PY-IT based devices of PEDOT:PSS, 2PACz and CA. (d) Schematic diagram of open-air blade coating device fabrication by using PM6:eC11 blend solution dissolved in ortho-xylene on PEDOT:PSS, 2PACz and CA surface. Relative (e) J-V characteristics and (f) EQE spectra.

Table 5.6 Photovoltaic parameters for OSCs based on different photo-active systems and anodes

Systems & Anodes	$V_{OC}(V)$	J_{SC} (mA cm ²) ^a	FF (%)	PCE (%) ^b
PM1:PTQ10:m-BTP-ph0	C6			
bare ITO	0.560	25.28/24.43	66.3	9.39 (8.35±0.75)
PEDOT:PSS	0.878	26.65/25.86	81.0	18.95 (18.51±0.30)
2PACz	0.870	27.46/26.32	79.8	19.06 (18.55±0.40)
CA	0.876	27.57/26.61	80.8	19.51 (19.14±0.29)
PBQx-Cl:PY-IT				

PEDOT:PSS	0.945	23.27/22.51	78.3	17.22	
2PACz	0.942	24.08/23.42	77.3	17.53	
CA	0.945	24.08/23.36	78.1	17.77	
PM6:eC11 (blade coating)					
PEDOT:PSS	0.830	26.64/26.15	77.8	17.20	
2PACz	0.826	27.45/27.02	77.1	17.46	
CA	0.835	27.37/26.91	77.5	17.71	

^aEQE integrated J_{SC} values are listed after the slashes. ^bThe brackets contain averages and standard errors of PCEs based on at least 20 devices.

5.4 Summary

In summary, our work demonstrated a co-adsorbed (CA) approach to rationally modify the SAM based HTL layer, yielding significantly improved stability and PCEs for both PSCs and OSCs of p-i-n configuration. Theoretical investigations reveal that PyCA-3F, through co-adsorbed strategy with 2PACz, facilitates the formation of a smooth surface and a favorable energy band alignment, thereby reducing the energy barrier between 2PACz and the perovskite/organic layers. Furthermore, the CA approach flattens the buried interface of perovskite layer, leading to an enhanced heterointerface energy and a defect-free interface feature, thus minimizing the energy loss therein. This improvement is effectively translated to promoted efficiency and operational stability of corresponding PSCs and OSCs. Our study demonstrates a successful case of a facile, rational, and effective modification on SAM-based HTL layer towards more efficient solution-processable processable PVs.

Chapter 6 Methoxy-Terminated Self-Assembled Monolayers Enable Highly Efficient Inverted Perovskite Solar Cells with Preferable Tridentate Bonding

6.1 Introduction

The global imperative to transition towards sustainable energy sources has driven extensive significant research interest into PSCs, owing to their remarkable PCE and low-cost manufacturing. Both conventional (n-i-p) and inverted (p-i-n) configurations of PSCs have achieved PCEs exceeding 26%, bringing them closer to the theoretical Shockley-Queisser limit. However, in the commonly used n-i-p structure, HTLs often suffer from poor conductivity and stability, which hinders the overall performance and long-term reliability of the devices.

In contrast, IPSCs with a p-i-n structure offer several advantages, such as low-temperature processing, compatibility with flexible substrates, and potential for tandem applications. In particular, SAMs have emerged as a promising HTL alternative for IPSCs, owing to their compact and tunable molecular structure, which enables higher transparency and conductivity, improved J_{SC} , and enhanced FF, which are critical parameters for achieving high-efficiency IPSCs. 302,303 Unlike traditional HTLs like PTAA, PEDOT:PSS and NiO_x, SAMs' tunable molecular structure and solvent-friendly nature, most can be dissolved in ethanol, reducing solvent toxicity and making them an environmentally friendly option. 29

Structurally, SAMs are composed of three key components: the anchoring group, the linker group, and the terminal group. The anchoring groups such as phosphonic acid (PA), carboxylic acid (CA), boric acid (BA) or trimethoxysilane (TMPS) to form robust bonds with transparent conductive oxide (TCO) substrates. 41,106,304,305 The terminal groups (e.g., triphenylamine, benzothiophene, phenothiazine or carbazole) determine the surface properties and interact with the active layers. 103,275,306,307 The linker groups, which anchor and terminal group, play a crucial role in dictating the overall molecular arrangement and electronic properties of the SAM. 308 Compared to conventional HTLs,

the molecular flexibility and tunability of SAMs offer significant advantages in optimizing the interface for efficient charge transport.³⁰⁹

Despite their promise, achieving high-density, well-ordered SAM layers remain a challenge. The formation of such layers is essential for minimizing interfacial energy losses, reducing recombination, and enhancing device stability.³¹⁰ One critical parameter that governs the performance of SAM-based devices is the molecular dipole moment, which influences charge transfer and work function (W_F) alignment at the SAM/substrate interface. Optimizing the molecular dipole orientation and maximizing molecular packing density are thus pivotal for improving charge extraction and minimizing energy losses in IPSCs. For instance, flexible alkyl linkers can allow excessive rotational freedom, compromising the structural integrity and stability of SAMs. In contrast, conjugated linkers provide greater molecular rigidity and stronger intermolecular interactions, improving π - π stacking and molecular ordering. For example, Zhu and coworkers developed the series SAMs with carboxylic acids containing conjugated linkers, which merits from enhanced charged transport and stabilized arylamine terminal groups to achieve stable and highly efficient IPSCs. 116 Similarly, Xu and coworkers incorporated a rigid phenylene linker to SAM (Me-PhpPACz), the strategy enhances the aspect ratio of molecular, improving dipole moment and facilitate charge transfer to achieve a high efficiency of 26.17% for IPSCs.311

Beyond alternative linkers, molecular engineering in terminal groups, such as the introduction of methyl groups, halide groups, phenylene groups has been shown to improve dipole moment, the terminal group directly contact with perovskite is beneficial for effective passivation at the interface, enhancing device performance. For example, Tang reported asymmetric SAM with the introduction of Br atom, which is expected to enlarge the dipole moment and deeper E_F. The resultant BCBBr-C4PA is suggested to reduce the energy loss caused by hole extraction at SAM/absorber interface, contributing to improved performance for BDBBr-C4PA based photovoltaics,

as well as perovskite/organic tandems.³¹² Similarly, Jen et. al developed π -expanded carbazoles as terminal group, the helical π -expansion is expected for enlarged dipole moment and improved π - π interaction between SAMs. The suitable energy level, favorable dipole moment and dense packing patterns enable optimal electronic properties of SAMs as well as IPSCs.^{102,313}

In this study, we systematically designed and synthesized two PA-based SAMs, namely PABDCB and MeO-PABDCB, to regulate the linker and terminal group. The concept was realized by modification 4PADCB in two aspects: 1) modulating the linker group from flexible alkyl chains to conjugated phenylene linkers (PABDCB). 2) further engineering of terminal group with methoxy group (MeO-PABDCB). Specifically, the relationship between the enhancement by the modification of linker and terminal group is investigated. The new SAM exhibited preferable tridentate bonding to ITO and showed enhanced conductivity, resulting in reduced tensile strain and traps states. Moreover, the most attractive optoelectronic properties with a champion PCE of 26.25% with improved stability were achieved by applying MeO-PABDCB as new SAMs in IPSCs.

6.2 Experimental Section

6.2.1 Materials

Cesium iodide (CsI), Methylamine hydrochloride (MACl), Formamidinium iodide (FAI), Lead bromide (PbBr₂) Methylamine hydrobromide (MABr) and Lead iodide (PbI₂) are purchased from Advanced Election Co., Ltd. C₆₀, and BCP are obtained from Xian Yurisolar Co., Ltd. 4PADCB and MeO-DCB were obtained from Zhengzhou Alfa Chemical Co., Ltd. Other chemicals and solvents were purchased from Sigma-Aldrich Co., Ltd. and used without further purification.

6.2.2 Device Fabrication

The ITO substrates were first washed by detergent and then sonicated with

deionized water, acetone and ethanol subsequently, and dried by N₂. The cleaned substrates were treated with UV-Ozone for 40 min. Afterward, SAMs (4PADCB, PABDCB and MeO-PABDCB, 0.3 mg/ml in EtOH) was spin-coated to the substrates at 4000 rpm for 30 s, followed by annealing at 100°C for 10 min. After cooling down to room temperature, perovskite solution, for perovskite precursor deposition, perovskite solution with a molar concentration of 1.6 M was prepared with a stoichiometric composition of Cs_{0.05}(FA_{0.98}MA_{0.02})_{0.95}Pb(I_{0.98}Br_{0.02})₃ by adding corresponding CsI, MACl, FAI, PbI₂ and MAPbBr₃ in to mixed DMF/DMSO solution (4:1). After virgous stirring for 2 h at room temperature, 50 μL precursor is dripped onto different SAM substrates and spin-coating at 1000 (200 ramp) for 10 s and 5000 rpm for 30 s (2000 ramp), while antisolvent (anisole) is dripped at the last 5 s. Then the perovskite films are immediately annealed at 110°C for 20 min. Then the films are transferred to evaporation chamber, C₆₀ and BCP are thermal evaporated successively for 37 nm (0.3 Å/s) and 8 nm (0.1 Å/s), respectively. The devices are completed with deposition 100 nm Cu.

6.2.3 Device Characterization

UV-vis absorption spectra were measured using a Shimadzu UV-2500 recording spectrophotometer. Atomic Force Microscope (AFM) and Kevin Probe Force Microscope (KPFM) measurements were obtained by using a Multimode 8-HR (AFM, Bruker) in a tapping mode. SEM-EDX were recorded by a Hitachi SU8230 scanning electron microscope (SEM) with an accelerating voltage of 5 kV. X-ray diffraction (XRD) analyses were conducted utilizing a Bruker ECO D8 diffractometer, equipped with Cu K α radiation (λ = 1.5418 Å). X-ray photoelectron spectroscopy (XPS) and ultraviolet photoelectron spectroscopy (UPS) measurements were performed using an ESCALAB XI electron analyzer (Thermo Fisher Scientific) with X-ray source (Al K α , hv = 1486.7 eV) and helium ionization source (He I α , hv = 21.22 eV). To mitigate the impact on the measured work function by the instrument, a bias voltage of -5 V was

systematically applied during the experiments. Steady-state photoluminescence (PL) and time-resolved photoluminescence (TRPL) transient decay spectra were acquired using an FLS920 PL spectrometer from Edinburgh Instruments. The ¹H NMR spectra were recorded on the Bruker AVANCE III 400 MHz spectrometer. And the mass spectrometry was conducted on triple quadrupole GC/MS (7890B GC & 5977A Series GC/MSD, Agilent).

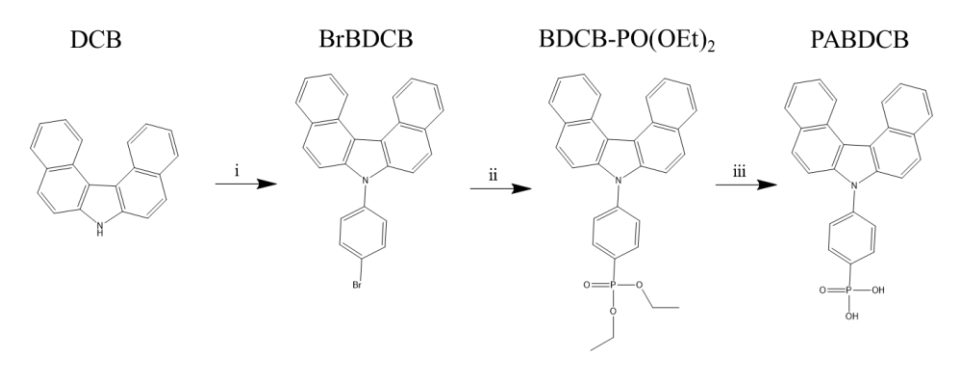
The J-V characteristics of the devices were tested using a Keysight B2901A Source Meter inside a glove box under AM 1.5G illumination (100 mW/cm²) with an Enlitech SS-F7-3A solar simulator. The contact area of the device was 0.086 cm², while the illuminated area during measurements was 0.084 cm², defined by a non-reflective metal mask. The J-V scans were conducted in reverse (from 1.30 V to -0.02 V) followed by forward scanning (from -0.02 V to 1.30 V) with a voltage increment of 0.02 V and a delay of 10 ms per step. The EQE spectrum was obtained using the QE-R3011 Measurement System (Enlitech Co., Ltd.) in AC mode, with light intensity at each wavelength calibrated using a standard monocrystalline silicon photovoltaic cell. The operational stability of unencapsulated devices was assessed using a commercial multichannel stability testing system (Wuhan 91PVKSolar) under maximum power point (MPP) tracking mode in a nitrogen environment. Illumination was provided by a white-light LED simulating 1-sun conditions, with intensity adjusted to match the J_{SC} observed in standard AM 1.5G solar simulator measurements at 100 mW/cm².

The ground-state geometry optimization was calculated using the density functional theory (DFT) method at the B3LYP (d,p) level of theory in ethanol solvent based on density (SMD) implicit solvation model with the Gaussian 16 program package. The optimized structures were found to be stable. Theoretical adsorption mode between ITO and SAMs were carried out based on periodic DFT using a generalized gradient approximation within the Perdew-Burke-Ernzerh (PBE) of exchange correction functional. 4PADCB, PABDCB and MeO-PABDCB molecules were adsorbed on the ITO surface. The SAMs on perovskite surface was constructed

similarly. The wave functions were constructed from the expansion of plane waves with an energy cutoff of 450 eV. Gamma centered k points of $3\times3\times1$ have been used for geometry optimization. The consistency tolerances for geometry optimization are set as 1.0×10^{-4} eV/atom for total energy and 0.05 eV/Å for force, respectively. To avoid the interaction between the two surfaces, a large vacuum gap of 15 Å has been selected in the periodically repeated slabs. The structural stability was checked with frequency calculation.

The synthetic routes are illustrated in Scheme 1 and Scheme 2.

Scheme S1: The synthetic route of PABDCB ((4-(7H-dibenzo[c,g]carbazol-7-yl)phenyl)phosphonic acid).



i: 1,4-dibromobenzene, K₂CO₃, CuI, DMF, 165°C

ii: diethyl phosphite, Pd(pph₃)₄, triethylamine, 1,4-dioxane, 110°C

iii: TMSBr, DCM, RT

Figure 6.1 The synthetic route of PABDCB.

BrBDCB (7-(4-bromophenyl)-7H-dibenzo[c,g]carbazole): To a 100 mL round-bottom flask, DCB (1.12 g, 4.2 mmol) was introduced with 20 mL of DMF. 1,4-dibromobenzene (3.76 g, 16.0 mmol), K_2CO_3 (1.6 g, 11.6 mol) and CuI (0.4 g, 2.1 mmol) were added subsequently. The resultant mixture was then maintained under a nitrogen atmosphere at 160 °C over 24 h. Then the mixture was extracted with DCM, dried by MgSO₄, and concentrated under vacuum. The crude product was purification via chromatography on silica gel using a (eluent PE/DCM=4:1) to afford BrBDCB white solid (1.1 g, yield 62%). ¹H NMR (400 MHz, Chloroform-d) δ 9.24 (d, J = 8.5 Hz, 2H),

8.05 (dd, J = 8.1, 1.4 Hz, 2H), 7.85 (d, J = 8.8 Hz, 2H), 7.83 – 7.76 (m, 2H), 7.71 (ddd, J = 8.4, 6.8, 1.4 Hz, 2H), 7.59 – 7.51 (m, 4H), 7.51 – 7.44 (m, 2H).

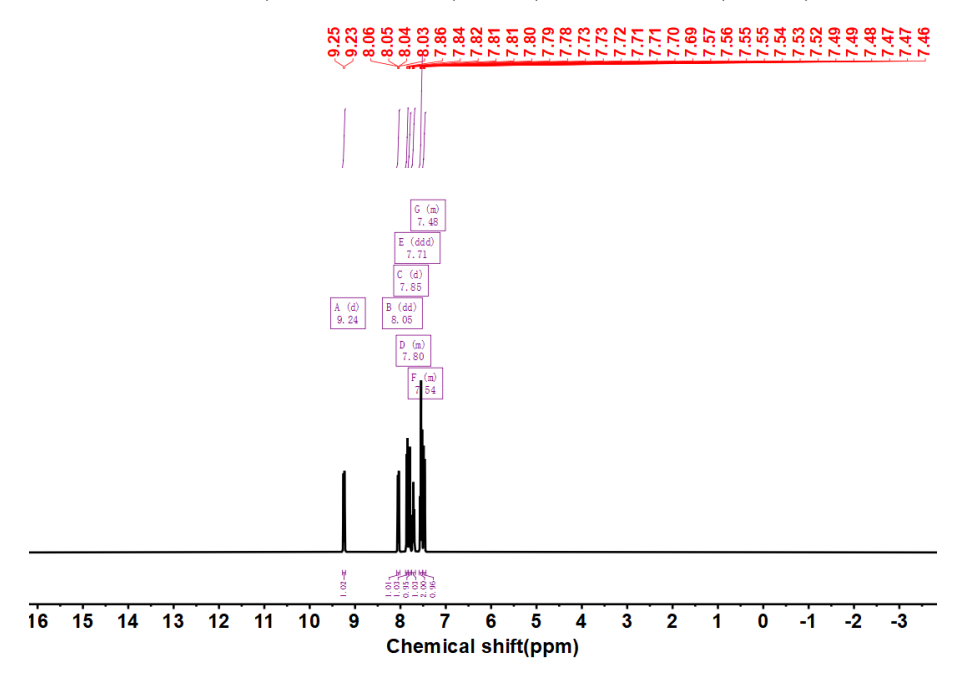


Figure 6.2 ¹H NMR results of BrBDCB (7-(4-bromophenyl)-7H-dibenzo[c,g]carbazole).

BDCB-PO(OEt)2 (diethyl (4-(7H-dibenzo[c,g]carbazol-7-yl)phenyl)phosphonate): A mixture of BrBDCB (1 g, 2.37 mmol), diethyl phosphite (0.513 g, 3.71 mmol), Pd(pph₃)₄ (140 mg, 0.121 mmol) and 5 ml triethylamine in 30 mL of 1,4-dioxane was stirred at 110 °C for 24 hours under nitrogen atmosphere. The resulting mixture was extracted with DCM, dried over MgSO₄, and concentrated under vacuum. The crude product was purified via chromatography on silica gel using DCM/EA (8:1) as the eluent to get white solid (0.65 g, yield 57%). ¹H NMR (400 MHz, Chloroform-d) δ 9.24 (d, J = 8.5 Hz, 2H), 8.12 (dd, J = 13.1, 8.2 Hz, 2H), 8.05 (dd, J = 8.1, 1.4 Hz, 2H), 7.86 (d, J = 8.9 Hz, 2H), 7.77 – 7.67 (m, 5H), 7.63 – 7.51 (m, 4H), 4.36 – 4.16 (m, 4H), 1.43 (t, J = 7.1 Hz, 6H).

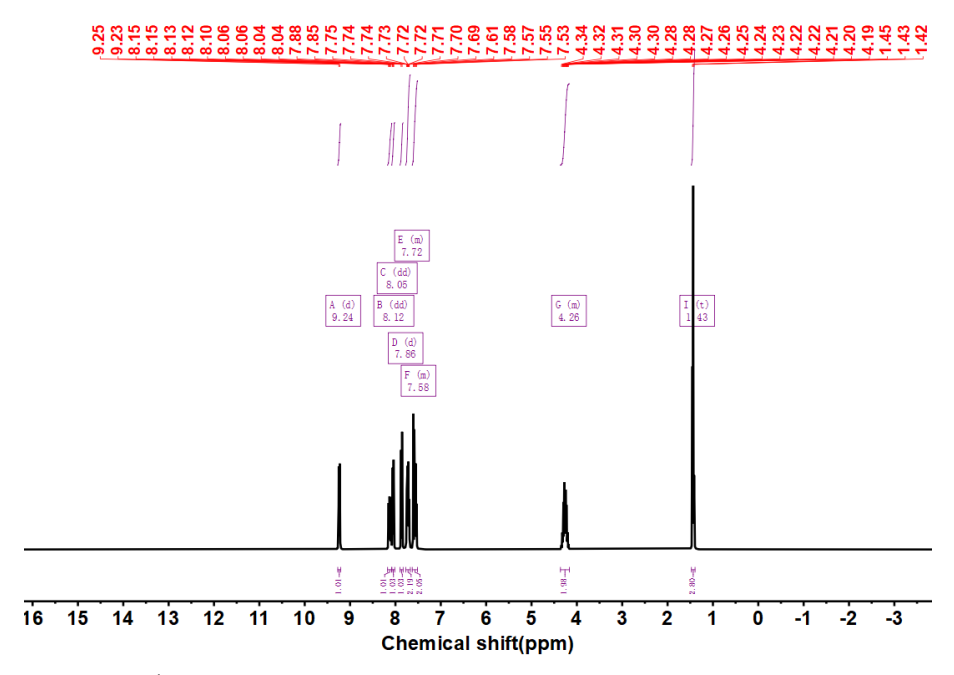


Figure 6.3 ¹H NMR results of BDCB-PO(OEt)₂ (diethyl (4-(7H-dibenzo[c,g]carbazol-7-yl)phenyl)phosphonate).

PABDCB ((4-(7H-dibenzo[c,g]carbazol-7-yl)phenyl)phosphonic acid): BDCB-PO(OEt)₂ (0.3 g, 0.63 mmol) was dissolved in 15 mL DCM under nitrogen atmosphere. TMSBr (1.29 ml, 9.8 mmol) was added dropwise, and the reaction mixture was allowed to react overnight. Upon completion of the reaction, the DCM was removed under reduced pressure, and 5 mL of methanol was added subsequently. The resulting solution was stirred at room temperature for 2 hours. Distilled water (30 mL) was then added dropwise until the solution became opaque. The resulting precipitate was filtered off and washed with water to yield a white solid. (0.22 g, yield 80%). 1 H NMR (400 MHz, DMSO- d_6) δ 9.22 (d, J = 8.5 Hz, 2H), 8.25 (dd, J = 8.2, 1.3 Hz, 2H), 8.19 – 8.09 (m, 2H), 8.09 (d, J = 9.0 Hz, 2H), 7.95 – 7.83 (m, 4H), 7.75 – 7.64 (m, 4H). HR-MS (GC-MS): calcd. for $C_{26}H_{19}NO_{3}P$ [M] $^{+}$ 424.10971; Found: 423.10976.

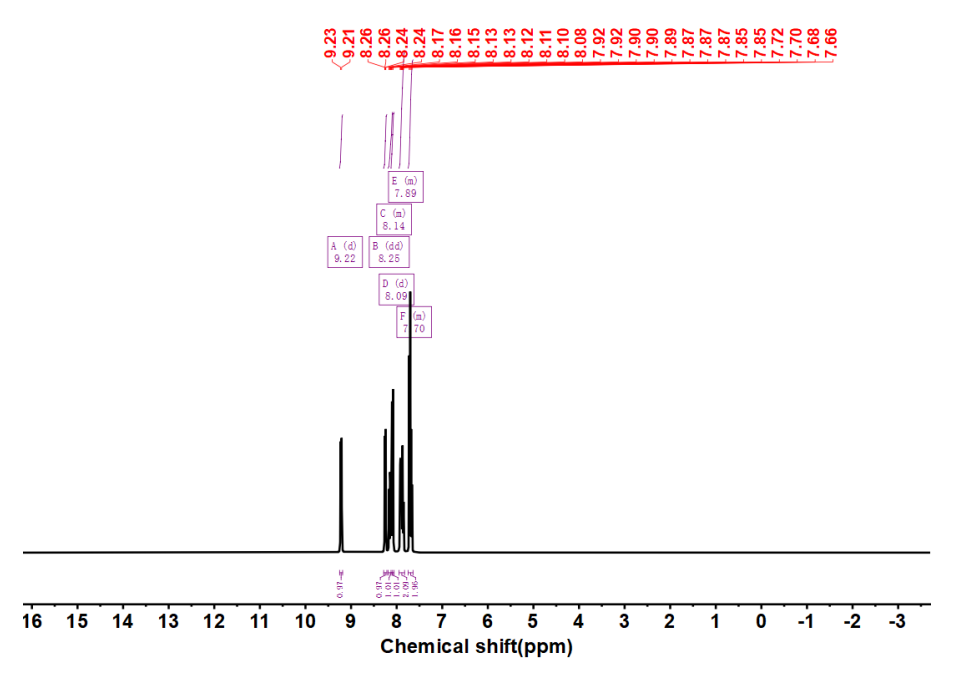


Figure 6.4 ¹H NMR results of PABDCB (4-(7H-dibenzo[c,g]carbazol-7-yl)phenyl)phosphonic acid).

Scheme S2: The synthetic route of MeO-PABDCB ((4-(3,11-dimethoxy-7H-dibenzo[c,g]carbazol-7-yl)phenyl)phosphonic acid).

MeO-DCB MeO-BrbDCB MeO-BDCB-PO(OEt)₂ MeO-PABDCB

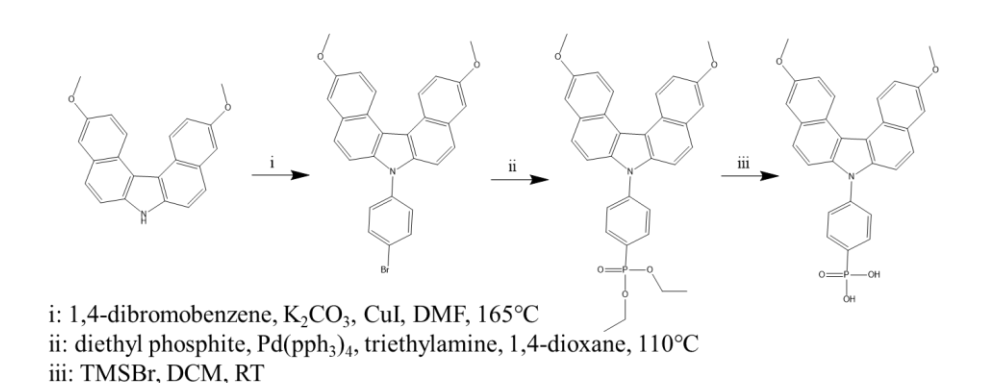


Figure 6.5 The synthetic route of MeO-PABDCB.

MeO-BrBDCB

(7-(4-bromophenyl)-3,11-dimethoxy-7H-

dibenzo[c,g]carbazole): To a 100 mL round-bottom flask, MeO-DCB (0.5 g 1.53 mmol) was introduced with 12 mL of DMF. 1,4-dibromobenzene (1.44 g, 6.11 mmol), K₂CO₃ (0.8 g, 5.8 mol) and CuI (0.2 g, 1.05 mmol) were added subsequently. The resultant mixture was then maintained under a nitrogen atmosphere at 160 °C over 24 h. Then

the mixture was extracted with DCM, dried by MgSO₄, and concentrated under vacuum. The crude product was purification via chromatography on silica gel using a (eluent PE/DCM=4:1) to afford MeO-BrBDCB white solid (0.43 g, yield 58%). ¹H NMR (400 MHz, Chloroform-d) δ 9.10 (d, J = 8.9 Hz, 2H), 7.82 – 7.71 (m, 4H), 7.55 – 7.42 (m, 4H), 7.42 – 7.32 (m, 4H), 4.00 (s, 6H).

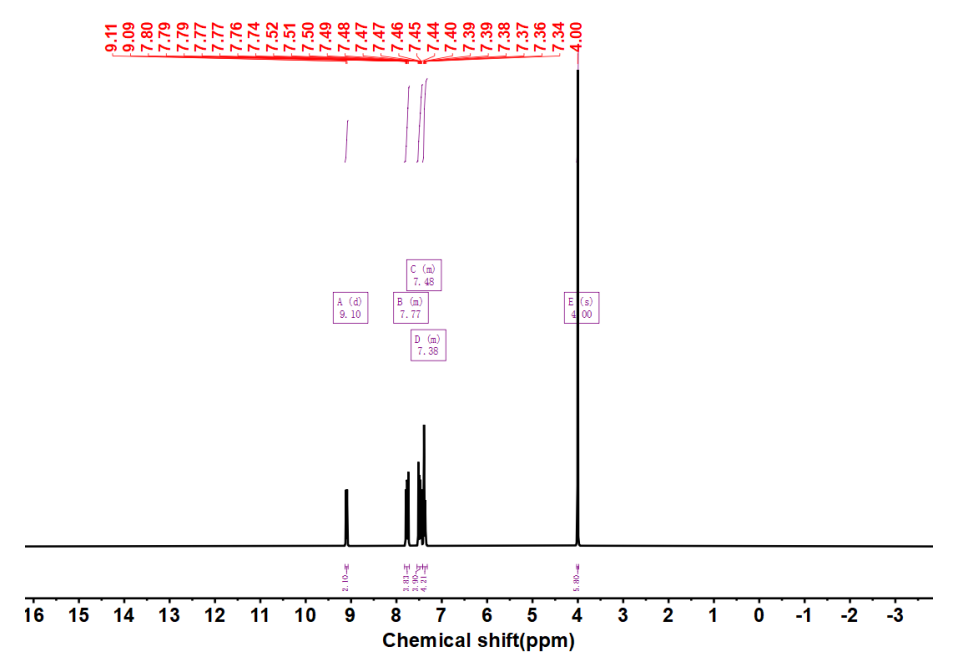


Figure 6.6 ¹H NMR results of MeO-BrBDCB (7-(4-bromophenyl)-3,11-dimethoxy-7H-dibenzo[c,g]carbazole).

MeO-BDCB-PO(OEt)² (diethyl (4-(3,11-dimethoxy-7H-dibenzo[c,g]carbazol-7-yl)phenyl)phosphonate): A mixture of MeO-BrBDCB (0.4 g, 0.829 mmol), diethyl phosphite (0.5 g, 3.62 mmol), Pd(pph₃)⁴ (70 mg, 0.06 mmol) and 3 ml triethylamine in 15 mL of 1,4-dioxane was stirred at 110 °C for 24 hours under nitrogen atmosphere. The resulting mixture was extracted with DCM, dried over MgSO₄, and concentrated under vacuum. The crude product was purified via chromatography on silica gel using DCM/EA (10:1) as the eluent to get white solid (0.30 g, yield 58%). ¹H NMR (400 MHz, Chloroform-*d*) δ 9.09 (d, J = 8.9 Hz, 2H), 8.15 – 8.06 (m, 2H), 7.79 – 7.69 (m, 4H), 7.58 (d, J = 8.8 Hz, 2H), 7.42 – 7.34 (m, 4H), 4.35 – 4.16 (m, 4H), 4.01 (s, 6H), 1.43 (t, J = 7.1 Hz, 6H).

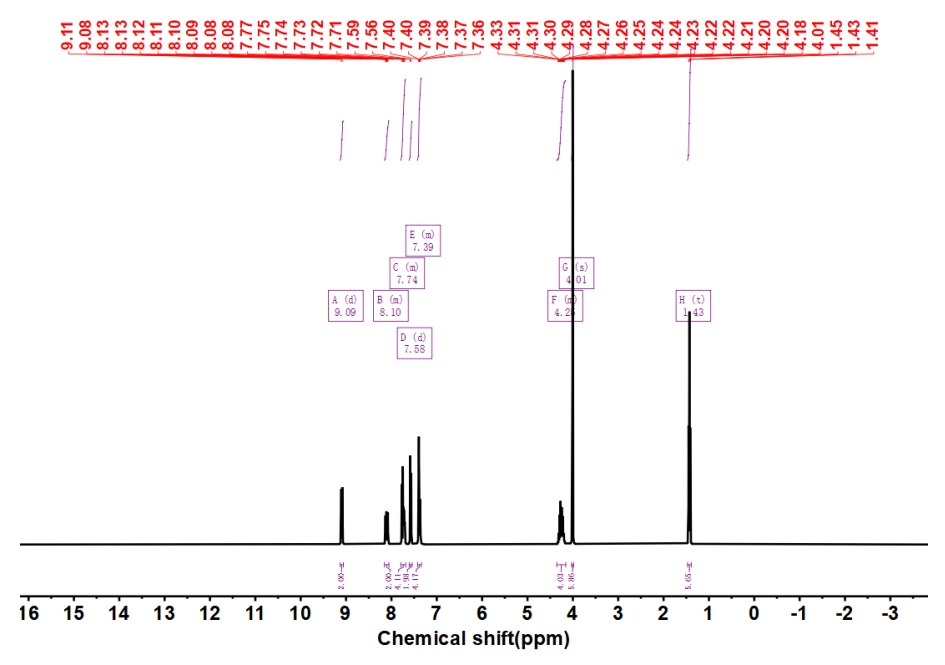


Figure 6.7 ¹H NMR results of MeO-BDCB-PO(OEt)₂ (diethyl (4-(3,11-dimethoxy-7H-dibenzo[c,g]carbazol-7-yl)phenyl)phosphonate)).

MeO-PABDCB ((4-(3,11-dimethoxy-7H-dibenzo[c,g]carbazol-7-

yl)phenyl)phosphonic acid): MeO-BDCB-PO(OEt)₂ (0.18 g, 0.333 mmol) was dissolved in 10 mL DCM under nitrogen atmosphere. TMSBr (1 ml, 7.58 mmol) was added dropwise, and the reaction mixture was allowed to react overnight. Upon completion of the reaction, the DCM was removed under reduced pressure, and 5 mL of methanol was added subsequently. The resulting solution was stirred at room temperature for 2 hours. Distilled water (30 mL) was then added dropwise until the solution became opaque. The resulting precipitate was filtered off and washed with water to yield a white solid. (0.14 g, yield 83%). ¹H NMR (400 MHz, DMSO- d_6) δ 8.98 (d, J = 9.2 Hz, 2H), 8.07 – 7.98 (m, 2H), 7.89 (d, J = 9.0 Hz, 2H), 7.78 (dd, J = 8.3, 2.9 Hz, 2H), 7.62 – 7.55 (m, 4H), 7.42 (dd, J = 9.2, 2.7 Hz, 2H), 3.95 (s, 6H). HR-MS (GC-MS): calcd. for C₂₉H₂₃NO₅P [M]⁺ 484.13084; Found: 484.13118.

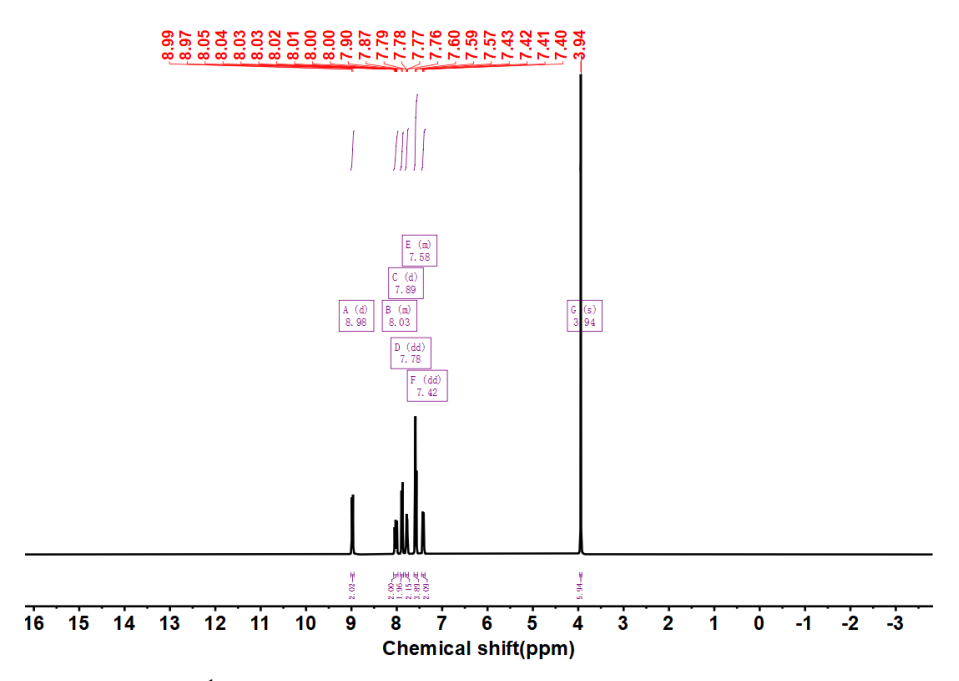


Figure 6.8 ¹H NMR results of MeO-PABDCB (4-(3,11-dimethoxy-7H-dibenzo[c,g]carbazol-7-yl)phenyl)phosphonic acid).

6.3 Results and Discussion

To examine the molecular properties, the molecular structures of the SAMs (4PADCB, PABDCB, and MeO-PABDCB) are illustrated in **Figure 6.9a**. All of these three SAMs show similar molecular structure with phosphonic acid (PA) as anchoring group and 7H-dibenzocarbazole (DCB) as core of terminal group. The DCB backbone is widely reported in previous work with favorable uniformity and suppressed self-aggregation for SAMs. ¹⁰³ In the case of PABDCB, the flexible alkyl linker of 4PADCB is replaced by a rigid phenyl group, which is designed to enhance π – π stacking and promote better molecular ordering during self-assembly. ³¹⁴ The modification is further innovated by the introduction of a hydrophilic methoxy group in MeO-PABDCB, the methoxy group can act as Lewis base that has been shown in previous studies to improve device performance. ⁹⁶ Hence the application of fully-benzene rings skeleton in both PABDCB and MeO-PABDCB, rather than the existence of alkyl chains found in 4PADCB, further strengthens the molecular rigidity, which in turn is expected to mitigate structural disorganization, thereby enhancing device stability. ³¹⁴

The synthetic routes for PABDCB and MeO-PABDCB are presented in Scheme

S1-S2 and Figure S1-S2, and the corresponding information of intermediates and final products were analyzed by nuclear magnetic resonance (NMR) spectroscopy and provided in Figure S3-S8. To gain deeper insight into the electronic properties of the SAMs, the optimal molecular structure was calculated by density functional theory (DFT) with B3LYP/6-31G package. Figure 1b revealed the calculated electrostatic surface potential (ESP) of the molecules with distinct positive-charge (red) and negative-charge (blue) regions. Modification of the linker results in an increased negative charge on the phenylene moiety, indicating effective electron delocalization across the incorporated phenyl linker and the expanded π -conjugated core upon linker modification.³¹⁵ Notably, the terminal group in MeO-PABDCB exhibits a strong positive charge on its surface, attributed to the unpaired electron on the oxygen atom in the methoxy group, which is conducive to enhance the intermolecular interaction at the perovskite/SAM interface. We further investigated the role of linker and terminal group in modulating dipole moments, which in turn directly influence charge transfer dynamics at interfaces. The calculated dipole moments of 4PADCB, PABDCB, and MeO-PABDCB were 2.63 D, 1.66 D, and 5.32 D, respectively, indicating significant variations in molecular polarity (Figure 6.10). These findings suggest that the properties of linker and terminal groups play a crucial role in governing interfacial charge transfer behavior, with higher dipole moments potentially enhancing charge transfer efficiency.³¹⁶ The introduction of phenyl groups may enhance the symmetry and cause a slight decrease in dipole moment for PABDCB. In contrast, the introducing of methoxy group on terminal group significantly enlarges the dipole moment. This significant increase in dipole moment for MeO-PABDCB is anticipated to facilitate a downshift in the work function (W_F) of the ITO substrate, thereby improving hole extraction at the ITO/SAM interface, which will be discussed later. 105

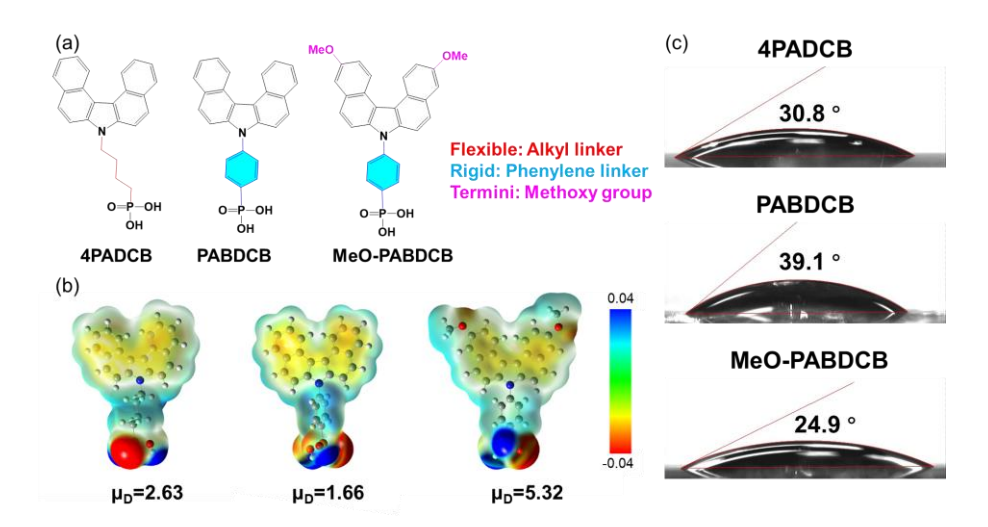


Figure 6.9 (a) chemical structures of 4PADCB, PABDCB and MeO-PABDCB. (b) electrostatic surface potential (ESP) of 4PADCB, PABDCB and MeO-PABDCB. (c) contact angles on 4PADCB, PABDCB and MeO-PABDCB substrates of perovskite precursor.

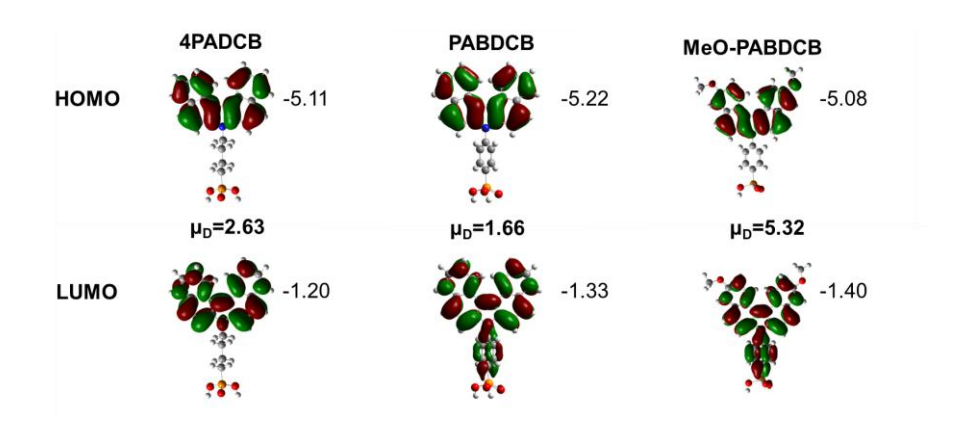


Figure 6.10 The calculated HOMO and LUMO of 4PADCB, PABDCB and MeO-PABDCB.

Thermogravimetric analysis (TGA) was employed to assess the intrinsic thermal stability of three SAMs. As illustrated in **Figure 6.11**, MeO-PABDCB exhibited a markedly higher thermal decomposition temperature (450 °C) compared to 4PADCB (342 °C) and PABDCB (317 °C), indicating its potential for enhanced stability in IPSCs when subjected to operational and thermal stimuli, in accordance with previous report.³¹⁴ In addition, to assess the wettability of the SAMs, contact angle measurements were performed and shown in **Figure 6.9c**. The perovskite precursor showed a relatively low contact angle for all substrates, where 4PADCB, PABDCB and MeO-PABDCB presented angles of 30.8°, 39.1° and 24.9°, respectively. Similar results can

be found in water contact angles (**Figure 6.12**). Among them, MeO-PABDCB exhibited significantly lower contact angles for both perovskite precursor and water solutions compared to 4PADCB and PABDCB, indicating superior wettability. This enhancement in wettability is likely attributed to the hydrophilic nature of the methoxy group in MeO-PABDCB, which promotes more uniform and compact SAM formation. The improvement in SAMs layer quality is crucial for the subsequent deposition of the perovskite layer, as it directly affects the morphology and performance of IPSCs.

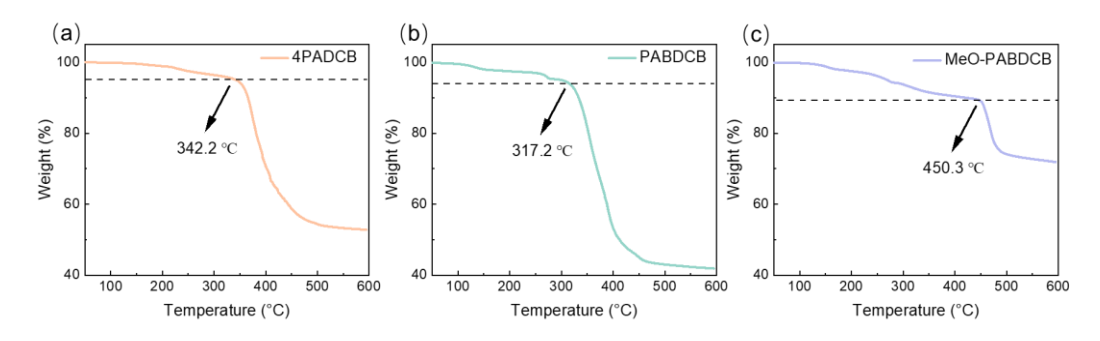


Figure 6.11. Thermogravimetric analysis results of 4PADCB, PABDCB and MeO-PABDCB.



Figure 6.12 Water contact angle of 4PADCB, PABDCB and MeO-PABDCB.

To investigate the binding behavior between SAMs and ITO, X-ray photoelectron spectroscopy (XPS) measurements were conducted (**Figur 6.13**). As shown in **Figure 6.15a** of the C (1s) spectra, the peak could be attributed to C-C peaks, moreover, the peak at 286.5 eV in MeO-PABDCB could be attributed to methoxy group. ³¹⁷ In addition, it is widely reported that there are two main typical binding modes for phosphonic acid on ITO, including bidentate and tridentate modes. ³¹⁸ The distinctive O (1s) peaks around 531.5 eV and 532.3 eV are typical tridentate binding mode and bidentate modes, which originated from the signals of P-O-In and P=O-In, and all the SAMs show both tridentate and bidentate binding modes (**Figure 6.15b**). ^{319,320} In 4PADCB film, a

comparable intensity of tridentate and bidentate bonds, However, in PABDCB and MeO-PABDCB films, an overwhelming majority of tridentate binding mode than bidentate mode can be found, demonstrating a preferable tridentate binding behavior between the rigid linker-based SAMs and ITO. The more favorable tridentate binding mode than bidentate predominated binding modes between SAM and ITO is expected to construct more robust and stable interfaces. To further examine the surface coverage of different SAMs on ITO, semi-quantitative elemental analysis was performed using high-resolution X-ray photoelectron spectroscopy (HR-XPS) to evaluate the molecular density of the substrates. The surface coverage was quantified by the ratio of P from the SAMs to In from the ITO layer. As summarized in Table 6.1, the P/In ratios were 0.022, 0.025, and 0.026 for substrates modified with 4PADCB, PABDCB, and MeO-PABDCB, respectively. These results demonstrated a clear enhancement in surface coverage for the MeO-PABDCB-modified substrates. This improved surface coverage, along with the reduced contact angle, is crucial for enhancing the quality of the deposited perovskite films.

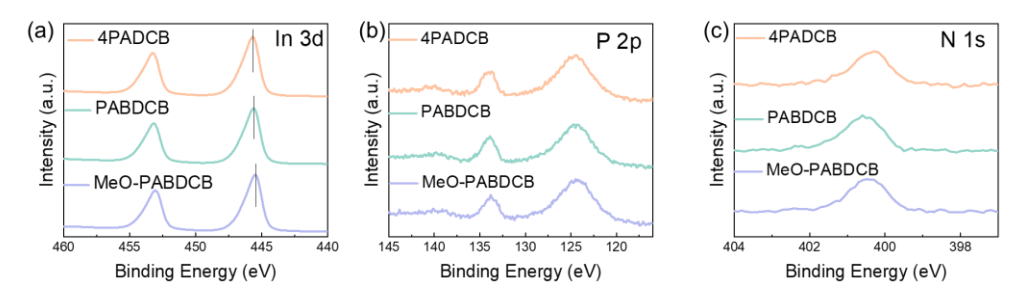


Figure 6.13 XPS spectra of In 3d, P 2p and N 1s of 4PADCB, PABDCB and MeO-PABDCB.

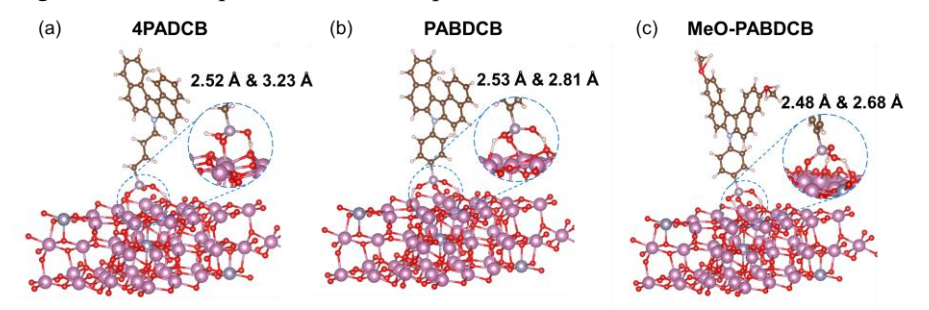


Figure 6.14 Adsorbing conditions of 4PADCB, PABDCB and MeO-PABDCB on ITO.

Table 6.1 The fitted XPS area of P 2p and In 3d.

Samples	P 2p Area	In $3d_{3/2}$ Area	P/In ratios
4PADCB	10972.60	497728.27	0.022

PABDCB	11484.74	459907.24	0.025	
MeO-PABDCB	12264.55	464639.85	0.026	

To gain deeper insight into interfacial properties, the adsorption modes of these SAMs on ITO were investigated by DFT. As shown in **Figure 6.14**, all SAMs showed similar adsorption structure with phosphonic acid-anchored on ITO. As previously described, two common binding modes at the phosphonic acid-ITO interface are bidentate and tridentate. The bidentate mode involves a strong P-O-Sn covalent bond along with a hydrogen bond, while the tridentate mode features a P-O-Sn covalent bond and two hydrogen bonds. Notably, the bidentate binding mode is observed between 4PADCB and ITO. In contrast, phenyl-based PABDCB and MeO-PABDCB exhibit enhanced tridentate binding, with additional hydrogen bond likely resulting from the hetero-condensation of the hydroxy group, demonstrating a more preferable tridentate binding mode in PABDCB and MeO-PABDCB based substrates. Additionally, the hydrogen bonding for MeO-PABDCB, showing the bond length of 2.48 Å and 2.68 Å, giving a higher bonding property than those of 4PADCB (2.52 Å and 3.23 Å) and PABDCB (2.52 Å and 2.81 Å). The smaller bond length may result from the stronger tridentate binding properties of PABDCB and MeO-PABDCB.

To better elucidate the behavior of SAMs with different linkers on ITO, **Figure 6.15d** illustrates the evolution of binding modes. Flexible alkyl chain-based SAMs, exemplified by 4PADCB, exhibit a disordered arrangement characterized by a mix of bidentate and tridentate binding modes. In contrast, SAMs with rigid phenyl linkers preferentially adopt a tridentate binding mode, which promotes a more compact and ordered substrate on ITO. Consequently, the predominantly tridentate binding mode and strong bonding properties of SAMs with phenyl linker enable the formation of a compact, robust substrate that supports the growth of high-quality perovskite films.³²⁴

The surface energy of ITO/SAM plays a pivotal role in determining the PCE of IPSCs. To gain more insight into the SAM/ITO interface on the effect of W_F, Kevin

probe force microscopy (KPFM) measurement was conducted. As shown in Figure **6.16**, a lower contact potential difference (CPD) with reduced surface roughness can be obtained for MeO-PABDCB. Moreover, the more centered CPD distribution with lower CPD value demonstrates a substantial improvement in the uniformity and deeper E_F properties for MeO-PABDCB SAM layer (Figure 6.17).325 In fact, Ultraviolet Photoelectron Spectroscopy (UPS) spectroscopy confirmed the energy band levels of SAM-modified ITO substrates, as shown in Figure 6.18, the 4PADCB demonstrated a W_F of 4.82 eV, after modulating linker into PABDCB, the W_F upshifted to 4.75 eV, particularly for MeO-PABDCB, which exhibits the deepest W_F value of 4.91 eV with methoxy terminal group, in correspondence with the KPFM results. 106 To further elucidate the band alignment at ITO/SAMs/perovskite interfaces, as shown in Figure 6.15e to 6.15g, the ITO/PABDCB/perovskite prefers a downward bending of the perovskite energy band, creating a substantial barrier to hole extraction while promoting electron transfer and causing energy loss at the interface. Conversely, the ITO/4PADCB/perovskite interface displays an upward band bending with a moderate energy offset of 0.60 eV, enabling efficient hole extraction while effectively blocking electron transport. The ITO/MeO-PABDCB/perovskite interface also exhibits upward band bending, but with a slightly smaller offset of 0.58 eV, attributed to its deeper Fermi level. This deeper work function reduces the interfacial energy mismatch, enhancing hole extraction and contributing to increased V_{OC} and FF in IPSCs. The increased W_F and uniform surface of SAM layer, therefore, could directly correlate with the superior photovoltaic performance in IPSCs.

To further assess the hole transport properties of 4PADCB, PABDCB, and MeO-PABDCB, hole-only devices with an ITO/SAM/PTAA/Au architecture were employed, utilizing the space-charge-limited current (SCLC) technique to quantify hole mobility (**Figure 6.15c**). MeO-PABDCB-based devices exhibited the highest hole mobility among the three SAMs, while 4PADCB and PABDCB showed comparatively lower values. Similar trends were observed in single-carrier devices with an

ITO/SAM/Au configuration (**Figure 6.19**), corroborating the superior hole mobility of MeO-PABDCB.³²⁷ This enhanced hole mobility is attributed to the favorable molecular structure of MeO-PABDCB, which facilitates efficient charge transport through reduced molecular disorder and improved interfacial alignment.

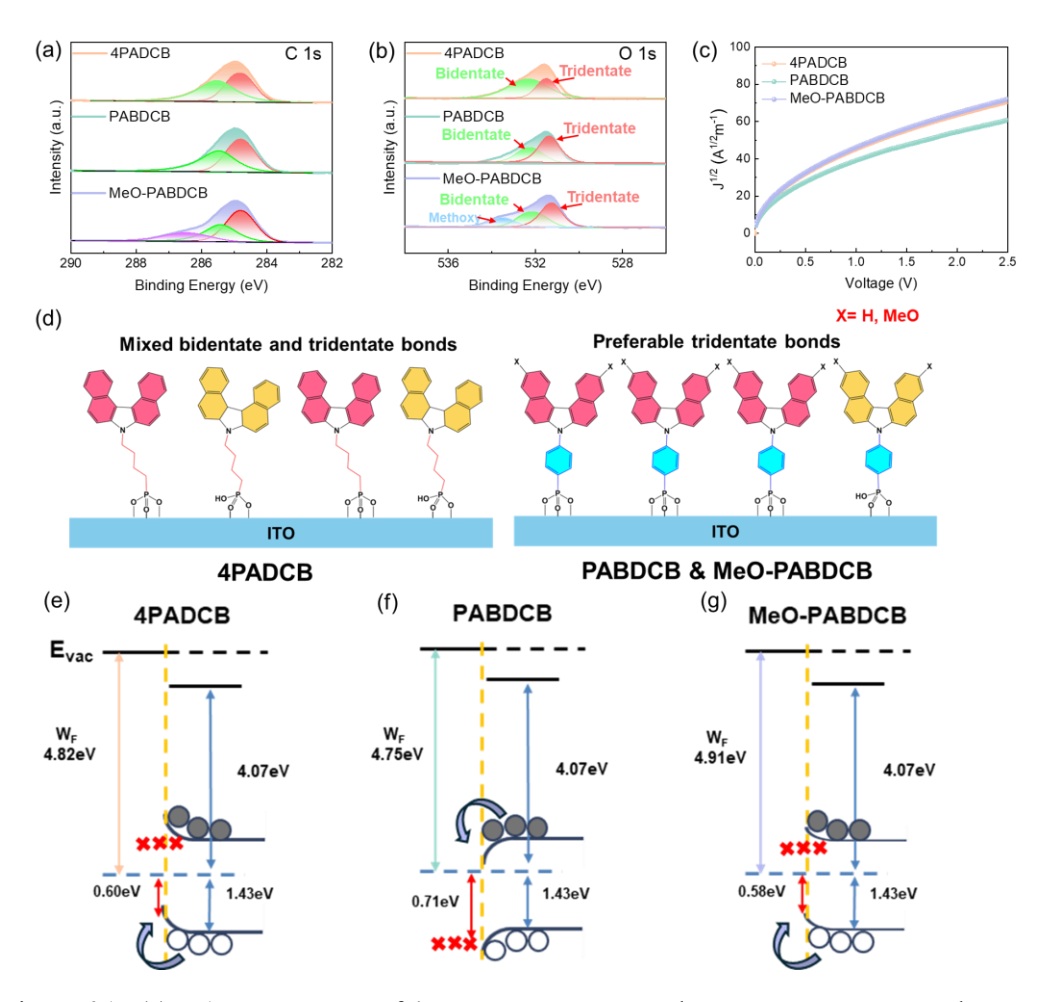


Figure 6.15 (a) C 1s XPS spectra of 4PADCB, PABDCB and MeO-PABDCB covered ITO . (b) O 1s XPS spectra of 4PADCB, PABDCB and MeO-PABDCB covered ITO. (c) I-V curves of hole-only device based on ITO/SAMs/PTAA/Au on 4PADCB, PABDCB and MeO-PABDCB. (d) Schematic binding diagram of alkyl-chain based SAMs and phenyl based SAMs. (e) Energy diagram of ITO/4PADCB/perovskite. (f) Energy diagram of ITO/PABDCB/perovskite. (g) Energy diagram of ITO/MeO-PABDCB/perovskite.

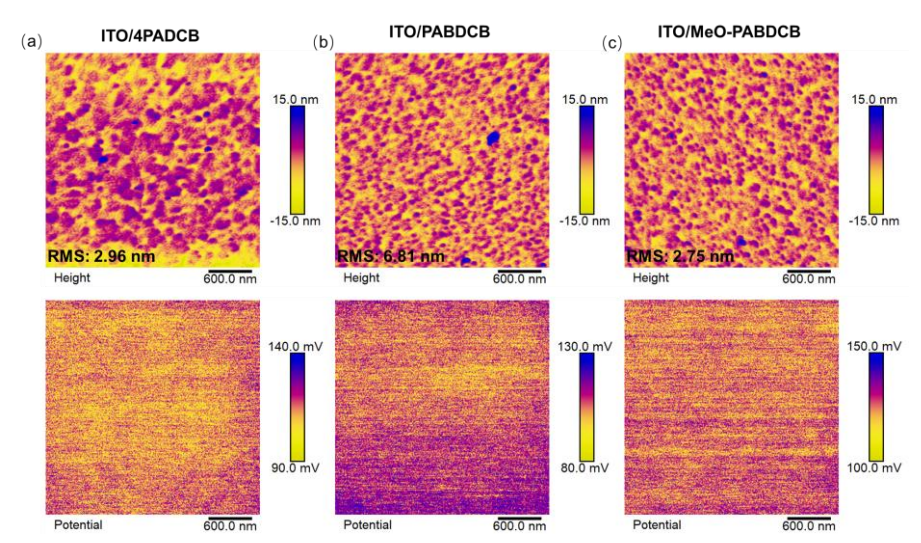


Figure 6.16 KPFM images of 4PADCB, PABDCB and MeO-PABDCB.

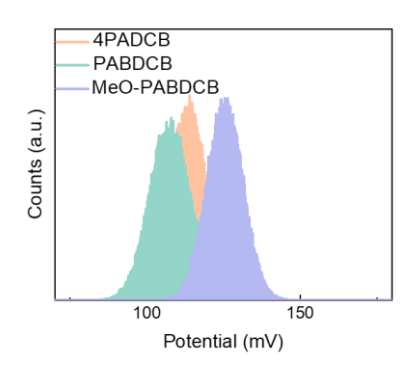


Figure 6.17 CPD distribution images of 4PADCB, PABDCB and MeO-PABDCB.

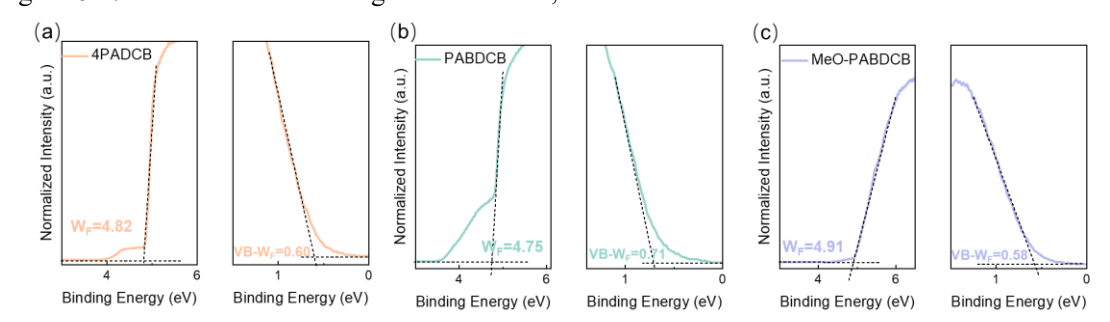


Figure 6.18 UPS spectra of 4PADCB, PABDCB and MeO-PABDCB.

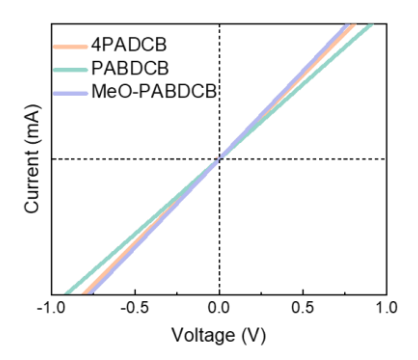


Figure 6.19 Single-carrier devices with device structure of ITO/SAMs/Au based on 4PADCB, PABDCB and MeO-PABDCB.

Moreover, the absorption behavior was investigated to get further insight into the interaction between perovskite and SAMs. **Figure 6.20a to 6.20c** showed the absorbed SAMs lying on perovskite surface with a preferrable orientation for passivation. The adsorption energy (E_{ads}) is first calculated, where 4PADCB, PABDCB and MeO-PABDCB with perovskite gives E_{ads} values of -0.61 eV, -0.56 eV and -0.80 eV, respectively. The calculated interaction between MeO-PABDCB was found to be stronger than those of 4PABDCB and PABDCB. Moreover, the significantly short Pb-O distance in MeO-PABDCB (3.10 Å) enables a dense package between perovskite and MeO-PABDCB, which can be derived from the passivation between O and Pb.

To gain more information SAMs on the influence of perovskite, the carrier dynamics is investigated using photoluminescence (PL) and time-resolved PL (TRPL) spectroscopy to probe the perovskite films deposited on SAM/ITO substrates. As illustrated in **Figure 6.20d and 6.20e**, the MeO-PABDCB-based films exhibited both the highest PL intensity and the longest PL lifetime ($\tau_2 = 808$ ns). This significant increase in lifetime indicates that the distinctive molecular with enhanced interface properties effectively reduces non-radiative recombination at the interface. By contrast, the shorter PL lifetimes of 4PADCB and PABDCB reflect higher levels of interfacial recombination. Thus, the improved carrier dynamics observed in the MeO-PABDCB can be attributed to more ordered molecular distribution and stronger dipole moment, both of which facilitate better charge separation and transport.³²⁸

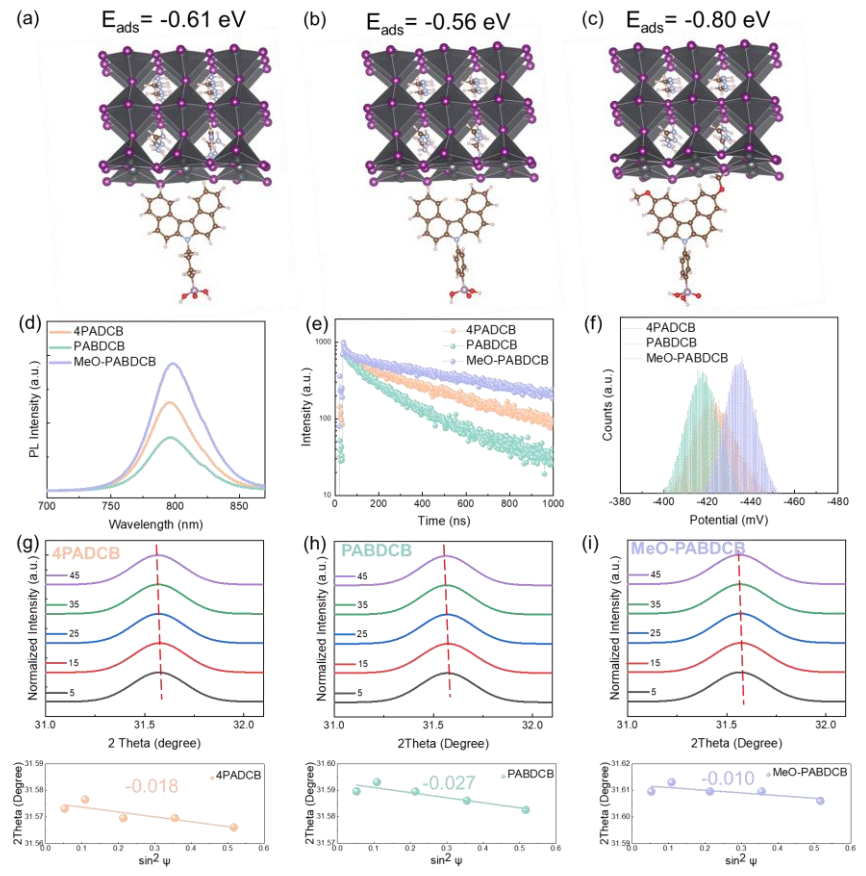


Figure 6.20 (a) Scheme of 4PADCB on perovskite. (b) Scheme of PABDCB on perovskite. (c) Scheme of MeO-PABDCB on perovskite. (d) Steady-state PL spectra of perovskite films on 4PADCB, PABDCB and MeO-PABDCB substrates. (e) Transient PL spectra of perovskite films on 4PADCB, PABDCB and MeO-PABDCB substrates. (f) Surface potential distribution of perovskite films on 4PADCB, PABDCB and MeO-PABDCB substrates. (g) GIXRD spectra and corresponding linear fit plots for perovskite films on 4PADCB. (h) GIXRD spectra and corresponding linear fit plots for perovskite films on PABDCB. (i) GIXRD spectra and corresponding linear fit plots for perovskite films on MeO-PADCB.

Table 6.2 The fitted carrier lifetime of perovskite films obtained from the TRPL measurements

Sample	$\tau_1(ns)$	A ₁ (%)	$\tau_2(ns)$	A ₂ (%)	$\tau_{\rm avg}({\rm ns})$
4PADCB	68.4	3.06	461.4	96.94	459.6
PABDCB	49.9	7.51	243.8	92.49	240.6
MeO-PABDCB	35.4	1.38	808.6	98.62	808.1

The perovskite surface morphology on varied SAM/ITO substrates was further analyzed using scanning electron microscopy (SEM) and atomic force microscopy (AFM). Notably, no significant morphological differences were observed across these films (**Figure 6.21 and 6.22**). This observation aligns with the X-ray diffraction (XRD)

measurement, which revealed similar crystallographic orientation and crystallization behavior in all perovskite films (**Figure 6.23**). However, KPFM measurements indicated a slightly lower variability and reduced CPD distribution in MeO-PABDCB-based perovskite films, suggesting a more n-type character and uniform electronic landscape (**Figure 6.20f**). This electronic uniformity likely facilitates more efficient electron transfer at the perovskite surface, in agreement with the results discussed above.

To further understand the SAMs on the structural impact of perovskite, grazing-incidence X-ray diffraction (GIXRD) was performed to analyze the residual strain in the perovskite films. The 2θ -sin² φ images revealed tensile stress in all samples, but the magnitude of the stress varied significantly (**Figure 6.20g to 6.20i**). PABDCB exhibited the largest slope (0.027), indicating considerable tensile strain, which can be detrimental to device performance. In contrast, MeO-PABDCB exhibited the smallest slope (0.010), suggesting a substantial reduction in tensile strain. This reduction in strain can be linked to improved crystallinity and molecular packing, key factors that contribute to the high performance of the MeO-PABDCB-based devices.^{329,330}

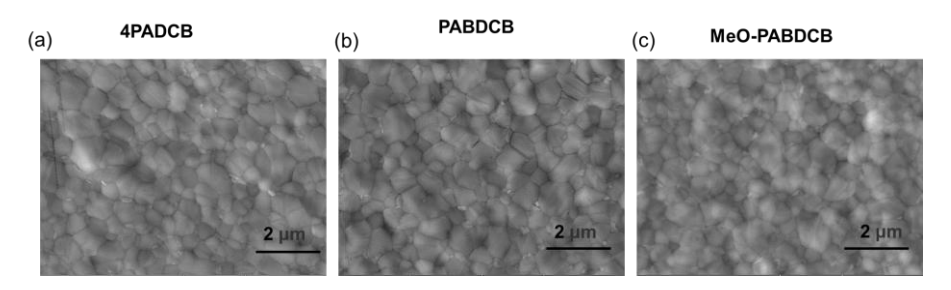


Figure 6.21 SEM top images of perovskite surface deposited on 4PADCB, PABDCB and MeO-PABDCB.

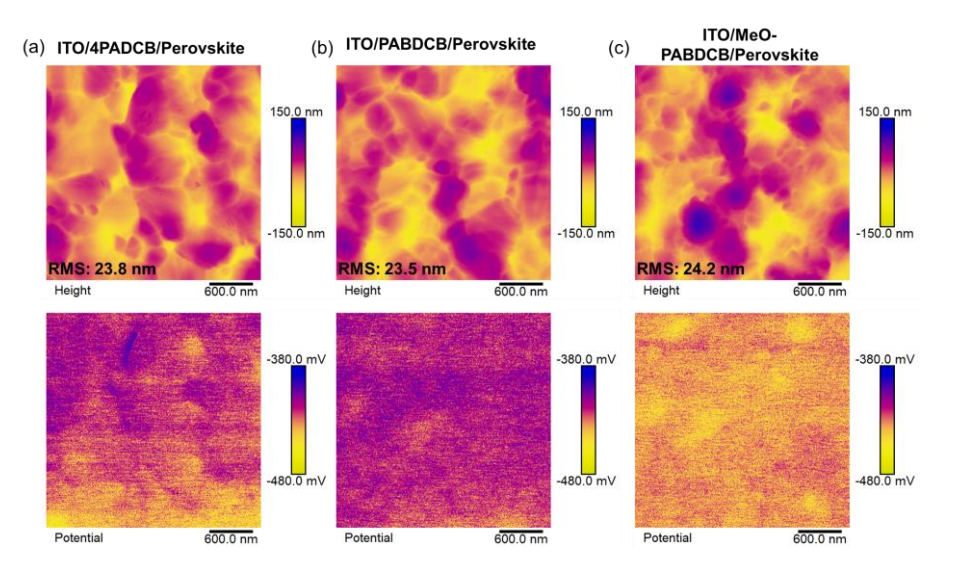


Figure 6.22 AFM and KPFM images of the perovskite surface deposited on 4PADCB, PABDCB and MeO-PABDCB.

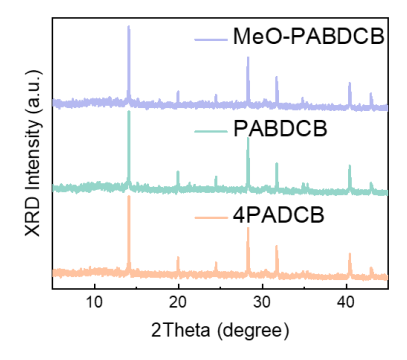


Figure 6.23 XRD images of perovskite surface deposited on 4PADCB, PABDCB and MeO-PABDCB.

Obviously, varied SAMs' properties take critical roles of the IPSCs. The photovoltaic performance incorporating the three SAMs was evaluated using a device structure of ITO/SAM/Perovskite/ C_{60} /BCP/Cu (**Figure 6.24a**). Subsequently, as shown in **Figure 6.24b**, the MeO-PABDCB-based device achieved a cheerful PCE of 26.25% ($V_{OC} = 1.18 \text{ V}$, $J_{SC} = 25.8 \text{ mA/cm}^2$, FF = 86.4%), outperforming the devices based on 4PADCB (PCE = 25.62%) and PABDCB (PCE = 24.44%). The device performances were summarized in **Figure 6.25 and 6.26**. The increased efficiency could be attributed to the ascended energy level, improved charge transfer, wettability, and reduced recombination facilitated by the MeO-PABDCB. The external quantum efficiency (EQE) spectra confirmed the consistency of the J_{SC} values obtained from the J-V curves

(**Figure 6.27**). In addition, the steady-state power output (SPO) of the MeO-PABDCB-based device was tracked under continuous 1 sun illumination, showing a stabilized PCE of 25.5%, further validating its superior performance (**Figure 6.24c**).

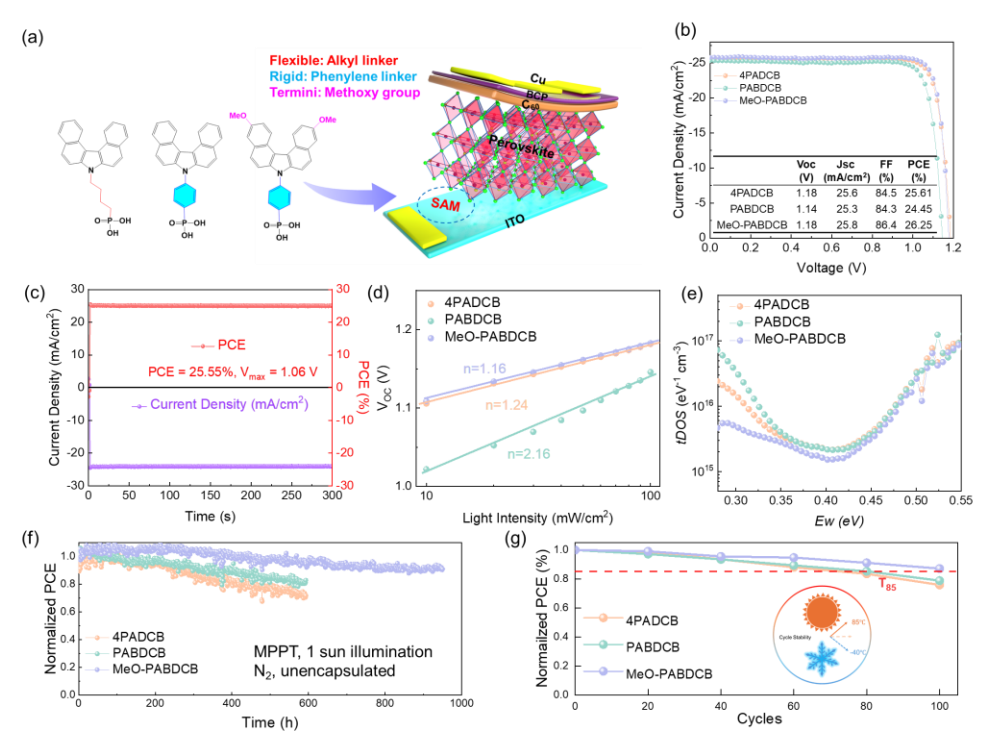


Figure 6.24 (a) Device structure of IPSCs based on 4PADCB, PABDCB and MeO-PABDCB. (b) J-V curves of 4PADCB, PABDCB and MeO-PABDCB based IPSCs. (c) Steady-output of the champion devices based on MeO-PABDCB. (d) Light intensity-dependent V_{OC} of IPSCs based on 4PADCB, PABDCB and MeO-PABDCB. (e) tDOS distribution defect energy level $E\omega$ of 4PADCB-PABDCB and MeO-PABDCB. (f) Operational stability of IPSCs based on 4PADCB, PABDCB and MeO-PABDCB. (g) Cycle stability of IPSCs based on 4PADCB and MeO-PABDCB.

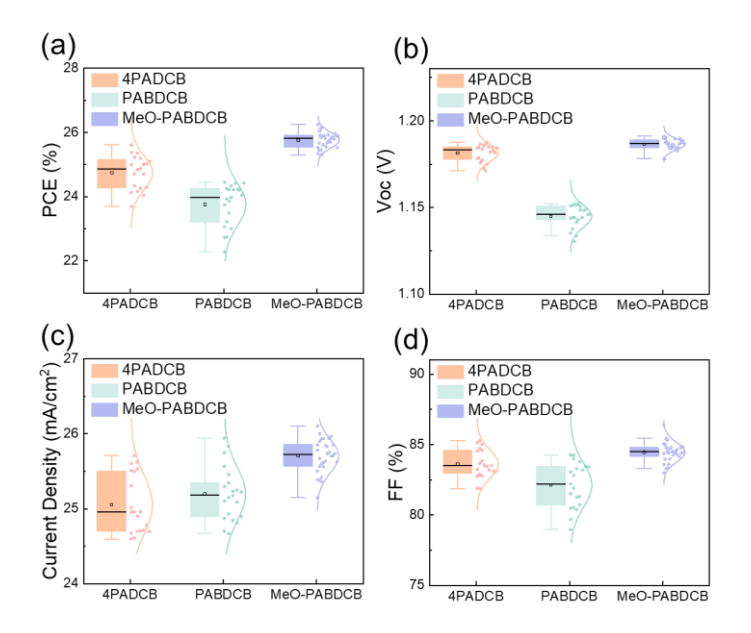


Figure 6.25 Devices performance on 4PADCB, PABDCB and MeO-PABDCB.

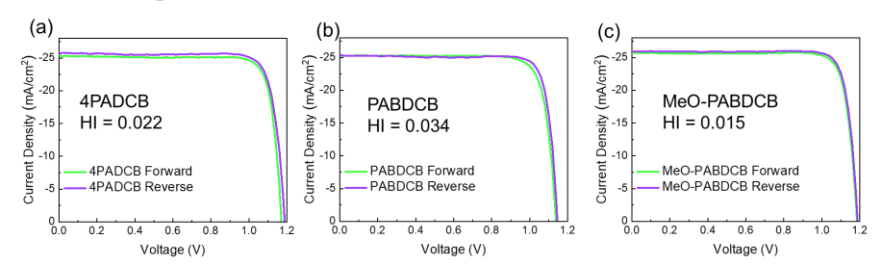


Figure 6.26 Reverse and forward scans based on 4PADCB, PABDCB and MeO-PABDCB.

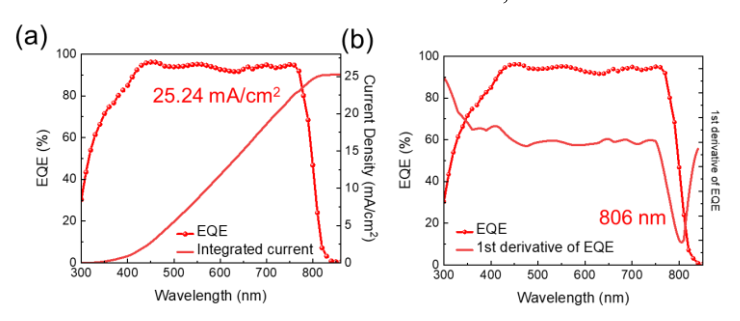


Figure 6.27 EQE spectra and its 1st derived plot of the best performance IPSCs based on MeO-PABDCB.

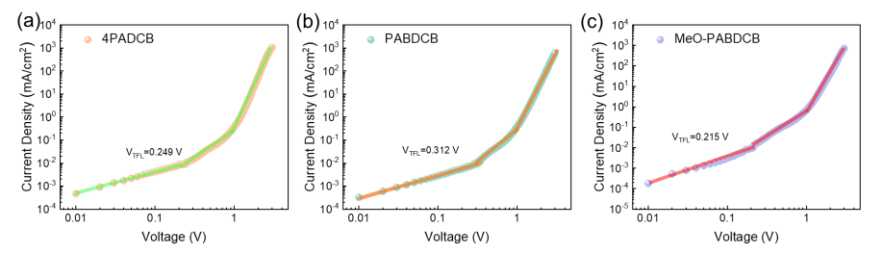


Figure 6.28 SCLC results with device structure of ITO/SAM/Perovskite/PTAA/Au based on 4PADCB, PABDCB and MeO-PABDCB.

To further probe the recombination mechanisms in the IPSCs, light-intensity dependent measurements of V_{OC} and J_{SC} were performed (**Figure 6.25d**). The ideality factors for 4PADCB, PABDCB, and MeO-PABDCB were found to be 1.25, 2.08, and 1.16, respectively. An ideality factor closer to 1 suggests a more ideal diode behavior, with reduced trap-assisted recombination. The significantly lower ideality factor for MeO-PABDCB indicates that this SAM more effectively suppresses trap states, which correlates with better charge extraction and overall device performance.³³¹ This result is consistent with the improved hole mobility and longer PL lifetime observed in MeO-PABDCB-based devices.

To further investigate varied SAMs on the influence of trap density in perovskite devices, SCLC with hole-only device structure of ITO/SAM/Perovskite/PTAA/Au. As shown in **Figure 6.28**, the trap density can be calculated by the equation. The V_{TFL} and calculated trap density were summarized in **Table 6.3**, the lowest V_{TFL} of MeO-PABDCB among these three SAMs, demonstrating a reduced trap density as well as suppressed non-radiative recombination loss, which beneficial for the device performance.³³² Thermal admittance spectroscopy (TAS) measurement was also conducted to explore the impact of SAMs on the distribution of trap density in IPSCs in **Figure 6.25e**. The shallow energy level below 0.45 eV is significantly reduced while negligible change is observed at deeper energy levels. Unveiling the reduction of traps at lower energy levels, demonstrating that MeO-PABDCB effectively mitigated traps in IPSCs.³³³

In terms of operational stability, devices were evaluated under maximum power point (MPP) conditions in a nitrogen atmosphere (**Figure 6.25f**). After 1000 hours of continuous operation, the MeO-PABDCB-based device retained approximately 90% of its initial efficiency, while the 4PADCB and PABDCB-based devices exhibited significant degradation. Moreover, as shown in **Figure 6.25g**, the MeO-PABDCB-based device maintained over 87% of its initial PCE after 100 cycles of alternating exposure to -40°C and 85°C, whereas the 4PADCB and PABDCB-based devices

preserved merely ~75% of their performance under the same conditions. The flexible alkyl linker allows free rotation, which induces interfacial instability issues under external stimuli, however, substituting the alkyl linker with a rigid phenyl group can effectively delocalize electrons and enhance the intrinsic stability of PABDCB-based devices. Moreover, MeO-PABDCB benefits from a strong intermolecular action with perovskite, enables a robust and enhanced resist to external perturbations. As a result, the enhanced stability observed in MeO-PABDCB-based devices can be attributed to improved interfacial properties, such as preferable tridentate bonging modes and reduced strain at the interfaces. These factors collectively contribute to the long-term operational durability of the device.

Table 6.3 Summarized trap density and hole mobility from SCLC results.

Samples	V_{TFL} (V)	$N_t (10^{15} \text{ cm}^{-3})$	Mobility (10 ⁻⁵ cm ⁻² V ⁻¹ s-1)
4PADCB	0.249	0.50	8.2
PABDCB	0.312	0.76	7.1
MeO-PABDCB	0.197	0.52	8.2

6.4 Summary

In conclusion, the challenges posed by flexible alkyl linkers in SAMs, such as disordered packing, poor charge transport, and instability, are systematically addressed through strategic molecular design. By integrating rigid phenylene linkers and methoxy termini into PABDCB and MeO-PABDCB, we achieve ordered SAM architectures with robust tridentate ITO binding and enhanced π - π interactions. Density functional theory and XPS confirm that the methoxy group in MeO-PABDCB amplifies dipole moments (5.32 D) and passivates interfacial defects, thereby suppressing non-radiative recombination. These innovations culminate in IPSCs with an efficiency of 26.25%, exhibiting unparalleled stability and superior cycle stability under extreme thermal stress, outperforming conventional SAMs. Our findings underscore the critical interplay between molecular rigidity and terminal group functionality in SAM design,

providing a universal framework for high-efficiency, durable perovskite photovoltaics. This work bridges molecular-level precision with device performance, charting a path toward scalable, industrial-grade solar technologies.

Chapter 7 Conclusion and Outlook

7.1 Conclusion

To accelerate the commercialization of PSCs, addressing energy loss at the interfaces is of vital importance. The key challenges include minimizing the trap states at both top surface and buried interface. Moreover, the self-aggregation of SAMs poses significant barrier for the further development of IPSCs, limiting the device performance and stability. In this thesis, based on interfacial engineering in IPSCs, we introduce new approaches aimed at reducing interface-related energy losses. The strategies are organized in three key aspects: i) minimizing the trap states with surface passivation; ii) enhancing the interfacial stability by mitigating the self-aggregation of SAMs; iii) developing novel SAMs tailored for interfacial performance and stability in IPSCs.

In chapter 4, a merit polymerized small molecule acceptor, PY-IT, was introduced at the top surface of perovskite. The incorporation of this PSMA is aimed to address interfacial issues by passivating the interfacial traps, thereby improving charge transport and reducing recombination losses. And the up-shifting the E_F and the smooth perovskite surface with low surface potential variations, resulting in a more n-type perovskite surface and significantly improved electron transfer with reduced recombination. Consequently, PSMA-treat IPSCs exhibited enhanced efficiency and stability.

In chapter 5, to overcome the self-aggregation of SAMs, a celebrated co-adsorbed strategy is achieved by incorporating PyCA-3F. By both experimental and theoretical investigations, we found that the CA strategy facilitates the formation of a smooth surface and a favorable energy band alignment, thereby reducing the energy barrier between 2PACz and the perovskite/organic layers. Furthermore, the CA approach flattens the buried interface of the perovskite layer, leading to an enhanced heterointerface energy and a defect-free interface feature, thus minimizing the energy loss therein. This improvement is effectively translated to promote efficiency and

operational stability of corresponding IPSCs and OSCs with p-i-n configurations.

Chapter 6 investigates the design and synthesis of novel self-assembled SAM in IPSCs. Two SAMs, PABDCB and MeO-PABDCB, featuring rigid phenylene linkers, were developed to construct densely packed, organized HTLs. Through methoxy group modification, MeO-PABDCB demonstrated significantly enhanced charge transport and passivation properties, leading to a high PCE of 26.25%. Both SAMs form strong tridentate binding modes with ITO substrates, and the methoxy group effectively passivates the perovskite layer, as confirmed by theoretical analysis. These emphasize that the molecular structure can play a pivotal role in enhancing photovoltaic performance, demonstrating the potential of SAM design in next-generation photovoltaic applications.

The comprehensive findings of this thesis contribute valuable insights into material interactions at the interface level, providing a robust pathway to achieving higher efficiency and better stability in IPSCs. These results lay a foundation for future large-scale implementation of perovskite technology in renewable energy solutions.

7.2 Outlook

Moving forward, the focus in PSCs research should expand beyond achieving record PCEs to ensure long-term operational stability and environmental compatibility. Future investigations should explore new materials for interface engineering that not only optimize performance but are also sustainable and cost-effective. Additionally, integrating these findings into scalable manufacturing techniques, such as roll-to-roll processing and other large-scale deposition methods, will be crucial for transitioning PSCs from the laboratory to commercial applications. Innovative studies on advanced characterization methods and computational modeling will aid in deepening the understanding of interfacial phenomena, guiding the design of next-generation perovskite-based solar cells. The continuous development of adaptive and multifunctional interface materials promises to bridge the gap between high

performance and practical usability, ensuring that PSCs contribute meaningfully to the global renewable energy fields.

The advancements outlined in this thesis pave the way for future research development in IPSCs. Moving forward, it is critical to focus on scaling these interface engineering strategies for industrial-scale production, emphasizing cost-effective and environmentally friendly processes. Key considerations in this phase will include optimizing the scalability of deposition techniques, reducing non-radiative recombination loss at the interface, and enhancing the real-world operation stability of large-area PSCs.

Another promising direction for future research lies in the development of tandem/multijunction PSCs, which have the potential to balance light utilization and cost. Interface engineering plays a pivotal role in these multijunction structures, where the seamless integration of different materials and the careful tuning of charge transport and recombination dynamics are crucial for optimizing the overall performance. By precisely controlling these interfaces, it has potential to reduce energy losses and improve the interfacial compatibility between different layers, thereby enhancing the PCE and stability.

Furthermore, addressing the long-term operational stability of interfaces in PSCs is paramount. Future research should focus on understanding how these interfaces behave under various environmental stressors such as humidity, temperature fluctuations, and UV exposure. Investigating the long-term resilience of perovskite materials and their interfaces will be essential for ensuring the commercial viability of these solar cells. Research into encapsulation techniques, degradation mechanisms, and the development of robust materials for interface layers will be crucial to achieving not only high efficiency but also longevity in real-world applications.

In conclusion, this thesis provides a steppingstone for the ongoing innovation in PSCs technology, with a particular focus on interface engineering. Continued advancements in both material science and manufacturing processes will be key to accelerating the transition of PSCs from laboratory demonstrations to commercially viable, large-scale energy solutions. The combination of enhanced efficiency, stability, and cost-effectiveness holds the potential to transform the renewable energy landscape.

ReferenceUncategorized References

- 1 Rajbongshi, B. M., Verma, A. . *Emerging Nanotechnology for Third Generation Photovoltaic Cells*. (2019).
- Meillaud, F., Shah, A., Droz, C., Vallat-Sauvain, E. & Miazza, C. Efficiency limits for single-junction and tandem solar cells. *Sol. Energy Mater. Sol. Cells* **90**, 2952-2959, doi:10.1016/j.solmat.2006.06.002 (2006).
- Girtan, M. & Rusu, M. Role of ITO and PEDOT:PSS in stability/degradation of polymer:fullerene bulk heterojunctions solar cells. *Sol. Energy Mater. Sol. Cells* **94**, 446-450, doi:10.1016/j.solmat.2009.10.026 (2010).
- 4 Becquerel, E. Mémoire sur les effets électriques produits sous l'influence des rayons solaires. *Comptes Rendus* **9**, 561-567 (1839).
- Hertz, H. Ueber einen Einfluss des ultravioletten Lichtes auf die electrische Entladung. *Ann. Phys.* **267**, 983-1000 (1887).
- 6 Einstein, A. Über einen die Erzeugung und Verwandlung des Lichtes betreffenden heuristischen Gesichtspunkt. *Ann. Physik.* **17**, 132-148 (1905).
- Wang, K. *et al.* Overcoming Shockley-Queisser limit using halide perovskite platform? *Joule* **6**, 756-771, doi:10.1016/j.joule.2022.01.009 (2022).
- 8 Shockley, W. & Queisser, H. J. Detailed Balance Limit of Efficiency ofpnJunction Solar Cells. *J. Appl. Phys.* **32**, 510-519, doi:10.1063/1.1736034 (1961).
- Rühle, S. Tabulated values of the Shockley–Queisser limit for single junction solar cells. *Sol. Energy* **130**, 139-147, doi:10.1016/j.solener.2016.02.015 (2016).
- da Silva, E. L., Skelton, J. M., Parker, S. C. & Walsh, A. Phase stability and transformations in the halide perovskite CsSnI₃. *Phys. Rev.* **91**, 144107, doi:10.1103/PhysRevB.91.144107 (2015).
- Kieslich, G., Sun, S. & Cheetham, A. K. An extended Tolerance Factor approach for organic—inorganic perovskites. *Chem. Sci.* **6**, 3430-3433, doi:10.1039/c5sc00961h (2015).
- McMeekin, D. P. *et al.* A mixed-cation lead mixed-halide perovskite absorber for tandem solar cells. *Science* **351**, 151-155, doi:10.1126/science.aad5845 (2016).
- Masi, S., Gualdrón-Reyes, A. F. & Mora-Seró, I. Stabilization of Black Perovskite Phase in FAPbI₃ and CsPbI₃. *ACS Energy Lett.* **5**, 1974-1985, doi:10.1021/acsenergylett.0c00801 (2020).
- 14 Kim, B., Kim, J. & Park, N. First-principles identification of the charge-shifting mechanism and ferroelectricity in hybrid halide perovskites. *Sci. Rep.* **10**, 19635, doi:10.1038/s41598-020-76742-7 (2020).
- Adinolfi, V., Peng, W., Walters, G., Bakr, O. M. & Sargent, E. H. The Electrical and Optical Properties of Organometal Halide Perovskites Relevant to Optoelectronic Performance. *Adv. Mater.* **30**, 170076, doi:10.1002/adma.201700764 (2018).

- Stranks, S. D. & Snaith, H. J. Metal-halide perovskites for photovoltaic and light-emitting devices. *Nat. Nanotechnol.* **10**, 391-402, doi:10.1038/nnano.2015.90 (2015).
- Huang, J., Yuan, Y., Shao, Y. & Yan, Y. Understanding the physical properties of hybrid perovskites for photovoltaic applications. *Nat. Rev. Mater.* **2**, 1-19, doi:10.1038/natrevmats.2017.42 (2017).
- 18 Chen, J. & Park, N. G. Causes and Solutions of Recombination in Perovskite Solar Cells. *Adv. Mater.* **31**, e1803019, doi:10.1002/adma.201803019 (2019).
- Dai, Z. & Padture, N. P. Challenges and opportunities for the mechanical reliability of metal halide perovskites and photovoltaics. *Nat Energy* **8**, 1319-1327, doi:10.1038/s41560-023-01378-6 (2023).
- Song, F. *et al.* Mechanical Durability and Flexibility in Perovskite Photovoltaics: Advancements and Applications. *Adv. Mater.* **36**, e2312041, doi:10.1002/adma.202312041 (2024).
- Wang, J. *et al.* Highly efficient all-inorganic perovskite solar cells with suppressed non-radiative recombination by a Lewis base. *Nat. Commun.* **11**, 177, doi:10.1038/s41467-019-13909-5 (2020).
- Liu, S. *et al.* High-efficiency organic solar cells with low non-radiative recombination loss and low energetic disorder. *Nat.Photonics* **14**, 300-305, doi:10.1038/s41566-019-0573-5 (2020).
- Deng, Y. H. & Nest, L. G. Analysis of misidentifications in TEM characterisation of organic-inorganic hybrid perovskite material. *J. Microsc.* **282**, 195-204, doi:10.1111/jmi.13000 (2021).
- Si, H. *et al.* Emerging Conductive Atomic Force Microscopy for Metal Halide Perovskite Materials and Solar Cells. *Adv. Energy Mater.* **10**, 1903922, doi:10.1002/aenm.201903922 (2020).
- 25 Kang, Z. *et al.* Kelvin probe force microscopy for perovskite solar cells. *Sci. China Mater.* **62**, 776-789, doi:10.1007/s40843-018-9395-y (2019).
- Qin, M., Chan, P. F. & Lu, X. A Systematic Review of Metal Halide Perovskite Crystallization and Film Formation Mechanism Unveiled by In Situ GIWAXS. *Adv. Mater.* **33**, 2105290, doi:10.1002/adma.202105290 (2021).
- Wu, J. *et al.* A Comparison of Charge Carrier Dynamics in Organic and Perovskite Solar Cells. *Adv. Mater.* **34**, 2101833, doi:10.1002/adma.202101833 (2021).
- Röhr, J. A., Kirchartz, T. & Nelson, J. On the correct interpretation of the low voltage regime in intrinsic single-carrier devices. *J. Phys.:Condens. Matter* **29**, 205901, doi:10.1088/1361-648X/aa66cc (2017).
- Zhang, Y. *et al.* A Theoretical Investigation of Transport Layer Free Homojunction Perovskite Solar Cells via a Detailed Photoelectric Simulation. *Adv. Energy Mater.* **13**, 2203366, doi:10.1002/aenm.202203366 (2023).
- Lin, R. *et al.* All-perovskite tandem solar cells with 3D/3D bilayer perovskite heterojunction. *Nature* **620**, 994-1000, doi:10.1038/s41586-023-06278-z

- (2023).
- Nelson, J. The physics of solar cells *Imperial College Press* (2003).
- Kojima, A., Teshima, K., Shirai, Y. & Miyasaka, T. Organometal halide perovskites as visible-light sensitizers for photovoltaic cells. *J. Am. Chem. Soc.* **131**, 6050-6051, doi:10.1021/ja809598r (2009).
- Cai, B., Xing, Y., Yang, Z., Zhang, W.-H. & Qiu, J. High performance hybrid solar cells sensitized by organolead halide perovskites. *Energy Environ. Sci.* **6**, 1480, doi:10.1039/c3ee40343b (2013).
- Li, L., Zhang, S., Yang, Z., Berthold, E. E. S. & Chen, W. Recent advances of flexible perovskite solar cells. *J. Energy Chem.* **27**, 673-689, doi:10.1016/j.jechem.2018.01.003 (2018).
- Zhu, Z., Mao, K. & Xu, J. Perovskite tandem solar cells with improved efficiency and stability. *J. Energy Chem.* **58**, 219-232, doi:10.1016/j.jechem.2020.09.022 (2021).
- Jeng, J. Y. *et al.* Nickel oxide electrode interlayer in CH₃NH₃PbI₃ perovskite/PCBM planar-heterojunction hybrid solar cells. *Adv. Mater.* **26**, 4107-4113, doi:10.1002/adma.201306217 (2014).
- Zhu, Z. *et al.* High-Performance Hole-Extraction Layer of Sol-Gel-Processed NiO Nanocrystals for Inverted Planar Perovskite Solar Cells. *Angew. Chem. Int. Ed.* **126**, 12779-12783, doi:10.1002/ange.201405176 (2014).
- You, J. *et al.* Improved air stability of perovskite solar cells via solution-processed metal oxide transport layers. *Nat. Nanotechnol.* **11**, 75-81, doi:10.1038/nnano.2015.230 (2016).
- 39 Li, G., Chu, C. W., Shrotriya, V., Huang, J. & Yang, Y. Efficient inverted polymer solar cells. *Appl. Phys. Lett.* **88**, 253503, doi:10.1063/1.2212270 (2006).
- Shrotriya, V., Li, G., Yao, Y., Chu, C.-W. & Yang, Y. Transition metal oxides as the buffer layer for polymer photovoltaic cells. *Appl. Phys. Lett.* **88**, 073508, doi:10.1063/1.2174093 (2006).
- 41 Al-Ashouri, A. *et al.* Monolithic perovskite/silicon tandem solar cell with >29% efficiency by enhanced hole extraction. *Science* **370**, 1300-1309, doi:10.1126/science.abd4016 (2020).
- 42 Ma, F. *et al.* Nickel oxide for inverted structure perovskite solar cells. *J. Energy Chem.* **52**, 393-411, doi:10.1016/j.jechem.2020.04.027 (2021).
- Liu, T., Chen, K., Hu, Q., Zhu, R. & Gong, Q. Inverted Perovskite Solar Cells: Progresses and Perspectives. *Adv. Energy Mater.* **6**, 1600457, doi:10.1002/aenm.201600457 (2016).
- Mahapatra, A. *et al.* A review of aspects of additive engineering in perovskite solar cells. *J. Mater. Chem. A* **8**, 27-54, doi:10.1039/c9ta07657c (2020).
- Tao, S. *et al.* Absolute energy level positions in tin- and lead-based halide perovskites. *Nat. Commun.* **10**, 2560, doi:10.1038/s41467-019-10468-7 (2019).
- 46 Minemoto, T. & Murata, M. Theoretical analysis on effect of band offsets in

- perovskite solar cells. *Sol. Energy Mater. Sol. Cells* **133**, 8-14, doi:10.1016/j.solmat.2014.10.036 (2015).
- Raoui, Y., Ez-Zahraouy, H., Kazim, S. & Ahmad, S. Energy level engineering of charge selective contact and halide perovskite by modulating band offset: Mechanistic insights. *J. Energy Chem.* **54**, 822-829, doi:10.1016/j.jechem.2020.06.030 (2021).
- Gao, F., Zhao, Y., Zhang, X. & You, J. Recent Progresses on Defect Passivation toward Efficient Perovskite Solar Cells. *Adv. Energy Mater.* **10**, 1902650, doi:10.1002/aenm.201902650 (2019).
- 49 Ball, J. M. & Petrozza, A. Defects in perovskite-halides and their effects in solar cells. *Nat Energy* **1**, 1-13, doi:Artn 16149
- 10.1038/Nenergy.2016.149 (2016).
- Ran, C., Xu, J., Gao, W., Huang, C. & Dou, S. Defects in metal triiodide perovskite materials towards high-performance solar cells: origin, impact, characterization, and engineering. *Chem. Soc. Rev.* 47, 4581-4610, doi:10.1039/c7cs00868f (2018).
- Chen, B., Rudd, P. N., Yang, S., Yuan, Y. & Huang, J. Imperfections and their passivation in halide perovskite solar cells. *Chem. Soc. Rev.* **48**, 3842-3867, doi:10.1039/c8cs00853a (2019).
- 52 Shockley, W. & Read, W. T. Statistics of the Recombinations of Holes and Electrons. *Phys. Rev.* **87**, 835-842, doi:10.1103/PhysRev.87.835 (1952).
- Xin, D., Tie, S., Zheng, X., Zhu, J. & Zhang, W.-H. Defect passivation through electrostatic interaction for high performance flexible perovskite solar cells. *J. Energy Chem.* **46**, 173-177, doi:10.1016/j.jechem.2019.11.015 (2020).
- Bi, C. *et al.* Non-wetting surface-driven high-aspect-ratio crystalline grain growth for efficient hybrid perovskite solar cells. *Nat. Commun.* **6**, 7747, doi:10.1038/ncomms8747 (2015).
- Wan, Z. *et al.* Interfacial engineering in lead-free tin-based perovskite solar cells. *J. Energy Chem.* **57**, 147-168, doi:10.1016/j.jechem.2020.08.053 (2021).
- Ma, S. *et al.* Pyridine-triphenylamine hole transport material for inverted perovskite solar cells. *J. Energy Chem.* **54**, 395-402, doi:10.1016/j.jechem.2020.06.002 (2021).
- Dunlap-Shohl, W. A., Zhou, Y., Padture, N. P. & Mitzi, D. B. Synthetic Approaches for Halide Perovskite Thin Films. *Chem. Rev.* **119**, 3193-3295, doi:10.1021/acs.chemrev.8b00318 (2019).
- Yang, S. *et al.* Tailoring Passivation Molecular Structures for Extremely Small Open-Circuit Voltage Loss in Perovskite Solar Cells. *J. Am. Chem. Soc.* **141**, 5781-5787, doi:10.1021/jacs.8b13091 (2019).
- Wu, S. *et al.* 2D metal-organic framework for stable perovskite solar cells with minimized lead leakage. *Nat. Nanotechnol.* **15**, 934-940, doi:10.1038/s41565-020-0765-7 (2020).
- 60 Degani, M. et al. 23.7% Efficient inverted perovskite solar cells by dual

- interfacial modification. Sci. Adv. 7, eabj7930, doi:10.1126/sciadv.abj7930 (2021).
- Wu, S. *et al.* Low-Bandgap Organic Bulk-Heterojunction Enabled Efficient and Flexible Perovskite Solar Cells. *Adv. Mater.* **33**, e2105539, doi:10.1002/adma.202105539 (2021).
- Li, Z. *et al.* Organometallic-functionalized interfaces for highly efficient inverted perovskite solar cells. *Science* **376**, 416-420, doi:10.1126/science.abm8566 (2022).
- Ni, Z. *et al.* Resolving spatial and energetic distributions of trap states in metal halide perovskite solar cells. *Science* **367**, 1352-1358, doi:10.1126/science.aba0893 (2020).
- Tang, G. *et al.* Solution-Phase Epitaxial Growth of Perovskite Films on 2D Material Flakes for High-Performance Solar Cells. *Adv. Mater.* **31**, e1807689, doi:10.1002/adma.201807689 (2019).
- Liu, X. *et al.* 20.7% highly reproducible inverted planar perovskite solar cells with enhanced fill factor and eliminated hysteresis. *Energy Environ. Sci.* **12**, 1622-1633, doi:10.1039/c9ee00872a (2019).
- Huang, Y. *et al.* Bridging the Interfacial Contact for Improved Stability and Efficiency of Inverted Perovskite Solar Cells. *Small* **18**, e2201694, doi:10.1002/smll.202201694 (2022).
- Stolterfoht, M. *et al.* Visualization and suppression of interfacial recombination for high-efficiency large-area pin perovskite solar cells. *Nat Energy* **3**, 847-854, doi:10.1038/s41560-018-0219-8 (2018).
- 68 Li, B. *et al.* Reduced bilateral recombination by functional molecular interface engineering for efficient inverted perovskite solar cells. *Nano Energy* **78**, 105249, doi:10.1016/j.nanoen.2020.105249 (2020).
- Wang, C. *et al.* Deciphering the Reduced Loss in High Fill Factor Inverted Perovskite Solar Cells with Methoxy-Substituted Poly(Triarylamine) as the Hole Selective Contact. *Acs Appl Mater Inter* **14**, 12640-12651, doi:10.1021/acsami.1c23942 (2022).
- Zhang, S. *et al.* The Role of Bulk and Interface Recombination in High-Efficiency Low-Dimensional Perovskite Solar Cells. *Adv. Mater.* **31**, e1901090, doi:10.1002/adma.201901090 (2019).
- Wolff, C. M., Caprioglio, P., Stolterfoht, M. & Neher, D. Nonradiative Recombination in Perovskite Solar Cells: The Role of Interfaces. *Adv. Mater.* **31**, e1902762, doi:10.1002/adma.201902762 (2019).
- Zhou, Q. *et al.* Multifunctional Chemical Bridge and Defect Passivation for Highly Efficient Inverted Perovskite Solar Cells. *ACS Energy Lett.*, 1596-1606, doi:10.1021/acsenergylett.1c00291 (2021).
- Yu, W. *et al.* Multiple methoxy-substituted hole transporter for inverted perovskite solar cells. *J. Energy Chem.* **56**, 127-131, doi:10.1016/j.jechem.2020.07.056 (2021).

- Xu, X. *et al.* Improving Contact and Passivation of Buried Interface for High-Efficiency and Large-Area Inverted Perovskite Solar Cells. *Adv. Funct. Mater.* **32**, 2109968, doi:10.1002/adfm.202109968 (2021).
- Yang, C. *et al.* Colloidal CsCu₅S₃ nanocrystals as an interlayer in high-performance perovskite solar cells with an efficiency of 22.29%. *Chem. Eng. J.* **406**, 126855, doi:10.1016/j.cej.2020.126855 (2021).
- Kotta, A., Seo, I., Shin, H.-S. & Seo, H.-K. Room-temperature processed hole-transport layer in flexible inverted perovskite solar cell module. *Chem. Eng. J.* **435**, 134805, doi:10.1016/j.cej.2022.134805 (2022).
- Xu, R. *et al.* D-π-D molecular layer electronically bridges the NiO hole transport layer and the perovskite layer towards high performance photovoltaics. *J. Energy Chem.* **67**, 797-804, doi:10.1016/j.jechem.2021.11.029 (2022).
- Zhang, J. & Yu, H. Reduced energy loss enabled by thiophene-based interlayers for high performance and stable perovskite solar cells. *J. Mater. Chem. A* **9**, 4138-4149, doi:10.1039/d0ta10270a (2021).
- Pao, H. *et al.* Samarium-Doped Nickel Oxide for Superior Inverted Perovskite Solar Cells: Insight into Doping Effect for Electronic Applications. *Adv. Funct. Mater.* **31**, 2102452, doi:10.1002/adfm.202102452 (2021).
- Wang, S. *et al.* Critical Role of Removing Impurities in Nickel Oxide on High-Efficiency and Long-Term Stability of Inverted Perovskite Solar Cells. *Angew. Chem. Int. Ed.* **134**, e202116534, doi:10.1002/anie.202116534 (2022).
- Chen, W. *et al.* Molecule-Doped Nickel Oxide: Verified Charge Transfer and Planar Inverted Mixed Cation Perovskite Solar Cell. *Adv. Mater.* **30**, e1800515, doi:10.1002/adma.201800515 (2018).
- Chen, W. *et al.* Alkali Chlorides for the Suppression of the Interfacial Recombination in Inverted Planar Perovskite Solar Cells. *Adv. Energy Mater.* **9**, 1803872, doi:ARTN 1803872
- 10.1002/aenm.201803872 (2019).
- Zhang, J. *et al.* Obstructing interfacial reaction between NiOx and perovskite to enable efficient and stable inverted perovskite solar cells. *Chem. Eng. J.* **426**, 131357, doi:10.1016/j.cej.2021.131357 (2021).
- Zhang, B. *et al.* NiO/Perovskite Heterojunction Contact Engineering for Highly Efficient and Stable Perovskite Solar Cells. *Adv. Sci.* **7**, 1903044, doi:10.1002/advs.201903044 (2020).
- Liu, Y. *et al.* Stabilization of Highly Efficient and Stable Phase-Pure FAPbI₃ Perovskite Solar Cells by Molecularly Tailored 2D-Overlayers. *Angew. Chem. Int. Ed.* **59**, 15688-15694, doi:10.1002/anie.202005211 (2020).
- Chen, B. *et al.* Passivation of the Buried Interface via Preferential Crystallization of 2D Perovskite on Metal Oxide Transport Layers. *Adv. Mater.* **33**, e2103394, doi:10.1002/adma.202103394 (2021).
- 87 Chen, Y. *et al.* Design of an Inorganic Mesoporous Hole-Transporting Layer for Highly Efficient and Stable Inverted Perovskite Solar Cells. *Adv. Mater.* **30**,

- e1805660, doi:10.1002/adma.201805660 (2018).
- Sadegh, F. *et al.* Copolymer-Templated Nickel Oxide for High-Efficiency Mesoscopic Perovskite Solar Cells in Inverted Architecture. *Adv. Funct. Mater.* **31**, 2102237, doi:10.1002/adfm.202102237 (2021).
- Liu, Z. *et al.* Tailoring carrier dynamics in inverted mesoporous perovskite solar cells with interface-engineered plasmonics. *J. Mater. Chem. A* **9**, 2394-2403, doi:10.1039/d0ta10242c (2021).
- Ohen, Y. *et al.* Thermally stable methylammonium-free inverted perovskite solar cells with Zn²⁺ doped CuGaO₂ as efficient mesoporous hole-transporting layer. *Nano Energy* **61**, 148-157 (2019).
- Yu, S. *et al.* Homogenized NiO_X nanoparticles for improved hole transport in inverted perovskite solar cells. *Science* **382**, 1399-1404, doi:10.1126/science.adj8858 (2023).
- Liu, C. *et al.* Bimolecularly passivated interface enables efficient and stable inverted perovskite solar cells. *Science* **382**, 810-815, doi:10.1126/science.adk1633 (2023).
- 93 Yalcin, E. *et al.* Semiconductor self-assembled monolayers as selective contacts for efficient pin perovskite solar cells. *Energy Environ. Sci.* **12**, 230-237, doi:10.1039/c8ee01831f (2019).
- Magomedov, A. *et al.* Self-Assembled Hole Transporting Monolayer for Highly Efficient Perovskite Solar Cells. *Adv. Energy Mater.* **8**, 1801892, doi:10.1002/aenm.201801892 (2018).
- Li, L. *et al.* Flexible all-perovskite tandem solar cells approaching 25% efficiency with molecule-bridged hole-selective contact. *Nat Energy* **7**, 708-717, doi:10.1038/s41560-022-01045-2 (2022).
- Al-Ashouri, A. *et al.* Conformal monolayer contacts with lossless interfaces for perovskite single junction and monolithic tandem solar cells. *Energy Environ. Sci.* **12**, 3356-3369, doi:10.1039/c9ee02268f (2019).
- Azmi, R. *et al.* Damp heat-stable perovskite solar cells with tailored-dimensionality 2D/3D heterojunctions. *Science* **376**, 73-77, doi:10.1126/science.abm5784 (2022).
- Jiang, Q. *et al.* Surface reaction for efficient and stable inverted perovskite solar cells. *Nature* **611**, 278-283, doi:10.1038/s41586-022-05268-x (2022).
- 99 Al-Ashouri, A. *et al.* Monolithic perovskite/silicon tandem solar cell with >29% efficiency by enhanced hole extraction. *Science* **370**, 1300-1309, doi:10.1126/science.abd4016 (2020).
- Ullah, A. et al. Novel Phenothiazine-Based Self-Assembled Monolayer as a Hole Selective Contact for Highly Efficient and Stable p-i-n Perovskite Solar Cells. Adv. Energy Mater. 12, 2103175, doi:ARTN 2103175
- 10.1002/aenm.202103175 (2022).
- 101 Ullah, A. *et al.* Versatile Hole Selective Molecules Containing a Series of Heteroatoms as Self-Assembled Monolayers for Efficient p-i-n Perovskite and

- Organic Solar Cells. *Adv. Funct. Mater.* **32**, 2208793, doi:ARTN 2208793 10.1002/adfm.202208793 (2022).
- Jiang, W. *et al.* Spin-coated and vacuum-processed hole-extracting self-assembled multilayers with H-aggregation for high-performance inverted perovskite solar cells. *Angew. Chem. Int. Ed.*, e202411730, doi:10.1002/anie.202411730 (2024).
- 103 He, R. *et al.* Improving interface quality for 1-cm2 all-perovskite tandem solar cells. *Nature* **618**, 80-86, doi:10.1038/s41586-023-05992-y (2023).
- Wang, G. *et al.* Molecular engineering of hole-selective layer for high band gap perovskites for highly efficient and stable perovskite-silicon tandem solar cells. *Joule* 7, 2583-2594, doi:10.1016/j.joule.2023.09.007 (2023).
- Li, Z. *et al.* Stabilized hole-selective layer for high-performance inverted p-i-n perovskite solar cells. *Science* **382**, 284-289, doi:10.1126/science.ade9637 (2023).
- Tang, H. *et al.* Reinforcing self-assembly of hole transport molecules for stable inverted perovskite solar cells. *Science* **383**, 1236-1240, doi:10.1126/science.adj9602 (2024).
- 107 Shao, Y., Xiao, Z., Bi, C., Yuan, Y. & Huang, J. Origin and elimination of photocurrent hysteresis by fullerene passivation in CH3NH3PbI3 planar heterojunction solar cells. *Nat. Commun.* **5**, 5784, doi:10.1038/ncomms6784 (2014).
- Wu, C.-G., Chiang, C.-H. & Chang, S. H. A perovskite cell with a record-high-Voc of 1.61 V based on solvent annealed CH3NH3PbBr3/ICBA active layer. *Nanoscale* **8**, 4077-4085, doi:10.1039/c5nr07739g (2016).
- Jiang, X. *et al.* Ultra-high open-circuit voltage of tin perovskite solar cells via an electron transporting layer design. *Nat. Commun.* **11**, 1245, doi:10.1038/s41467-020-15078-2 (2020).
- Hou, E. *et al.* Cross-Linkable Fullerene Electron Transport Layer with Internal Encapsulation Capability for Efficient and Stable Inverted Perovskite Solar Cells. *Angew. Chem. Int. Ed.*, e202416703, doi:10.1002/ange.202416703 (2024).
- Wang, W. *et al.* Inverted Planar Heterojunction Perovskite Solar Cells Employing Polymer as the Electron Conductor. *Acs Appl Mater Inter* **7**, 3994-3999, doi:10.1021/am506785k (2015).
- Han, Y. *et al.* Controlled n-Doping in Air-Stable CsPbI₂Br Perovskite Solar Cells with a Record Efficiency of 16.79%. *Adv. Funct. Mater.* **30**, 1909972, doi:10.1002/adfm.201909972 (2020).
- Yin, L. *et al.* Polymerized non-fullerene small molecular acceptor as a versatile electron-transport material for 24.50 % efficiency inverted perovskite solar cells with extended spectral response. *Chem. Eng. J.* **501**, 157542, doi:10.1016/j.cej.2024.157542 (2024).
- 114 Chen, W. et al. N-type conjugated polymer as efficient electron transport layer

- for planar inverted perovskite solar cells with power conversion efficiency of 20.86%. *Nano Energy* **68**, 104363, doi:10.1016/j.nanoen.2019.104363 (2020).
- Docampo, P., Ball, J. M., Darwich, M., Eperon, G. E. & Snaith, H. J. Efficient organometal trihalide perovskite planar-heterojunction solar cells on flexible polymer substrates. *Nat. Commun.* **4**, 2761, doi:10.1038/ncomms3761 (2013).
- Zhang, S. et al. Conjugated Self-Assembled Monolayer as Stable Hole-Selective Contact for Inverted Perovskite Solar Cells. ACS Mater. Lett. 4, 1976-1983, doi:10.1021/acsmaterialslett.2c00799 (2022).
- Jia, X. *et al.* Power Conversion Efficiency and Device Stability Improvement of Inverted Perovskite Solar Cells by Using a ZnO:PFN Composite Cathode Buffer Layer. *Acs Appl Mater Inter* **8**, 18410-18417, doi:10.1021/acsami.6b03724 (2016).
- You, J. *et al.* Improved air stability of perovskite solar cells via solution-processed metal oxide transport layers. *Nat. Nanotechnol.* **11**, 75-81, doi:10.1038/nnano.2015.230 (2015).
- Zhu, Z. *et al.* Enhanced Efficiency and Stability of Inverted Perovskite Solar Cells Using Highly Crystalline SnO₂ Nanocrystals as the Robust Electron-Transporting Layer. *Adv. Mater.* **28**, 6478-6484, doi:10.1002/adma.201600619 (2016).
- 120 Kim, S. Y. *et al.* Fullerene-Free p-i-n Perovskite Solar Cells: Direct Deposition of Tin Oxide on Perovskite Layer Using Ligand Bridges. *Adv. Energy Mater.*, 2402433, doi:10.1002/aenm.202402433 (2024).
- Li, F. *et al.* Regulating Surface Termination for Efficient Inverted Perovskite Solar Cells with Greater Than 23% Efficiency. *J. Am. Chem. Soc.* **142**, 20134-20142, doi:10.1021/jacs.0c09845 (2020).
- Yang, J. *et al.* The poly(styrene-co-acrylonitrile) polymer assisted preparation of high-performance inverted perovskite solar cells with efficiency exceeding 22%. *Nano Energy* **82**, 105731, doi:10.1016/j.nanoen.2020.105731 (2021).
- 123 Chen, C. *et al.* Interfacial engineering of a thiophene-based 2D/3D perovskite heterojunction for efficient and stable inverted wide-bandgap perovskite solar cells. *Nano Energy* **90**, 106608, doi:10.1016/j.nanoen.2021.106608 (2021).
- Zhang, F. *et al.* Comprehensive passivation strategy for achieving inverted perovskite solar cells with efficiency exceeding 23% by trap passivation and ion constraint. *Nano Energy* **89**, 106370, doi:10.1016/j.nanoen.2021.106370 (2021).
- Zhou, L. et al. Synergistic Interface Layer Optimization and Surface Passivation with Fluorocarbon Molecules toward Efficient and Stable Inverted Planar Perovskite Solar Cells. Research 2021, 9836752, doi:10.34133/2021/9836752 (2021).
- Luo, D. *et al.* Enhanced photovoltage for inverted planar heterojunction perovskite solar cells. *Science* **360**, 1442-1446, doi:10.1126/science.aap9282 (2018).
- Ren, Z. et al. Room-temperature multiple ligands-tailored SnO₂ quantum dots

- endow in situ dual-interface binding for upscaling efficient perovskite photovoltaics with high V_{OC} . *Light Sci. Appl.* **10**, 239, doi:10.1038/s41377-021-00676-6 (2021).
- Hu, H. *et al.* Perovskite Quantum Wells Formation Mechanism for Stable Efficient Perovskite Photovoltaics-A Real-Time Phase-Transition Study. *Adv. Mater.* **33**, e2006238, doi:10.1002/adma.202006238 (2021).
- Huang, Y. *et al.* Antisolvent Engineering to Optimize Grain Crystallinity and Hole-Blocking Capability of Perovskite Films for High-Performance Photovoltaics. *Adv. Mater.* **33**, e2102816, doi:10.1002/adma.202102816 (2021).
- Gao, L., You, J. & Liu, S. Superior photovoltaics/optoelectronics of two-dimensional halide perovskites. *J. Energy Chem.* **57**, 69-82, doi:10.1016/j.jechem.2020.08.022 (2021).
- Proppe, A. H. *et al.* Multication perovskite 2D/3D interfaces form via progressive dimensional reduction. *Nat. Commun.* **12**, 3472, doi:10.1038/s41467-021-23616-9 (2021).
- 132 Chen, H. *et al.* Quantum-size-tuned heterostructures enable efficient and stable inverted perovskite solar cells. *Nat Photonics* **16**, 352-358, doi:10.1038/s41566-022-00985-1 (2022).
- Wang, Y. *et al.* Improvement in the Performance of Inverted 3D/2D Perovskite Solar Cells by Ambient Exposure. *Sol. RRL* **6**, 2200224, doi:10.1002/solr.202200224 (2022).
- Liu, X. *et al.* Full Defects Passivation Enables 21% Efficiency Perovskite Solar Cells Operating in Air. *Adv. Energy Mater.* **10**, 2001958, doi:10.1002/aenm.202001958 (2020).
- Gharibzadeh, S. *et al.* Two birds with one stone: dual grain-boundary and interface passivation enables >22% efficient inverted methylammonium-free perovskite solar cells. *Energy Environ. Sci.* **14**, 5875-5893, doi:10.1039/d1ee01508g (2021).
- Xu, W. *et al.* Suppressing Defects-Induced Nonradiative Recombination for Efficient Perovskite Solar Cells through Green Antisolvent Engineering. *Adv. Mater.* **32**, e2003965, doi:10.1002/adma.202003965 (2020).
- 137 Cao, Q. *et al.* Efficient and stable inverted perovskite solar cells with very high fill factors via incorporation of star-shaped polymer. *Sci. Adv.* 7, eabg0633, doi:10.1126/sciadv.abg0633 (2021).
- Zheng, M. *et al.* Spatial configuration engineering of perylenediimide-based non-fullerene electron transport materials for efficient inverted perovskite solar cells. *J. Energy Chem.* **56**, 374-382, doi:10.1016/j.jechem.2020.08.012 (2021).
- Han, W. *et al.* Improving the performance of perovskite solar cells by surface passivation. *J. Energy Chem.* **46**, 202-207, doi:10.1016/j.jechem.2019.11.004 (2020).
- Taylor, A. D. *et al.* A general approach to high-efficiency perovskite solar cells by any antisolvent. *Nat. Commun.* **12**, 1878, doi:10.1038/s41467-021-22049-8

- (2021).
- Yang, S. *et al.* Stabilizing halide perovskite surfaces for solar cell operation with wide-bandgap lead oxysalts. *Science* **365**, 473-478, doi:10.1126/science.aax3294 (2019).
- Lu, Y.-N. *et al.* Constructing an n/n⁺ homojunction in a monolithic perovskite film for boosting charge collection in inverted perovskite photovoltaics. *Energy Environ. Sci.* **14**, 4048-4058, doi:10.1039/d1ee00918d (2021).
- Min, H. *et al.* Perovskite solar cells with atomically coherent interlayers on SnO₂ electrodes. *Nature* **598**, 444-450, doi:10.1038/s41586-021-03964-8 (2021).
- Yoo, J. J. *et al.* Efficient perovskite solar cells via improved carrier management. *Nature* **590**, 587-593, doi:10.1038/s41586-021-03285-w (2021).
- Dou, J. *et al.* Improved interfacial adhesion for stable flexible inverted perovskite solar cells. *J. Energy Chem.* **76**, 288-294, doi:10.1016/j.jechem.2022.09.044 (2023).
- Wu, S. *et al.* Modulation of Defects and Interfaces through Alkylammonium Interlayer for Efficient Inverted Perovskite Solar Cells. *Joule* **4**, 1248-1262, doi:10.1016/j.joule.2020.04.001 (2020).
- Wang, S. *et al.* Tailoring the mercaptan ligands for high performance inverted perovskite solar cells with efficiency exceeding 21%. *J. Energy Chem.* **60**, 169-177, doi:10.1016/j.jechem.2020.12.035 (2021).
- Ma, R. *et al.* Rational Anode Engineering Enables Progresses for Different Types of Organic Solar Cells. *Adv. Energy Mater.* **11**, 2100492, doi:10.1002/aenm.202100492 (2021).
- Li, J. *et al.* Universal Bottom Contact Modification with Diverse 2D Spacers for High-Performance Inverted Perovskite Solar Cells. *Adv. Funct. Mater.* **31**, 2104036, doi:10.1002/adfm.202104036 (2021).
- 150 Chen, Y. *et al.* Ion Compensation of Buried Interface Enables Highly Efficient and Stable Inverted MA Free Perovskite Solar Cells. *Adv. Funct. Mater.*, 2206703, doi:10.1002/adfm.202206703 (2022).
- Zhao, Y. *et al.* Inactive (PbI₂)2RbCl stabilizes perovskite films for efficient solar cells. *Science* **377**, 531-534, doi:10.1126/science.abp8873 (2022).
- Jeong, J. *et al.* Pseudo-halide anion engineering for alpha-FAPbI₃ perovskite solar cells. *Nature* **592**, 381-385, doi:10.1038/s41586-021-03406-5 (2021).
- Kim, M. *et al.* Conformal quantum dot-SnO₂ layers as electron transporters for efficient perovskite solar cells. *Science* **375**, 302-306, doi:10.1126/science.abh1885 (2022).
- Rong, Y. *et al.* Challenges for commercializing perovskite solar cells. *Science* **361**, 1214, doi:10.1126/science.aat8235 (2018).
- Kang, Q. *et al.* A New PEDOT Derivative for Efficient Organic Solar Cell with a Fill Factor of 0.80. *Adv. Energy Mater.* **12**, 2103892, doi:10.1002/aenm.202103892 (2022).

- Mei, A. *et al.* Stabilizing Perovskite Solar Cells to IEC61215:2016 Standards with over 9,000-h Operational Tracking. *Joule* **4**, 2646-2660, doi:10.1016/j.joule.2020.09.010 (2020).
- Zheng, X. *et al.* Managing grains and interfaces via ligand anchoring enables 22.3%-efficiency inverted perovskite solar cells. *Nat Energy* **5**, 131-140, doi:10.1038/s41560-019-0538-4 (2020).
- Fakharuddin, A., Schmidt-Mende, L., Garcia-Belmonte, G., Jose, R. & Mora-Sero, I. Interfaces in Perovskite Solar Cells. *Adv. Energy Mater.* 7, 1700623, doi:10.1002/aenm.201700623 (2017).
- Zheng, X. *et al.* Quantum Dots Supply Bulk- and Surface-Passivation Agents for Efficient and Stable Perovskite Solar Cells. *Joule* **3**, 1963-1976, doi:10.1016/j.joule.2019.05.005 (2019).
- Zhang, M. *et al.* Reconfiguration of interfacial energy band structure for high-performance inverted structure perovskite solar cells. *Nat. Commun.* **10**, 4593, doi:10.1038/s41467-019-12613-8 (2019).
- Wang, S. *et al.* Targeted Therapy for Interfacial Engineering Toward Stable and Efficient Perovskite Solar Cells. *Adv. Mater.* **31**, 1903691, doi:10.1002/adma.201903691 (2019).
- Yao, Y. *et al.* Organic Hole-Transport Layers for Efficient, Stable, and Scalable Inverted Perovskite Solar Cells. *Adv. Mater.* **34**, 2203794, doi:10.1002/adma.202203794 (2022).
- Han, T. H. *et al.* Interface and Defect Engineering for Metal Halide Perovskite Optoelectronic Devices. *Adv. Mater.* **31**, 1803515, doi:10.1002/adma.201803515 (2019).
- Fu, L. *et al.* Defect passivation strategies in perovskites for an enhanced photovoltaic performance. *Energy Environ. Sci.* **13**, 4017-4056, doi:10.1039/d0ee01767a (2020).
- 165 Cacovich, S. *et al.* Imaging and quantifying non-radiative losses at 23% efficient inverted perovskite solar cells interfaces. *Nat. Commun.* **13**, 2868, doi:10.1038/s41467-022-30426-0 (2022).
- Luo, X. *et al.* Effective Passivation with Self-Organized Molecules for Perovskite Photovoltaics. *Adv. Mater.* **34**, 2202100, doi:10.1002/adma.202202100 (2022).
- Qin, M. *et al.* Fused-Ring Electron Acceptor ITIC-Th: A Novel Stabilizer for Halide Perovskite Precursor Solution. *Adv. Energy Mater.* **8**, 1703399, doi:10.1002/aenm.201703399 (2018).
- Yang, Q. *et al.* Hydroxylated non-fullerene acceptor for highly efficient inverted perovskite solar cells. *Energy Environ. Sci.* **14**, 6536-6545, doi:10.1039/d1ee02248b (2021).
- Hu, Q. *et al.* Improving Efficiency and Stability of Perovskite Solar Cells Enabled by A Near-Infrared-Absorbing Moisture Barrier. *Joule* **4**, 1575-1593, doi:10.1016/j.joule.2020.06.007 (2020).

- Liu, X. *et al.* Energy level-modulated non-fullerene small molecule acceptors for improved V_{OC} and efficiency of inverted perovskite solar cells. *J. Mater. Chem. A* 7, 3336-3343, doi:10.1039/c8ta12028e (2019).
- Yang, G., Qin, P., Fang, G. & Li, G. A Lewis Base-Assisted Passivation Strategy Towards Highly Efficient and Stable Perovskite Solar Cells. *Sol. RRL* **2**, 1800055, doi:10.1002/solr.201800055 (2018).
- Han, G. & Yi, Y. Molecular Insight into Efficient Charge Generation in Low-Driving-Force Nonfullerene Organic Solar Cells. *Acc. Chem. Res.* **55**, 869-877, doi:10.1021/acs.accounts.1c00742 (2022).
- Li, W., Liu, D. & Wang, T. Stability Of Non-Fullerene Electron Acceptors and Their Photovoltaic Devices. *Adv. Funct. Mater.* **31**, 2104552, doi:10.1002/adfm.202104552 (2021).
- Zhang, Z. G. & Li, Y. Polymerized Small-Molecule Acceptors for High-Performance All-Polymer Solar Cells. *Angew. Chem. Int. Ed.* 60, 4422-4433, doi:10.1002/anie.202009666 (2021).
- Zhang, Z. G. *et al.* Constructing a Strongly Absorbing Low-Bandgap Polymer Acceptor for High-Performance All-Polymer Solar Cells. *Angew. Chem. Int. Ed.*56, 13503-13507, doi:10.1002/anie.201707678 (2017).
- Qin, P. L. *et al.* Stable and Efficient Organo-Metal Halide Hybrid Perovskite Solar Cells via pi-Conjugated Lewis Base Polymer Induced Trap Passivation and Charge Extraction. *Adv. Mater.* **30**, 1706126, doi:10.1002/adma.201706126 (2018).
- 177 Cheng, Q. *et al.* Molecular Self-Assembly Regulated Dopant-Free Hole Transport Materials for Efficient and Stable n-i-p Perovskite Solar Cells and Scalable Modules. *Angew. Chem. Int. Ed.* **61**, 202210613, doi:10.1002/anie.202210613 (2022).
- 178 Cui, C., Li, Y. & Li, Y. Fullerene Derivatives for the Applications as Acceptor and Cathode Buffer Layer Materials for Organic and Perovskite Solar Cells. *Adv. Energy Mater.* 7, 1601251, doi:10.1002/aenm.201601251 (2017).
- Wu, T. *et al.* Efficient Defect Passivation for Perovskite Solar Cells by Controlling the Electron Density Distribution of Donor-π-Acceptor Molecules. *Adv. Energy Mater.* **9**, 1803766, doi:10.1002/aenm.201803766 (2019).
- Wang, J. *et al.* A New Polymer Donor Enables Binary All-Polymer Organic Photovoltaic Cells with 18% Efficiency and Excellent Mechanical Robustness. *Adv. Mater.* **34**, 2205009, doi:10.1002/adma.202205009 (2022).
- Ma, R. *et al.* Achieving high efficiency and well-kept ductility in ternary all-polymer organic photovoltaic blends thanks to two well miscible donors. *Matter* 5, 725-734, doi:10.1016/j.matt.2021.12.002 (2022).
- Aydin, E., De Bastiani, M. & De Wolf, S. Defect and Contact Passivation for Perovskite Solar Cells. *Adv. Mater.* **31**, 1900428, doi:10.1002/adma.201900428 (2019).
- Deng, X. et al. Highly efficient and stable perovskite solar cells enabled by a

- fluoro-functionalized TiO₂ inorganic interlayer. *Matter* **4**, 3301-3312, doi:10.1016/j.matt.2021.08.012 (2021).
- 184 Xiong, Z. *et al.* Simultaneous Interfacial Modification and Crystallization Control by Biguanide Hydrochloride for Stable Perovskite Solar Cells with PCE of 24.4%. *Adv. Mater.* **34**, 2106118, doi:10.1002/adma.202106118 (2022).
- Gao, Y. *et al.* Highly Stable Lead-Free Perovskite Field-Effect Transistors Incorporating Linear π-Conjugated Organic Ligands. *J. Am. Chem. Soc.* **141**, 15577-15585, doi:10.1021/jacs.9b06276 (2019).
- Wang, Y. *et al.* Stabilizing heterostructures of soft perovskite semiconductors. *Science* **365**, 687-691, doi:10.1126/science.aax8018 (2019).
- 187 Cho, S. H. *et al.* Investigation of Defect-Tolerant Perovskite Solar Cells with Long-Term Stability via Controlling the Self-Doping Effect. *Adv. Energy Mater.* **11**, 2100555, doi:10.1002/aenm.202100555 (2021).
- Wang, H. B. *et al.* Pre-annealing treatment for high-efficiency perovskite solar cells via sequential deposition. *Joule* **6**, 2869-2884, doi:10.1016/j.joule.2022.10.001 (2022).
- Huang, K. *et al.* High-Performance Flexible Perovskite Solar Cells via Precise Control of Electron Transport Layer. *Adv. Energy Mater.* **9**, 1901419, doi:10.1002/aenm.201901419 (2019).
- 190 Chen, W. *et al.* Precise Control of Crystal Growth for Highly Efficient CsPbI₂Br Perovskite Solar Cells. *Joule* **3**, 191-204, doi:10.1016/j.joule.2018.10.011 (2019).
- 191 Choi, H. *et al.* A Facile Surface Passivation Enables Thermally Stable and Efficient Planar Perovskite Solar Cells Using a Novel IDTT Based Small Molecule Additive. *Adv. Energy Mater.* 11, 2003829, doi:10.1002/aenm.202003829 (2021).
- Zhou, X. *et al.* Integrated Ideal-Bandgap Perovskite/Bulk-Heterojunction Solar Cells with Efficiencies > 24%. *Adv. Mater.* **34**, 2205809, doi:10.1002/adma.202205809 (2022).
- Yang, D. *et al.* Stable Efficiency Exceeding 20.6% for Inverted Perovskite Solar Cells through Polymer-Optimized PCBM Electron-Transport Layers. *Nano Lett.* 19, 3313-3320, doi:10.1021/acs.nanolett.9b00936 (2019).
- Jiang, J. *et al.* Polymer Doping for High-Efficiency Perovskite Solar Cells with Improved Moisture Stability. *Adv. Energy Mater.* **8**, 1701757, doi:10.1002/aenm.201701757 (2018).
- Bai, S. *et al.* Planar perovskite solar cells with long-term stability using ionic liquid additives. *Nature* **571**, 245-250, doi:10.1038/s41586-019-1357-2 (2019).
- Zhang, J., Jiang, X., Liu, X., Guo, X. & Li, C. Maximizing Merits of Undesirable δ-FAPbI₃ by Constructing yellow/black Heterophase Bilayer for Efficient and Stable Perovskite Photovoltaics. *Adv. Funct. Mater.* **32**, 2204642, doi:10.1002/adfm.202204642 (2022).
- Du, T. et al. Additive-Free, Low-Temperature Crystallization of Stable alpha-

- FAPbI₃ Perovskite. *Adv. Mater.* **34**, 2107850, doi:10.1002/adma.202107850 (2022).
- 198 Pering, S. R. *et al.* Azetidinium lead iodide for perovskite solar cells. *J. Mater. Chem. A* **5**, 20658-20665, doi:10.1039/c7ta07545f (2017).
- 199 Chen, A. Z. *et al.* Crystallographic orientation propagation in metal halide perovskite thin films. *J. Mater. Chem. A* **5**, 7796-7800, doi:10.1039/c7ta02203d (2017).
- Zhang, F. *et al.* Isomer-Pure Bis-PCBM-Assisted Crystal Engineering of Perovskite Solar Cells Showing Excellent Efficiency and Stability. *Adv. Mater.* **29**, 1606806, doi:10.1002/adma.201606806 (2017).
- Zhan, Y. *et al.* Elastic Lattice and Excess Charge Carrier Manipulation in 1D-3D Perovskite Solar Cells for Exceptionally Long-Term Operational Stability. *Adv. Mater.* **33**, 2105170, doi:10.1002/adma.202105170 (2021).
- Jeong, S. *et al.* Cyclohexylammonium-Based 2D/3D Perovskite Heterojunction with Funnel-Like Energy Band Alignment for Efficient Solar Cells (23.91%). *Adv. Energy Mater.* **11**, 2102236, doi:10.1002/aenm.202102236 (2021).
- Shao, Y., Xiao, Z., Bi, C., Yuan, Y. & Huang, J. Origin and elimination of photocurrent hysteresis by fullerene passivation in CH3NH₃PbI₃ planar heterojunction solar cells. *Nat. Commun.* **5**, 5784, doi:10.1038/ncomms6784 (2014).
- Wang, F., Bai, S., Tress, W., Hagfeldt, A. & Gao, F. Defects engineering for high-performance perovskite solar cells. *Npj Flex Electron* **2**, 22, doi:ARTN 22 10.1038/s41528-018-0035-z (2018).
- Wang, W. T. *et al.* Synergistic Reinforcement of Built-In Electric Fields for Highly Efficient and Stable Perovskite Photovoltaics. *Adv. Funct. Mater.* **30**, 1909755, doi:10.1002/adfm.201909755 (2020).
- Xiong, S. *et al.* Direct Observation on p- to n-Type Transformation of Perovskite Surface Region during Defect Passivation Driving High Photovoltaic Efficiency. *Joule* **5**, 467-480, doi:10.1016/j.joule.2020.12.009 (2021).
- Sun, Y. *et al.* Simultaneously Enhanced Efficiency and Mechanical Durability in Ternary Solar Cells Enabled by Low-Cost Incompletely Separated Fullerenes. *Macromol. Rapid Commun.* **43**, e2200139, doi:10.1002/marc.202200139 (2022).
- 208 Kataria, M. et al. Y-Series-Based Polymer Acceptors for High-Performance All-Polymer Solar Cells in Binary and Non-binary Systems. ACS Energy Lett. 7, 3835-3854, doi:10.1021/acsenergylett.2c01541 (2022).
- 209 Glowienka, D. & Galagan, Y. Light Intensity Analysis of Photovoltaic Parameters for Perovskite Solar Cells. *Adv. Mater.* **34**, 2105920, doi:10.1002/adma.202105920 (2021).
- Caprioglio, P. *et al.* On the Origin of the Ideality Factor in Perovskite Solar Cells. *Adv. Energy Mater.* **10**, 2000502, doi:10.1002/aenm.202000502 (2020).
- 211 Xiong, L. et al. Fully High-Temperature-Processed SnO₂ as Blocking Layer and

- Scaffold for Efficient, Stable, and Hysteresis-Free Mesoporous Perovskite Solar Cells. *Adv. Funct. Mater.* **28**, 1706276, doi:10.1002/adfm.201706276 (2018).
- von Hauff, E., Dyakonov, V. & Parisi, J. Study of field effect mobility in PCBM films and P3HT:PCBM blends. *Sol. Energy Mater. Sol. Cells* **87**, 149-156, doi:10.1016/j.solmat.2004.06.014 (2005).
- Jiang, Y. *et al.* An alcohol-dispersed conducting polymer complex for fully printable organic solar cells with improved stability. *Nat Energy* 7, 352-359, doi:10.1038/s41560-022-00997-9 (2022).
- Jung, S.-K. *et al.* Nonfullerene Electron Transporting Material Based on Naphthalene Diimide Small Molecule for Highly Stable Perovskite Solar Cells with Efficiency Exceeding 20%. *Adv. Funct. Mater.* **28**, 1800346, doi:10.1002/adfm.201800346 (2018).
- Wu, F. *et al.* Efficient small-molecule non-fullerene electron transporting materials for high-performance inverted perovskite solar cells. *J. Mater. Chem. A* **6**, 4443-4448, doi:10.1039/c8ta00492g (2018).
- Said, A. A. *et al.* Efficient Inverted Perovskite Solar Cells by Employing N-Type (D-A1-D-A2) Polymers as Electron Transporting Layer. *Small* **15**, e1803339, doi:10.1002/smll.201803339 (2019).
- Wang, H. L. *et al.* Interface engineering with a novel n-type small organic molecule for efficient inverted perovskite solar cells. *Chem. Eng. J.* **392**, 123677, doi:10.1016/j.cej.2019.123677 (2020).
- Cheng, Z. *et al.* Interfacial and Permeating Modification Effect of n-type Nonfullerene Acceptors toward High-Performance Perovskite Solar Cells. *Acs Appl Mater Inter* **13**, 40778-40787, doi:10.1021/acsami.1c13447 (2021).
- Jia, J., Wu, F., Zhu, L. & Yang, C. Unfused Electronic Acceptor-Based Polymers as Interfacial Materials for Efficient Inverted Perovskite Solar Cells. *Acs Appl Mater Inter* **13**, 33328-33334, doi:10.1021/acsami.1c09269 (2021).
- Xue, B. *et al.* The Role of Ending Groups in Nonfullerene Acceptors for Interfacial Modification in Perovskite Solar Cells. *Sol. RRL* **6**, 2100864, doi:10.1002/solr.202100864 (2021).
- Fan, Y. *et al.* A perylene diimide dimer-based electron transporting material with an A–D–A structure for efficient inverted perovskite solar cells. *J. Mater. Chem. C* **10**, 2544-2550, doi:10.1039/d1tc04176b (2022).
- Huang, J. *et al.* A dithieno[3,2-a:3',2'-j][5,6,11,12]chrysene diimide based polymer as an electron transport layer for efficient inverted perovskite solar cells. *J. Mater. Chem. C* **10**, 2703-2710, doi:10.1039/d1tc03942c (2022).
- Hu, S. *et al.* Optimized carrier extraction at interfaces for 23.6% efficient tin–lead perovskite solar cells. *Energy Environ. Sci.* **15**, 2096-2107, doi:10.1039/d2ee00288d (2022).
- Feng, K. *et al.* Non-fullerene electron-transporting materials for high-performance and stable perovskite solar cells. *Nat. Mater.* **24**, 770-777, doi:10.1038/s41563-025-02163-4 (2025).

- Li, N., Niu, X., Chen, Q. & Zhou, H. Towards commercialization: the operational stability of perovskite solar cells. *Chem. Soc. Rev.* **49**, 8235-8286, doi:10.1039/d0cs00573h (2020).
- Domanski, K., Alharbi, E. A., Hagfeldt, A., Grätzel, M. & Tress, W. Systematic investigation of the impact of operation conditions on the degradation behaviour of perovskite solar cells. *Nat Energy* **3**, 61-67, doi:10.1038/s41560-017-0060-5 (2018).
- Wang, J. *et al.* Tuning an Electrode Work Function Using Organometallic Complexes in Inverted Perovskite Solar Cells. *J. Am. Chem. Soc.* **143**, 7759-7768, doi:10.1021/jacs.1c02118 (2021).
- Wang, G. *et al.* Customizing a Coordinative Crab Molecule BCP-3N with Multifunctionality for High-Performance Inverted Perovskite Solar Cells. *Sol. RRL* **6**, 2200559, doi:10.1002/solr.202200559 (2022).
- Grancini, G. *et al.* One-Year stable perovskite solar cells by 2D/3D interface engineering. *Nat. Commun.* **8**, 15684, doi:10.1038/ncomms15684 (2017).
- Yan, C. *et al.* Ambipolar-transport wide-bandgap perovskite interlayer for organic photovoltaics with over 18% efficiency. *Matter* **5**, 2238-2250, doi:10.1016/j.matt.2022.04.028 (2022).
- Zhao, X. *et al.* Accelerated aging of all-inorganic, interface-stabilized perovskite solar cells. *Science* **377**, 307-310, doi:10.1126/science.abn5679 (2022).
- Li, Y., Xie, H., Lim, E. L., Hagfeldt, A. & Bi, D. Recent Progress of Critical Interface Engineering for Highly Efficient and Stable Perovskite Solar Cells. *Adv. Energy Mater.* **12**, 2102730, doi:10.1002/aenm.202102730 (2021).
- Zhan, L. *et al.* Manipulating Charge Transfer and Transport via Intermediary Electron Acceptor Channels Enables 19.3% Efficiency Organic Photovoltaics. *Adv. Energy Mater.* **12**, 2201076, doi:10.1002/aenm.202201076 (2022).
- 234 Xiong, X. *et al.* Melamine-Doped Cathode Interlayer Enables High-Efficiency Organic Solar Cells. *ACS Energy Lett.* **6**, 3582-3589, doi:10.1021/acsenergylett.1c01730 (2021).
- Jeong, B., Gkoupidenis, P. & Asadi, K. Solution-Processed Perovskite Field-Effect Transistor Artificial Synapses. *Adv. Mater.* **33**, 2104034, doi:10.1002/adma.202104034 (2021).
- Kang, Q. *et al.* n-doped inorganic molecular clusters as a new type of hole transport material for efficient organic solar cells. *Joule* **5**, 646-658, doi:10.1016/j.joule.2021.01.011 (2021).
- Yu, R. *et al.* Efficient interface modification via multi-site coordination for improved efficiency and stability in organic solar cells. *Energy Environ. Sci.* **15**, 822-829, doi:10.1039/d1ee03263a (2022).
- Bai, Y., Meng, X. & Yang, S. Interface Engineering for Highly Efficient and Stable Planar p-i-n Perovskite Solar Cells. *Adv. Energy Mater.* **8**, 1701883, doi:10.1002/aenm.201701883 (2018).

- Zhu, L. *et al.* Single-junction organic solar cells with over 19% efficiency enabled by a refined double-fibril network morphology. *Nat. Mater.* **21**, 656-663, doi:10.1038/s41563-022-01244-y (2022).
- 240 Chin, Y. C., Daboczi, M., Henderson, C., Luke, J. & Kim, J. S. Suppressing PEDOT:PSS Doping-Induced Interfacial Recombination Loss in Perovskite Solar Cells. *ACS Energy Lett.* 7, 560-568, doi:10.1021/acsenergylett.1c02577 (2022).
- Vitoratos, E. *et al.* Thermal degradation mechanisms of PEDOT:PSS. *Org. Electron.* **10**, 61-66, doi:10.1016/j.orgel.2008.10.008 (2009).
- Cameron, J. & Skabara, P. J. The damaging effects of the acidity in PEDOT:PSS on semiconductor device performance and solutions based on non-acidic alternatives. *Mater. Horiz.* **7**, 1759-1772, doi:10.1039/c9mh01978b (2020).
- Yun, J. M. *et al.* Solution-processable reduced graphene oxide as a novel alternative to PEDOT:PSS hole transport layers for highly efficient and stable polymer solar cells. *Adv. Mater.* **23**, 4923-4928, doi:10.1002/adma.201102207 (2011).
- Labban, A. E. *et al.* Improved Efficiency in Inverted Perovskite Solar Cells Employing a Novel Diarylamino-Substituted Molecule as PEDOT:PSS Replacement. *Adv. Energy Mater.* **6**, 1502101, doi:10.1002/aenm.201502101 (2016).
- Chen, W.-Y. *et al.* Low-cost solution-processed copper iodide as an alternative to PEDOT:PSS hole transport layer for efficient and stable inverted planar heterojunction perovskite solar cells. *J. Mater. Chem. A* **3**, 19353-19359, doi:10.1039/c5ta05286f (2015).
- 246 Kim, S. Y., Cho, S. J., Byeon, S. E., He, X. & Yoon, H. J. Self-Assembled Monolayers as Interface Engineering Nanomaterials in Perovskite Solar Cells. *Adv. Energy Mater.* **10**, 2002606, doi:10.1002/aenm.202002606 (2020).
- Dai, Z. *et al.* Interfacial toughening with self-assembled monolayers enhances perovskite solar cell reliability. *Science* **372**, 618-622, doi:10.1126/science.abf5602 (2021).
- Jiang, W. *et al.* π-Expanded Carbazoles as Hole-Selective Self-Assembled Monolayers for High-Performance Perovskite Solar Cells. *Angew. Chem. Int. Ed.* **61**, 202213560, doi:10.1002/anie.202213560 (2022).
- Lin, J. *et al.* Dual Surface Modifications of NiOx/Perovskite Interface for Enhancement of Device Stability. *Acs Appl Mater Inter* **15**, 24437-24447, doi:10.1021/acsami.3c02156 (2023).
- Deng, X. *et al.* Co-assembled Monolayers as Hole-Selective Contact for High-Performance Inverted Perovskite Solar Cells with Optimized Recombination Loss and Long-Term Stability. *Angew. Chem. Int. Ed.* **61**, 202203088, doi:10.1002/anie.202203088 (2022).
- Wang, S. *et al.* Water-Soluble Triazolium Ionic-Liquid-Induced Surface Self-Assembly to Enhance the Stability and Efficiency of Perovskite Solar Cells. *Adv.*

- Funct. Mater. 29, 1900417, doi:10.1002/adfm.201900417 (2019).
- Wolff, C. M. *et al.* Perfluorinated Self-Assembled Monolayers Enhance the Stability and Efficiency of Inverted Perovskite Solar Cells. *ACS Nano* **14**, 1445-1456, doi:10.1021/acsnano.9b03268 (2020).
- Liu, M. *et al.* Compact Hole-Selective Self-Assembled Monolayers Enabled by Disassembling Micelles in Solution for Efficient Perovskite Solar Cells. *Adv. Mater.* **35**, 2304415, doi:10.1002/adma.202304415 (2023).
- Vidyasagar, D. *et al.* Surface-functionalized hole-selective monolayer for high efficiency single-junction wide-bandgap and monolithic tandem perovskite solar cells. *J. Energy Chem.* **88**, 317-326, doi:10.1016/j.jechem.2023.09.023 (2024).
- Kulkarni, A. *et al.* A Universal Strategy of Perovskite Ink Substrate Interaction to Overcome the Poor Wettability of a Self-Assembled Monolayer for Reproducible Perovskite Solar Cells. *Adv. Funct. Mater.* **33**, 2305812, doi:10.1002/adfm.202305812 (2023).
- Farag, A. *et al.* Evaporated Self-Assembled Monolayer Hole Transport Layers: Lossless Interfaces in p-i-n Perovskite Solar Cells. *Adv. Energy Mater.* **13**, 2203982, doi:10.1002/aenm.202203982 (2023).
- Phung, N. *et al.* Enhanced Self-Assembled Monolayer Surface Coverage by ALD NiO in p-i-n Perovskite Solar Cells. *Acs Appl Mater Inter* **14**, 2166-2176, doi:10.1021/acsami.1c15860 (2021).
- Kapil, G. *et al.* Tin–Lead Perovskite Solar Cells Fabricated on Hole Selective Monolayers. *ACS Energy Lett.* **7**, 966-974, doi:10.1021/acsenergylett.1c02718 (2022).
- Park, S. M. *et al.* Low-loss contacts on textured substrates for inverted perovskite solar cells. *Nature* **624**, 289-294, doi:10.1038/s41586-023-06745-7 (2023).
- Shi, Y. *et al.* New Ruthenium Sensitizers Featuring Bulky Ancillary Ligands Combined with a Dual Functioned Coadsorbent for High Efficiency Dye-Sensitized Solar Cells. *Acs Appl Mater Inter* 5, 144-153, doi:10.1021/am302318z (2012).
- Lin, Y. *et al.* Self-Assembled Monolayer Enables Hole Transport Layer-Free Organic Solar Cells with 18% Efficiency and Improved Operational Stability. *ACS Energy Lett.* **5**, 2935-2944, doi:10.1021/acsenergylett.0c01421 (2020).
- Bin, H. *et al.* Finetuning Hole-Extracting Monolayers for Efficient Organic Solar Cells. *Acs Appl Mater Inter* **14**, 16497-16504, doi:10.1021/acsami.2c01900 (2022).
- Thompson, A. P. *et al.* LAMMPS a flexible simulation tool for particle-based materials modeling at the atomic, meso, and continuum scales. *Comput. Phys. Commun.* **271**, 108171, doi:10.1016/j.cpc.2021.108171 (2022).
- Jorgensen, W. L. & Tirado-Rives, J. The OPLS [optimized potentials for liquid simulations] potential functions for proteins, energy minimizations for crystals

- of cyclic peptides and crambin. *J. Am. Chem. Soc.* **110**, 1657-1666, doi:10.1021/ja00214a001 (1988).
- Dodda, L. S., Cabeza de Vaca, I., Tirado-Rives, J. & Jorgensen, W. L. LigParGen web server: an automatic OPLS-AA parameter generator for organic ligands. *Nucleic Acids Res.* **45**, W331-W336, doi:10.1093/nar/gkx312 (2017).
- Meltzer, C. *et al.* Indentation and Self-Healing Mechanisms of a Self-Assembled Monolayer—A Combined Experimental and Modeling Study. *J. Am. Chem. Soc.* **136**, 10718-10727, doi:10.1021/ja5048076 (2014).
- Rappe, A. K., Casewit, C. J., Colwell, K. S., Goddard, W. A. & Skiff, W. M. UFF, a full periodic table force field for molecular mechanics and molecular dynamics simulations. *J. Am. Chem. Soc.* **114**, 10024-10035, doi:10.1021/ja00051a040 (2002).
- Stukowski, A. Visualization and analysis of atomistic simulation data with OVITO–the Open Visualization Tool. *Modell. Simul. Mater. Sci. Eng.* **18**, 015012, doi:10.1088/0965-0393/18/1/015012 (2010).
- Kralj, S. *et al.* Impact of the TCO Microstructure on the Electronic Properties of Carbazole-Based Self-Assembled Monolayers. *ACS Energy Lett.*, 366-374, doi:10.1021/acsmaterialslett.3c01166 (2023).
- Spadafora, E. J., Demadrille, R., Ratier, B. & Grévin, B. Imaging the Carrier Photogeneration in Nanoscale Phase Segregated Organic Heterojunctions by Kelvin Probe Force Microscopy. *Nano Lett.* 10, 3337-3342, doi:10.1021/nl101001d (2010).
- Guan, S. *et al.* Self-Assembled Interlayer Enables High-Performance Organic Photovoltaics with Power Conversion Efficiency Exceeding 20%. *Adv. Mater.*, 2400342, doi:10.1002/adma.202400342 (2024).
- Tan, Q. et al. Inverted perovskite solar cells using dimethylacridine-based dopants. *Nature* **620**, 545-551, doi:10.1038/s41586-023-06207-0 (2023).
- Liu, T. *et al.* Tailoring vertical phase distribution of quasi-two-dimensional perovskite films via surface modification of hole-transporting layer. *Nat. Commun.* **10**, 878, doi:10.1038/s41467-019-08843-5 (2019).
- Shu, H. *et al.* Self-Assembled Hydrophobic Molecule-Based Surface Modification: A Strategy to Improve Efficiency and Stability of Perovskite Solar Cells. *ACS Sustainable Chem. Eng.* **8**, 10859-10869, doi:10.1021/acssuschemeng.0c02983 (2020).
- Wu, J. *et al.* Bisphosphonate-Anchored Self-Assembled Molecules with Larger Dipole Moments for Efficient Inverted Perovskite Solar Cells with Excellent Stability. *Adv. Mater.*, 2401537, doi:10.1002/adma.202401537 (2024).
- Li, D. *et al.* In Situ Interface Engineering for Highly Efficient Electron-Transport-Layer-Free Perovskite Solar Cells. *Nano Lett.* **20**, 5799-5806, doi:10.1021/acs.nanolett.0c01689 (2020).
- Zhang, S. *et al.* Minimizing buried interfacial defects for efficient inverted perovskite solar cells. *Science* **380**, 404-409, doi:10.1126/science.adg3755

- (2023).
- Hao, M. *et al.* Flattening Grain-Boundary Grooves for Perovskite Solar Cells with High Optomechanical Reliability. *Adv. Mater.* **35**, 2211155, doi:10.1002/adma.202211155 (2023).
- 279 Rohrer, G. S. Grain boundary energy anisotropy: a review. *J. Mater. Sci.* **46**, 5881-5895, doi:10.1007/s10853-011-5677-3 (2011).
- Wu, X. *et al.* Backbone Engineering Enables Highly Efficient Polymer Hole-Transporting Materials for Inverted Perovskite Solar Cells. *Adv. Mater.* **35**, 2208431, doi:10.1002/adma.202208431 (2023).
- Fan, R. *et al.* Tungstate-mediated In-situ Passivation of Grain Boundary Grooves in Perovskite Solar Cells. *Angew. Chem. Int. Ed.* **62**, 202303176, doi:10.1002/anie.202303176 (2023).
- Fu, S. *et al.* Efficient Passivation with Lead Pyridine-2-Carboxylic for High-Performance and Stable Perovskite Solar Cells. *Adv. Energy Mater.* **9**, 1901852, doi:10.1002/aenm.201901852 (2019).
- Zhang, K. *et al.* Efficient Inorganic Vapor-Assisted Defects Passivation for Perovskite Solar Module. *Adv. Mater.* **35**, 2211593, doi:10.1002/adma.202211593 (2023).
- Paniagua, S. A. *et al.* Phosphonic Acid Modification of Indium—Tin Oxide Electrodes: Combined XPS/UPS/Contact Angle Studies. *J. Phys. Chem. C* **112**, 7809-7817, doi:10.1021/jp710893k (2008).
- 285 Koh, S. E. *et al.* Phenylphosphonic Acid Functionalization of Indium Tin Oxide: Surface Chemistry and Work Functions. *Langmuir* **22**, 6249-6255, doi:10.1021/la052379e (2006).
- Qin, P. L. *et al.* Stable and Efficient Organo-Metal Halide Hybrid Perovskite Solar Cells via π-Conjugated Lewis Base Polymer Induced Trap Passivation and Charge Extraction. *Adv. Mater.* **30**, 1706126, doi:10.1002/adma.201706126 (2018).
- 287 Chen, J., Kim, S.-G., Ren, X., Jung, H. S. & Park, N.-G. Effect of bidentate and tridentate additives on the photovoltaic performance and stability of perovskite solar cells. *J. Mater. Chem. A* 7, 4977-4987, doi:10.1039/c8ta11977e (2019).
- Steele, J. A. *et al.* How to GIWAXS: Grazing Incidence Wide Angle X-Ray Scattering Applied to Metal Halide Perovskite Thin Films. *Adv. Energy Mater.*, 202300760, doi:10.1002/aenm.202300760 (2023).
- Yang, T. *et al.* One-stone-for-two-birds strategy to attain beyond 25% perovskite solar cells. *Nat. Commun.* **14**, 839, doi:10.1038/s41467-023-36229-1 (2023).
- 290 Chen, P. *et al.* Efficient Inverted Perovskite Solar Cells via Improved Sequential Deposition. *Adv. Mater.* **35**, 2206345, doi:10.1002/adma.202206345 (2023).
- Wang, L. *et al.* Interface regulation enables hysteresis free wide-bandgap perovskite solar cells with low V_{OC} deficit and high stability. *Nano Energy* **90**, 106537, doi:10.1016/j.nanoen.2021.106537 (2021).
- 292 Khenkin, M. V. et al. Consensus statement for stability assessment and reporting

- for perovskite photovoltaics based on ISOS procedures. *Nat Energy* **5**, 35-49, doi:10.1038/s41560-019-0529-5 (2020).
- Fei, C. *et al.* Strong-bonding hole-transport layers reduce ultraviolet degradation of perovskite solar cells. *Science* **384**, 1126-1134, doi:10.1126/science.adi4531 (2024).
- Chai, G. *et al.* Fine-tuning of side-chain orientations on nonfullerene acceptors enables organic solar cells with 17.7% efficiency. *Energy Environ. Sci.* **14**, 3469-3479, doi:10.1039/d0ee03506h (2021).
- Bao, S. *et al.* Volatilizable Solid Additive-Assisted Treatment Enables Organic Solar Cells with Efficiency over 18.8% and Fill Factor Exceeding 80. *Adv. Mater.* **33**, 2105301, doi:10.1002/adma.202105301 (2021).
- Ge, Z. *et al.* Suppressing Trap Assisted Nonradiative Recombination via Interface Modification for Achieving Efficient Organic Solar Cells. *Adv. Energy Mater.* **14**, 2400203, doi:10.1002/aenm.202400203 (2024).
- Karki, A. *et al.* Unifying Charge Generation, Recombination, and Extraction in Low-Offset Non-Fullerene Acceptor Organic Solar Cells. *Adv. Energy Mater.*10, 2001203, doi:10.1002/aenm.202001203 (2020).
- Luo, Z. *et al.* Precisely Controlling the Position of Bromine on the End Group Enables Well-Regular Polymer Acceptors for All-Polymer Solar Cells with Efficiencies over 15%. *Adv. Mater.* **32**, 2005942, doi:10.1002/adma.202005942 (2020).
- 299 Cui, Y. *et al.* Organic photovoltaic cell with 17% efficiency and superior processability. *Natl. Sci. Rev.* **7**, 1239-1246, doi:10.1093/nsr/nwz200 (2020).
- 300 Chen, H. *et al.* Improved charge extraction in inverted perovskite solar cells with dual-site-binding ligands. *Science* **384**, 189-193, doi:10.1126/science.adm9474 (2024).
- Zhou, J. *et al.* Highly efficient and stable perovskite solar cells via a multifunctional hole transporting material. *Joule* **8**, 1691-1706, doi:10.1016/j.joule.2024.02.019 (2024).
- Al-Ashouri, A. *et al.* Conformal monolayer contacts with lossless interfaces for perovskite single junction and monolithic tandem solar cells. *Energy & Environmental Science* **12**, 3356-3369, doi:10.1039/c9ee02268f (2019).
- Jiang, Q. & Zhu, K. Rapid advances enabling high-performance inverted perovskite solar cells. *Nature Reviews Materials* **9**, 399-419, doi:10.1038/s41578-024-00678-x (2024).
- Yalcin, E. *et al.* Semiconductor self-assembled monolayers as selective contacts for efficient PiN perovskite solar cells. *Energy & Environmental Science* **12**, 230-237, doi:10.1039/c8ee01831f (2019).
- Guo, H. *et al.* Neglected acidity pitfall: boric acid-anchoring hole-selective contact for perovskite solar cells. *Natl. Sci. Rev.* **10**, nwad057, doi:10.1093/nsr/nwad057 (2023).
- 306 Jiang, W. et al. π-Expanded Carbazoles as Hole-Selective Self-Assembled

- Monolayers for High-Performance Perovskite Solar Cells. *Angew. Chem. Int. Ed.* **134**, e202213560, doi:10.1002/ange.202213560 (2022).
- 307 Ullah, A. *et al.* Novel Phenothiazine-Based Self-Assembled Monolayer as a Hole Selective Contact for Highly Efficient and Stable p-i-n Perovskite Solar Cells. *Adv. Energy Mater.* **12**, 2103175, doi:10.1002/aenm.202103175 (2021).
- Paniagua, S. A. *et al.* Phosphonic Acids for Interfacial Engineering of Transparent Conductive Oxides. *Chem. Rev.* **116**, 7117-7158, doi:10.1021/acs.chemrev.6b00061 (2016).
- Azam, M. *et al.* Dual functionality of charge extraction and interface passivation by self-assembled monolayers in perovskite solar cells. *Energy Environ. Sci.* **17**, 6974-7016, doi:10.1039/d4ee02661f (2024).
- Hotchkiss, P. J. *et al.* The Modification of Indium Tin Oxide with Phosphonic Acids: Mechanism of Binding, Tuning of Surface Properties, and Potential for Use in Organic Electronic Applications. *Acc. Chem. Res.* **45**, 337-346, doi:10.1021/ar200119g (2011).
- Qu, G. *et al.* Conjugated linker-boosted self-assembled monolayer molecule for inverted perovskite solar cells. *Joule* **8**, 2123-2134, doi:10.1016/j.joule.2024.05.005 (2024).
- Wang, W. *et al.* Versatile Self-Assembled Molecule Enables High-Efficiency Wide-Bandgap Perovskite Solar Cells and Organic Solar Cells. *Adv. Energy Mater.* **13**, 2300694, doi:10.1002/aenm.202300694 (2023).
- Jiang, W. *et al.* π-Expanded Carbazoles as Hole-Selective Self-Assembled Monolayers for High-Performance Perovskite Solar Cells. *Angewandte Chemie International Edition* **61**, e202213560, doi:10.1002/anie.202213560 (2022).
- Li, C. *et al.* Fully Aromatic Self-Assembled Hole-Selective Layer toward Efficient Inverted Wide-Bandgap Perovskite Solar Cells with Ultraviolet Resistance. *Angew. Chem. Int. Ed.* **136**, e202315281, doi:10.1002/ange.202315281 (2023).
- Jiang, W. *et al.* Spin-Coated and Vacuum-Processed Hole-Extracting Self-Assembled Multilayers with H-Aggregation for High-Performance Inverted Perovskite Solar Cells. *Angew. Chem. Int. Ed.* **63**, e202411730, doi:10.1002/anie.202411730 (2024).
- Wu, J. *et al.* Bisphosphonate-Anchored Self-Assembled Molecules with Larger Dipole Moments for Efficient Inverted Perovskite Solar Cells with Excellent Stability. *Adv. Mater.* **36**, 2401537, doi:10.1002/adma.202401537 (2024).
- Plank, M. *et al.* Photo-Arbuzov Reactions as a Broadly Applicable Surface Modification Strategy. *Adv. Funct. Mater.*, 2403408, doi:10.1002/adfm.202403408 (2024).
- Paramonov, P. B. *et al.* Theoretical Characterization of the Indium Tin Oxide Surface and of Its Binding Sites for Adsorption of Phosphonic Acid Monolayers. *Chem. Mater.* **20**, 5131-5133, doi:10.1021/cm8014622 (2008).
- 319 Zhang, W. et al. Structure, stability and electrochromic properties of polyaniline

- film covalently bonded to indium tin oxide substrate. *Appl. Surf. Sci.* **367**, 542-551, doi:10.1016/j.apsusc.2016.01.041 (2016).
- Chen, B. *et al.* Dual-Function Self-Assembled Molecules as Hole-Transport Layers for Thermally Evaporated High-Efficiency Blue Perovskite Light-Emitting Diodes. *Adv. Mater.*, 2411451, doi:10.1002/adma.202411451 (2024).
- 321 Köbl, J. *et al.* Adsorption of phenylphosphonic acid on rutile TiO2(110). *Surf. Sci.* **698**, 121612, doi:10.1016/j.susc.2020.121612 (2020).
- Zhang, C. *et al.* Phosphonic acid anchored tripodal molecular films on indium tin oxide. *Phys. Chem. Chem. Phys.* **26**, 11360-11369, doi:10.1039/d4cp00892h (2024).
- Ali, F., Roldán-Carmona, C., Sohail, M. & Nazeeruddin, M. K. Applications of Self-Assembled Monolayers for Perovskite Solar Cells Interface Engineering to Address Efficiency and Stability. *Adv. Energy Mater.* **10**, 2002989, doi:10.1002/aenm.202002989 (2020).
- Chang, Y. *et al.* Highly Oriented and Ordered Co-Assembly Monolayers for Inverted Perovskite Solar Cells. *Angew. Chem. Int. Ed.*, e202418883, doi:10.1002/ange.202418883 (2024).
- Li, D. *et al.* Co-adsorbed self-assembled monolayer enables high-performance perovskite and organic solar cells. *Nat. Commun.* **15**, 7605, doi:10.1038/s41467-024-51760-5 (2024).
- Zhang, X. *et al.* 3D Conjugated Hole Transporting Materials for Efficient and Stable Perovskite Solar Cells and Modules. *Adv. Mater.* **36**, 2310619, doi:10.1002/adma.202310619 (2024).
- Wu, M. *et al.* Reconstruction of the Indium Tin Oxide Surface Enhances the Adsorption of High-Density Self-Assembled Monolayer for Perovskite/Silicon Tandem Solar Cells. *Adv. Funct. Mater.* **33**, 2304708, doi:10.1002/adfm.202304708 (2023).
- 328 Xu, D., Wu, P. & Tan, H. Self-assembled monolayers for perovskite solar cells. *Information & Functional Materials* **1**, 2-25, doi:10.1002/ifm2.8 (2024).
- 329 Liu, D. *et al.* Strain analysis and engineering in halide perovskite photovoltaics. *Nat. Mater.* **20**, 1337-1346, doi:10.1038/s41563-021-01097-x (2021).
- Zhu, C. *et al.* Strain engineering in perovskite solar cells and its impacts on carrier dynamics. *Nat. Commun.* **10**, 815, doi:10.1038/s41467-019-08507-4 (2019).
- 331 Tress, W. *et al.* Interpretation and evolution of open-circuit voltage, recombination, ideality factor and subgap defect states during reversible light-soaking and irreversible degradation of perovskite solar cells. *Energy Environ. Sci.* **11**, 151-165, doi:10.1039/c7ee02415k (2018).
- Wang, J., Bi, L., Fu, Q. & Jen, A. K. Y. Methods for Passivating Defects of Perovskite for Inverted Perovskite Solar Cells and Modules. *Adv. Energy Mater.* **14**, 2401414, doi:10.1002/aenm.202401414 (2024).
- Ni, Z. et al. Resolving spatial and energetic distributions of trap states in metal

halide perovskite solar cells. *Science* **367**, 1352-1358, doi:10.1126/science.aba0893 (2020).